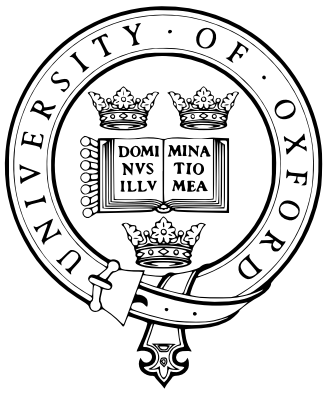
# Metal-Metal Bonding in Low-Dimensional Structures




Harry W. T. Morgan
University College
University of Oxford

A thesis submitted for the degree of
*Doctor of Philosophy*

Trinity 2021

# Acknowledgements

Firstly and foremostly I must thank John McGrady, who has over the past eight years been as magnificent a tutor, supervisor, and mentor as I could have imagined.
Heartfelt thanks to Lauren, Mum, Dad, Anna, and the rest of my family, for unwavering love and support.
This journey has been enjoyable thanks to Nick, Dom, Ali, Tom, and all the other friends with whom I have walked it, and from whom I have learned so much.
Finally, thanks to you, the reader, without whom this whole thing would have been pointless.

# Abstract

This thesis presents two computational investigations into the properties and behaviour of transition metal compounds. The first focuses on bonding patterns in endohedral Zintl clusters, and the second on structural processes in low-dimensional perovskites. Working across the ionic and covalent bonding paradigms, and molecular and periodic structures, we gain deeper insights into the chemical manifestations of fundamental principles of transition metal chemistry. We employ electronic structure theories and analytical tools which allow us to compare the behaviour of transition elements, and particularly the contrast between open and closed shell atoms, in a broad range of chemical environments. The majority of the research herein is performed in collaboration with experimental efforts, where we use theoretical insights to guide synthesis, aid analysis, and join the dots of experiment to draw a complete picture of the underlying chemistry.

# Statement of Originality

The work presented in this thesis is the original work of the author, except where references have been made to other sources. No part of this work has previously been submitted for any other degree.
Harry W. T. Morgan

# Contents


**1 Introduction** **1**

**2 Theoretical Background** **5**

2.1 Computation - Electronic Structure Theory . . . . . 5

2.1.1 Foundations . . . . . 5

2.1.2 Hartree-Fock theory . . . . . 6

2.1.3 Density functional theory . . . . . 8

2.1.3.1 Exchange-correlation functionals . . . . . 11

2.1.4 Post-Hartree-Fock theories . . . . . 12

2.1.4.1 CASSCF . . . . . 14

2.1.4.2 GASSCF . . . . . 16

2.1.5 Basis functions . . . . . 17

2.1.5.1 Slater-type orbitals . . . . . 17

2.1.5.2 Gaussian-type orbitals . . . . . 18

2.1.5.3 Plane waves . . . . . 19

2.1.5.4 Size, quality, and notation . . . . . 19

2.1.5.5 Core electrons . . . . . 21

2.2 Analysis - Molecular Symmetry . . . . . 21

2.3 Analysis - Chemical Bonding . . . . . 25

2.3.1 Foundations . . . . . 25

2.3.2 Molecular orbital theory . . . . . 25

2.3.3 The theoretical basis of some modern bond order measures . . 27

2.3.3.1 Mayer bond order . . . . . 28

2.3.3.2 Density matrices . . . . . 29

2.3.3.3 Atoms in Molecules . . . . . 31

2.3.3.4 Delocalization indices . . . . . 33

2.3.4 Energy decomposition analysis . . . . . 34

2.4 Electronic structure of solids . . . . . 35

2.4.1 Foundations . . . 35
2.4.2 Density of states . . . 36
2.4.3 Local projections . . . 37

**3 Metal-metal bonding in ligand-free clusters 39**
3.1 Introduction to clusters . . . 39
3.1.1 Boranes . . . 40
3.1.2 Bonding models and electron counting in clusters . . . 41
3.1.3 Group 14 Zintl ions . . . 42
3.1.4 TM-encapsulated group 14 clusters . . . 44
3.1.5 Quantum chemical studies of group 14 clusters . . . 47
3.2 $[M@Ge_{10}]^{3-}$ and $[M_2Ge_{16}]^{4-}$ fused pentagonal clusters . . . 49
3.2.1 Introduction . . . 49
3.2.2 Methods . . . 51
3.2.3 Results . . . 51
3.2.3.1 DFT studies of $[M@Ge_{10}]^{3-}$ . . . 51
3.2.3.2 DFT studies of $[M_2Ge_{16}]^{4-}$ . . . 53
3.2.3.3 The jigsaw bonding model . . . 57
3.2.3.4 Density of states analysis . . . 59
3.2.3.5 Multiconfigurational wavefunctions from CASSCF and GASSCF . . . 61
3.2.4 Conclusions . . . 67
3.3 Linear metal trimers $[(M@E_9)M'(M@E_9)]^{q-}$ . . . 69
3.3.1 Introduction . . . 69
3.3.2 Methods . . . 70
3.3.3 Results . . . 70
3.3.3.1 Understanding structural diversity . . . 70
3.3.3.2 Electronic structure, orbital analysis, and connection to $[(Ni@Ge_9)Ni(Ni@Ge_9)]^{4-}$ . . . 73
3.3.3.3 $[(Fe@Sn_9)Fe(Fe@Sn_9)]^{4-}$: an open-shell analogue of $[(Ni@Ge_9)Ni(Ni@Ge_9)]^{4-}$ . . . 75
3.3.4 Conclusions . . . 79
3.4 Growth patterns of coinage metal cores in lead shells . . . 80
3.4.1 Introduction . . . 80
3.4.2 Methods . . . 83

3.4.3 Results . . . 84
3.4.3.1 $[MPb_{11}]^{3-}$ and $[M_2Pb_{11}]^{2-}$ . . . 84
3.4.3.2 $[M_4Pb_{22}]^{4-}$ dimers . . . 88
3.4.3.3 $[Cu_4Pb_{22}]^{4-}$ and $[Cu_4Pb_{18}]^{4-}$ . . . 90
3.4.3.4 $[Fe_4Pb_{18}]^{4-}$: an open-shell analogue . . . 94
3.4.3.5 Larger gold clusters: $[Au_8Pb_{33}]^{6-}$ and $[Au_{12}Pb_{44}]^{8-}$ . . . 96
3.4.4 Summary and conclusions . . . 103
3.5 Conclusions and outlook . . . 106

**4 Structural processes in Ruddlesden-Popper oxyhydrides 111**
4.1 Introduction to oxyhydrides . . . 111
4.2 High-pressure phase transitions in oxyhydrides . . . 116
4.2.1 Methods . . . 116
4.2.2 $B1 - B2$ transitions in binary oxides . . . 117
4.2.3 Structural changes in vanadium oxyhydrides under pressure . . . 118
4.2.4 Pressure-dependent electronic behaviour of vanadium . . . 122
4.2.5 Sequential $B1 - B2$ transitions in $Ba_2YHO_3$ . . . 126
4.3 Hydride conduction in scandium oxyhydrides . . . 130
4.3.1 Methods . . . 130
4.3.2 Hydride conduction mechanisms in $Ba_2ScHO_3$ . . . 131
4.3.3 Anion disorder-dependence of diffusivity . . . 136
4.3.4 High pressure mechanism change . . . 136
4.3.5 Improved hydride conduction in $Sr_2ScHO_3$ . . . 141
4.3.6 Discussion . . . 143
4.4 Summary and conclusions . . . 145

**Perspective 147**

**Bibliography 149**

# List of Publications

The following publications have resulted from the work presented in this thesis, listed here in the order in which they appear in the text.

H. W. T. Morgan, K.-S. Csizi, Y.-S. Huang, Z.-M. Sun, J. E. McGrady. Open shells in endohedral clusters: structure and bonding in the $[Fe_2@Ge_{16}]^{4-}$ anion and comparison to isostructural $[Co_2@Ge_{16}]^{4-}$. *Journal of Physical Chemistry A*, **2021**, 125 (21), 4578

C. Zhang, H. W. T. Morgan, Z.-C. Wang, C. Liu, Z.-M. Sun, J. E. McGrady. Structural isomerism in the $[(Ni@Sn_9)In(Ni@Sn_9)]^{5-}$ Zintl ion. *Dalton Transactions*, **2019**, 48 (42), 15888

L. Qiao, C. Zhang, C.-C. Shu, H. W. T. Morgan, J.E. McGrady, Z.-M. Sun. $[Cu_4@E_{18}]^{4-}$ (E = Sn, Pb): Fused derivatives of endohedral stannaspherene and plumbaspherene. *Journal of the American Chemical Society*, **2020**, 142 (31), 13288

C.-C. Shu, H. W. T. Morgan, L. Qiao, J. E. McGrady, Z.-M. Sun. A family of lead clusters with precious metal cores. *Nature Communications*, **2020**, 11, 3477

T. Yamamoto, H. W. T. Morgan, D. Zeng, T. Kawakami, M. Amano Patino, M. A. Hayward, H. Kageyama, J. E. McGrady. Pressure-Induced Transitions in the 1-Dimensional Vanadium Oxyhydrides $Sr_2VO_3H$ and $Sr_3V_2O_5H_2$, and Comparison to 2-Dimensional $SrVO_2H$. *Inorganic Chemistry*, **2019**, 58 (22), 15393

H. W. T. Morgan, H. J. Stroud, N. L. Allan, Improving hydride conductivity in layered perovskites via crystal engineering, *Chemistry of Materials*, **2021**, 33 (1), 177185

# Chapter 1

# Introduction

The transition metals are the elements which occupy the large central block of the periodic table, called the "transition series" or "d-block". They are collectively known for certain physical and chemical properties which are common to most or all of them: the ability to form compounds containing unpaired electrons; variable oxidation states; ionic and covalent bonding modes; and brightly coloured compounds. These properties can, directly or indirectly, be traced back to the radial distribution functions (RDFs) of the valence $d$ orbitals, which are shown for Fe and Ru in Figure 1.1 alongside RDFs for the core and higher-lying orbitals. The Fe $3d$ RDF has

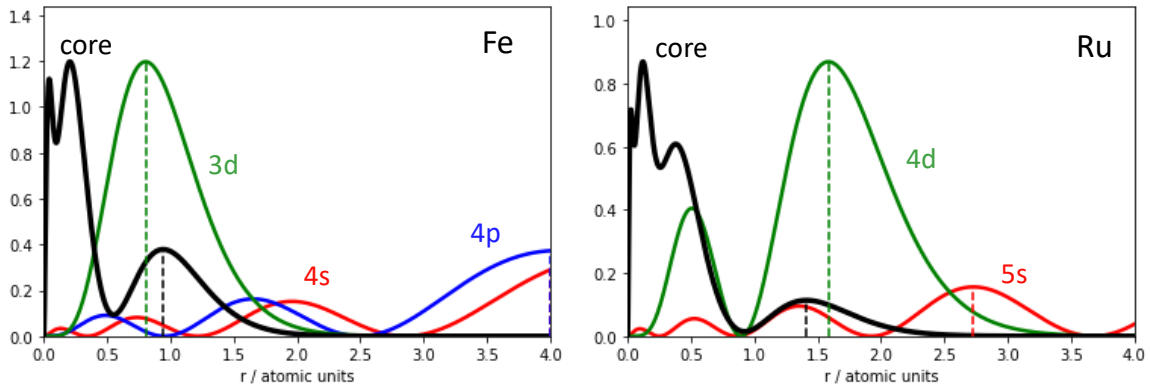



Figure 1.1: Radial distribution functions for the core and valence orbitals of Fe and Ru, plotted using parameters from Clementi[1, 2].

three features, common to all first-row transition metals, which define the chemical properties of these elements. Firstly, it lies mostly within the core, so covalent overlap between the $3d$ and a neighbouring atom is impaired by repulsion from the core electrons. Secondly, it has no inner radial maximum, unlike the $3s$ and $3p$ shells, so the $3d$ electrons are much higher in energy than $3s/p$ electrons due to shielding, but are stabilized more dramatically than the $4s/p$ by increases in the nuclear charge $Z$.

Thirdly, it has a narrow radial dispersion, meaning that a large number of electrons are contained within the same region of space and thus repel each other strongly. Since parallel spin electrons have a lower probability of being very close to each other in space than those with antiparallel spins, this leads to the propensity of $3d$ metals to contain multiple unpaired electrons. The Ru RDF shows similar behaviour, but to a lesser extent; the $4d$ maximum is further out from the core, there is an inner radial maximum allowing some penetration, and the peak is broader, reducing electron repulsions. These distinctions explain the chemical trends down any group in the transition series. In short, the transition metals show remarkable diversity in their ionic and covalent chemistry, adopting multiple oxidation states, spin states, and coordination geometries, all of which may change during the course of a reaction. These fundamental properties underpin the many roles played by transition metals in chemical applications. The ability to break and reform bonds during a reaction enables them to act as catalysts, in organometallic complexes and metalloenzymes, while variable oxidation states and strongly correlated electronic behaviour underpin their performance in solid state technological devices. It is clear that if we wish to improve the performance of transition metal compounds in any application we must do it by understanding the fundamentals.

Theoretical modelling and prediction of the behaviour of transition metal compounds has been a focus of research for some decades, and the field continues to grow today thanks to developments in theoretical descriptions of chemical behaviour and improvements in computing hardware. Nevertheless, transition metals present an enduring challenge to theories of electronic structure for the fundamental reasons described above - the distinct character of valence $d$ orbitals are often poorly captured by the approximate descriptions of electrons made by computationally efficient theories. Semi-empirical methods, like extended Hückel theory and Slater's $X_\alpha$ method, dominated in the later part of the $20^{\text{th}}$ century. *Ab initio* electronic structure theory calculations became widely available to researchers in the 1990s, with the implementation of Density Functional Theory (DFT) into software packages such as Gaussian and Amsterdam Density Functional for molecules, and the Vienna Ab Initio Simulation Package for solids. At this point, DFT became the method of choice for most computational chemistry problems, and even more so for solid-state physics, and for many applications this is still the case today. More recent developments, such as DLPNO-CC and multireference calculations, are also used with increasing frequency but are generally restricted to specific applications. As methods develop, the range of chemical problems which can be tackled increases. Computational transition metal

chemistry in the late 1990s and early 2000s was largely limited to model systems with small numbers of atoms, and focused on ground state properties such as structure, bonding, spectroscopy, and magnetism. By 2010 reactivity could be studied in detail, with more accurate DFT methods and transition state searches enabling computational chemists to deduce reaction mechanisms and study catalysis. Additionally, larger systems such as organometallic complexes, enzymes, and surfaces could be modelled with greater accuracy. Other developments have come through integration of electronic structure calculations with other theoretical descriptions of complex chemical systems, such as statistical mechanics. Applications in this area include thermodynamic modelling, electrochemistry, and dynamics simulations of condensed phases. High-throughput computational studies, involving automated calculations of vast numbers of chemical species, have also grown rapidly in recent years. These can be oriented towards crystal structure prediction, data-driven "cheminformatics", and machine learning of chemical information.

So, where does that bring us? Computational transition metal chemistry has grown into a diverse field, with many methods to tackle as many applications. Nevertheless, all are connected by the same properties of the elements, and this principle must lie at the heart of research in this area. In this thesis we investigate the behaviour of open and closed shell transition metal ions in distinct chemical contexts, using analytical tools that will allow us to compare behaviour in different environments. The first project concerns group 14 Zintl clusters encapsulating transition metal atoms. These molecular species have a remarkable array of possible structures, providing a range of chemical environments for the transition metal atoms within. Their unusual bonding properties require detailed investigation if we wish to guide future developments in this field. In particular, we focus on two connected aspects of endohedral Zintl cluster chemistry; the influence of the transition metal on the cage structure, and the bonding consequences of open transition metal shells. These phenomena are discussed in three groups of clusters: pentagonal prismatic germanium clusters containing one or two metal atoms; germanium and tin clusters containing linear metal trimers; and an oligomeric series of lead clusters encapsulating coinage metal cores of varying sizes. Each group contains a pair of open and closed shell isostructural analogues, so we have several opportunities to discuss the behaviour of paramagnetic metal centres. The second project concerns the structural chemistry of low-dimensional perovskites containing oxide and hydride anions. Perovskites have long been the subject of research for technological materials development, and mixed-anion materials have attracted particular interest in recent years. We first explore the interplay between structural

and electronic properties in controlling crystallographic transitions and electron transport in low-dimensional oxyhydrides, and then investigate the mechanism of hydride conduction in layered oxyhydrides containing $d^0$ transition metal cations and predict new materials for improved performance. Dimensionality is shown to be particularly important in determining trends in groups of related compounds, and design principles for future materials design are developed on this basis. Each of these projects has its own scientific background and body of literature, so detailed introductions are given in the relevant chapters. By understanding parallels between the behaviour of transition metals in distinct chemical contexts, we aim to gain deeper insights into these intriguing elements.

# Chapter 2

# Theoretical Background

This chapter will introduce most of the fundamentals required to perform and understand the research later in this thesis. It is divided into two major categories; "Computation", which describes the electronic structure theory upon which modern quantum chemical methods are based, and "Analysis", which describes the theory behind some important concepts which we will use extensively to interpret results, notably chemical bonding and molecular symmetry. The computation section charts the development of quantum chemistry from its foundations in the early twentieth century to the plethora of methods available today, focusing on those which will be employed extensively here. The applicabilities of the methods to molecular and periodic chemical systems will be discussed; the molecular methods will be used in our studies of encapsulated clusters, while the periodic methods relate to our studies of oxyhydrides. The analysis section focuses on the tools available for interpreting molecular calculations. We will summarize the mathematical description of molecular symmetry, and describe approaches to understanding bonding in molecules including the Lewis model, molecular orbital theory, and modern methods based on quantum chemical calculations.

## 2.1 Computation - Electronic Structure Theory

### 2.1.1 Foundations

Much of computational chemistry is concerned with finding solutions to the time-independent Schrödinger equation (TISE) for the total energy of a system:

$$\hat{H}\Psi = E\Psi \tag{2.1}$$

The Hamiltonian is the total energy operator, composed of terms which describe different interactions in a system of electrons and nuclei.

$$\hat{H} = \hat{T}_e + \hat{T}_n + \hat{V}_{ne} + \hat{V}_{ee} + \hat{V}_{nn} \tag{2.2}$$

The term $\hat{V}_{ee}$ is the interaction potential between pairs of electrons. As negatively charged particles, electrons interact with each other via Coulomb's law, so the strength of their interaction depends on the distance between them. However, being quantum particles, their positions cannot be specified precisely and are instead described by a probability distribution. Furthermore, their positions are mutually dependent, or "correlated", as they will avoid each other to reduce Coulomb repulsions. This means that the distances between electron pairs and the resulting interaction energies cannot be calculated analytically. This is known as the "many-body problem" and it renders the Schrödinger equation insoluble for any system with more than one electron. Thus, we may refine our earlier statement to say that much of computational chemistry is devoted to finding accurate *approximate* solutions to the Schrödinger equation.
An important step in simplifying the TISE is the Born-Oppenheimer approxmation, which says that the nuclei are so much heavier than the electrons that they are stationary on the timescale of electronic motion. This reduces the nuclear kinetic energy term $\hat{T}_n$ to zero and the internuclear potential $\hat{V}_{nn}$ to a constant, allowing us to define an electronic Hamiltonian and associated Schrödinger equation:

$$\hat{H}_e = \hat{T}_e + \hat{V}_{ne} + \hat{V}_{ee} \tag{2.3}$$

$$\hat{H}_e \Psi_e = E_e \Psi_e \tag{2.4}$$

Another significant result in quantum chemistry is the variational principle. This states that if we guess a trial wavefunction $\Psi'$ for a system, the associated trial energy $E'$ must be higher than the true ground state energy. We can therefore improve our estimate of the ground state energy by searching for the lowest energy wavefunction within a set of eligible wavefunctions; in practice this can be done by minimizing the trial energy with respect to parameters within the trial wavefunction.

$$E' = \frac{\langle \Psi' | \hat{H} | \Psi' \rangle}{\langle \Psi' | \Psi' \rangle} \geq E_0 = \frac{\langle \Psi_0 | \hat{H} | \Psi_0 \rangle}{\langle \Psi_0 | \Psi_0 \rangle} \tag{2.5}$$

### 2.1.2 Hartree-Fock theory

When formulating the Schrödinger equation we are still faced with the problem of unknown interactions between electrons. One solution is given by Hartree-Fock theory, which describes each electron as moving in the average field of all other electrons.

The total N-electron wavefunction is then given as an antisymmetrized product of N one-electron wavefunctions often written as a "Slater determinant":

$$\Psi_{HF} = \frac{1}{\sqrt{N!}} \begin{vmatrix} \psi_1(1) & \psi_2(1) & \cdots & \psi_N(1) \\ \psi_1(2) & \psi_2(2) & \cdots & \psi_N(2) \\ \vdots & \vdots & \ddots & \vdots \\ \psi_1(N) & \psi_2(N) & \cdots & \psi_N(N) \end{vmatrix} \tag{2.6}$$

In this notation each column describes a single-electron wavefunction, called a molecular orbital (MO) in molecular quantum chemistry, while each row corresponds to a particular electron. A determinant is used to ensure that the wavefunction is antisymmetric with respect to exchange of any pair of electrons, as required by the Pauli principle.

But where do these MOs come from? In molecules with multiple electrons the orbitals cannot be found by solving the Schrödinger equation analytically, so we require an Ansatz. We will use the Linear Combination of Atomic Orbitals (LCAO) method, whereby we construct MOs from the atomic orbitals of the atoms in the molecule:

$$\psi_i = c_A\phi_A + c_B\phi_B + \ldots \tag{2.7}$$

$$\psi_i - \text{Molecular orbital } i \tag{2.8}$$

$$\phi_A - \text{Atomic orbital } A \tag{2.9}$$

$$c_A - \text{coefficient of } \phi_A \text{ in the expansion of } \psi_i \tag{2.10}$$

This intuitive approach is particularly useful for understanding chemical trends because it allows us to compare the behaviour of different compounds by examining their constituent atoms.

The variational freedom when minimizing the energy of the total wavefunction is in the choice of the one-electron orbitals - more precisely, the coefficients in Equation 2.7. These are optimised by the Hartree-Fock equations:

$$\hat{f}_i\psi_a(i) = \varepsilon_a\psi_a(i) \tag{2.11}$$

$\psi_a$ and $\varepsilon_a$ are the one-electron eigenfunctions and energy eigenvalues of the one-particle Hamiltonian $\hat{f}_i$ for electron $i$ in spin-orbital $a$, called the Fock operator:

$$\hat{f}_i = -\frac{1}{2}\nabla_i^2 - \sum_A^M \frac{Z_A}{r_{iA}} + \sum_b [\hat{J}_b(i) - \hat{K}_b(i)] \tag{2.12}$$

The first two terms in this operator are the kinetic and electron-nuclear interaction energies, which make up the one-electron "core" Hamiltonian. The final sum, over

all occupied spin-orbitals, is the Hartree-Fock potential, made up of the Coulomb operator $\hat{J}$ and the exchange operator $\hat{K}$ whose expectation values can be written in bra-ket notation:

$$\langle\psi_a(i)|\hat{J}_b(i)|\psi_a(i)\rangle = \langle\psi_a^*(i)\psi_a(i)|\frac{1}{r_{ij}}|\psi_b^*(j)\psi_b(j)\rangle \tag{2.13}$$

$$\langle\psi_a(i)|\hat{K}_b(i)|\psi_a(i)\rangle = \langle\psi_a^*(i)\psi_b(i)|\frac{1}{r_{ij}}|\psi_b^*(j)\psi_a(j)\rangle \tag{2.14}$$

$\hat{J}$, the Coulomb integral, can be understood fairly straightforwardly. It describes the electrostatic interaction of electron $i$ in spin-orbital $\psi_a$ with electron $j$ in spin-orbital $\psi_b$ where the positions of the electrons have been averaged over their one-electron orbitals. This is the essence of Hartree-Fock theory, replacing the two-electron potential which depends on the instantaneous positions of the two electrons by a one-electron potential in which the position of one electron has been averaged. $\hat{K}$, the exchange integral, does not have a classical analogue and is more challenging to interpret. As we can see from equation 2.14, it describes an electrostatic interaction resulting from exchanging the orbitals of electrons $i$ and $j$. It is sometimes called a "non-local" quantity because, unlike $\hat{J}$, it does not have a single defined value at each point in space. We can also see that when $a = b$, $\langle J\rangle = \langle K\rangle$ so the orbital feels no Hartree-Fock potential from interaction with itself.
Comparing equation 2.11 to equations 2.13 and 2.14 we can see that the HF equations cannot be solved directly because the Fock operator $\hat{f}$ depends on the orbitals $\psi_a$. Instead, we must take an iterative approach. We guess an initial set of orbitals and solve the HF equations to get a new set; this procedure is repeated until the input and output orbitals differ by less than a predefined threshold. This approach is called the "Self-consistent field", or SCF, method. While Hartree-Fock theory treats the exchange interaction exactly, the mean-field approximation means that the electrons are under-correlated, so they are unable to avoid each other as real electrons would. HF electrons therefore spend too much time close together, so the Coulomb repulsion terms are overestimated. Alternative electronic structure methods, intended to improve upon HF theory, can be grouped into density functional methods, which change the Hamiltonian, and post-HF theories, or "wavefunction" theories, which change the wavefunction.

### 2.1.3 Density functional theory

The Hartree-Fock N-electron wavefunction depends on 3N spatial variables and N spin variables, making it very complex for large systems. Density functional theory

(DFT) is the result of the attempt to replace this wavefunction with the electron density, which depends only on 3 dimensions of space. This function of space then becomes the argument of a functional to give a physical observable such as the energy of the system. The theoretical justification for modern DFT came in the form of two theorems derived by Hohenberg and Kohn[3] in 1964:

1. The electron density uniquely defines the Hamiltonian and therefore all properties of the system

2. The functional which gives the ground state energy of the system obeys the variational theorem, *i.e.* it gives the lowest energy if and only if the input density is the true ground state density

These theorems are significant because they prove the legitimacy of the electron density as a route to the ground state energy. However, they do not provide a way to construct the true functional which gives the ground state energy, so we are forced to make approximations. This is a problem because the second theorem only applies to the true functional; this opens up the possibility of underestimating energies and makes it impossible to identify the best estimate of the ground state energy as in a variational method. In the absence of an analytical form for the exact functional, we must construct an approximation. The earliest of these was developed by Thomas and Fermi, long before the Hohenberg-Kohn theorems, on the basis of statistical distributions of electrons in atoms, and has the simple form:

$$E^{TF}\{\rho(\boldsymbol{r})\} = C\int \rho^{\frac{5}{3}}(\boldsymbol{r})d\boldsymbol{r} - Z\int \frac{\rho(\boldsymbol{r})}{r}d\boldsymbol{r} + \frac{1}{2}\int\int \frac{\rho(\boldsymbol{r}_1)\rho(\boldsymbol{r}_2)}{|\boldsymbol{r}_1 - \boldsymbol{r}_2|}d\boldsymbol{r}_1 d\boldsymbol{r}_2 \qquad (2.15)$$

The three terms in this expression describe kinetic energy, electron-nucleus interactions and electron-electron interactions respectively. The largest contribution to the total energy is the kinetic energy, so this is where the need for a good approximation is greatest. Unfortunately, the Thomas-Fermi kinetic energy is insufficiently accurate for chemical applications, failing to predict the formation of any bonds, and this remains the major barrier to DFT methods which utilize the density directly, often called "orbital-free DFT" for reasons which we will now see.
To make progress with accurate kinetic energy calculations we will use the exact expressions for kinetic energy and density, in terms of orbitals, for a system of $N$

non-interacting electrons:

$$T_0 = \sum_i^N \langle \psi_i | \tfrac{-1}{2} \nabla^2 | \psi_i \rangle \tag{2.16}$$

$$\rho(\boldsymbol{r}) = \sum_i^N |\psi_i(\boldsymbol{x})|^2 \tag{2.17}$$

Kohn and Sham applied this to quantum chemistry by introducing a reference system of non-interacting electrons with the same density as the real system, so the kinetic energy expression above can be used to calculate its kinetic energy very accurately. The total energy functional is then:

$$E^{KS}\{\rho(\boldsymbol{r})\} = T_0\{\rho(\boldsymbol{r})\} + \frac{1}{2}\int\int \frac{\rho(\boldsymbol{r}_1)\rho(\boldsymbol{r}_2)}{|\boldsymbol{r}_1 - \boldsymbol{r}_2|} d\boldsymbol{r}_1 d\boldsymbol{r}_2 + E_{xc}\{\rho(\boldsymbol{r})\} + \int \rho(\boldsymbol{r})\nu(\boldsymbol{r}) d\boldsymbol{r} \tag{2.18}$$

These terms respectively describe the kinetic energy of the non-interacting reference system, the classical electrostatic energy of the charge density, an energy functional for the exchange and correlation energies, and the electrostatic interaction of the electron density with the nuclei. This treatment of the kinetic energy is much more accurate than the orbital-free approach because small variations in the curvature of the total density can be addressed much more effectively when decomposed into individual electron contributions. However, it reintroduces the need for an iterative, self-consistent approach based on the Kohn-Sham equations:

$$\left[\tfrac{-1}{2}\nabla^2 + \nu_{\text{eff}}(\boldsymbol{r})\right]\psi_i(\boldsymbol{r}) = \epsilon_i \psi_i(\boldsymbol{r}) \tag{2.19}$$

$$\nu_{\text{eff}}(\boldsymbol{r}) = \nu(\boldsymbol{r}) + \int \frac{\rho(\boldsymbol{r}')}{|\boldsymbol{r} - \boldsymbol{r}'|} d\boldsymbol{r}' + \nu_{xc}(\boldsymbol{r}) \tag{2.20}$$

The terms of the effective one-particle potential $\nu_{\text{eff}}$ describe the interaction of each electron with the nuclei, the electrostatic interaction with the other electrons, and the exchange-correlation potential, respectively. This is non-linear in the same manner as the Hartree-Fock equations because $\nu_{\text{eff}}$ depends on the density $\rho$ and therefore on the orbitals $\psi_i$. The broad success of DFT in describing real chemical systems can be attributed to the strategy of treating the largest contributions to the energy as accurately as possible, and approximating the smaller exchange and correlation terms.

#### 2.1.3.1 Exchange-correlation functionals

This scheme only works in practice if good approximations to the exchange-correlation functional can be found. The simplest type of approximation is the Local Density Approximation (LDA) which assumes that the exchange-correlation energy $E_{xc}$ depends only on the density at a point $\boldsymbol{r}$:

$$E_{xc}^{LDA}[\rho] = \int \rho(\boldsymbol{r})\epsilon_{xc}(\rho(\boldsymbol{r}))\, d\boldsymbol{r} \tag{2.21}$$

$\epsilon_{xc}$ is the exchange-correlation energy per particle, which can be separated into a sum of exchange and correlation terms $\epsilon_x + \epsilon_c$.
The most successful LDA functionals are based on a uniform electron gas model, in which the number of electrons and the volume of the gas approach infinity but the electron density is constant everywhere. The benefit of this model is that it is the only system for which we have an accurate description of the exchange and correlation energy functionals. The homogeneous electron gas resembles a perfect crystal of valence electrons and smeared-out ion cores, and so it provides a reasonable description of simple metals but a poor one for molecules, in which electron density is far from homogeneous.
The LDA is not often accurate enough for chemical applications, but it can be improved upon by including information about the gradient of the charge density at a particular point to account for non-homogeneity in real systems. Called the "Generalized Gradient Approximation" (GGA), this is much like taking the first two terms in a Taylor expansion of the electron density:

$$E_{xc}^{GGA}[\rho] = \int \rho(\boldsymbol{r})\epsilon_{xc}(\rho(\boldsymbol{r}), \nabla\rho(\boldsymbol{r}))\, d\boldsymbol{r} \tag{2.22}$$

This is an important class of functional due to a good cost:accuracy ratio, particularly when working with Slater or plane-wave basis sets - see Section 2.1.5. Widely-used examples include BP86[4] and PBE[5], the second of which remains the workhorse of computational solid-state chemistry.
Some errors of Hartree-Fock theory are consistently over-corrected by GGA functionals. In transition metal chemistry, for example, HF theory generally favours high-spin states while GGAs favour low-spin states. An appealing strategy is therefore to combine the two methods in a "hybrid functional" in which the electronic exchange is partially described as in Hartree-Fock theory, *i.e.* exactly, and correlation is dealt with by a DFT functional. This is common practice in molecular DFT, and the B3LYP[4, 6] functional has become a standard choice for organic chemistry[7]. Such

functionals can be formulated in slightly different ways, which we will illustrate with some examples. The simplest hybrid functionals replace a fixed fraction of the GGA exchange energy with that from HF theory:

$$E_{xc}^{hybrid} = \alpha E_x^{GGA} + (1-\alpha)E_x^{HF} + E_c^{GGA} \tag{2.23}$$

For example, PBE0 uses PBE as its GGA basis and $\alpha = \frac{1}{4}$[8]. The choice of one quarter is derived from perturbation theory, but many alternative parameterizations have been proposed based either on theoretical grounds or by fitting results to experimental data. The B3LYP functional uses three such parameters for the exchange and correlation terms, and others may use far more. HSE06[9], increasingly popular in solids, tries to capture the accuracy of a hybrid functional at minimal additional computational cost by using a form like that of PBE0 at short range and PBE at long range, with an error function to vary smoothly between the two.

A systematic failure of LDA and GGA is their tendency to underestimate the Coulomb interaction between electrons in strongly correlated systems, where the weakly interacting electron gas description is unreasonable. A computationally inexpensive solution to this problem is to add an extra repulsion term, called the Hubbard U, to the total energy calculation. DFT+U is widely used to model transition metal oxides as it frequently reproduces experimentally observed insulating ground states when ordinary DFT predicts metallic conductivity[10]. It is an alternative to the hybrid methodology, used extensively in solid-state chemistry due to the cost of hybrid functional calculations in a plane-wave basis but rarely seen in molecular chemistry.

DFT functionals remain an active field of research, with ever more complex, costly and (hopefully) accurate methods being developed. Since GGA improved on LDA by including the first derivative of the density, we may continue this Taylor expansion to get a meta-GGA, which also considers the Laplacian of the density or the kinetic energy density. Alternatively, we may extend the hybrid idea of using HF theory for the exchange term by describing some correlation using MP2, founded on perturbation theory. Since we have no information on the nature of the true functional promised by the Hohenberg-Kohn theorems, any of these methods may give a prediction that matches an experimental observation; a "good" functional must do so across a range of systems at a manageable computational cost.

### 2.1.4 Post-Hartree-Fock theories

In HF theory we wrote the wavefunction as a Slater determinant, which is an antisymmetric product of all occupied one-electron orbitals in the system. These one-

electron orbitals exist because of the mean-field HF approximation, which avoids the many-body problem by averaging the electron-electron repulsions. The resulting uncorrelated electron behaviour is the root of inaccuracies in HF theory, so we need a way to reintroduce the effects of electron correlation into our wavefunction.

The Slater determinant corresponds to an electron configuration that we might write in an MO diagram, with individual orbitals occupied or vacant. In some cases a single determinant is enough to describe a wavefunction, such as that for the ground state of helium:

$$\Psi_{He} = \frac{1}{\sqrt{2}}(\phi_{1s}(1)\phi_{1s}(2)) \times (\alpha(1)\beta(2) - \beta(1)\alpha(2)) \tag{2.24}$$

$$= \frac{1}{\sqrt{2}} \begin{vmatrix} \phi_{1s}(1)\alpha(1) & \phi_{1s}(1)\beta(1) \\ \phi_{1s}(2)\alpha(2) & \phi_{1s}(2)\beta(2) \end{vmatrix} \tag{2.25}$$

This wavefunction describes the possibilities of either electron being spin-$\alpha$ and the other being spin-$\beta$. However, many wavefunctions, particularly those for open-shell systems, cannot be described by a single Slater determinant. For example, the open-shell singlet excited state of helium must be expressed as a linear combination of two determinants:

$${}^1\Psi^*_{He} = \frac{1}{2}(\phi_{1s}(1)\phi_{2s}(2) + \phi_{1s}(2)\phi_{2s}(1)) \times (\alpha(1)\beta(2) - \beta(1)\alpha(2)) \tag{2.26}$$

$$= \frac{1}{2} \begin{vmatrix} \phi_{1s}(1)\alpha(1) & \phi_{2s}(1)\beta(1) \\ \phi_{1s}(2)\alpha(2) & \phi_{2s}(2)\beta(2) \end{vmatrix} - \frac{1}{2} \begin{vmatrix} \phi_{1s}(1)\beta(1) & \phi_{2s}(1)\alpha(1) \\ \phi_{1s}(2)\beta(2) & \phi_{2s}(2)\alpha(2) \end{vmatrix} \tag{2.27}$$

Neither of these determinants is enough by itself to describe the wavefunction. The first only describes the $\alpha$ electron in $\phi_{1s}$ and the $\beta$ electron in $\phi_{2s}$, while the second describes only the opposite, so both are required to capture the full range of configurations contributing to this wavefunction. A linear combination of this form is called a "configuration state function" (CSF).

To give our wavefunction more flexibility while keeping the one-electron orbitals, we can expand it by adding other configuration state functions. This is akin to mixing excited electronic states into the ground state, and is called the "configuration interaction" (CI) method. Our new wavefunction is a linear combination of CSFs, with coefficients which must be optimized. If we were to include every possible CSF, *i.e.* every excited electronic state, in our wavefunction, then we would effectively solve the many-body problem. Needless to say, this is impossible in practice for all but the smallest systems because the size of the calculation scales exponentially with the number of electrons. Instead, we must decide which CSFs to include in our expansion of the wavefunction. This approach can be justified by the idea that very high

energy states are unlikely to contribute significantly to the wavefunction. One way to truncate the expansion is to include states describing excitations of a small number of electrons. For example, a "CISD" calculation is one where we include all single and double excitations. CI in this form is not widely used as it does not have a good cost-accuracy tradeoff.

#### 2.1.4.1 CASSCF

For systems with low-lying excited states, a single Slater determinant may be insufficient to describe the wavefunction due to quantum mechanical mixing of states. Examples might include molecules undergoing bond dissociation, or first row transition metal complexes which form weak metal-ligand bonds due to the small radial extent of the $3d$ valence orbitals. In such cases it is important that our description of the wavefunction accounts for these states, which can be done with a multiconfigurational self-consistent field (MCSCF) approach. A particularly important member of this class is the complete active space self-consistent field (CASSCF, or CAS) method. In this method we divide the orbitals in the molecule into three subsets, or 'spaces':

1. Occupied - low-energy orbitals which contain two electrons
2. Active - orbitals which we believe to contribute strongly to the multiconfigurational character of the wavefunction
3. Virtual - high-energy empty orbitals

The partitioning scheme is illustrated on the left-hand side of Figure 2.1. CASSCF calculations are described as 'CAS$(m, n)$' where the active space contains $m$ electrons in $n$ orbitals. We then perform a calculation on the active space in which we optimize the orbitals and CI expansion coefficients while considering all possible excitations, and treat the occupied orbitals with HF theory.

'State averaging' is an important part of the CASSCF method. The active space generates a large number of excited states, all of which are constructed from the same set of orbitals. We have a choice about which excited states are used to create these orbitals. The simplest option, analogous to CI and indeed HF calculations, is to use only the ground state to form the orbitals. However, CASSCF is designed for systems with low-lying excited states which contribute significantly to the true ground state wavefunction, so it may be preferable in such cases to use orbitals which are formed by averaging over a particular set of states. It is also possible to use orbitals generated from just one excited state. The best state averaging strategy depends on the system

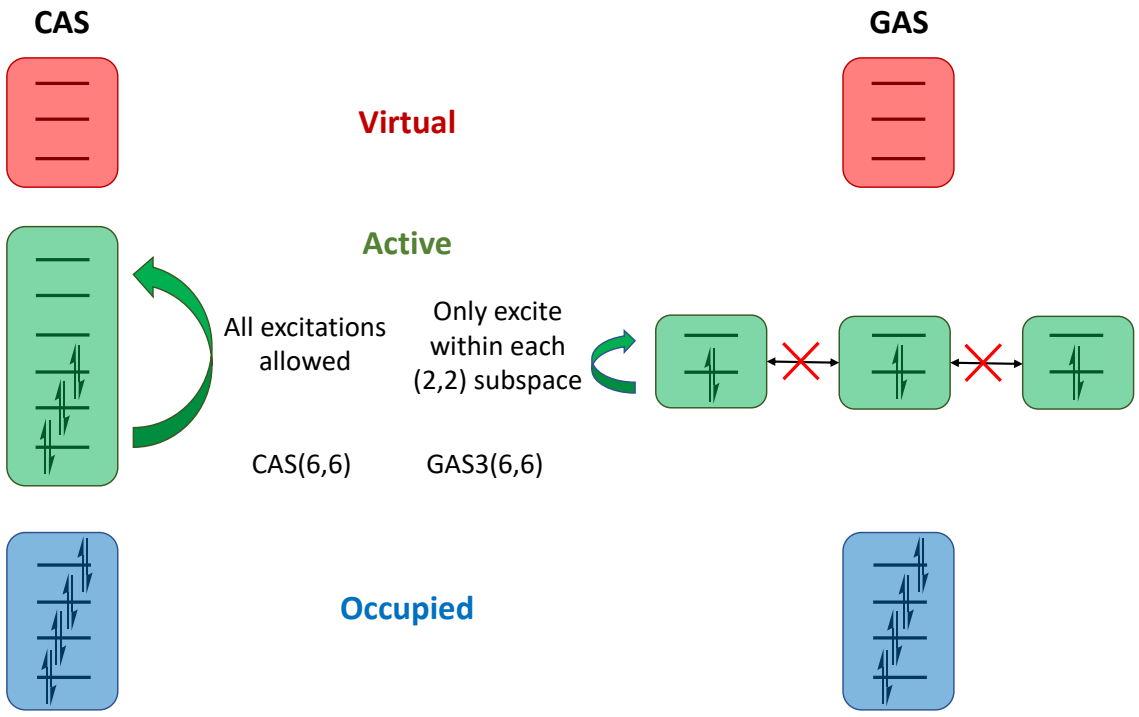



Figure 2.1: The division of molecular orbitals into spaces according to the CASSCF and GASSCF methods.

and the purpose of the calculation.

As discussed, post-HF methods improve the description of electron correlation which was lost by the HF approximation. The correlation energy $E_{corr}$ is often defined in this way, since it does not correspond to any quantum-mechanical property:

$$E_{corr}^{exact} = E^{exact} - E^{HF} \tag{2.28}$$

It is common to divide correlation in post-HF methods into 'static' and 'dynamic' correlation. Static correlation refers to errors in HF theory arising from the description of the wavefunction by a single Slater determinant, due to degenerate or near-degenerate electron configurations, while dynamic correlation describes the reduction in repulsion energy from electrons avoiding each other in space which is not described by the HF mean-field approach. The distinction between static and dynamic is not physically well-defined but may be a useful guide for identifying a suitable theoretical method for a chemical problem. CASSCF addresses static correlation only, but dynamic correlation may well be important for accurate energies. In the CASPT2 method, an energy correction for dynamic correlation is calculated using perturbation theory, closely related to the MP2 method for improving HF energies.

#### 2.1.4.2 GASSCF

The cost of CASSCF calculations increases exponentially with the size of the active space. In practice, the largest manageable calculations with current computational resources are around CAS(16,16). For systems where such a calculation would be insufficient to describe the number of strongly correlated orbitals, such as those involving multiple transition metal atoms, modifications to the method are required. One such is the 'Generalized active space' (GASSCF, or GAS) method, which reduces computational cost by reducing the complexity of the active space. In a CAS calculation we consider all possible excited states within the active space, but this may incur great computational expense for states which turn out to make a negligible contribution to the wavefunction. GASSCF removes these near-zero matrix elements by partitioning the active space into orbital subspaces which have strong correlation within each group, but not between them, as illustrated in Figure 2.1. If the GAS subspaces are chosen appropriately then much larger active spaces can be calculated without a problematic loss of accuracy - this may be possible for symmetrical systems, where many excitations are symmetry-forbidden, or systems with "active regions" (e.g. transition metal atoms) which are far apart in space or otherwise non-interacting.
An alternative strategy for reducing the cost of a multiconfigurational calcuation is the 'Restricted active space' (RASSCF, or RAS) method. In this approach the active orbitals are divided between three groups, each with a different restriction on the number of electrons which it may contain:

- RAS1 - The lowest-energy group. Excitations from this group are limited by a minimum occupancy for the group.
- RAS2 - Excitations in and out of this group are unrestricted, as in a CAS calculation.
- RAS3 - The highest-energy group. Excitations into this group are limited by a maximum occupancy.

This approach aims to remove highly excited configurations, involving population of many high-energy active orbitals or depopulation of low-energy active orbitals, as these are likely to make a minimal contribution to the wavefunction. However, there may not be a well-defined way to assign orbitals to the RAS groups, and this method does not remove excitations which make negligible contributions to the wavefunction due to symmetry considerations.

### 2.1.5 Basis functions

HF-theory and DFT both provide ways to compute the electronic structure of chemical systems, but a set of basis functions is required alongside the operators. These functions are the building blocks from which we construct the wavefunction and any molecular orbitals. In molecular systems, we use localised atomic-orbital-like functions as the basis, while in solids, which possess translational symmetry, we may instead use periodic plane waves.

#### 2.1.5.1 Slater-type orbitals

Our starting point for developing basis functions which mimic atomic orbitals is to consider the forms of the orbitals themselves, given by the solutions to the Schrödinger equation for the hydrogen atom. In the orbital approximation we assume that the atomic orbitals for many-electron atoms are similar to those for hydrogen and that the total wavefunction is an antisymmetrized product of these one-electron orbitals. The radial parts of the hydrogenic orbitals, which describe the change in the wavefunctions as the distance from the nucleus changes, depend upon distance exponentially:

$$\psi(r) \propto L(r)e^{-\alpha r} \tag{2.29}$$

$L(r)$ are the Legendre polynomials, which depend on the quantum numbers of the orbitals and dictate the number of radial nodes.
The most intuitive set of basis functions are therefore the Slater-type orbitals (STOs) which have the form:

$$\psi^{STO}(r) = Nr^{n-1}e^{-\zeta r} \tag{2.30}$$

$n$ is the principal quantum number of the orbital, and N is a normalization constant, and $\zeta$ controls the rate of exponential decay. In a minimal basis of one STO per orbital, $\zeta$ is the effective nuclear charge.
Basis functions of this form correctly reproduce the shape of the hydrogenic orbitals very close to the nucleus, known as "Kato's cusp condition", and have the same exponential decay. The only substantial difference between an STO and a hydrogenic orbital is that the former contains no radial nodes. A "minimal basis" might use a single STO to model each atomic orbital, while a larger basis would use multiple STOs for each AO. The basis set may also be expanded by the inclusion of "polarization functions", which allow the the shapes of the atomic orbitals to change from their spherically symmetric characters (spherical for $s$, dumbbell-shaped for $p$, and so on)

as may be required in a molecule. For example, adding polarization functions to an $s$ orbital might mean adding $p$-type functions to allow the $s$ orbital to distort from being perfectly spherical. This adds flexibility, allowing us to better model subtle changes in the wavefunction of a molecule. Unfortunately, calculations involving STOs are relatively slow. Spatial overlaps between these functions are challenging to evaluate, since the functions are not separable in $x, y, z$ and products of STOs have a very complicated form, making two-electron Coulomb and exchange integrals computationally expensive. This makes STOs less practical for calculations involving Hartree-Fock exchange, such as hybrid DFT functionals and post-HF methods. We will use STOs for the majority of our DFT investigations into cluster compounds, as hybrid functionals are not required and they are the basis functions used by the Amsterdam Density Functional (ADF) software package.

#### 2.1.5.2 Gaussian-type orbitals

An alternative basis function form is the Gaussian function:

$$\psi^{GTO}(r) = Nr^l e^{-\zeta r^2} \tag{2.31}$$

$l$ is the orbital angular momentum quantum number.
The important difference here is the $r^2$ term in the exponent. This makes the wavefunction decay much more quickly than in an STO, and it also changes the shape of the function close to the nucleus, so at first glance GTOs appear to be an inferior model of atomic orbitals. However, they have substantial practical advantages. They are separable in $x, y, z$, and the product of two Gaussian functions is another Gaussian, so the two-electron integrals are far easier to compute and calculations are much faster. It is therefore practical to use multiple Gaussian functions, called "primitives" to model a single atomic orbital, as the acceleration relative to using STOs outweighs the additional cost of using many Gaussians. A minimal basis set may model each atomic orbital by a single basis function, which is formed by a fixed linear combination of Gaussian primitives. Larger basis sets, ubiquitous in modern computational chemistry, describe each orbital with multiple basis functions, each composed of a linear combination of Gaussians. Polarization functions can be added to GTOs just as for STOs, and it is also possible to add "diffuse functions" - slow-decaying exponentials which may capture electron density held far from the nucleus, particularly for anions. A GTO basis will be used for our multiconfigurational calculations on $[M@Ge_{10}]^{3-}$ and $[M_2@Ge_{16}]^{4-}$ because CASSCF/GASSCF are post-HF

methods which require two-electron exchange integrals, as well as our investigation into $[Ni_2InGe_{18}]^{5-}$ because the ORCA software package uses a GTO basis.

#### 2.1.5.3 Plane waves

An entirely different approach to building up the wavefunction is possible in periodic systems. Rather than using basis functions located on each atom, we can use plane wave functions which have the same periodicity as the lattice. A plane wave is a function which oscillates in one spatial direction and is constant in the other two directions. In three dimensions they have the form:

$$F(\boldsymbol{r}) = e^{i\boldsymbol{k}\cdot\boldsymbol{r}} \tag{2.32}$$

where the plane wave has wavevector $\boldsymbol{k}$, the magnitude of which is the angular wavenumber $k$.
Combining this with Bloch's theorem (see section 2.4) allows us to write the solutions to the Schrödinger equation, called the "Bloch orbitals" in this context, as a linear combination of plane waves multiplied by a function with the periodicity of the lattice:

$$\psi_n(\boldsymbol{r}) = \sum_{\boldsymbol{G}} c_{n,(\boldsymbol{k}+\boldsymbol{G})} e^{i(\boldsymbol{k}+\boldsymbol{G})\cdot\boldsymbol{r}} \tag{2.33}$$

where $\boldsymbol{G}$ are the reciprocal lattice vectors and $c_{n,(\boldsymbol{k}+\boldsymbol{G})}$ are the coefficients of the plane waves. The sum in Equation 2.33 runs over all plane waves in the basis. This expression is analogous to a linear combination of atomic orbitals, but the localized orbitals have been replaced by delocalized waves (which are localized in reciprocal space).

#### 2.1.5.4 Size, quality, and notation

Describing a Slater-type basis is relatively straightforward due to the similarities between STOs and hydrogenic orbitals. The size of the basis set is generally described in terms of $\zeta$ to refer to the exponents in the STOs used to model the AO. A minimal basis would be described as "single zeta" (SZ), while a "double zeta" (DZ) basis uses two STOs per AO, and so on. This is known as "split valence" as each valence orbital is separated into multiple basis functions. A triple-zeta basis with one polarization function per AO would be denoted "TZP".
GTO basis sets are more complex to describe, partly because so many primitives can be used, and partly because many different basis sets have been developed. The

simplest are Pople's STO-nG basis sets, where each STO is modelled by n Gaussians. Much more accurate are split-valence basis sets, in which the valence orbitals are split into multiple basis functions as in the same way as was done for STOs. The Pople split valence basis sets are denoted X-YZG, where each core orbital is modelled by X Gaussian primitives, and each valence orbital is split into two basis functions composed of Y and Z primitives respectively. Polarization functions are denoted by a *, and diffuse functions by a +. For example, the 6-31+G* basis set is a double-zeta basis set with one diffuse function and one polarization function per orbital. More modern basis sets have been developed which give superior results. One example is the Karlsruhe "def2" sets[11], where double zeta with polarization is denoted def2-SVP, triple zeta with polarization def2-TZVP, and diffuse functions are denoted D. Generally, a larger basis set should give better results than a smaller one as the wavefunction can be constructed to a finer level of detail. However, there is no systematic way to improve a GTO basis set, as shown by the number of possible families available for use.

Plane wave basis sets are much easier to describe as they contain no fitting parameters and their size is controlled by a single number. An infinite number of basis functions would be required to reconstruct the true wavefunction precisely, but in practice we must truncate the expansion. Low-energy waves, with small $k$, generally make a more important contribution to the wavefunction than very high-energy waves, so we include all waves up to a certain cut-off energy:

$$\frac{1}{2}|\boldsymbol{k}+\boldsymbol{G}|^2 < E_{cut} \tag{2.34}$$

The relationship between angular wavenumber and energy is given by the de Broglie relation:

$$k = \frac{p}{\hbar} = \frac{\sqrt{2mE}}{\hbar} \tag{2.35}$$

The quality of the description of the wavefunction increases monotonically as we increase the size of the basis by raising $E_{cut}$. The dependence of the size of the basis set on the size of the unit cell, shown by Equation 2.34, introduces a source of error in structural optimizations, called Pulay stresses, in which a change to the lattice parameters changes the basis set during the calculation. This leads to a change in the total energy and favours contraction of the cell, which increases $\boldsymbol{G}$ and effectively increases the basis set. In practice this issue is negligible if a sufficiently large basis set is used, which is achievable in routine calculations with modern computational resources.

#### 2.1.5.5 Core electrons

In many-electron atoms, core orbitals are held sufficiently close to the nucleus and are of such low energy that they do not generally contribute to bonding. For light atoms, it may be feasible to explicitly calculate all electrons, while for heavier atoms we can describe only the valence orbitals, and treat the core approximately. This approach makes calculations more economical, and may improve accuracy because the core electrons interact strongly with the nucleus and may be affected by relativity, so our treatment of them could strongly influence the total energy of the molecule without providing useful chemical information. The core of a heavy atom can be modelled in one of two main ways. The first is the "frozen core" approximation, in which all electrons are present in the calculation but the core orbitals are not optimized in the SCF procedure. The second is to model the nucleus and core by an electrostatic object, located around the nucleus, called a "pseudopotential" with which the valence electrons interact. Both approaches may be used in calculations with an STO/GTO basis, but for plane-wave calculations it is necessary to use pseudopotentials. This is because a great deal of flexibility is required to reproduce the dramatic curvature of the wavefunction near the nuclei, which means that the plane wave basis must include very high-energy (*i.e.* high frequency) functions.

## 2.2 Analysis - Molecular Symmetry

In section 2.1.2 we introduced the LCAO method for constructing molecular orbitals. In symmetrical molecules, the MOs, and therefore the electronic structure more generally, can be described in terms of the symmetry properties of the molecule. The mathematical basis of this approach is founded in group theory and matrix algebra, but we will discuss this only where necessary. Symmetry analysis will be used extensively in our studies of molecular clusters, and is a central part of the computational machinery in ADF, so it is worth exploring the origins of these ideas. To give some examples, our GASSCF investigations of germanium clusters encapsulating iron and cobalt atoms will use symmetry to partition the CAS(10,10) active space by removing symmetry-forbidden excitations, and when studying gold-encapsulated lead clusters we will understand the formation of an icosahedral molecular fragment by decomposing the bonding energy into symmetry components.
Molecules can be symmetrical in a variety of ways, such as rotation or reflection. Any transformation which leaves the molecule unchanged, such as a 180° rotation in a water molecule, is called a "symmetry operation". Every symmetry operation has

a corresponding "symmetry element", which in the $H_2O$ example would be the axis of rotation. Molecules may only have certain specific combinations of symmetry elements, as the symmetry elements are related to each other. Each combination defines a "point group", where the symmetry elements form a mathematical group which obeys the axioms of group theory. This description of molecular symmetry therefore allows us to use the established results of group theory to understand chemical properties. Within a point group, there is a limited number of ways in which a function of space can transform under the symmetry operations of the group. Each of these ways is called an "irreducible representation", or "irrep". Every group contains the "totally symmetric irreducible representation" (TSIR), which is symmetrical under every operation in the group, and other irreps which are antisymmetric under some of the group operations. When analysing the electronic structure of a molecule, we generally begin with a basis of valence orbitals on every atom and consider how each orbital is changed by each symmetry operation. This allows us to construct a "representation" of the group, which can be expressed as a sum of irreps. We may then identify which combinations of basis functions (i.e. linear combinations of atomic orbitals) are needed to construct MOs of particular symmetries.
We will illustrate these ideas by describing the symmetry of a water molecule. The symmetry elements of water are a 180° rotation, a mirror plane containing all three atoms, and a mirror plane perpendicular to the first which contains only the oxygen nucleus. These elements, shown in Figure 2.2, are denoted $C_2$, $\sigma_v$ and $\sigma_v'$ respectively. Taken together with the identity $E$, which describes the trivial symmetry operation

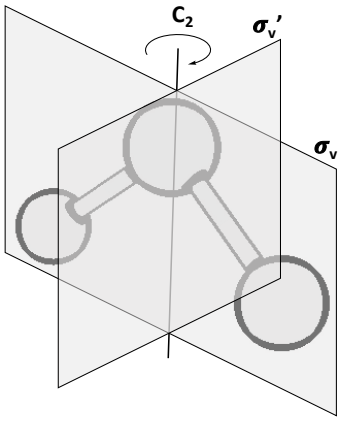



Figure 2.2: Symmetry elements of a water molecule.

of leaving the molecule unchanged, these symmetry elements define the point group $C_{2v}$. This provides a demonstration of the statement that only certain combinations

of symmetry elements can form mathematical groups; in $C_{2v}$ the $C_2$ axis and one mirror plane together generate the other mirror plane, so there is no point group containing only $C_2$ and one $\sigma_v$ mirror plane as this would break the axiom of closure. The information for the point group is contained in a character table, reproduced here in Table 2.1. The symmetry operations appear across the top row, and the leftmost column contains the irreps. The numbers show the characters of these irreps under each symmetry operation - a character of 1 shows that the irrep is symmetric under that operation, while -1 shows that it is antisymmetric. For example, a function with $a_2$ symmetry has two-fold rotational symmetry but no reflection symmetry.

| | $E$ | $C_2$ | $\sigma_v$ | $\sigma'_v$ |
|---|---|---|---|---|
| $a_1$ | 1 | 1 | 1 | 1 |
| $a_2$ | 1 | 1 | -1 | -1 |
| $b_1$ | 1 | -1 | 1 | -1 |
| $b_2$ | 1 | -1 | -1 | 1 |

Table 2.1: Character table for the $C_{2v}$ point group.

Consider now the $2p$ orbitals of oxygen. By convention we define the $z$ axis as the principal rotation axis. A different definition of the axes may change some labels in parts of the subsequent analysis, but will not change the description of the molecule. The $2p_z$ is therefore unchanged by every symmetry operation and transforms as the $a_1$ irrep. $2p_x$ and $2p_y$, however, are perpendicular to the $C_2$ axis and so are antisymmetric under it. Each contains one mirror plane, so $2p_x$ transforms as $b_2$ and $2p_y$ as $b_1$.
To understand the symmetry properties of the hydrogen orbitals, we must calculate the representation of a basis of both hydrogen $1s$ orbitals together. We cannot treat each one separately as they do not individually possess all the symmetries of the point group. The irreps spanned by these orbitals are:

$$\Gamma_{H1s} = a_1 + b_2 \tag{2.36}$$

which can be assigned to two linear combinations - the in-phase combination has all symmetry elements of the group, so it is the $a_1$ irrep, and the out-of-phase combination has $b_2$ symmetry. These are called "symmetry-adapted linear combinations", or "SALCs", as they allow the representation of the H $1s$ basis to be reduced into a sum of irreps.
In general, only SALCs of the same symmetry species can interact with each other, as those of different symmetry will show exact cancellation of constructive and destructive overlap regions. We can use this to identify possible interactions in $H_2O$

between oxygen and the hydrogen SALCs. The in-phase H combination and O $2p_z$ both have $a_1$ symmetry so they can form bonding and antibonding combinations, as can the out-of-phase combination and O $2p_x$. O $2p_y$, with $b_1$ symmetry, has no symmetry match with any combination of the H $1s$ orbitals, so it does not interact with them and is a non-bonding orbital. This is consistent with the fact that $2p_y$ is perpendicular to the O-H bonds and so has zero net overlap with each H $1s$ orbital. This analysis can be used to construct a molecular orbital diagram for $H_2O$, as in Figure 2.3. This diagram includes the O $2s$ orbital, with $a_1$ symmetry, as well as the $2p$ set. All basis functions of the same symmetry combine to give in-phase and out of phase molecular orbitals of the same symmetry, shown by dotted lines. Of particular note is the $1b_1$ orbital, which is simply the O $2p_y$ atomic orbital since it has no symmetry match on the hydrogens. This atomic orbital has no interaction with the H basis functions, so it is entirely localized on O and its energy in the molecule is the same as it would be in the atom.

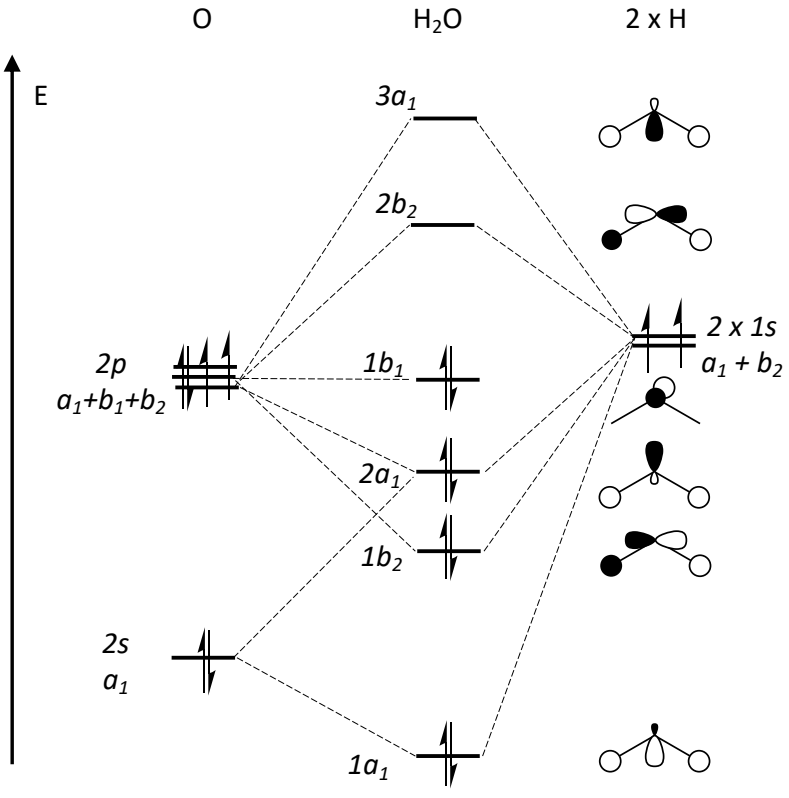



Figure 2.3: Molecular orbital diagram for $H_2O$.

## 2.3 Analysis - Chemical Bonding

Understanding the bonds which hold chemical substances together is among the most fundamental challenges to the inorganic chemist. Different ideas about the nature of bonding have evolved during the history of chemistry, each based on contemporary ideas about quantum mechanics and the theoretical methods available. In this section we will follow the development of models of chemical bonds from Lewis' localized pairs of electrons to delocalized models, and connect these to *ab initio* methods of calculation.

### 2.3.1 Foundations

Developments in atomic theory in the early $20^{\text{th}}$ century, such as the Bohr model of the atom, provided a basis for the theory that atoms interact with each other through their electrons. A consequent bonding model was first formulated by Gilbert Lewis in 1916 when he proposed that a bond is formed when two atoms share a pair of electrons[12]. At the time, Lewis's ideas about bonding were based on his "cubical atom" model, in which atoms have a tendency to hold eight electrons distributed symmetrically over the corners of a cube - an idea which developed (without cubic symmetry) into the octet rule. This simple idea is very successful in predicting the formulae and geometries of stable compounds, which are represented in modern chemistry by "Lewis structures" or "dot-cross diagrams", some examples of which are shown in Figure 2.4. A particular strength of the theory is that it is able to predict both covalent compounds, in which electrons are shared between two atoms, and ionic compounds, in which electrons are transferred from one atom to another. However, it does have some limitations, being unable to explain well-known chemical phenomena such as the paramagnetic ground state of dioxygen or aromaticity in benzene. Developments in quantum mechanics, most notably the Schrödinger equation, led researchers to seek to reconcile covalent bonding with wavefunction-based descriptions of electrons, which Lewis's theory could not do. The two prevalent theories to emerge were valence-bond (VB) theory, a two-atom localized description of bonding, and molecular orbital (MO) theory, which describes electrons as distributed over whole molecules. We will now focus on the latter of these as it is now far more prevalent in quantum chemistry.

### 2.3.2 Molecular orbital theory

In section 2.1.2 we showed that a molecular wavefunction may be constructed by the LCAO method *via* molecular orbitals (MOs), which are single-electron wavefunctions

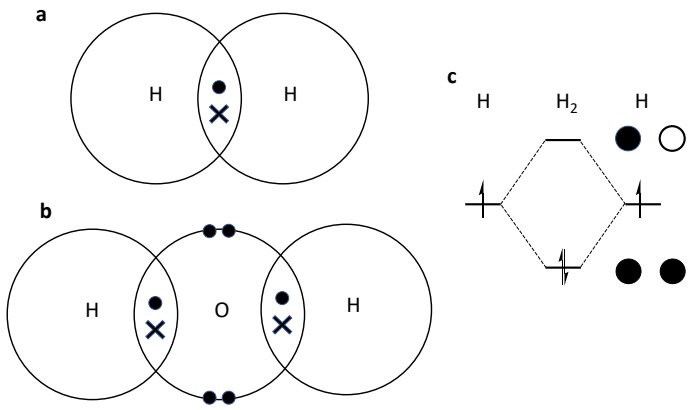



Figure 2.4: Bonding diagrams for simple molecules. (a,b) Lewis structures for $H_2$ and $H_2O$ respectively. (c) MO diagram for $H_2$.

in a molecule. In MO theory, we use the shapes and properties of the MOs to understand and predict the behaviour of the molecule. The MO diagram for $H_2$ is shown in Figure 2.4. We begin with two atomic orbitals, the H $1s$, so we can form two linear combinations - in-phase and out of phase. The in-phase combination is at a lower energy than the atomic orbitals and is called a "bonding" orbital, since electronic occupation of this orbital holds the atoms together. The out of phase combination is higher energy than the atomic orbitals and is an "antibonding" orbital. Occupation of this orbital would result in a repulsive force between the atoms as the electrons would be more stable in two separate H atoms. Since we always have as many molecular orbitals as atomic orbitals, every bonding combination must have a corresponding antibonding combination. Orbitals may be described as "non-bonding" if they have no net bonding or antibonding interaction between atoms; such orbitals are generally localized on a single atom or on multiple atoms which are too far apart to interact with each other. The most important difference between MO theory and Lewis bonding is that the MOs are described by linear combinations of all atomic orbitals in the molecule, not just orbitals on neighbouring atoms, so in polyatomic molecules it is not generally possible to identify a particular electron pair forming a bond between two specific atoms. Instead, electrons may be found in MOs which are bonding with respect to all pairs of atoms in the molecule, or just some pairs. To illustrate this, we will refer back to the MO diagram for $H_2O$ in Figure 2.3. The lowest-energy $1a_1$ orbital is bonding with respect to all three atoms, while the $1b_2$ is bonding between each O-H pair but antibonding between the two H atoms. The $1b_1$ orbital, which we previously said was localized entirely on oxygen as O $2p_y$ is orthogonal to the H $1s$ combinations, is strictly non-bonding, so occupation of this

MO will have no impact on the O-H interaction.
Bonds are not a quantum mechanical observable, so they cannot be extracted from a molecular wavefunction. They are nevertheless a useful concept for understanding chemical behaviour, as shown by the broad success of Lewis structures, so we need a way to include them in our interpretation of MO diagrams. In simple cases this is done by calculating the "bond order", which measures the excess of bonding electrons in a molecule:

$$BO = \frac{n_b - n_a}{2} \tag{2.37}$$

where $n_b$ and $n_a$ are the number of bonding and antibonding electrons respectively. This is very straightforward for $H_2$; the bonding orbital contains two electrons and the antibonding orbital none, so the bond order is 1. This corresponds precisely to the single bond that comes from the Lewis picture of the two H atoms sharing a pair of electrons. In $H_2O$ we must look more closely at the shapes of the occupied MOs. The $1a_1$ and $1b_2$ orbitals are clearly bonding, so their electrons contribute to $n_b$. The $2a_1$ also has the right symmetry to be a bonding combination, but the O $2p_z$ orbital is distorted away from the H $1s$ combination so the overlap is minimal. We therefore regard this orbital as non-bonding, but not in the same way that the $1b_1$ is non-bonding due to symmetry constraints. The two antibonding orbitals, $2b_2$ and $3a_1$, are empty, so $n_a$ is zero. We therefore calculate a bond order of 2 for the whole molecule, which we can interpret as two O-H single bonds.

### 2.3.3 The theoretical basis of some modern bond order measures

Not all bonds are created equal. Some are far stronger than others, as shown by physical measurements, such as vibrational frequencies and dissociation energies, and chemical reactivity concerns. For example, in the first row diatomics, $N_2$ is a strongly bound unreactive molecule, while $F_2$ is the opposite. Lewis rationalized this by allowing pairs of atoms to share multiple pairs of electrons, forming multiple bonds - in $N_2$ the strong bond is in fact a triple bond, while $F_2$ has only a single bond. Equation 2.37 shows how the idea of "bond order" is extended to MO theory, and in Figure 2.3 we applied this to a water molecule. While this method reproduced the familiar Lewis structure of water, we can begin to see issues around deciding whether an orbital is bonding or antibonding, and determining which atoms are bonded to each other. These problems become more severe in larger molecules, particularly those

without a single central atom, as the MOs become more delocalized and more numerous. We therefore need a way to extract bond orders directly from our quantum chemical calculations, rather than by inspection of an MO diagram.

#### 2.3.3.1 Mayer bond order

The simplest definition of a bond order from a molecular orbital (MO) calculation was that suggested by Coulson for $\pi$ interactions in Hückel theory[13]:

$$B_{AB} = \sum_i c_{iA} c_{iB} \tag{2.38}$$

$c_{iA}$ is the coefficient of atomic orbital (AO) $\phi_A$ on atom A in the $i^{th}$ doubly occupied MO.

These are the off-diagonal elements of the so-called "charge-and-bond-order" (CBO) matrix $\boldsymbol{D}$:

$$D_{st} = \sum_i n_i c_{is} c_{it} \tag{2.39}$$

$D_{st}$ is the element of the CBO matrix between any two orbitals $s, t$ in the molecule, $c_{is}$ is the coefficient of orbital $s$ in MO $i$, and $n_i$ is the occupation number of the $i^{th}$ MO. Note that Hückel theory describes only one orbital per atom, in which case this general equation reduces to the expression for $B_{AB}$ in Equation 2.38.

Each element of this matrix is a sum of products of pairs of AO coefficients in MOs. It is not an overlap - Hückel theory assumes all overlaps between orbitals on different atoms to be zero - but instead describes the distribution of an orbital over two atoms. It is maximal when the two coefficients are equal, and zero when one coefficient is zero.

$\boldsymbol{D}$ is more generally called the density matrix, as we shall do henceforward, because it describes a quantum probability density. The CBO appears when we write the one-particle density matrix in an orbital basis, in which case the electron density $\rho$ is given by:

$$\rho = \sum_s \sum_t D_{st} \phi_s \phi_t \tag{2.40}$$

Coulson's bond order was designed for electronic structure models with only one orbital per atom, so we can generalize by summing up off-diagonal elements of the density matrix for all pairs of orbitals on a pair of atoms:

$$B_{AB} = \sum_s^A \sum_t^B D_{st} \tag{2.41}$$

This is the basis of the Wiberg bond index, which is quadratic in the off-diagonal density matrix elements:

$$W_{AB} = \sum_{s}^{A} \sum_{t}^{B} (D_{st})^2 \tag{2.42}$$

This definition was intended for electronic structure methods which used an orthogonalized set of atomic orbital basis functions.
We must now take a significant step towards modern electronic structure theory by including the overlap $S$ between orbitals on different atoms. This allows us to define the population matrix $\boldsymbol{P}$:

$$P_{st} = D_{st} S_{st} \tag{2.43}$$

The sum of all elements of the population matrix gives the total number of electrons in the system. The off-diagonal elements of $P_{st}$ describe the number of electrons being shared between two orbitals. These are known as Mulliken overlap populations, and may be used as an indicator of bonding between two atoms. However, in practical electronic structure theory they are well known for depending strongly on the basis set used in the calculation. The ideas of the Mulliken overlap population and the Wiberg quadratic bond index were combined by Mayer:

$$B_{AB}^{Mayer} = \sum_{s}^{A} \sum_{t}^{B} (P_{st})^2 \tag{2.44}$$

This is closely related to Mulliken overlap population, and therefore shares the strong dependence on basis set[14]. It can therefore only be used to compare bonds in closely related compounds which have been studied using similar methods, and is no longer used extensively in electronic structure theory. Nevertheless, it represents an important landmark in the development of *ab initio* calculations of bond order.

#### 2.3.3.2 Density matrices

For the study of chemical bonds by other methods, we will make use of the first and second order density matrices in terms of spatial coordinates[15, 16]:

$$\rho(\boldsymbol{r_1}; \boldsymbol{r'_1}) = N \int \psi(x_1 \dots x_N) \psi^*(x_1 \dots x_N)\, ds_1 dx_2 \dots dx_N \tag{2.45}$$

$$\Gamma(\boldsymbol{r_1}, \boldsymbol{r_2}; \boldsymbol{r'_1}, \boldsymbol{r'_2}) = N(N-1) \int \psi(x_1 \dots x_N) \psi^*(x_1 \dots x_N)\, ds_1 ds_2, dx_3 \dots dx_N \tag{2.46}$$

with

$N$ – number of electrons in the system

$\psi$ – electronic wavefunction

$x_i$ – spatial ($r_i$) and spin ($s_i$) coordinates of electron $i$

Primes refer to $\psi^*$

We integrate over all spatial and spin coordinates except for the spatial coordinates of which the density is a function. For $\rho(\boldsymbol{r_1; r'_1})$ this is just $x_1$, while for $\Gamma(\boldsymbol{r_1, r_2; r'_1, r'_2})$ this is $x_1$ and $x_2$.

The first order density matrix (Eq. 2.45) describes simply the probable electron density at a point $r_1$, and is equivalent to Eq. 2.40 when integrated over all space. The second order density matrix (Eq. 2.46) describes the total pair density of electrons, *i.e.* the probable number of electron pairs which have one partner at $r_1$ and the other at $r_2$.

For a single-determinant wavefunction, such as in Hartree-Fock theory, we can express the pair density in terms of the one-electron density matrix[17, 15]:

$$\Gamma(\boldsymbol{r_1, r_2; r'_1, r'_2}) = \frac{1}{2}\begin{vmatrix}\rho(\boldsymbol{r_1; r'_1}) & \rho(\boldsymbol{r_1; r'_2})\\ \rho(\boldsymbol{r_2; r'_1}) & \rho(\boldsymbol{r_2; r'_2})\end{vmatrix} \tag{2.47}$$

which can be simplified to[16]:

$$\Gamma(\boldsymbol{r_1, r_2}) = \rho(\boldsymbol{r_1})\rho(\boldsymbol{r_2}) - \frac{1}{2}|\rho(\boldsymbol{r_1, r_2})|^2 \tag{2.48}$$

The first of the terms on the RHS of Eq. 2.48 describes the pair density arising from independent sets of two electrons, and may be called the Coulomb term. The second term describes density arising from electron exchange and correlated electronic motion, distinguishing between the pair density arising from independent electrons and that from "true" electron pairs. Accordingly, it may be called the exchange-correlation density and labelled $\Gamma_{xc}$:

$$\Gamma_{xc} = \rho(\boldsymbol{r_1})\rho(\boldsymbol{r_2}) - \Gamma(\boldsymbol{r_1, r_2}) \tag{2.49}$$

To better understand the meaning of $\Gamma_{xc}$ we first note that if two atoms A and B are covalently bonded, the shared electrons will each contribute to density at $\boldsymbol{r_1}$ and $\boldsymbol{r_2}$ so the product $\rho(\boldsymbol{r_1})\rho(\boldsymbol{r_2})$ contains spurious self-interaction terms where density contributions at separate points arising from the *same* electron interact with each other. $\Gamma_{xc}$ therefore serves to remove these self-interactions from the total pair density, and

this is the way in which we can interpret the meaning of $\rho(\boldsymbol{r_1}, \boldsymbol{r_2})$ as a 2-centre 1-electron density matrix.[16]
$\Gamma_{xc}$ describes a one-electron density, so integration of Eq. 2.49 over all pairs of positions (since it depends on two spatial coordinates) must recover the total electron population of the molecule:

$$\begin{aligned} \int\int \Gamma_{xc}(\boldsymbol{r_1}, \boldsymbol{r_2})\, d\boldsymbol{r_1} d\boldsymbol{r_2} &= N^2 - N(N-1) \\ &= N \end{aligned} \tag{2.50}$$

One approach to computing bond orders is to divide this integral into one-atom and two-atom contributions in order to count the number of electrons which are localized one one atom and delocalized over a pair of atoms, respectively.

#### 2.3.3.3 Atoms in Molecules

The Quantum Theory of Atoms in Molecules - "QTAIM", or often simply "AIM" - has become a popular approach to molecular electronic structure analysis since its development by Bader in the 1960s[18]. The central tenet of AIM is that molecules should be studied through the topology of the electron density, rather than the wavefunction, as this is a real, observable property which allows us to devise clear definitions of simple chemical concepts like atoms and bonds. It defines an atom in a molecule by an "atomic basin" $\Omega$ bounded by a zero-flux surface of electron density $\boldsymbol{S}$:

$$\nabla\rho(\boldsymbol{r}) \cdot \boldsymbol{n}(\boldsymbol{r}) = 0 \;\forall\; \boldsymbol{r} \in \boldsymbol{S} \tag{2.51}$$

with

$$\begin{aligned} \rho(\boldsymbol{r}) &- \text{Electron density} \\ \boldsymbol{n}(\boldsymbol{r}) &- \text{Unit vector normal to the surface at } \mathbf{r} \end{aligned}$$

With the set of quantum atoms $\{\Omega_A, \Omega_B, \dots\}$ thus defined, any one-electron property of an atom can be calculated by integration of that property over the atomic basin. For example, the electronic population of an atom is given by:

$$N(A) = \int_{\Omega_A} \rho(\boldsymbol{r}) d\boldsymbol{r} \tag{2.52}$$

Integration of a property over all atomic basins will recover the property of the complete molecule, since there are no overlaps or gaps between the basins. Just as a one-electron property is decomposed into a sum over atomic basins, a two-electron

property is decomposed into a sum over all pairs of atoms.
Critical points (CP) in the electron density, defined by Eq. 2.53, are important in AIM as they are stationary points in the electron density gradient.

$$\nabla\rho = 0 \tag{2.53}$$

A critical point at $\boldsymbol{r}$ can be classified by the eigenvalues of the Hessian matrix, the matrix of second derivatives of $\rho(\boldsymbol{r})$, as these describe the rate of change in the density in different directions. More precisely, a $(\sigma, \lambda)$ critical point has a Hessian matrix of rank $\sigma$ with the signs of the eigenvalues adding up to $\lambda$. (3,-3) CPs are located at maxima in the electron density in all three spatial directions, since all three eigenvalues of the Hessian are negative, and therefore appear at the nuclear positions. (3,-1) CPs are maxima in two directions but minima in the third, which describes a "bond critical point" (BCP) between two atoms. (3, +1) and (3, +3) CPs are termed "ring" and "cage" critical points respectively as this describes where they appear in relation to neighbouring atoms. If two nuclei share a BCP then these three critical points define an "atomic interaction line", or "bond path".
To determine the nature of this interaction, i.e. the degree of covalency in the bond, we examine the Laplacian of the electron density, shown in Eq. 2.54.

$$\nabla^2\rho = \frac{\partial^2\rho}{\partial x^2} + \frac{\partial^2\rho}{\partial y^2} + \frac{\partial^2\rho}{\partial z^2} \tag{2.54}$$

The sign of the Laplacian of the density at a BCP describes whether that BCP is a site of local charge concentration, shown by a negative $\nabla^2\rho$, or local charge depletion, shown by a positive $\nabla^2\rho$. The former case is generally held to be the signature of a covalent interaction, while the latter indicates a non-covalent or "closed shell" interaction. Bond order may be determined in conjunction with this classification by examining the density itself, since a larger density along the bond path implies a higher bond order, and comparing to reference compounds where the bond orders are known from other methods. Alternatively, interactions may be classified by the total, kinetic and potential electronic energy densities at the BCP, respectively labelled $H_{\mathrm{BCP}}$, $G_{\mathrm{BCP}}$ and $V_{\mathrm{BCP}}$[19, 20, 21]. If $H_{\mathrm{BCP}} < 0$ then the accumulation of electron density at the BCP is stabilizing, which may be interpreted as indicating a covalent interaction. The ratio $\frac{-G_{\mathrm{BCP}}}{V_{\mathrm{BCP}}}$ may also describe covalency because electron delocalization through covalent bonding reduces the electronic kinetic energy, so $\frac{-G_{\mathrm{BCP}}}{V_{\mathrm{BCP}}} < 1$ or 0.5 may indicate covalency depending on the chemical system. Computed AIM properties have been shown to be sensitive to methodology when calculating challenging molecules, such as gold clusters[22, 23].

#### 2.3.3.4 Delocalization indices

In AIM, as discussed above, atoms are defined by atomic basins $\Omega$ bounded by zero-flux surfaces. We can use this definition and the exchange-correlation density in Eq. 2.50 to define localization (Eq. 2.56) and delocalization (Eq. 2.55) indices for atoms A and B:

$$\delta(A,B) = 2\int_{\Omega_A}\int_{\Omega_B} \Gamma_{xc}(\boldsymbol{r_1},\boldsymbol{r_2})d\boldsymbol{r_1}d\boldsymbol{r_2} \tag{2.55}$$

$$\lambda(A) = \int_{\Omega_A}\int_{\Omega_A} \Gamma_{xc}(\boldsymbol{r_1},\boldsymbol{r_2})d\boldsymbol{r_1}d\boldsymbol{r_2} \tag{2.56}$$

The delocalization index $\delta(A,B)$ describes the number of electrons which are delocalized over the two atomic basins, and has been shown to be a useful measure of bond order[24, 25]. Analogously, the localization index $\lambda(A)$ describes electrons localized within one atomic basin; the ratio $\frac{\lambda(A)}{N(A)}$ gives a measure of proportional localization, approaching 1 for closed-shell atoms.[17]
These expressions are general, and can be used for any electronic structure method provided the density matrices are known. In practice, most methods construct the wavefunction and therefore the density from molecular orbitals (MOs) in the linear combination of atomic orbitals (LCAO) approach, so corresponding expressions for $\delta(A,B)$ and $\lambda(A)$ in terms of orbital overlaps also exist. It is also not restricted to the AIM method of partitioning real space into atomic basins, and can be used in conjunction with other methods.
Another significant result can be derived by integrating Eq. 2.49 over the two atomic basins[25, 24]:

$$\delta(A,B) = 2\int_{\Omega_A}\int_{\Omega_B} \Gamma_{xc}(\boldsymbol{r_1},\boldsymbol{r_2})d\boldsymbol{r_1}d\boldsymbol{r_2} \tag{2.57}$$

$$= 2\int_{\Omega_A}\int_{\Omega_B} \rho(\boldsymbol{r_1})\rho(\boldsymbol{r_2})d\boldsymbol{r_1}d\boldsymbol{r_2} - 2\int_{\Omega_A}\int_{\Omega_B} \Gamma(\boldsymbol{r_1},\boldsymbol{r_2})d\boldsymbol{r_1}d\boldsymbol{r_2} \tag{2.58}$$

$$= 2\langle N_A\rangle\langle N_B\rangle - 2\langle N_A N_B\rangle \tag{2.59}$$

This is the precise expression for the covariance between the atomic populations of A and B, implying that the electronic populations of two bonded atoms are statistically correlated. Delocalization indices from Hartree-Fock calculations generally agree with the bond orders predicted by Lewis structures. However, post-HF methods such as CI or CASSCF tend to significantly reduce $\delta(A,B)$ as they introduce correlation by mixing excited antibonding states into the total wavefunction.

### 2.3.4 Energy decomposition analysis

*Ab initio* electronic structure theories turn an electronic wavefunction or density into a total energy for the chemical system of interest, which generally describes the energy of the molecule relative to a state in which all electrons and nuclei are infinitely far away from each other. Other reference states are possible - for example, the ADF software package[26]uses a reference state of non-interacting atoms or chemical fragments in the same geometry as the molecule, called a "promolecule", evaluating the energy of the difference electron density between the promolecule and the molecule. To aid chemical analysis, we may wish to decompose the total energy into physically interpretable components, such as electrostatic and covalent interactions. This is usually called "Energy decomposition analysis" (EDA). The components cannot be measured directly, as they are not eigenvalues of a quantum operator, but they can still be useful for understanding chemical behaviour.
The decomposition procedure implemented in ADF, based on schemes devised by Morokuma, Ziegler and Rauk[27, 28], divides the interaction energy between the fragments in the promolecule into three terms:

$$\Delta E = \Delta V_{\text{elst}} + \Delta E_{\text{Pauli}} + \Delta E_{\text{orb}} \tag{2.60}$$

$$\Delta V_{\text{elst}} - \text{Electrostatic interaction} \tag{2.61}$$

$$\Delta E_{\text{Pauli}} - \text{Pauli repulsion} \tag{2.62}$$

$$\Delta E_{\text{orb}} - \text{Orbital interaction} \tag{2.63}$$

$\Delta V_{\text{elst}}$ describes the classical electrostatic interaction between the charge densities of the fragments in the promolecule. $\Delta E_{\text{Pauli}}$ describes the energy change in going from the sum of the fragment densities to an antisymmetrized wavefunction which obeys the Pauli principle. These first two terms often almost cancel each other, and can be added together to give a "steric interaction". $\Delta E_{\text{orb}}$ describes the energy arising from optimization of the wavefunction, capturing all bonding, polarization and charge transfer resulting from the interaction between fragments. In symmetrical molecules $\Delta E_{\text{orb}}$ may be further decomposed into contributions from each irreducible representation of the molecular point group. In certain high-symmetry cases this can allow us to separate chemical features such as $\sigma$ and $\pi$ bonding, or the interactions between particular atomic orbitals.

## 2.4 Electronic structure of solids

### 2.4.1 Foundations

The most important difference between free molecules and crystalline solids from an electronic structure perspective is that crystals possess translational symmetry. Different approaches to describing the electronic structure of solids exist, from the fully delocalised "free electron" model to the "tight-binding" model based on atomic orbitals. The difference between these descriptions lies in the strength of the interaction between the electrons and the periodic potential of the ions in the crystal. Translational symmetry is central to the way in which wavefunctions are derived for the infinite perfect crystal. The theoretical basis for this is in Bloch's theorem:

$$\psi_k(x) = e^{ikx} \cdot u(x) \tag{2.64}$$

$u(x)$ is any periodic function such that $u(x) = u(x + a)$
In words, this means that the eigenstates $\psi_k$ of a one-electron Hamiltonian with a periodic potential $V(r)$ such that $V(r) = V(r+T)$ for all lattice translations $T$ can be chosen to be plane waves multiplied by a function with the periodicity of the lattice. The plane waves are necessary to account for the changing phase of the wavefunction between unit cells.
The eigenstates, or "Bloch waves", are quantized and symmetry-adapted by the index $k$. This quantum number is inversely proportional to the lattice vector $a$, so it exists in "reciprocal space"; while conceptually challenging, reciprocal space simplifies descriptions of infinite structures like crystals. $k$-points correspond to phase relationships between unit cells; in real space a description of the different possible phase relationships would require modelling the entire (infinite) crystal, but since they are confined to a finite region of reciprocal space they can be described more effectively in this way.
Each $k$-point corresponds to an electronic energy as the curvature of a wavefunction is related to its energy. The unique values of $k$ are confined to the range:

$$\frac{-\pi}{a} \leq k \leq \frac{\pi}{a} \tag{2.65}$$

N.B.

$$E(k) = E(-k)$$

This region of reciprocal space is called the "(first) Brillouin zone", and may be considered to be a unit cell in reciprocal space. Calculating the total energy and

electronic structure of a crystal requires us to sample reciprocal space by calculating the energy at different $k$-points; the more $k$-points we use, the more precise and more expensive our calculation will be. A large unit cell in real space turns into a small Brillouin zone in reciprocal space, so smaller $k$-point grids are required to describe systems with larger unit cells.

The most chemically familiar way to describe bonding in solids is the "tight binding" description, closely related to the Linear Combination of Atomic Orbitals (LCAO) approach to constructing molecular wavefunctions. A crucial difference between the molecular and crystalline cases is simply the number of orbitals involved; while a molecule has a small number of orbitals which can be conveniently depicted individually on an MO diagram, the $\approx 10^{23}$ orbitals in a crystal are better described by a continuous "band" which can be plotted as a function of $k$, as in Figure 2.5.

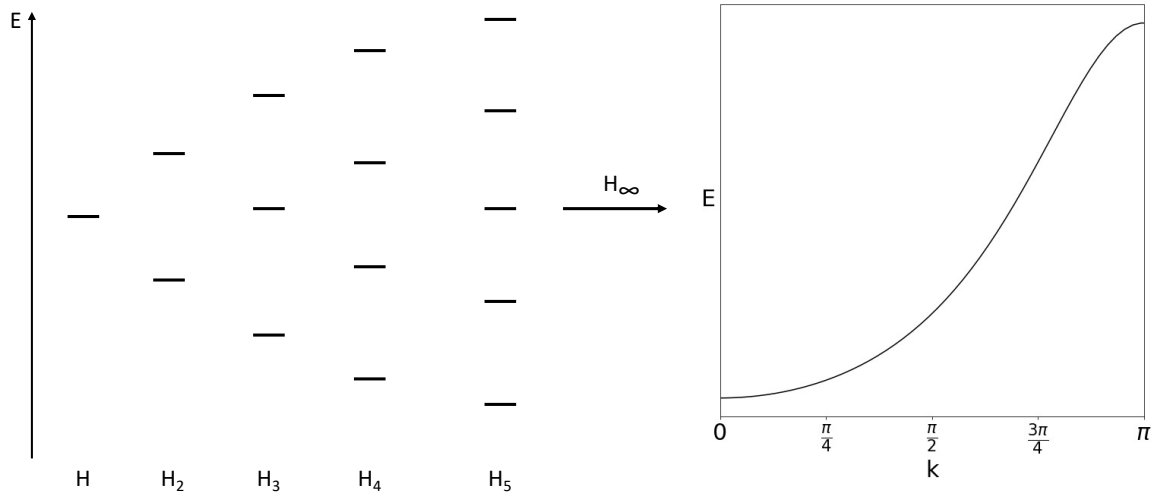



Figure 2.5: MOs of a lengthening chain of H atoms and the band structure of an infinitely long chain.

### 2.4.2 Density of states

To more easily assess the electronic structure of a crystalline material we can instead plot the Density of States (DOS) which describes the number of one-electron states in an infinitessimal energy interval $dE$. The DOS is therefore the reciprocal gradient of the band structure. This is illustrated in Figure 2.6 which shows the band structure and DOS for the infinite chain of H atoms, calculated using extended Hückel theory. In regions of $k$-space in which the band energy varies slowly, in this case close to the edges of the Brillouin zone, there are many electronic states in the energy interval $dE$

so the DOS shows large peaks, while in the middle of the band where the gradient is steep, there are relatively few states per energy unit so the DOS is low. The shape of the DOS plot shown in Figure 2.6 is a particular feature of one-dimensional systems.

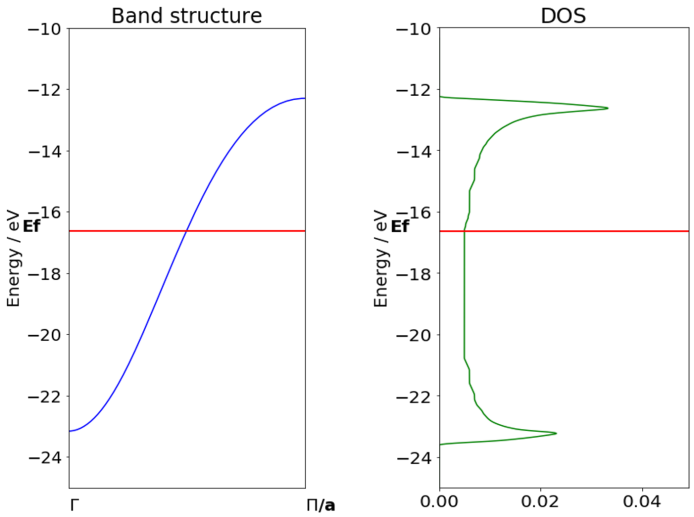



Figure 2.6: Band structure and DOS diagrams for the 1D H chain calculated using periodic extended Hückel theory.

The DOS can tell us about the electron transport properties of the solid. The Fermi level, $E_F$, is defined as lying half way between the highest occupied state and the lowest unoccupied state. If the DOS at $E_F$ is non-zero then we expect metallic conductivity, whereas if there is an energy gap between the filled "valence" and empty "conduction" bands then we predict semiconductivity or insulation depending on the size of the band gap.

### 2.4.3 Local projections

In periodic calculations, our wavefunction is constructed from delocalized plane wave basis functions. This wavefunction describes delocalized electrons interacting with ionic centres, formed of nuclei and their core electrons. In order to understand chemical behaviour and trends, we would like to extract properties of individual atoms from our calculation. Common examples include charge and spin densities, and the "projected density of states" (PDOS) which is the DOS arising from a particular atom or atomic orbital. There is no single correct way to define an atom in a crystal, in quantum mechanical terms, so we must select a method for projecting the delocalized wavefunction onto the atoms.

Perhaps the simplest approach is to assign a spherical radius to each atom, called the

"Wigner-Seitz radius", and integrate the properties of the wavefunction within each sphere. This approach is qualitatively accurate in most cases, but suffers from some quantitative problems. The spheres of neighbouring atoms may overlap, leading to ambiguity over whether an electron "belongs" to one atom or another, and some regions of space will be lost in between spheres, so the sum of any property over all the projection spheres may not be equal to the sum for the whole unit cell. Furthermore, these radii can be rigorously defined only for pure elements (by setting the radius such that the sum of all spherical volumes add up to the cell volume).

A more sophisticated, but more computationally expensive, approach is to use a set basis functions for the projection, rather than simple spheres. A basis of local orbitals - Slater orbitals have been shown to be effective - is placed on each atom and this basis is then optimized to best reproduce the total wavefunction[29]. This generally gives quantitatively superior reconstruction of the wavefunction than the Wigner spheres, though the qualitative behaviour of atoms may not be very different. Another advantage of this method is that it allows use of the basis-function-based analysis methods originally developed in molecular quantum chemistry, such as Mulliken population analysis. Particularly significant are the crystal orbital overlap population (COOP) and crystal orbital Hamiltonian population (COHP)[30]. COOP is the solid-state analogue of the Mulliken overlap population, and tells us whether the interaction between two atoms is bonding or antibonding as a function of energy. COHP then tells us whether the interaction between two atoms lowers or raises the total energy of the system, which is closely related to bonding and antibonding and is most valuable for understanding energetic preferences for one structure over another.

# Chapter 3

# Metal-metal bonding in ligand-free clusters

## 3.1 Introduction to clusters

This chapter describes three related investigations into the chemistry of cluster compounds in which group 14 cages encapsulate one or more transition metal atoms. We will begin by describing the established chemistry of these clusters, from classic boranes to more recent encapsulated group 14 clusters, and the principal theoretical methods used to study them. The compounds on which our research focuses have a range of structures and compositions, but in each case we aim to understand the details of the metal-cage and metal-metal interactions and show how they relate to the observed structures. We then hope to use these insights to inform experimental analysis and guide future synthesis. The first investigation concerns $[M@Ge_{10}]^{3-}$ and $[M_2@Ge_{16}]^{4-}$ (M = Fe, Co), a quartet of clusters with three-connected structures in which we will explore metal-cage and metal-metal interactions using DFT and CASSCF. The two methods provide complementary perspectives on electronically complex materials, and each sheds its own light on the correlated electronic behaviour in covalently bonded clusters. The second examines $[(Ni@Sn_9)In(Ni@Sn_9)]^{5-}$, $[(Ni@Ge_9)Ni(Ni@Ge_9)]^{4-}$, and $[(Fe@Sn_9)Fe(Fe@Sn_9)]^{4-}$, all of which contain two $E_9{}^{4-}$ cages linked by a linear metal trimer, where we will explore changes to the structures as the valence electron counts vary. Where the first study considered open and closed shell metal dimers, the $Ni_3$ and $Fe_3$ clusters here allow us to explore the same issue in linear trimers. The final study explores the structural evolution of lead clusters containing the coinage metals Cu, Ag, and Au, where we will seek to explain the geometries favoured by each metal. One of these clusters, $[Cu_4Pb_{18}]^{4-}$, also has an iron analogue $[Fe_4Pb_{18}]^{4-}$ which will allow us to consider the way in which this cluster

architecture can accomodate metal cores with very different bonding character. All of these investigations have a common theme of comparing isostructural closed-shell and open-shell clusters. The first has been published in *Journal of Physical Chemistry A*[31], the second in *Dalton Transactions*[32] and the third in *Journal of the American Chemical Society*[33] and *Nature Communications*[34].

### 3.1.1 Boranes

The compounds most synonymous with electron-deficient cluster chemistry are the boranes ($B_nH_m$). Their chemistry was pioneered by Alfred Stock, who developed methods for synthesizing and separating boranes in the early 20$^{th}$ century[35, 36]. Borane structural chemistry advanced greatly in later decades due to the use of X-ray crystallography to determine their remarkable structures, such as that of $B_{10}H_{14}$ in 1948[37]. Substantial progress was made by Lipscomb, using experimental methods such as XRD alongside quantum chemical calculations, for which he won the 1976 Nobel prize in chemistry. The boranes continue to fascinate chemists to this day by their structures, quite unlike their hydrocarbon neighbours, which have shaped our ideas about chemical bonding and continue to challenge them. A particularly famous example is diborane ($B_2H_6$), a classic example of a compound featuring a three-centre two-electron (3c2e) bond. The correct structure, shown in Figure 3.1 was first proposed by Longuet-Higgins while an undergraduate at Oxford, at a time when the concept of multicentre bonding was not well-established, and was subsequently validated by vibrational spectroscopy and electron diffraction[38]. Many $B_nH_m$ compounds now exist, mostly with $n \leqslant 12$. Their structures are generally deltahedral, based on polyhedra with predominantly triangular faces, and can be categorized according to the number of vertices missing from the polyhedral structure. A cluster containing $n$ boron atoms may have the following structure types:

- *closo-* $n$-vertex closed polyhedron
- *nido-* $n+1$-vertex polyhedron with one vertex removed
- *arachno-* $n+2$-vertex polyhedron with two vertices removed
- *conjuncto-* multiple polyhedra sharing vertices, edges or faces

The general trend is that the clusters adopt more "open" structures as they become more electron-rich. An example of each type is shown in Figure 3.1, including $[B_6H_6]^{2-}$, $B_5H_9$, and $B_4H_{10}$ which are *closo, nido* and *arachno* derivatives of an octahedron.

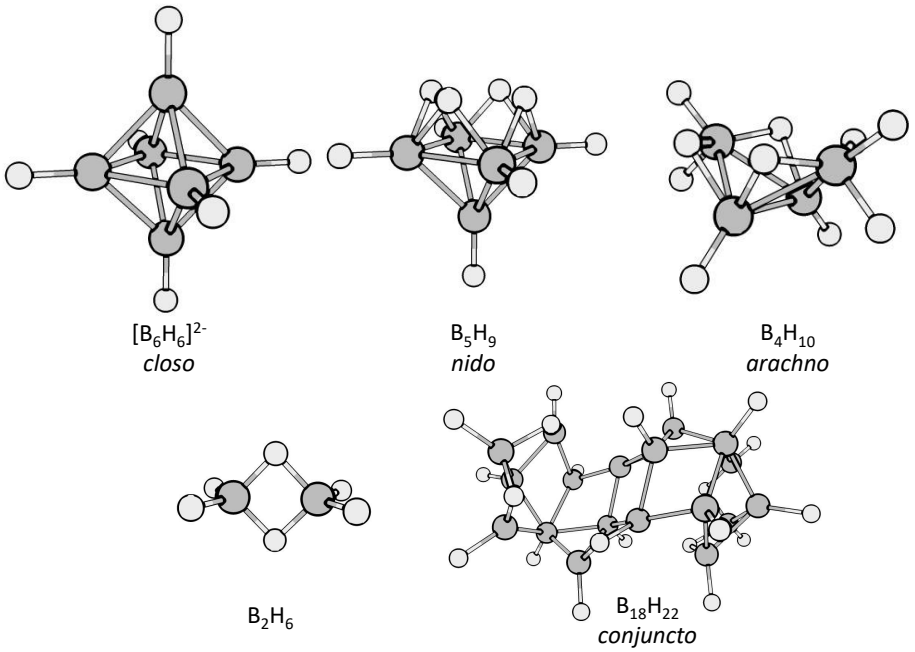



Figure 3.1: Boranes illustrating the different structural classes of deltahedral clusters.

### 3.1.2 Bonding models and electron counting in clusters

The polyhedral structures of boranes, and other cluster compounds, are driven by the fact that they are "electron-deficient", lacking the electrons required to form a two-centre two-electron (2c2e) bond between every pair of neighbouring atoms. Instead, high-connectivity structures are adopted to maximise the stabilization of the available electrons by delocalized bonding. This is illustrated most simply by the 3c2e bond in diborane, shown on the MO diagram in Figure 3.2(b). While the terminal B−H bonds are formed by a pair of electrons, *i.e.* a normal 2c2e bond, the bridging bonds are formed from a pair of electrons delocalized over both boron atoms and the bridging hydrogen. This gives the bridging B−H bonds a formal bond order of 0.5, which is reflected in the structure as they are longer than the terminal bonds, as shown in Figure 3.2(a). The structures of polyhedral clusters - *closo, nido* and so on - can be rationalized by counting the number of electron pairs available for cluster bonding, sometimes called "skeletal electron pairs". The relationship between electron count and structure is summarized by the Wade-Mingos rules[39, 40], which can be used as follows:

1. Calculate the total valence electron count (TVEC) of the cluster

2. Calculate the skeletal electron count (SEC) by subtracting electrons involved in non-cluster bonding (exterior bonds or lone pairs)

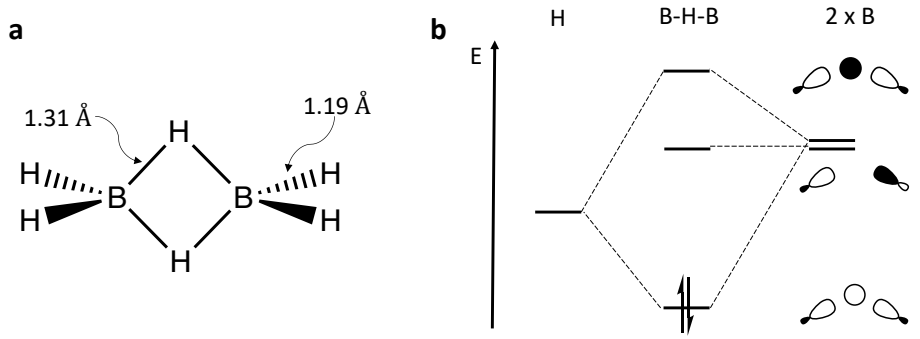



Figure 3.2: Structure and bonding in $B_2H_6$. (a) Molecular structure annotated with bridging and terminal B-H bond lengths. (b) Fragment MO diagram showing the 3-centre 2-electron B-H-B bridging bonds.

3. Write the SEC in terms of the number of vertices to determine the structure:

   - $(n+1)$ *closo*
   - $(n+2)$ *nido*
   - $(n+3)$ *arachno*

Jemmis has extended this method to *conjuncto* boranes, metalloboranes and metallocenes through the "*mno* rule"[41]. It states that the number of electron pairs required by a stable structure is $m+n+o$ where $m$ is the number of polyhedra, $n$ the number of vertices, and $o$ the number of single-vertex-sharing condensations. Wade's rules are the special case of $m = 1, o = 0$.
These rules are founded on general MO theory arguments, so they are not restricted to boranes but can be applied to any electron-deficient molecule. Fragments other than BH that can act as cluster vertices include group 14 atoms such as Pb, in clusters like the *closo*-icosahedral $Pb_{12}{}^{2-}$ "plumbaspherene", or transition metal fragments like $Os(CO)_3$ which can form a *closo* cluster $[Os_6(CO)_{18}]^{2-}$[42, 43]. Two fragments with similar electronic character, *i.e.* valence orbital energy and shape, are said to be "isolobal" and can combine to form new clusters. Examples range from the fairly straightforward BH and $CH^+$ fragments of carboranes like $C_2B_4H_6$, to the more surprising isolobality between BH and $Fe(CO)_3$ when forming $B_4H_8Fe(CO)_3$[44].

### 3.1.3 Group 14 Zintl ions

Small anionic complexes of p-block metals, such as $Sn_4{}^{4-}$ and $Pb_4{}^{4-}$ are often called "Zintl ions", named after Eduard Zintl who observed their formation in liquid ammonia solutions containing main group and alkali metals[45]. His name is also given

to "Zintl phases", solid-state intermetallic compounds of an electronegative p-block metal and an electropositive s-block metal, which have some salt-like character due to their polarity. The two families were thought to be separate until the Zintl phase $Cs_4Ge_9$ was found to contain $Ge_9^{4-}$, which became the first Zintl ion to be synthesized in solution and in the solid state[46]. Of particular interest in this thesis are Zintl ions without supporting ligands, of which a number of sizes and shapes exist for homoatomic clusters of the lower group 14 elements Ge, Sn, and Pb. Selected structures are shown in Figure 3.3. We will begin by describing these $E_n^{q-}$ (n = 4, 5, 9, 10, 12) clusters in their pure form before considering chemical derivatives. $E_4^{4-}$ is a tetrahedral ion, isoelectronic to $P_4$, known in crystal structures but rare in

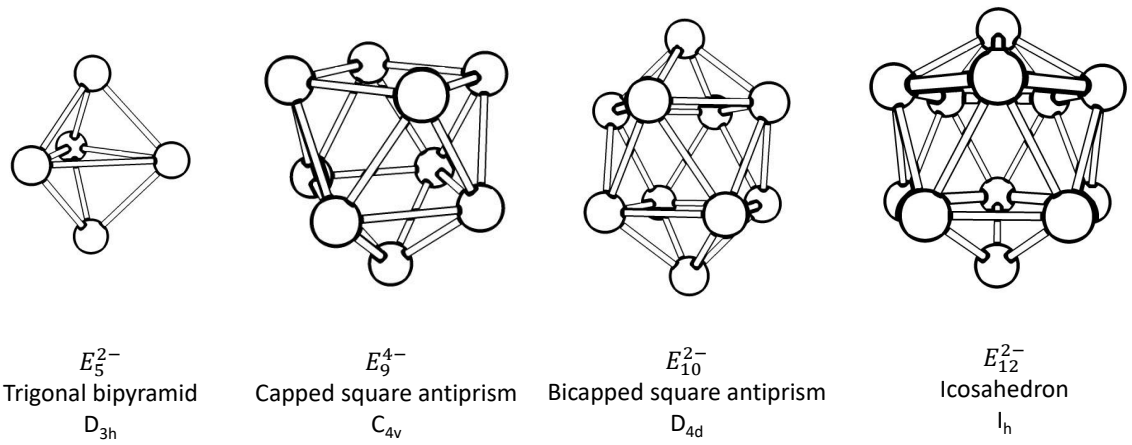



Figure 3.3: Deltahedral structures of $E_n^{q-}$ (n = 5, 9, 10, 12) Zintl clusters of Ge, Sn, and Pb.

solution[45, 47]. This is likely to reflect strongly reducing behaviour owing to their high charge density. $E_5^{2-}$ is trigonal bipyramidal, a *closo* structure consistent with its 12 skeletal electrons. Few derivatives of these ions have been described, but $Ge_5^{2-}$ has been shown to act as a nucleophile through Ge lone pairs without substantial change to the cluster shape[48]. $E_9^{4-}$ is known for Ge, Sn, and Pb, and the chemistry of $Ge_9^{4-}$ is particularly well developed - the ion can be condensed into oligomers, polymers and a mesoporous solid phase[49, 50, 51, 52, 53]. As well as this structural diversity, variable oxidation state behaviour in $Sn_9^{3-/4-}$ shows that the electronic states of these compounds are also finely balanced[54]. $E_{10}^{2-}$ clusters, with bicapped square antiprismatic structures, have been reported for Pb[55] and Ge[56], but the only ten-vertex Sn clusters reported to date are stabilized by ligands[57] or an encapsulated atom[58] (see below). Finally, icosahedral clusters $E_{12}^{2-}$ are known for Sn ("stannaspherene")[59] and Pb ("plumbaspherene")[42, 60] but $Ge_{12}^{2-}$ has not been

isolated, in an interesting contrast to the trend in $E_{10}^{2-}$ stabilities. DFT studies have predicted that the icosahedral form is not the lowest energy geometry because the Ge atoms prefer higher-connectivity vertices than an icosahedral structure allows[61]. This is because the Ge lone pairs, in *sp*-hybrid orbitals, have sufficient side-on overlap for appreciable $\pi$ bonding, which is not the case in $Sn_{12}^{2-}$ or $Pb_{12}^{2-}$ where the lone pairs have greater *s* character and are more localized - a manifestation of the inert pair effect - or in $[B_{12}H_{12}]^{2-}$, which has localized B−H bonds in place of lone pairs. The larger clusters are of greatest interest to us as they are large enough to encapsulate a transition metal atom. Such encapsulated clusters will be a major focus of research in this thesis, so we will now survey structure and bonding in previously characterized examples.

### 3.1.4 TM-encapsulated group 14 clusters

$[M@E_n]^{q-}$ is the general formula for a group 14 cluster containing an endohedral transition metal atom, of which examples are now known for a range of TMs and cages, as shown in Figure 3.4. The metal is generally from the later part of the transition series, and $E_{12}$ cages are relatively common, likely due to size effects. Some retain the perfect icosahedral structure of the empty $E_{12}^{2-}$ ion, while others have distorted icosahedral structures or a different geometry entirely. Examples of icosahedral $[M@E_{12}]^{q-}$ include $[Ir@Sn_{12}]^{3-}$, and $[M@Pb_{12}]^{q-}$ (M=Ni, Pd, Pt: q=2; M=Co, Rh, Ir: q=3)[62, 63, 64]. All of these can be straightforwardly described as $E_{12}^{2-}$ containing a $d^{10}$ metal ion, which is consistent with the undistorted geometry. Deviations from icosahedral symmetry can be found in $[Mn@Pb_{12}]^{3-}$, $[Co@Ge_{12}]^{3-}$, and one isomer of $[Rh@Sn_{12}]^{3-}$. Each is thought to have its own reason for distortion: $[Mn@Pb_{12}]^{3-}$ cannot be sensibly assigned a $d^{10}$ configuration, corresponding to $Mn^{3-}$, so the distortion is a result of changes to the cage bonding MO occupancies[65]; the $Ge_{12}$ cage in $[Co@Ge_{12}]^{3-}$ may be too small to contain Co if it adopts an icosahedral geometry, though the electronic effects for Ge discussed above may also be relevant[66]; finally, $[Rh@Sn_{12}]^{3-}$ crystallizes in two isomeric forms, one icosahedral and one distorted, but DFT calculations only find a minimum for the icosahedral structure so the distortion is likely due to electrostatic interactions in the crystal[58]. For the lighter group 14 elements Ge and Si we find entirely different structure types. Rather than the deltahedral structures characteristic of electron-deficient clusters, $[Ru@Ge_{12}]^{3-}$ and $[Mn@Si_{12}]^{+}$ adopt "three-connected" structures in which every atom is bonded to three neighbours[67, 68]. This bonding pattern is associated with electron-precise clusters which have enough electrons to form a 2c2e bond between every pair of

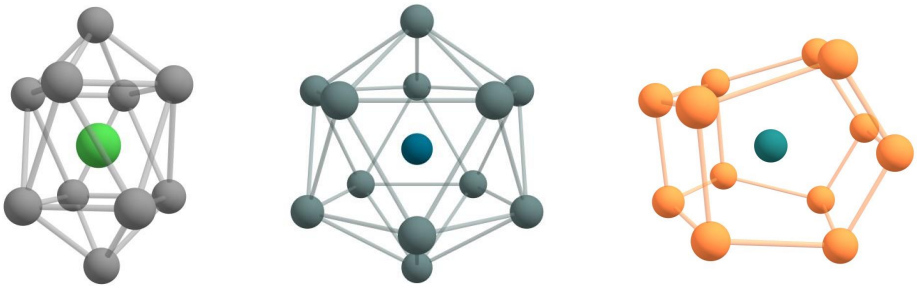



Figure 3.4: Monomeric $[M@E_n]^{q-}$ clusters with deltahedral and three-connected structures.

neighbouring atoms, eliminating the need for delocalized cluster bonding. The structures of these two clusters are nevertheless markedly different. $[Ru@Ge_{12}]^{3-}$ adopts a $D_{2d}$ structure featuring pentagonal faces, while $[Mn@Si_{12}]^{+}$ has a $D_{6h}$ structure and could be described as a sandwich complex like bis(benzene)chromium, with much shorter bonds between the two $E_6$ rings. This structural trend may be explained by extending the trend described above when comparing the structures of $Pb_{12}^{2-}$ and $Ge_{12}^{2-}$; the higher elements form stronger $\pi$ bonds due to better side-on overlap of the smaller valence orbitals, so $[Ru@Ge_{12}]^{3-}$ adopts a $\sigma$-bonded pseudo-spherical structure, while $[Mn@Si_{12}]^{+}$ has a hexagonal prismatic structure containing Hückel-aromatic $Si_6$ rings. Smaller cages can also accommodate transition metal atoms. $[Rh@Sn_{10}]^{3-}$ adopts a distorted bicapped square antiprismatic structure, similar to pristine $Pb_{10}^{2-}$, and the undistorted form is only slightly higher in energy. Small energy differences between structures have also been calculated for $[Fe@Sn_{10}]^{3-}$, for which the crystal structure has not been resolved due to disorder likely due to electrostatic interactions in the crystal. $[(Fe/Co)@Ge_{10}]^{3-}$ adopt a three-connected pentagonal prismatic structure[69, 70] which will be discussed in detail in the results below. Some nine-vertex clusters have been characterized, including $[Cu@E_9]^{3-}$ (E=Pb,Sn), $[Ni@Sn_9]^{4-}$, $[Co@Ge_9]^{5-}$, and $[Ru@Sn_9]^{6-}$. All of these are well described as $d^{10}$ metal ions in $E_9^{4-}$ cages[71, 72]. Particularly interesting is $[Ni@Sn_9]^{4-}$ as it preserves the 3-/4- redox activity of the empty cage, which suggests that it could be useful for catalysis, and $[Ru@Sn_9]^{6-}$ has been used as a precursor to a $CO_2$ reduction catalyst with a $CeO_2$ support[73]. Considerable structural diversity arises from oligomerization of $M@Ge_9^{4-}$ clusters, analogous to the oxidative coupling reactivity of $Ge_9^{4-}$ described above, and this will be described in more detail in the introduction to our investigation of $[Ni_2InGe_{18}]^{5-}$.

The monomeric $E_n$ cages described so far can only encapsulate one transition metal atom. Much synthetic and computational research is now devoted to cages containing multiple metal atoms, as these offer a wealth of possibilities for unusual bonding modes and metal-metal interactions. For this to be possible we require larger cages, which can be formed by condensation of monomers in the manner of *conjuncto* boranes. This may be done by sharing a single vertex, such as $[M_2Sn_{17}]^{q-}$ (M=Ni,Pt: q=4; M=Co: q=5), edges, as in $[Rh_3Sn_{24}]^{5-}$, or more complete polyhedral fusion to form a continuous cage such as $[Pd_2Ge_{18}]^{4-}$[74]. Examples of both of these types are shown in Figure 3.5. Some clusters, such as $[Ni_3Ge_{18}]^{4-}$[75] which will be discussed in detail alongside $[Ni_2InSn_{18}]^{5-}$, cannot be easily assigned to these categories and must be examined closely.

Important questions surround the nature of the M-M interactions in these clusters. The M-M internuclear distance is controlled, in a large part, by the geometry of the cage, so this alone cannot be used as an indicator of bonding as it can in less restricted organometallic complexes[76]. That said, direct M-M bonding can be ruled out in in some structures, such as $[Rh_3Sn_{24}]^{5-}$, by large interatomic distances[58]. Some clusters do feature direct M-M bonds, however; the dimeric clusters $[Ge_9M{-}MGe_9]^{6-}$ (M=Zn, Cd) are held together by a central M-M bond alone[77, 78]. Characterization and classification of M-M interactions in clusters is challenging, requiring careful use of multiple pieces of information, and will be the subject of a great deal of the results reported in this chapter. Heterometallic clusters have been of interest for some time as "embryonic alloys", capturing the same M-M' interactions as in an alloy, but in a small, atomically precise structure which can be studied in great depth experimentally and theoretically. A particularly striking example in this area is the "Matryoshka bronze" $[Sn@Cu_{12}@Sn_{20}]^{12-}$, called so because its concentric structure resembles a Russian nesting doll[79].

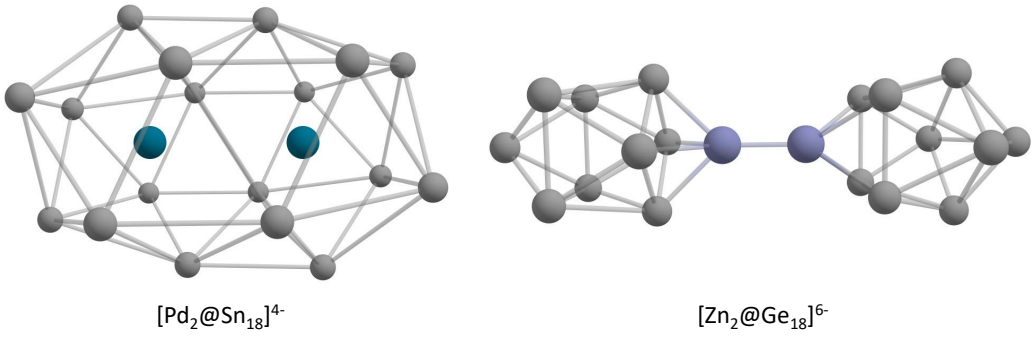



Figure 3.5: Group 14 clusters containing multiple transition metals.

### 3.1.5 Quantum chemical studies of group 14 clusters

Density functional theory is the quantum chemical tool used for the vast majority of computational studies of group 14 clusters. The most common purposes of such studies are MO calculations and determining structures of clusters which have been observed in the gas phase but not crystallized. This explains the enduring success of DFT in this area; structural optimizations are economical and reliable, applicable to even the largest clusters, and qualitative MO calculations are not jeopardised by the quantitative errors and functional dependencies that affect *e.g.* reaction barriers in organic chemistry. Nevertheless, wavefunction methods are becoming more accessible as computational resources expand. Coupled cluster calculations have been applied to monomeric encapsulated clusters for greater numerical accuracy when considering cluster formation energetics[80, 81]. Multireference calculations, such as CASSCF and its perturbative correction CASPT2, have been applied to the three-connected gas phase cluster $[Mn@Si_{14}]^+$ to provide a more sophisticated description of the wavefunction than DFT can provide[82]. This method allows for a reliable prediction of the ground spin state, a notoriously challenging area for DFT, and reveals charge transfer from the metal to the cage in the multiconfigurational wavefunction. In our studies of $[M@Ge_{10}]^{3-}$ we will use CASSCF to study metal-cage charge transfer, and we will then extend this to $[M_2@Ge_{16}]^{4-}$ using GASSCF as the second transition metal atom makes the system too large for a normal CASSCF calculation.

An increasingly broad array of methods for understanding cluster structure has been developed, beyond simply calculating the energies of different structures. Many are based on electron counting, where Wade's rules remain a cornerstone of descriptions of cluster bonding, and simple quantum mechanical models with analytical solutions can be powerful predictors of cluster sizes and properties. The "superatom" concept can be used very successfully to predict the sizes of large gold clusters - so-called "magic numbers" - by using the model of a quantum particle in a spherical potential well[83]. This allows pseudo-atomic electron configurations to be applied to clusters, and will be described in more detail in the section on coinage metal clusters.

Aromaticity is another popular concept when justifying the stability of particular clusters. Their highly symmetric polyhedral structures can be described by the simple model of a quantum particle moving on the surface of a sphere, the eigenstates and degeneracies of which leads to an electron counting rule of $2(N+1)^2$ for a stable electronic configuration[84]. This is called "spherical aromaticity" by analogy to the Hückel $4N+2$ rule for aromaticity in conjugated rings, which can be derived from the quantum mechanical "particle on a ring" model. For example, $[Zn@Sn_{10}]$

and [Zn@$Sn_{12}$] both have $8\pi$ conjugated systems and are therefore spherically aromatic, though they have bicapped square antiprismatic and icosahedral structures respectively[80]. The concept can be applied to $\sigma$ and $\pi$ bonding frameworks - the 68 electrons in $[V@Si_{16}]^+$ have been partitioned into $50\sigma + 18\pi$, both of which are spherically aromatic counts[85]. Note also that 68 electrons is a stable electron count according to the superatom model. For planar clusters like $B_{19}^-$, "disk aromaticity" has been proposed based on the circular potential well model, though these clusters are also commonly described as containing concentric aromatic rings[86, 87]. These descriptions are generally validated by calculations of nuclear-independent chemical shift (NICS) values, which measure ring currents associated with aromaticity[88].

The apparent absence of two-centre two-electron bonds in clusters makes them difficult to understand, so a number of localization methods have been developed to describe cluster bonding in more familiar terms of localized lone pairs and two-centre bonds. One commonly used method is "Adaptive Natural Density Partitioning" (AdNDP)[89], which can, for example, highlight the differences between the deltahedral and three-connected isomers of $[Co_2Ge_{16}]^{4-}$[90]. Bader's QTAIM[18] is a popular method in inorganic chemistry for classifying bonds in molecules, but the subtle electron density variations in clusters make this method difficult to apply. We will assess its use in a number of situations in this chapter.

So far, the methods we have discussed have been useful for describing the bonding in clusters where the structures are already known. An important frontier in this field is the ability to predict structures and formation pathways in solution. We will do this in our study of Au-Pb clusters on the basis of qualitative structural considerations, but sophisticated, automated computational methods have also been developed for this purpose. The "GA-RP" approach uses a genetic algorithm to generate isomers for a particular stoichiometry which can suggest pathways for isomerization and formation from fragments[71]. This has been applied to a family of Ta-Ge-As clusters in which important fragments were identified, though they are too transient to observe directly, and the role of transition metal redox was described.

## 3.2 $[M@Ge_{10}]^{3-}$ and $[M_2Ge_{16}]^{4-}$ fused pentagonal clusters

### 3.2.1 Introduction

In this section we will investigate a group of four encapsulated clusters $[M@Ge_{10}]^{3-}$ and $[M_2Ge_{16}]^{4-}$ (M=Fe, Co), which have remarkable cage architectures based on pentagonal prisms. The structures of these clusters as determined by X-ray crystallography, shown in Figure 3.6 with bond lengths annotated, are three-connected, rather than deltahedral, so we will begin with a discussion of the difference between the two bonding paradigms. Most group 14 clusters, as well as boranes, have deltahedral

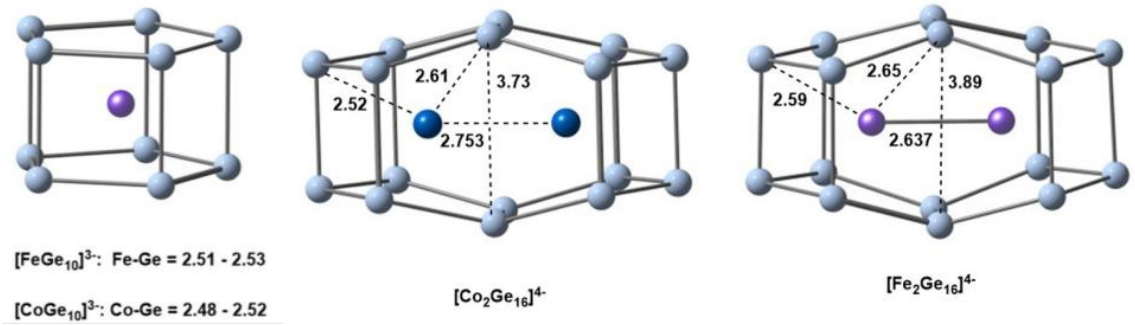



Figure 3.6: Structures of $[M@Ge_{10}]^{3-}$ and $[M_2Ge_{16}]^{4-}$ (M=Fe, Co) determined by X-ray diffraction annotated with bond lengths in Å[90]. Ge is shown in grey, iron in pruple, and cobalt in blue.

structures, with triangular faces and high-connectivity vertices. These are adopted by electron-deficient clusters, which do not have enough electrons to satisfy all atomic valences by two-centre two-electron bonds, and instead stabilize the electrons that they do have by delocalized bonding. However, more electron-rich clusters, often containing group 15 elements, can form two-centre two-electron bonds and therefore adopt three-connected cage structures. Examples in this class include $As_{11}{}^{3-}$, $S_4N_4$, and clusters like $[Ta@Ge_8As_4]^{3-}$ in the Ge-As-Ta series[71], where oxidation of Ta provides the electrons required for bonding in the cage.

The endohedral clusters $[Fe@Ge_{10}]^{3-}$[69] and $[Co@Ge_{10}]^{3-}$[70], first reported within weeks of each other in 2009, represent a landmark in Zintl ion chemistry as the first ligand-free group 14 clusters to adopt non-deltahedral structures. The original report of $[Co@Ge_{10}]^{3-}$[70] includes some discussion of computational results of investigations into this structural preference. The pentagonal prism is the calculated ground state for $[Co@Ge_{10}]^{3-}$ but for the isoelectronic analogues $[Ni@Ge_{10}]^{2-}$, $[Cu@Ge_{10}]^{-}$

and $[Zn@Ge_{10}]$, as well as the empty $[Ge_{10}]^{2-}$ cage, the calculated ground state is reported to be a bicapped square antiprism, a $D_{4d}$-symmetric *closo*-deltahedron. The $D_{5h} - D_{4d}$ energy gap was found to be large for the empty cluster but small for the Co and Ni compounds, consistent with the general observation that these cluster compounds have relatively flat potential energy surfaces. The structural trend across the first transition series, if we include the $D_{5h}$ structure for $[Fe@Ge_{10}]^{3-}$, suggests that the pentagonal prismatic structure is favoured by a larger central transition metal atom with diffuse, high-energy $d$ orbitals. The three-connected structure of $[Ru@Ge_{12}]^{3-}$ supports this picture as the more diffuse $4d$ valence orbitals of the second-row metal will further enable metal-cage covalency, and shows that the phenomenon is not restricted to 10-vertex clusters. The encapsulated metal can act as a source of electron density for the cage, crossing from the electron-deficient deltahedral bonding regime to the electron-precise three-connected regime. The fine balance between these two quite different bonding paradigms, and the dependence on the identity of the encapsulated metal, indicates a complex electronic interaction between the metal and the cage.

In 2015 Goicoechea and McGrady reported the synthesis of $[Co_2Ge_{16}]^{4-}$, a face-sharing dimer of $[Co@Ge_{10}]^{3-}$, with partial characterization based on mass spectrometry and DFT calculations[91]. The crystal structure was not resolved due to disorder, a phenomenon which was explained by DFT showing that this cluster could exist in two near-degenerate forms; a fused pentagonal dimer, with $D_{2h}$ symmetry, and a deltahedral $C_{2h}$ structure. Sun and Boldyrev confirmed in 2018 that the crystal contains both of these isomers, and showed by DFT calculations and the Adaptive Natural Density Partitioning method (AdNDP) that the two have markedly different bonding character[90]. The $D_{2h}$ isomer is composed of two-centre two-electron bonds, much like the $[Co@Ge_{10}]^{3-}$, while the bonding in the $C_{2h}$ isomer is far more delocalized, consistent with a deltahedral geometry associated with electron deficiency.

The latest addition to this series is $[Fe_2Ge_{16}]^{4-}$, which is to $[Fe@Ge_{10}]^{3-}$ as $[Co_2Ge_{16}]^{4-}$ is to $[Co@Ge_{10}]^{3-}$. This cluster has been characterized only in the $D_{2h}$ geometry seen for $[Co_2Ge_{16}]^{4-}$. The synthesis and structural determination by X-ray diffraction of $[Fe_2Ge_{16}]^{4-}$ were reported alongside the computational results presented here in *Journal of Physical Chemistry A*[31]. The total electron count of $[Fe_2Ge_{16}]^{4-}$ is smaller than that of $[Co_2Ge_{16}]^{4-}$ by two electrons, so the former is less electron-rich overall. However, since Fe has slightly higher energy $d$ orbitals and has a more accessible half-filled $d$ shell configuration it may be more able to transfer electron density to the $Ge_{16}$ cage. There are therefore two factors competing to determine the effect of the

metal on the electronic character of the cage, and therefore its structure. In this investigation we study the quartet of clusters $[M@Ge_{10}]^{3-}$ and $[M_2Ge_{16}]^{4-}$, M = Fe, Co, using DFT and multiconfigurational methods to understand the subtle interactions between the two transition metal atoms, and between the metals and the cage.

## 3.2.2 Methods

DFT calculations were performed with ADF[26], version 2019.304, using the PBE functional[5] with Slater-type TZP basis functions[92]. The crystalline environment was modelled using the COSMO continuum solvent model[93] with the dielectric constant of water. CASSCF and GASSCF calculations were performed using OpenMolcas[94, 95], version 18.0 (pymolcas driver version py2.02), with an all-electron atomic natural orbital basis set. All CASSCF and GASSCF calculations were done using the optimized geometries obtained from the DFT calculations. Calculations on $[M@Ge_{10}]^{3-}$ used the $D_{2h}$ subgroup rather than the full but non-Abelian $D_{5h}$ point symmetry, although results are labeled according to the latter. Calculations on $[M_2Ge_{16}]^{4-}$ used the full $D_{2h}$ molecular symmetry. The ANO basis for Co and Fe contain 17s12p9d primitives contracted to 5s4p2d, while for Ge a 17s15p9d primitive set is contracted to 5s4p1d (ANO-S-VDZ in the OpenMolcas library)[96, 97]. The continuum solvent model was also used in CASSCF and GASSCF calculations[93].

## 3.2.3 Results

### 3.2.3.1 DFT studies of $[M@Ge_{10}]^{3-}$

Our investigation begins with optimizations of the monomeric clusters $[Fe@Ge_{10}]^{3-}$ and $[Co@Ge_{10}]^{3-}$ in $D_{5h}$ symmetry. Structures annotated with bond lengths are shown in Figure 3.7 for both clusters. The computed bond lengths are a good match for those measured by X-ray diffraction for both clusters[69, 70], though fractionally longer, as is often the case in Zintl cluster chemistry, and the ratios of the symmetry-inequivalent Ge-Ge bonds are correct, so we are confident in our computational model. To understand the electronic structure of the transition metal atoms in these clusters we have plotted energy level diagrams for the 3*d*-based MOs, shown in Figure 3.8. As the diagram describes two compounds, we cannot give a quantitative energy scale. $[Co@Ge_{10}]^{3-}$ is a closed-shell singlet, while $[Fe@Ge_{10}]^{3-}$, having one fewer electron, is a doublet. The 3*d* orbitals are separated into three energy levels - $d_{z^2}$ has $a_1'$ symmetry, $d_{xy/x^2-y^2}$ form an $e_2'$ degenerate pair, and $d_{xz/yz}$ form an $e_1''$ degenerate pair. In both compounds the $d_{z^2}$ is highest in energy, followed by the in-plane $d_{xy/x^2-y^2}$, and the

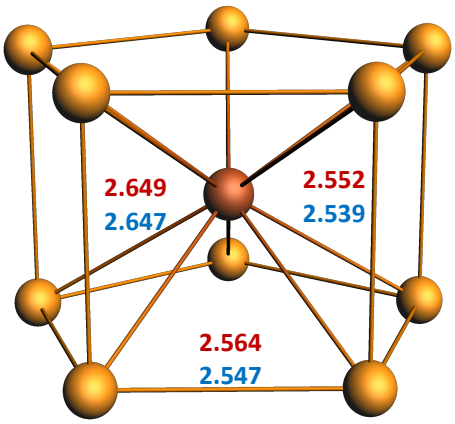



Figure 3.7: Bond lengths in $D_{5h}$-optimized $[M@Ge_{10}]^{3-}$ (M=Fe, Co), with M shown in red and Ge in orange. Bond lengths are given in Å. Red labels refer to M=Fe and blue labels refer to M=Co.

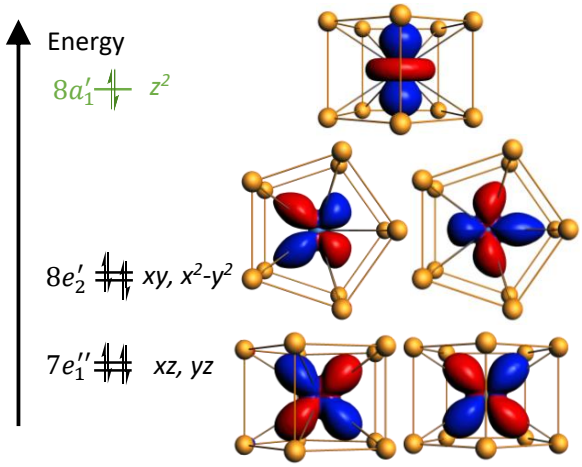



Figure 3.8: MO diagrams for the M 3$d$ orbitals in $[M@Ge_{10}]^{3-}$, plotted with isovalue = 0.05. The MOs highlighted in green is singly occupied in $[Fe@Ge_{10}]^{3-}$.

$d_{xz/yz}$ pair are lowest in energy. All Co 3$d$ MOs in $[Co@Ge_{10}]^{3-}$ are filled, so we can assign a formal $d^{10}$ electron configuration to Co and describe it as a closed-shell $Co^{-}$. As pointed out in the original report of this compound, this implies no covalent interaction between Co and the cage[69] - a description which we will reexamine with multiconfigurational methods below. In $[Fe@Ge_{10}]^{3-}$ the $d_{z^2}$ becomes singly occupied, giving a formal $d^9$ $Fe^{-}$ completely analogous to the Co case. We will consider the bonding in the $Ge_{10}$ cage in more detail in section 3.2.3.3.

### 3.2.3.2 DFT studies of $[M_2Ge_{16}]^{4-}$

Having understood the electronic structure of the pentagonal prismatic $[M@Ge_{10}]^{3-}$ clusters, we now investigate the $[M_2Ge_{16}]^{4-}$ clusters formed by fusion of two such pentagonal prisms through a square face. $[Co_2Ge_{16}]^{4-}$ crystallizes as a mixture of $D_{2h}$ and $C_{2h}$ isomers, while $[Fe_2Ge_{16}]^{4-}$ has been isolated in the $D_{2h}$ form alone. We therefore optimized both isomers for both compounds, finding a $D_{2h}$-$C_{2h}$ energy gap of 0.170 eV for Co and 0.235 eV for Fe. The slightly larger gap for Fe is consistent with the absence of the $C_{2h}$ isomer in the crystal structure of $[Fe_2Ge_{16}]^{4-}$. The structures are shown in Figure 3.9, annotated with nearest-neighbour M-Ge and M-M bond lengths. Due to the lower symmetry of the $C_{2h}$ isomer, M-Ge bond lengths to certain groups of Ge atoms, denoted by black brackets, are shown as a range rather than individual bond lengths for clarity. The computed bond lengths are once again

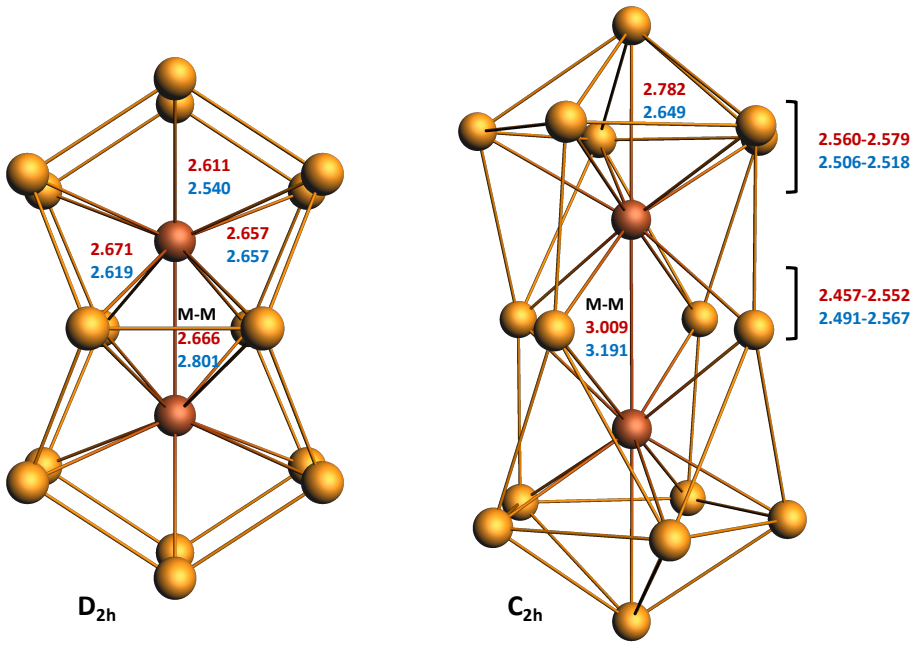



Figure 3.9: M-Ge and M-M bond lengths in $[M_2Ge_{16}]^{4-}$, with M shown in red and Ge in orange. Bond lengths are given in Å. Red labels refer to M=Fe and blue labels refer to M=Co.

a good match with experiment. Comparing the two structures, we can see that in the $D_{2h}$ isomer the M-Ge distances are longer and more evenly distributed, but the M-M bonds are approximately 12% shorter. Both isomers of $[Co_2Ge_{16}]^{4-}$ have singlet ground states, which we have confirmed by calculating triplet state energies which are 0.83 eV and 0.42 eV above the singlets for $D_{2h}$ and $C_{2h}$ respectively. $[Fe_2Ge_{16}]^{4-}$ contains two fewer electrons than the Co analogue, so multiple spin states may be

accessible. If both electrons come out of one orbital then a singlet state will result, while if two electrons of the same spin are lost then we will find a triplet. The ground state proves to be a triplet, reflecting the narrow energy separation between $d$ levels and the strong electronic repulsion in the contracted $3d$ orbitals. A closed-shell singlet state was found 0.37 eV above the triplet ground state, and an open-shell singlet, with $\alpha$-spin density accumulated on the Fe atoms and $\beta$-spin density on the cage, was found at +0.29 eV. A quintet was then found at +0.80 eV, indicating that any spin state higher than a triplet requires promotion of an electron to a much higher-energy orbital.

Our discussion of the electronic structure of these clusters now focuses on the $D_{2h}$ isomers as these have been shown by experiment and theory to be the ground state for both metals. MO diagrams for the $3d$ levels are shown in Figure 3.10 for $[Co_2Ge_{16}]^{4-}$ and $[Fe_2Ge_{16}]^{4-}$, analogous to those for $[M@Ge_{10}]^{3-}$ in Figure 3.8, with MOs which are doubly occupied in $[Co_2Ge_{16}]^{4-}$ but singly occupied in $[Fe_2Ge_{16}]^{4-}$ shown in green. The $d$-based MOs for $[Co_2Ge_{16}]^{4-}$ are fairly straightforward to understand because

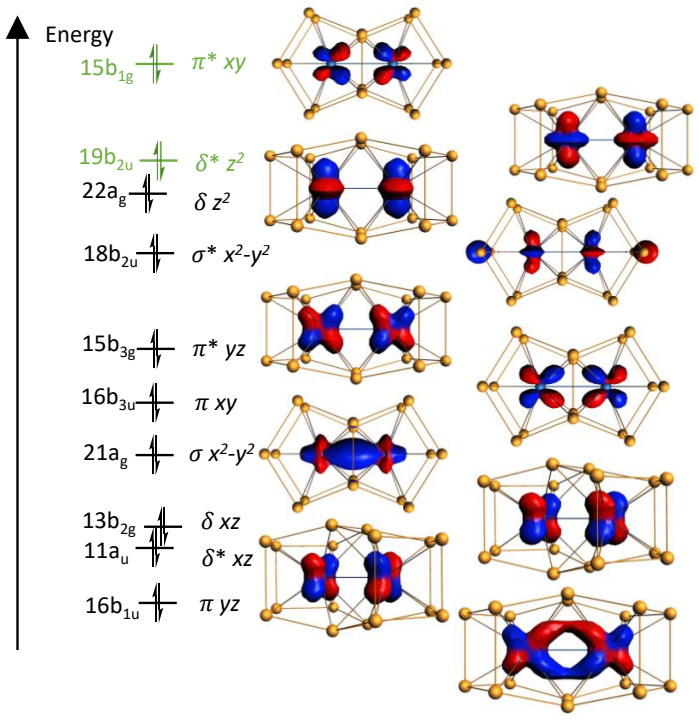



Figure 3.10: MO diagram for the $3d$ levels in $[Co_2Ge_{16}]^{4-}$ and $[Fe_2Ge_{16}]^{4-}$, plotted with isovalue = 0.036. MOs highlighted in green are singly occupied in $[Fe_2Ge_{16}]^{4-}$.

all bonding and antibonding combinations of $d$ orbitals are filled, as we might have expected from the $d^{10}$ configuration in $[Co@Ge_{10}]^{3-}$, so there is no formal Co-Co

bond. The energy orderings of the $d$ orbitals here reflect those in $[Co@Ge_{10}]^{3-}$, but the degenerate pairs in $D_{5h}$ symmetry are split by the reduction in symmetry and the formation of bonding and antibonding pairs. The energetic separation between such pairs is dictated by the spatial overlap between $d$ orbitals on the two metal atoms. For example, the $\delta/\delta^*$ $d_{xz}$ pair are almost degenerate due to minimal face-on overlap, while the $d_{yz}$ pair overlap much more strongly, with $\pi$ symmetry, so the $\pi^*$ $d_{yz}$ orbital lies above the bonding combinations of $d_{xy}$ and $d_{x^2-y^2}$.

As discussed above, $[Fe_2Ge_{16}]^{4-}$ has a triplet ground state which may be described by removing two spin-$\beta$ electrons from $[Co_2Ge_{16}]^{4-}$. These two electrons come from the highest $d$ MOs, which are the out-of-phase combinations of $d_{xy}$ and $d_{z^2}$, shown in green in Figure 3.10. The former is a $\pi^*$ orbital, with clear antibonding character, while the latter could be described as weakly $\delta$-antibonding or non-bonding due to the small overlap between $d_{z^2}$ orbitals, shown by the small energy difference between this MO ($19b_{2u}$) and the corresponding in-phase combination ($22a_g$). From this we can assign the Fe-Fe bond a formal bond order of 0.5, by describing the $d_{z^2}$-based MOs as non-bonding.

The small $\delta - \delta^*$ energy gap, which is the HOMO-LUMO gap in the $\beta$-spin channel, implies the existence of low-lying triplet excited states where the electron in the $22a_g$ orbital is promoted to $19b_{2u}$ ($\delta \rightarrow \delta^*$) or $15b_{1g}$ ($\delta \rightarrow \pi^*$). We have reoptimized the structure with these promotions, calculating the energies of these states to be 0.28 eV and 0.54 eV, respectively, above the ground state. The Fe-Fe bond lengths for the excited states are 2.714 Å and 2.894 Å respectively, which when compared to the ground state value of 2.666 Å show that occupation of the $\pi^*$ orbital has a much greater impact on the bond length than the $\delta^*$. This supports our suggestion that the $\delta^*$ orbital has effectively non-bonding character.

The presence of unpaired electrons, while a classic feature of transition metal chemistry, is uncommon for encapsulated clusters, where most transition metal atoms can be assigned a formal $d^{10}$ configuration. We can begin to explore the consequences of spin polarization in $[Fe@Ge_{10}]^{3-}$ and $[Fe_2Ge_{16}]^{4-}$ by plotting the spin densities and calculating Mulliken atomic spin populations, shown for both clusters in Figure 3.11. The spin densities in both clusters show spin-$\alpha$ density centred on Fe and accumulation of spin-$\beta$ density on the Ge cages, indicating transfer of $\beta$ electrons from Fe to the cage. The Fe spin populations of 1.39 in $[Fe@Ge_{10}]^{3-}$ and 1.50 in $[Fe_2Ge_{16}]^{4-}$ are substantially larger than the ideal value of 1.0 for a single unpaired electron. We also see substantial spin contamination - for $[Fe@Ge_{10}]^{3-}$, $\langle S^2 \rangle = 0.84$ rather than

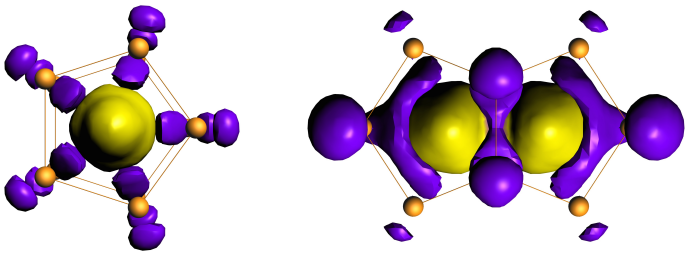



Figure 3.11: SCF spin densities of $[Fe@Ge_{10}]^{3-}$ and $[Fe_2Ge_{16}]^{4-}$ (isovalue = 0.0015) annotated with Fe Mulliken spin populations.

the exact value of 0.75, and for $[Fe_2Ge_{16}]^{4-}$, $\langle S^2 \rangle = 2.30$ rather than 2.0. This suggests that both clusters can be stabilized by the transfer of electron density from iron onto the germanium cages, reducing electron repulsion in the radially contracted $3d$ orbitals and amplifying the spin polarization. In the unrestricted Kohn-Sham (UKS) DFT formalism this is achieved by allowing the spin-$\alpha$ and spin-$\beta$ electrons to have separate sets of one-electron orbitals, so their spatial distributions differ, which leads to spin contamination.

To compare the metal-metal interactions in $[Fe_2Ge_{16}]^{4-}$ quantitatively, we have calculated topological properties of the electron density using Bader's Atoms in Molecules (QTAIM) theory[18]. We have calculated the delocalization index (DI), described in detail in the theory chapter, which measures the number of electron pairs delocalized over a pair of atoms and is therefore analogous to bond order, and which has been shown recently to give useful descriptions of bonding in transition metal chemistry[24]. The calculated delocalization indices for the Fe-Fe and Co-Co pairs are 0.76 and 0.28 respectively, suggesting that there is much more electron sharing between Fe atoms than Co atoms, and that the Fe-Fe bond order is indeed between 0.5 and 1.0 as indicated by the MO diagram. The non-zero value for Co-Co, formally an interaction between two closed-shell atoms, reflects the fact that the metal atoms bond significantly with the cage and thus, indirectly, with each other.

The presence of low-lying excited electronic states and spin contamination suggests that these clusters have strong multiconfigurational character in the wavefunction, which cannot be described by DFT and must instead be addressed with a suitable multireference method. We will do this in section 3.2.3.5 below.

#### 3.2.3.3 The jigsaw bonding model

These clusters pose a challenge to common methods of electron counting. We will first consider $[Co@Ge_{10}]^{3-}$, where we have assigned a -1 charge to the metal atom, on the basis of 3*d*-based MO occupancies, which implies a -2 charge on the cage. This gives a skeletal electron count of 22, with 2 bonding electrons coming from each Ge atom and 2 more from the charge, which by the Wade-Mingos rules predicts a $2n+2$ 10-vertex *closo*-deltahedral structure, i.e. the bicapped square antiprism seen for the empty $Ge_{10}^{2-}$ cluster and encapsulated analogues such as $[Ni@Pb_{10}]^{2-}$. The pentagonal prismatic geometry of $[Co@Ge_{10}]^{3-}$, with all cage vertices three-connected, is more akin to "electron-precise" clusters composed entirely of two-centre two-electron bonds. Such a description of this cluster would require a valence electron count of 50, from 15 Ge-Ge bonds and 10 Ge lone pairs. Each Ge has 4 valence electrons so the cage would need a formal -10 charge to make up the required 50 valence electrons. This in turn implies an assignment of a +7 charge to the encapsulated atom, with a $d^2$ configuration for Co or $d^1$ for Fe. Such extreme charge separation is clearly physically unreasonable, and the reality must be that extensive covalent bonding between metal and cage allows the cluster to adopt a state in between the limiting cases. Here we will describe this electron-sharing more rigorously with the "jigsaw model", which uses symmetry analysis and MO theory to describe metal-cage covalence in these three-connected encapsulated clusters.

$[Co@Ge_{10}]^{3-}$ has 52 valence electrons - 4 per Ge, 9 from Co, and 3 for the charge. In the MO theory description of electronic structure, these electrons occupy orbitals which can be classified by their symmetry into irreps of the molecular point group, which is $D_{5h}$ in $[Co@Ge_{10}]^{3-}$. A DFT calculation tells us that these occupied MOs have the following symmetries:

$$\Gamma_{calc} = 4a_1' + 2a_2'' + 3e_1' + 3e_2' + 2e_2' + 2e_2'' \tag{3.1}$$

This 26-dimensional representation can accommodate 52 electrons, consistent with the valence electron count calculated by summing the atomic valence electrons.

The three-connected structure of $[Co@Ge_{10}]^{3-}$ suggests that every Ge-Ge bond is a two-centre two-electron bond and that every Ge atom has a lone pair, so we will now use "pen-and-paper" symmetry analysis to find the irreps spanned by the Ge lone pairs, Ge-Ge bonds, and Co *d* orbitals. This analysis is closely related to the standard methods for using group theory to determine the symmetries of molecular orbitals or vibrational modes, by counting the number of functions of a chosen basis (*e.g.* atomic

orbitals) which are changed by each symmetry operation in the point group. Here we calculate the irreps spanned by the Ge lone pairs by using the Ge atoms as the basis, and those spanned by Ge-Ge bonds using a basis of bonds drawn between every nearest-neighbour pair of Ge atoms, as shown in Figure 3.7. This is valid for three-connected structures, which formally have a two-centre two-electron bond between every pair of neighbouring atoms, but would not be possible in a deltahedral cluster with more delocalized bonding. The central Co atom lies on an invariant point in $[Co@Ge_{10}]^{3-}$, so the symmetry species of the $d$ orbitals can be read directly from the $D_{5h}$ character table. This analysis gives:

$$\Gamma_{Ge\,lp} = 1a_1' + 1a_2'' + 1e_1' + 1e_2' + 1e_1'' + 1e_2'' \tag{3.2}$$

$$\Gamma_{Ge-Ge} = 2a_1' + 1a_2'' + 2e_1' + 2e_2' + 1e_1'' + 1e_2'' \tag{3.3}$$

$$\Gamma_{Co\,d} = a_1' + e_2' + e_1'' \tag{3.4}$$

$$\Gamma_{total} = 4a_1' + 2a_2'' + 3e_1' + 4e_2' + 3e_1'' + 2e_2'' \tag{3.5}$$

This differs from $\Gamma_{calc}$, the "true" cluster count given in equation 3.1, as it contains an additional $e_2' + e_1''$, which may accommodate 8 electrons. These orbitals are double-counted by this method of adding up the Ge and Co contributions separately, implying that pen-and-paper analysis produces duplicates of orbitals which are in reality contributed by metal and cage together. Based on this interpretation, they may be denoted $\Gamma_{shared}$:

$$\Gamma_{shared} = \Gamma_{total} - \Gamma_{calc} \tag{3.6}$$

$$= e_2' + e_1'' \tag{3.7}$$

They are therefore the orbitals which simultaneously contribute to the electron counts of cluster and metal to give a 50-electron cage and a $d^{10}$ metal. If we assign $\Gamma_{shared}$ exclusively to Co, giving it a $d^{10}$ configuration, we then have a 42-electron cage which Wade's rules would predict to be a bicapped square antiprism, just like $[Ni@Ge_{10}]^{2-}$. Alternatively, we may assign the electrons to the cage, giving it the correct electron-precise electron count but also giving an unphysical $[Co^{7+}@{Ge_{10}}^{10-}]$ charge separation. A realistic physical description must be somewhere in between these two extremes.
We can identify the orbitals localized exclusively on the metal by subtracting $\Gamma_{shared}$ from $\Gamma_{Co\,d}$, which gives $a_1'$. Co $d_{z^2}$ transforms as $a_1'$, so this doubly occupied orbital is non-bonding with respect to the cage, and increases the cluster electron count from 50 to 52. Another way to state this is that in the $[Co^{7+}@{Ge_{10}}^{10-}]$ picture, where $\Gamma_{shared}$ has been assigned exclusively to the $Ge_{10}$ cage, the two electrons on $Co^{7+}$ are in the

$d_{z^2}$ orbital. The orbital analysis for $[Fe@Ge_{10}]^{3-}$ is identical, since the two clusters are isostructural, and the electron counting differs only in that Fe has a singly occupied $d_{z^2}$ orbital so there is just one electron localized on the metal.
The jigsaw model description can be elegantly represented by a Venn diagram, as in Figure 3.12. The left- and right-hand-side circles represent the cage and encapsulated metal, respectively, and each region is annotated by the number of electrons counted for that cluster fragment. The diagram for $[Co@Ge_{10}]^{3-}$ shows 42 electrons assigned exclusively to the cluster, 2 electrons localized exclusively on the metal, and 8 electrons shared between the two. In contrast, $[Ni@Ge_{10}]^{2-}$ has no electrons in the overlap region because its *closo*-deltahedral structure is consistent with a 42-electron $Ge_{10}{}^{2-}$ cage encapsulating $d^{10}$ $Ni^0$.
Repeating the procedure for $[Co_2Ge_{16}]^{4-}$, a DFT calculation tells us that the cluster has 86 electrons with irreducible representations:

$$\Gamma_{calc} = 9a_g + 5b_{1g} + 4b_{2g} + 4b_{3g} + 3a_u + 6b_{1u} + 7b_{2u} + 5b_{3u} \tag{3.8}$$

Pen-and-paper group theory analysis gives the following irreps for the metal and cage components:

$$\Gamma_{Ge\ lp} = 3a_g + b_{1g} + 2b_{2g} + 2b_{3g} + a_u + 3b_{1u} + 2b_{2u} + 2b_{3u} \tag{3.9}$$

$$\Gamma_{Ge-Ge} = 5a_g + 3b_{1g} + 2b_{2g} + 2b_{3g} + 2a_u + 3b_{1u} + 4b_{2u} + 3b_{3u} \tag{3.10}$$

$$\Gamma_{Co\ d} = 2a_g + b_{1g} + b_{2g} + b_{3g} + a_u + b_{1u} + 2b_{2u} + b_{3u} \tag{3.11}$$

$$\Gamma_{total} = 10a_g + 5b_{1g} + 5b_{2g} + 5b_{3g} + 4a_u + 7b_{1u} + 8b_{2u} + 6b_{3u} \tag{3.12}$$

As before, we can identify the shared orbital set $\Gamma_{shared}$ as the ones which are double-counted in $\Gamma_{total}$, and then identify the orbitals localized on the metals by subtracting $\Gamma_{shared}$ from $\Gamma_{Co\ d}$:

$$\Gamma_{shared} = a_g + b_{2g} + b_{3g} + a_u + b_{1u} + b_{2u} + b_{3u} \tag{3.13}$$

$$\Gamma_{Co-Co} = a_g + b_{1g} + b_{2u} \tag{3.14}$$

We therefore have 14 electrons shared between metal and cluster, and three orbitals localized on the $Co_2$ dimer, shown on the Venn diagram in Figure 3.12.

#### 3.2.3.4 Density of states analysis

We have analysed the $[M@Ge_{10}]^{3-}$ and the $[M_2Ge_{16}]^{4-}$ pairs through their $3d$-based molecular orbitals, but we cannot easily compare $[M@Ge_{10}]^{3-}$ to $[M_2Ge_{16}]^{4-}$ directly in this way due to their different stoichiometries. We can, however, compare clusters

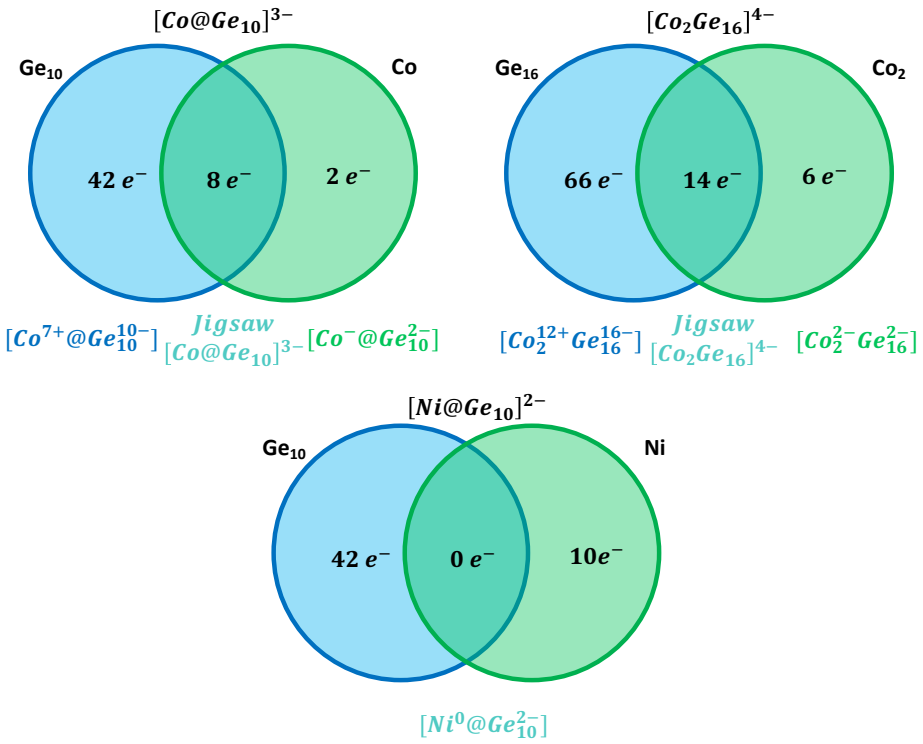



Figure 3.12: Venn diagrams illustrating the 'jigsaw' electron counting analysis for $[Co@Ge_{10}]^{3-}$, $[Co_2Ge_{16}]^{4-}$, and $[Ni@Ge_{10}]^{2-}$.

of different stoichiometries by analysing their density of states (DOS) and projected density of states (PDOS), which give us a broad picture of the energy distribution and orbital composition of MOs in a cluster. PDOS plots for all four clusters are shown in Figure 3.13, with projections on to the Co/Fe 3*d* and Ge 4*s*/4*p* orbitals. To highlight the parallels between the MO and DOS representations of the electronic structure we have marked important peaks with the relevant orbitals. The 3*d* orbitals contribute mostly to the DOS around the "Fermi level", consistent with our MO analysis. The Ge valence orbital PDOS shows peaks coincident with these M 3*d* peaks, indicative of substantial metal-cage covalency, contrary to previous analysis of $[Co@Ge_{10}]^{3-}$ in the literature[70]. Comparing the PDOS plots for the two clusters we can see that the 3*d* peaks appear at much the same energies, but are broader in $[M_2Ge_{16}]^{4-}$. This broadening results from the splitting of the 3*d* levels into bonding and antibonding combinations by the M-M interactions, so we can infer that the M-M interactions are weaker than the metal-cage interactions.

Another important observation is that the 3*d* orbitals are clearly separated energetically into groups that reflect their character in the jigsaw model. The shared orbitals, which contribute to the formal electron counts of metals and cage, are the

lower-energy group, while the orbitals localized on the metals are higher. The PDOS plots also show greater metal-cage peak coincidence for the shared orbitals than the localized ones, supported by the visible Ge character in the shared MOs.

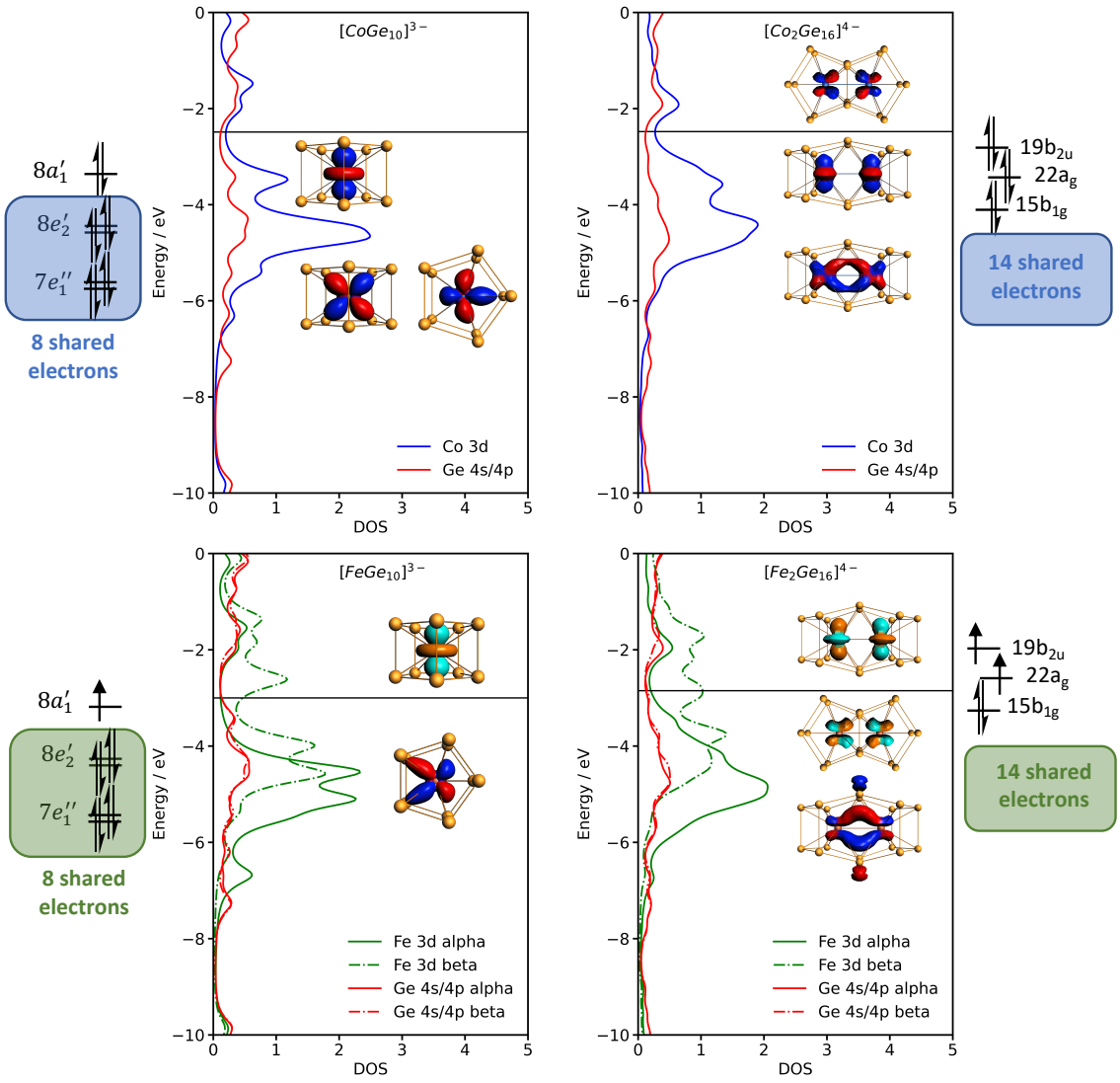



Figure 3.13: Density of states (DOS) plots for $[Co@Ge_{10}]^{3-}$, $[Co_2Ge_{16}]^{4-}$, $[Fe@Ge_{10}]^{3-}$ and $[Fe_2Ge_{16}]^{4-}$ with selected MOs. Black horizontal lines mark the mid-point between the HOMO and LUMO energies as an approximation to the Fermi level.

#### 3.2.3.5 Multiconfigurational wavefunctions from CASSCF and GASSCF

Our DFT results have indicated that these clusters, particularly those containing encapsulated iron atoms, may have substantial multiconfigurational character in the wavefunction. This is shown by the spin densities, Mulliken spin populations, and

spin contaminations for the open-shell clusters, which indicate appreciable transfer of electron density from encapsulated metal to cage in the unrestricted wavefunction. We must therefore consider the possibility of the wavefunction containing appreciable contributions from excited states in which metal $3d$ electrons have been promoted to cage-based orbitals of appropriate symmetry. To do so we have employed the Generalized Active Space SCF (GASSCF) method, conceptually similar to the more common CASSCF but more economical as it allows us to exclude excitations which make a near-zero contribution to the wavefunction. This exclusion is likely to be valid in these high-symmetry molecules as it should be possible to separate excitations from $d$ orbitals of different symmetry. We will confirm the validity of this separation for $[M@Ge_{10}]^{3-}$ by calculating the corresponding CASSCF wavefunctions, which involves no partitioning of the active space and is therefore more accurate in principle, but the sizes of the active spaces needed for $[M_2Ge_{16}]^{4-}$ prohibit the use of CASSCF. The calculations on $[M@Ge_{10}]^{3-}$ were done using the $C_{2v}$ point group as OpenMolcas only uses Abelian point groups, but results are presented using $D_{5h}$ symmetry labels as this is the point group of these clusters. This is shown to be valid by the fact that the $e_2'$ pairs have equal occupation numbers despite transforming as different irreps in $C_{2v}$, so the lower-symmetry calculation has preserved the degeneracies of the parent point group.

We began by constructing a GAS5(10,10) active space for $[Co@Ge_{10}]^{3-}$ containing all metal-cage bonding and antibonding orbitals with dominant $3d$ character. The label "GASp(e,o)" denotes an active space containing $e$ electrons in $o$ orbitals divided into $p$ active space partitions (ASPs), and each ASP can also be denoted (e,o) in the same way. In the GAS5(10,10) wavefunction the (10,10) active space is divided into 5 (2,2) ASPs - this maximal partitioning is called the "separated pair" approximation. Figure 3.14 shows the active orbitals for $[Co@Ge_{10}]^{3-}$ and their occupation numbers (black labels). The active space contains two degenerate pairs, $e_2'$ ($d_{xy}$, $d_{x^2-y^2}$) and $e_1''$ ($d_{xz}$, $d_{yz}$), with each (2,2) ASP containing a metal-cage bonding orbital, with dominant metal $d$ character, and the correlating antibonding orbital (denoted by *). The last ASP, with $a_1'$ symmetry contains the $3d_{z^2}$ orbital and the correlating $4d_{z^2}$ "double shell", as there is no metal-cage bonding/antibonding pair. The $e_2'$ and $e_1''$ ASP have occupation numbers of 1.92/0.08 and 1.90/0.10 respectively, indicating substantial multiconfigurational character. As anticipated from our DFT calculations, these excitations correspond to transfer of electrons from the metal $d$ orbitals onto the cage. However, the $a_1'$ ASP has occupation numbers of 1.98/0.02, indicating very little correlation for Co $d_{z^2}$. These results support the description given by the jigsaw model,

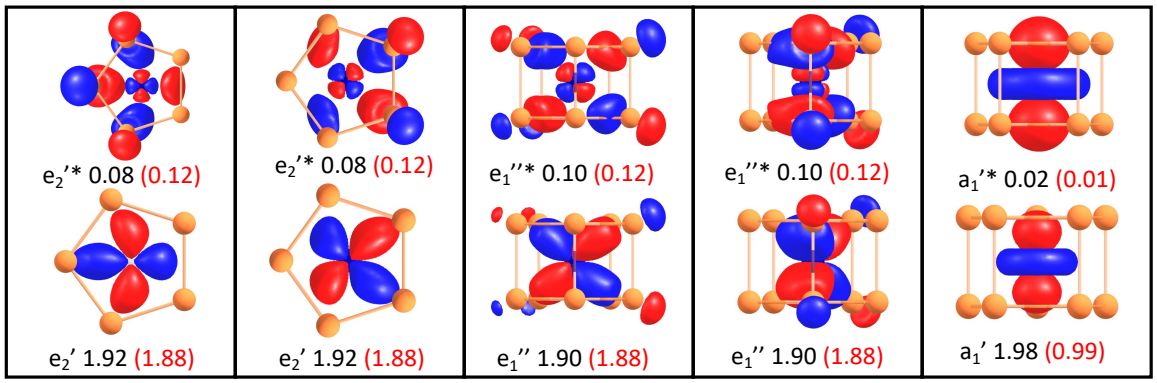



Figure 3.14: GASSCF active spaces for $[M@Ge_{16}]^{3-}$ with occupation numbers for M=Co in black and M=Fe in red. Orbitals plotted with isovalue = 0.05.

derived in section 3.2.3.3, in which the $a_1'$ $d_{z^2}$ is localized entirely on cobalt while the $e_2'$ and $e_1''$ orbitals contribute to the formal electron counts of the metal and the cage. The red labels in Figure 3.14 show the occupation numbers for the corresponding active orbitals for the $^2A_1'$ doublet state of $[Fe@Ge_{10}]^{3-}$. Fe has one electron fewer than Co, so this GAS5(9,10) calculation has a (1,2) $d_{z^2}$ ASP which shows very little multiconfigurational character, as was the case for Co. However, the occupation numbers in the other ASPs deviate more from the single-reference values of 2.00/0.00 than did their $[Co@Ge_{10}]^{3-}$ counterparts, *e.g.* 1.92/0.08 for Co vs 1.88/0.12 for Fe in the $e_2'$ ASPs, showing that more electron density is transferred from the metal to the cage in $[Fe@Ge_{10}]^{3-}$. It therefore appears that the presence of an unpaired electron polarizes the remaining metal $d$ electrons, leading to stronger metal-cage correlation. A more thorough way to analyse these multiconfigurational wavefunctions is to examine the configurations which have the greatest weight in the total wavefunction. These are tabulated for all four clusters in Table 3.1. For $[Co@Ge_{10}]^{3-}$ the dominant configuration, with all Co 3$d$ orbitals occupied and all correlating partners vacant, contributes 83% of the wavefunction. The largest minor configurations can be classified by the symmetries of the excited orbitals as $e_1''^2 e_1''^{*2}$ (5%), $e_2'^2 e_2'^{*2}$ (3%), and the cross-terms involving one-electron excitations in each of the $e_1''$ and $e_2'$ manifolds (4%). $[Fe@Ge_{10}]^{3-}$ shows similar qualitative behaviour, but slightly more multiconfigurational character as the dominant configuration has a weight of 77% and the minor configurations all make a greater contribution. These paint the same picture as the active orbital occupations, that electron density is transferred from the central metal to the cage and that the $d_{z^2}$ contributes minimally to the multireference character of the wavefunction. Excitation between metal-cage bonding and antibonding orbitals has been observed in the related $[Mn@Si_{14}]^+$ cluster, and may be described

as "in-out" correlation[82].

To confirm the validity of our use of GASSCF and the separated pair approximation we then did analogous CASSCF calculations, which may be more accurate and are certainly more computationally demanding, with (10,10) and (9,10) active spaces for $[Co@Ge_{10}]^{3-}$ and $[Fe@Ge_{10}]^{3-}$ respectively. This allows all possible excitations between active orbitals, rather than only those in the same ASP, increasing the number of configuration state functions (CSFs) in the wavefunction from 654 to 4956. These led to changes in MC-SCF energy of less than 0.2 eV, and changes in active space occupation numbers and configuration weights of less than 0.01 relative to the GAS5 results. These values are small in the context of multiconfigurational wavefunctions, confirming that the configurations excluded by the separated pair approximation make no meaningful contribution to the wavefunction. The separated-pair GAS method is therefore a powerful tool for reducing computational cost at minimal loss of accuracy in these clusters.

| | **Configuration** | **Weight(%)** |
|---|---|---|
| $[Co@Ge_{10}]^{3-}$ | $e_1''^4 e_1''^{*0} e_2'^4 e_2'^{*0} a_1'^2 a_1'^{*0}$ | 83 |
| | $e_1''^2 e_1''^{*2} e_2'^4 e_2'^{*0} a_1'^2 a_1'^{*0}$ | 5 |
| | $e_1''^4 e_1''^{*0} e_2'^2 e_2'^{*2} a_1'^2 a_1'^{*0}$ | 3 |
| | $e_1''^3 e_1''^{*1} e_2'^3 e_2'^{*1} a_1'^2 a_1'^{*0}$ | 4 |
| $[Fe@Ge_{10}]^{3-}$ | $e_1''^4 e_1''^{*0} e_2'^4 e_2'^{*0} a_1'^1 a_1'^{*0}$ | 77 |
| | $e_1''^2 e_1''^{*2} e_2'^4 e_2'^{*0} a_1'^1 a_1'^{*0}$ | 6 |
| | $e_1''^4 e_1''^{*0} e_2'^2 e_2'^{*2} a_1'^1 a_1'^{*0}$ | 4 |
| | $e_1''^3 e_1''^{*1} e_2'^3 e_2'^{*1} a_1'^1 a_1'^{*0}$ | 5 |
| $[Co_2@Ge_{16}]^{4-}$ | $[b_{1u}^2 b_{1u}^{*0} b_{3g}^2 b_{3g}^{*0}][b_{2g}^2 b_{2g}^{*0} a_u^2 a_u^{*0}][a_g^2 a_g^{*0} b_{3u}^2 b_{3u}^{*0}]$ $[b_{2u}^2 b_{2u}^{*0} b_{1g}^2 b_{1g}^{*0}][a_g^2 b_{3u}^2 b_{3u}^{*0}]$ | 64 |
| $[Fe_2@Ge_{16}]^{4-}$ | $[b_{1u}^2 b_{1u}^{*0} b_{3g}^2 b_{3g}^{*0}][b_{2g}^2 b_{2g}^{*0} a_u^2 a_u^{*0}][a_g^2 a_g^{*0} b_{3u}^2 b_{3u}^{*0}]$ $[b_{2u}^2 b_{2u}^{*0} b_{1g}^1 b_{1g}^{*0}][a_g^2 b_{3u}^1]$ | 44 |

Table 3.1: Leading Configurations in the GASSCF wavefunctions of the ground states of $[M@Ge_{10}]^{3-}$ and $[M_2Ge_{16}]^{4-}$. For the latter, orbitals are grouped in order GASa, GASb, GASc, GASd and GASe. Orbitals plotted with isovalue = 0.036.

The equivalent CAS calculations for the $[M_2Ge_{16}]^{4-}$ clusters would require (20,20) active spaces, far beyond the capacity of available resources, but we are now confident that GAS provides an excellent description of these wavefunctions. In $[M@Ge_{10}]^{3-}$ each ASP contained a metal-cage bonding/antibonding pair, but in $[M_2Ge_{16}]^{4-}$ we

have found that each ASP must contain a metal-metal bonding/antibonding orbital pair and the corresponding metal-cage antibonding orbitals for each of those, leading to (4,4) ASPs. This means that the separated pair approximation cannot be employed for the larger clusters, so the ideal GAS5(20,20) calculations are just out of reach. Instead, we have used GAS5(20,19) for $[Co_2Ge_{16}]^{4-}$ and GAS5(18,18) for $[Fe_2Ge_{16}]^{4-}$. The active space is shown in Figure 3.15 with occupation numbers for M=Co in black and M=Fe in red, divided into ASPs labelled GAS**a-e**, and the dominant configurations are shown in Table 3.1 divided similarly. The weights of the dominant configurations are 64% for $[Co_2Ge_{16}]^{4-}$ and just 44% for $[Fe_2Ge_{16}]^{4-}$, the substantially smaller values than those in $[M@Ge_{10}]^{3-}$ indicating much greater multiconfigurational character. Due to the more complex active space and the lack of degeneracy in the $D_{2h}$ clusters, specific minor configurations cannot be usefully listed here as no single one contributes more than 1.5% to the total. The orbitals shown are those for $[Co_2Ge_{16}]^{4-}$, but, as in $[M@Ge_{10}]^{3-}$, the corresponding iron cluster has essentially identical active orbitals. The orbitals which have been removed to reduce the total active space size from 20 are the correlating orbitals in GAS**e**, *i.e.* the $d_{z^2}$ double-shell combinations. For $[Fe_2Ge_{16}]^{4-}$ this (3,2) ASP contains only the $d_{z^2}$ bonding and antibonding combinations, while for $[Co_2Ge_{16}]^{4-}$ a (4,3) ASP is required to allow correlation. GAS**a-d** each contain the four MOs arising from a single metal $3d$ orbital. The patterns in the occupation numbers are broadly similar to those seen for $[M@Ge_{10}]^{3-}$ in Figure 3.14, with significant transfer of population from the metal-cage bonding orbitals to the antibonding counterparts. The deviations from the single-reference occupations are noticably larger here than in the monomeric clusters, for both metals, indicating stronger "in-out" correlation. The presence of two metals also allows for the possibility of "left-right" correlation, *i.e.* correlation between metal-metal bonding and antibonding orbitals. Since all metal-metal bonding and antibonding orbitals are occupied in the dominant configuration, as in the single-reference framework of our DFT calculations, direct $M - M \rightarrow M - M^*$ excitations introducing pure "left-right" correlation are not possible. We can, however, identify configurations which simultaneously describe "in-out" and "left-right" correlation. For example, the excited configuration resulting from $b_{2g} \rightarrow a_u^*$ excitation - $\delta$ bonding to the $\delta^*$ correlator - has 1.5% weight in the total wavefunction. Meanwhile, the purely "in-out" excitations have weights of 0.4% and 0.6%, close in magnitude to the "left-right" excitation. This coupling of metal-metal and metal-cage correlation explains the need for (4,4) ASPs. $[Fe_2Ge_{16}]^{4-}$ shows significantly larger deviations from single-determinant occupations than $[Co_2Ge_{16}]^{4-}$, and has a smaller weight for

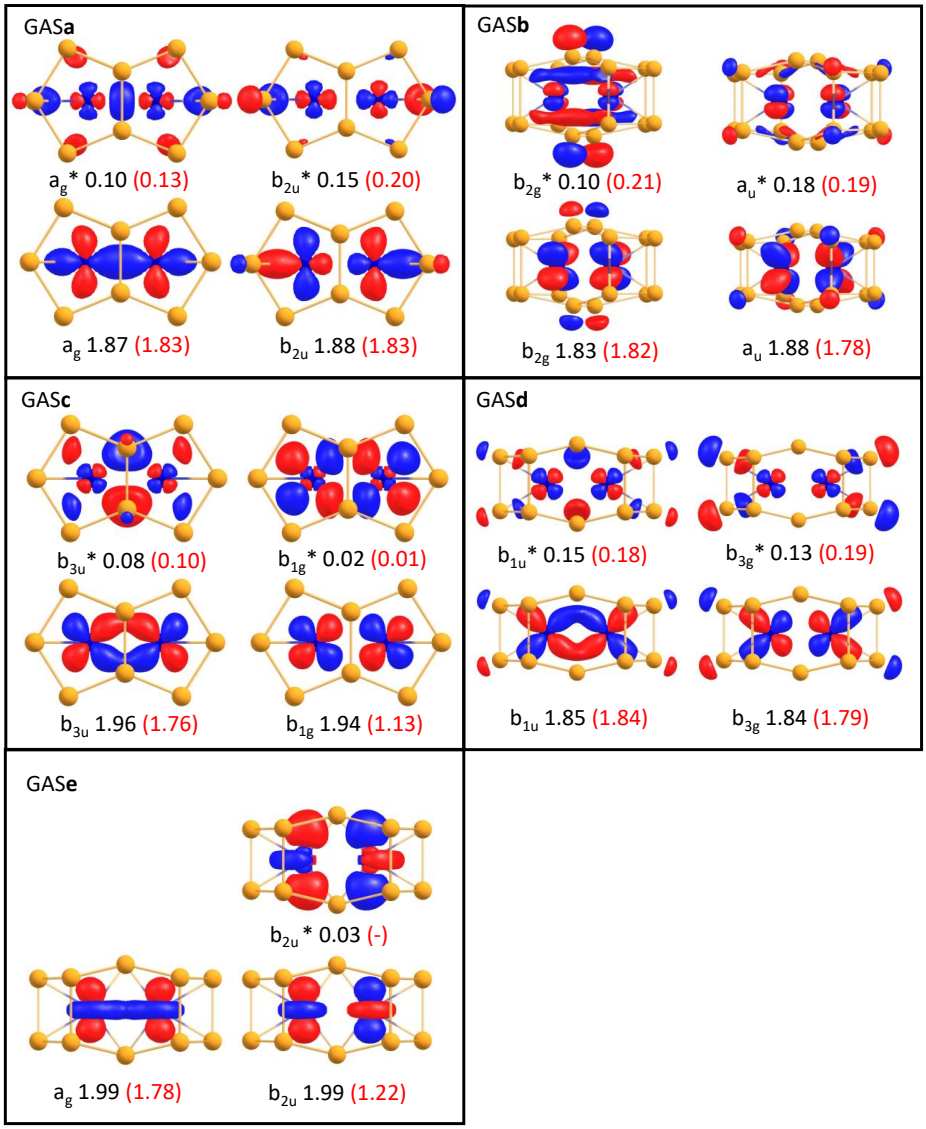



Figure 3.15: GASSCF active spaces for $[M_2Ge_{16}]^{4-}$ with occupation numbers for M=Co in black and M=Fe in red.

the dominant configuration in its total wavefunction. The difference between the two metals is greater in the dimeric clusters, supporting our hypothesis that the unpaired electrons, of which $[Fe_2Ge_{16}]^{4-}$ has two but $[Fe@Ge_{10}]^{3-}$ only one, polarize the remaining $d$ electron density and induce strong metal-cage correlation. $[Fe_2Ge_{16}]^{4-}$ can thus be stabilized in a multiconfigurational calculation reducing the Fe spin-$\beta$ density to achieve a half-filled shell, with a $d^5$ configuration, while Co, with lower-energy $3d$ orbitals, is more stable as $d^{10}$ $Co^-$. This leads to the interesting conclusion that the $Ge_{10}$ and $Ge_{16}$ cages are more electron-rich when the encapsulated metal has a smaller formal $d$ electron count. This counterintuitive trend may help to guide searches for deltahedral and three-connected clusters containing metals from the middle of the transition series.

On the basis of DFT calculations we estimated an Fe-Fe bond order in $[Fe_2Ge_{16}]^{4-}$ of 0.5, due to the singly occupied $\pi^*$ orbital. We can get a comparable measure from the occupancies of our GAS active orbitals by calculating the effective bond order (EBO)[98]:

$$\mathrm{EBO} = \frac{1}{2} \sum_{\text{orbitals}} (\eta_b - \eta_a) \tag{3.15}$$

where $\eta_{b/a}$ are the occupancies of active bonding/antibonding orbitals. Summing over GAS**a-d** gives an EBO of 0.36, almost entirely due to the $d_{xy}$ $\pi$ bonding in GAS**c**. GAS**e** has been excluded due to its minimal $d$ orbital overlap and non-bonding character. This is a bit lower than the 0.5 from DFT because of "left-right" correlation in the $d_{xy}$ ASP, in keeping with the general observation in computational studies that correlation reduces bond order measures[98].

### 3.2.4 Conclusions

We have used the quartet of clusters $[M@Ge_{10}]^{3-}$ and $[M_2Ge_{16}]^{4-}$ (M=Fe, Co) to explore the electronic effects of cluster growth and metal $d$ electron count, as it is rare to have a complete set of clusters in which we can make both comparisons. The metal-cage interactions have been found to depend strongly on the presence of unpaired electrons on the metal. The Fe clusters, which have open-shell metal atoms, are stabilized by the transfer of electron density from Fe to the cage to minimize electron repulsion in the $3d$ shell. Co cannot do this so effectively because it has a lower $3d$ orbital energy and is closer to a $d^{10}$ closed-shell configuration than a $d^5$ half-filled shell. In DFT calculations this effect manifests as a difference in the shapes of the

spin-$\alpha$ and spin-$\beta$ orbitals, which is the essence of unrestricted Kohn-Sham wavefunctions, whereas in GASSCF it results in multiconfigurational character, where the $\alpha$ and $\beta$ electrons have the same orbitals and the spin density is optimized by including excited electronic configurations in the total wavefunction. By exploring the metal-metal interactions in $[M_2Ge_{16}]^{4-}$ we have found that the Fe cluster contains some Fe-Fe bonding character, while the Co analogue does not, showing that internuclear distance is not a reliable indicator of bonding for encapsulated atoms. DFT molecular orbital diagrams, symmetry-driven electron counting, density of states plots, and MC-SCF wavefunction calculations have all contributed to a sophisticated and multidimensional picture of the cluster series.

# 3.3 Linear metal trimers $[(M@E_9)M'(M@E_9)]^{q-}$

## 3.3.1 Introduction

In the introduction to this chapter we described the chemistry of $E_9^{4-}$, which includes oligomerization and polymerization reactions for $Ge_9^{4-}$ and encapsulations of transition metal atoms by $Ge_9^{4-}$ and $Sn_9^{4-}$. The clusters investigated in this section, $[(Ni@Sn_9)In(Ni@Sn_9)]^{5-}$, $[(Ni@Ge_9)Ni(Ni@Ge_9)]^{4-}$[75], and $[(Fe@Sn_9)Fe(Fe@Sn_9)]^{4-}$, each contain two $E_9$ units, so we will now describe the structures of previously known $E_9^{4-}$ oligomers containing transition metal atoms.

The most common form of transition metal incorporation is for a TM atom to act as a shared vertex between the two $E_9$ sub-clusters. Examples in this category include $[Ge_9MGe_9]^{q-}$ (M = Cu, Zn, In)[99, 77, 100] and $[Sn_9MSn_9]^{q-}$[101, 102] (M = Ag, Hg), where q takes the value required by a formal description of $E_9^{4-}$ and a $d^{10}$ metal. The subclusters may have tricapped trigonal prismatic ($D_{3h}$) or capped square antiprismatic ($C_{4v}$) geometry, allowing for several possible cage-TM coordination modes. Most common are $\eta^3$ and $\eta^4$, and $[Sn_9AgSn_9]^{7-}$ has $\eta^1$ coordination for one of the subclusters. Particularly interesting is $[Ge_9ZnGe_9]^{6-}$ as it exists as $\eta^3:\eta^3$ and $\eta^4:\eta^4$ isomers just as $[(Ni@Ge_9)Ni(Ni@Ge_9)]^{4-}$ does, which will be described in 3.17.

Two $E_9$ cages may also be linked by a metal dimer, such as in $[Ge_9M{-}MGe_9]^{6-}$ (M = Zn, Cd)[78, 103], which are particularly exciting as the two halves of the cluster are held together solely by the M-M bond, and in $[Ge_9Au_3Ge_9]^{5-}$ they are linked by a triangular $Au_3^{3+}$ trimer[104]. The oligomerization reactions for pure $Ge_9^{4-}$ also have analogous reactions which incorporate TMs, giving dimeric $[Ge_9ZnGe_9ZnGe_9]^{10-}$[103], trimeric $[Hg_3(Ge_9)_4]^{10-}$[105] and polymeric $[MGe_9]^{2-}_{\infty}$ (M=Zn, Hg)[106, 107]. A particularly exotic example is $[Au_3Ge_{45}]^{9-}$, which may be described as four $Ge_9$ cages and an $Au_3$ triangular trimer, with the remaining 9 Ge atoms occuping the middle of the cluster[108]. Finally, dimerization can also occur between encapsulated $M@E_9$ units. The $[M_2Sn_{17}]^{q-}$ clusters (M = Ni, Pt, Co, q as required for a $d^{10}$ TM configuration) are formed by two $M@Sn_9$ units sharing an Sn vertex[109, 110, 111]. The clusters of greatest interest in this chapter are those where the encapsulated cages are linked by a TM atom, so the metals form a linear trimer which may have sufficiently short M-M distances to allow direct bonding. We will begin by addressing structural isomerism in $[(Ni@Sn_9)In(Ni@Sn_9)]^{5-}$ and compare its structure and bonding to the previously known cluster $[(Ni@Ge_9)Ni(Ni@Ge_9)]^{4-}$. We will then compare the newly

synthesized compound $[(Fe@Sn_9)Fe(Fe@Sn_9)]^{4-}$ to $[(Ni@Ge_9)Ni(Ni@Ge_9)]^{4-}$ as they are isostructural but not isovalent.

## 3.3.2 Methods

DFT calculations on $[(Ni@Sn_9)In(Ni@Sn_9)]^{5-}$ and $[(Ni@Ge_9)Ni(Ni@Ge_9)]^{4-}$ were performed with the ORCA software package[112] (version 4.1.1) using the BP86 functional[4] along with ma-def2-TZVP Gaussian basis sets on Ni/In and ma-def2-SVP on Sn/Ge[11]. Calculations were accelerated by means of the Resolution of Identity (RI) approximation with the def2/J auxiliary basis set[113]. The confining influence of the crystalline environment was approximated using a Conductor-like Polarizable Continuum Model (CPCM)[114] with the dielectric constant of water.
DFT calculations on $[(Fe@Sn_9)Fe(Fe@Sn_9)]^{4-}$ were performed with ADF[26], version 2019.304, using the PBE functional[5] and Slater-type TZP basis functions[92]. The crystalline environment was modelled using the COSMO continuum solvent model[93] with the dielectric constant of water. As noted in the text where relevant, comparable calculations on $[(Ni@Ge_9)Ni(Ni@Ge_9)]^{4-}$ were also performed using this method.

## 3.3.3 Results

### 3.3.3.1 Understanding structural diversity

We will begin our study of $[(Ni@Sn_9)In(Ni@Sn_9)]^{5-}$ by summarizing the experimental characterization, before discussing our computational studies and subsequent conclusions. This cluster was first synthesized in the group of Zhong-Ming Sun, in 2019, and shown by single crystal X-ray diffraction to exist in two isomeric forms, depending on the counterion in the crystal[32]. Structures and bond lengths for both isomers, determined by X-ray crystallography by Chao Zhang, are shown in Figure 3.16, reproduced from reference [32]. Both are formed by a dimerization of two $[Ni@Sn_9]$ sub-clusters by a linking In atom, but differ in the geometry of the sub-clusters and their mode of coordination to In. Two geometries are available to $Sn_9$; a tricapped trigonal prism, which binds to In in an $\eta^3$ fashion, and a capped square antiprism, which binds to In in an $\eta^4$ fashion through the uncapped square face[115]. The first observed isomer can be formed from two tricapped trigonal prismatic $Sn_9$ units bound $\eta^3 : \eta^3$ to In in an eclipsed pseudo-$D_{3h}$ geometry, and the second from one of each $Sn_9$ geometry in $\eta^3 : \eta^4$ coordination.
We began our computational study of this structural isomerism by optimizing staggered and eclipsed configurations of the $\eta^3 : \eta^3$ and $\eta^4 : \eta^4$ modes, the observed

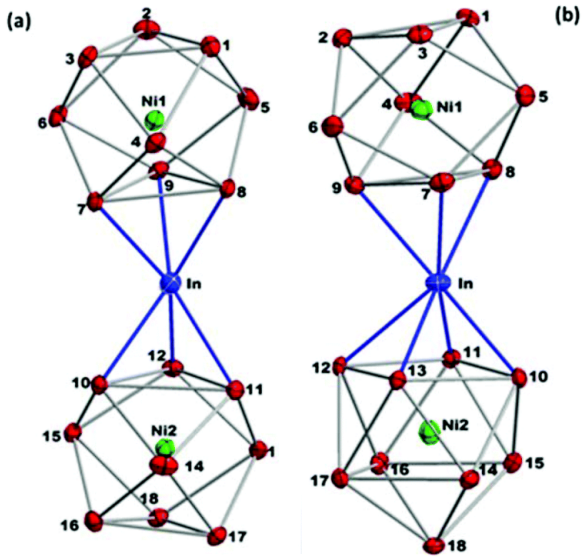



Figure 3.16: ORTEP plots of the isomers of $[(Ni@Sn_9)In(Ni@Sn_9)]^{5-}$ (drawn at 50% probability). Selected distances (Å) in (a): Sn(7)In(1) 3.0542, Sn(8)In(1) 3.0508, Sn(9)In(1) 3.1143, Sn(10)In(1) 3.0981, Sn(11)In(1) 3.1252, Sn(12)In(1) 2.9949, Sn(7)Sn(8) 3.2797, Sn(8)Sn(9) 3.2873, Sn(7)Sn(9) 3.2704, selected distances (Å) in (b): Sn(7)In(1) 3.1691, Sn(8)In(1) 3.1212, Sn(9)In(1) 3.1194, Sn(10)In(1) 2.9916, Sn(11)In(1) 3.0712, Sn(12)In(1) 3.2344, Sn(13)In(1) 3.0484, Sn(7)Sn(8) 3.2464, Sn(7)Sn(9), Sn(10)Sn(11) 3.2132, Sn(11)Sn(12) 3.0483, Sn(12)Sn(13) 3.0521, Sn(13)Sn(10) 3.2324. Figure reproduced from [32]. Measurements performed by Chao Zhang.

$\eta^3 : \eta^4$ form, and an $\eta^1 : \eta^4$ geometry isomeric to $[(Sn_9)Ag(Sn_9)]^{7-}$[101]. All species were treated as electronic singlets. Optimized geometries for the $\eta^3 : \eta^4$, $\eta^3 : \eta^3$ (staggered and eclipsed), and $\eta^4 : \eta^4$ (staggered) are shown in Figure 3.17 annotated with their relative energies, approximate point symmetries, and key bond lengths. Minima were located for the $\eta^3 : \eta^4$ ($C_s$) and eclipsed $\eta^3 : \eta^3$ ($D_{3h}$) geometries corresponding to the observed isomers, and also for the staggered $\eta^3 : \eta^3(D_{3d})$ and $\eta^4 : \eta^4$ ($D_{4d}$) hypothetical structures. All were confirmed to be minimum energy structures by the absence of imaginary frequencies.

The global minimum is the $C_s$ isomer, but the $D_{3d}$ and $D_{3h}$ geometries are only higher by 0.02 and 0.05 eV respectively. The $D_{4d}$ structure was found at +0.22 eV, clearly higher than the experimentally observed isomers, and minima for the $D_{4h}$ and $\eta^1 : \eta^4$ could not be located as optimizations starting with these structures instead relaxed to the global minimum.

The distribution of geometries according to their energies, with the experimentally observed $\eta^3 : \eta^4$ and $\eta^3 : \eta^3$ lying close together and far below the purely hypothetical

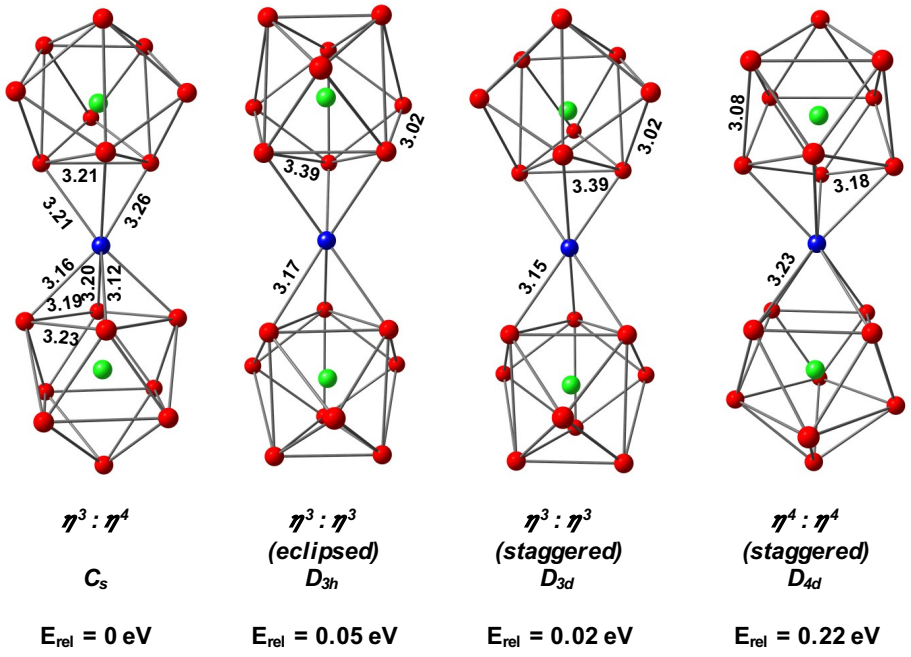



Figure 3.17: Optimized structures of $[(Ni@Sn_9)In(Ni@Sn_9)]^{5-}$ (Ni in green, In in blue, and Sn in red), with point symmetries, relative energies and important In-Sn and Sn-Sn bond lengths.

$\eta^4 : \eta^4$, indicates that our computational model describes this ion well. Figure 3.17 shows that the $\eta^3 : \eta^4$ and $\eta^3 : \eta^3$ geometries have similar Sn-In and Sn-Sn bond lengths as well as their similar energies, so we can conclude at this stage that the two have similar bonding characteristics, and the coexistence of the two isomers is a consequence of crystal packing effects, i.e. differences in the intermolecular interactions with the counterions, rather than different formation pathways under their respective synthetic conditions. The similarities between the $D_{3d}$ and $D_{3h}$ isomers suggest that the $[Ni@Sn_9]$ sub-clusters can probably rotate freely about the Ni-In-Ni axis in solution, so the $\eta^3 : \eta^3$ may be considered a single isomer.
We can also see that, despite relatively long Sn-Sn distances across the middle of the cluster, the two $Sn_9$ sub-units interact with each other directly. This is clear from the non-additivity of the energies, i.e. that:

$$E(\eta^3 : \eta^4) \neq \frac{E(\eta^3 : \eta^3) + E(\eta^4 : \eta^4)}{2} \tag{3.16}$$

We must therefore consider the electronic structure of the cluster as a whole.

#### 3.3.3.2 Electronic structure, orbital analysis, and connection to $[(Ni@Ge_9)Ni(Ni@Ge_9)]^{4-}$

We begin our analysis of the electronic structure of $[(Ni@Sn_9)In(Ni@Sn_9)]^{5-}$ by describing an isolated $[Sn_9]^{q-}$ cluster with skeletal electron pair theory, or the Wade-Mingos rules[39, 40]. Each Sn atom has four valence electrons of which two are localised in a lone pair, leaving two skeletal electrons per atom. Since a skeletal electron count (SEC) of $2n+2$ describes an $n$-vertex *closo*- deltahedron, and an SEC of $2n+4$ describes an $n+1$-vertex *nido*- deltahedron, we can predict the cluster structure for different charges. If $q = 2$ then we predict tricapped trigonal prismatic geometry, while if $q = 4$ we predict a monocapped square antiprism, as observed in compounds such as $K_4Sn_9$[116]. $Ge_9^{3-}$ species with $2n+3$ SECs, called "intermediate" as they are between *closo* and *nido*, have been characterised in compounds and shown to be stable in solution and have structures like those of $Ge_9^{4-}$[117]. Encapsulation of a $d^{10}$ transition metal atom such as Ni(0) will have no effect on this analysis.

$[(Ni@Sn_9)In(Ni@Sn_9)]^{5-}$ shows the same isomerism as $[Ge_9ZnGe_9]^{6-}$[77], which also contains $E_9$ tetrel units, but without encapsulated transition metal atoms, and can be partitioned into $Ge_9^{4-}Zn^{2+}Ge_9^{4-}$. By analogy, we can assign formal 4- charges to the $Ni@Sn_9$ units in $[(Ni@Sn_9)In(Ni@Sn_9)]^{5-}$, implying a $d^{10}$ Ni(0) assignment for the encapsulated Ni, and a 3+ charge for In.

While a useful approximation, this ionic picture has some obvious pitfalls. The assignment of a 4- charge to $Sn_9$ would lead us to predict a monocapped square antiprismatic geometry for both of these units, in accordance with Wade's rules, but in fact we see greater prevalence of the tricapped trigonal prismatic geometry associated with a 2- charge state. Since Sn and In are both heavy main group elements, with similar electronegativities, it is reasonable to propose some Sn-In charge transfer. Furthermore, the non-additivity of the energies shown in equation 3.16 demonstrates that the $E_9$ sub-units interact directly and influence each other's preferred structure, implying a covalent interaction which our ionic picture cannot account for. This argument can also be applied to $[Ge_9ZnGe_9]^{6-}$.

Another important analogue is $[(Ni@Ge_9)Ni(Ni@Ge_9)]^{4-}$[75] due to the obvious chemical similarities and the structural relationship between this cluster and the $D_{3d}$ form of $[(Ni@Sn_9)In(Ni@Sn_9)]^{5-}$. Ni has three fewer electrons than In and the charges differ by one, so $[(Ni@Ge_9)Ni(Ni@Ge_9)]^{4-}$ contains four fewer electrons than $[(Ni@Sn_9)In(Ni@Sn_9)]^{5-}$.

To understand the consequences of this electron count difference we have plotted the frontier molecular orbitals of the two clusters on a Walsh diagram in Figure

3.18. We can see that the two corresponding orbitals which are occupied in in

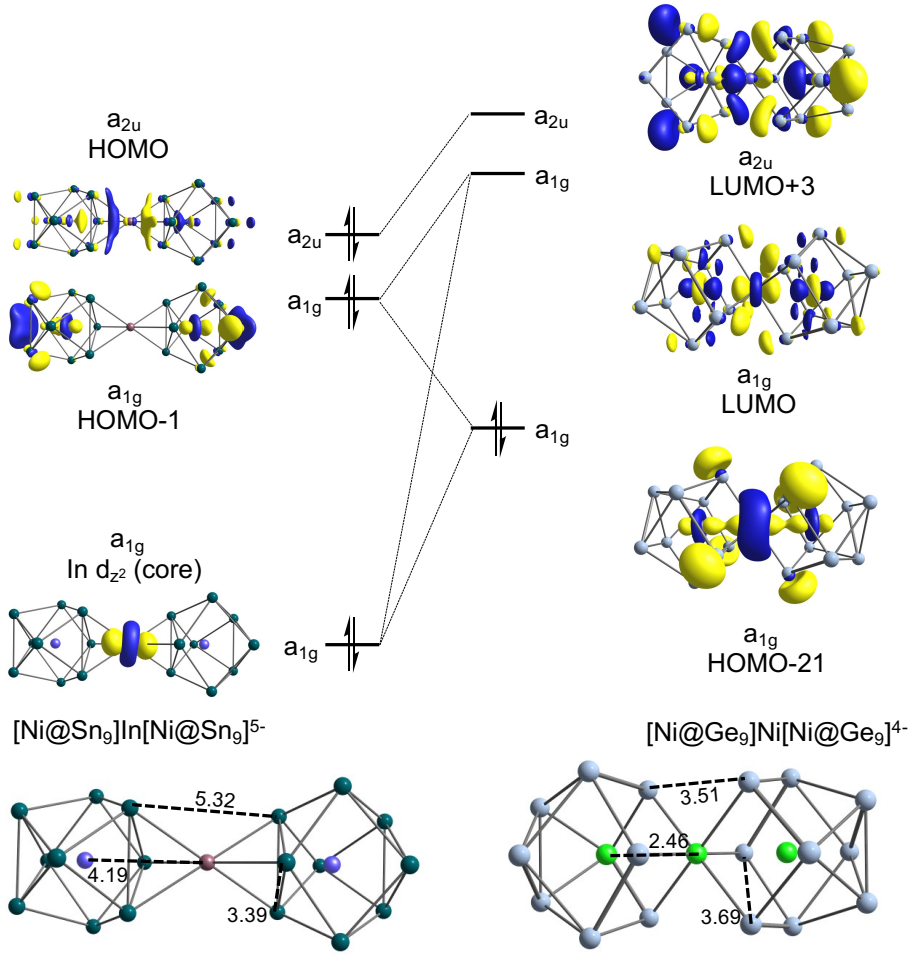



Figure 3.18: Walsh diagram comparing significant MOs in $[(Ni@Sn_9)In(Ni@Sn_9)]^{5-}$ and $[(Ni@Ge_9)Ni(Ni@Ge_9)]^{4-}$. Orbitals plotted with isovalue = 0.033.

$[(Ni@Sn_9)In(Ni@Sn_9)]^{5-}$ but vacant in $[(Ni@Ge_9)Ni(Ni@Ge_9)]^{4-}$ are of $a_{2u}$ and $a_{1g}$ symmetry, forming the HOMO and HOMO-1 in the former cluster and the LUMO and LUMO+3 in the latter, though the precise energy ranking is unimportant.

We will begin by exploring the $a_{2u}$ HOMO of $[(Ni@Sn_9)In(Ni@Sn_9)]^{5-}$, which is bonding within each triangular $Sn_3$ face coordinated to In but antibonding between these faces. This orbital has very little contribution from In, supporting the "ionic" picture of an $In^{3+}$ connecting two $Sn_9^{4-}$ clusters. It is closely related to the HOMO of some monomeric $E_9$ clusters, such as $[Ni@Ge_9]^{3-}$, where depopulation in synthetic derivatives leads to an opening of the triangular face[117, 118]. We see analogous behaviour here when we compare the two structures; depopulation of this orbital in $[(Ni@Ge_9)Ni(Ni@Ge_9)]^{4-}$ leads to expansion of the $\eta^3$ coordinating faces, with bond

lengths increasing from 3.39 Å to 3.69 Å, and the two halves of the cluster move closer together as the strong antibonding interaction between them is removed, with shortest E-E distances across the cluster falling from 5.32 Å to 3.51 Å.

When considering the $a_{1g}$ HOMO-1 of $[(Ni@Sn_9)In(Ni@Sn_9)]^{5-}$ we must also consider the other $a_{1g}$ MOs comprising metal $d_{z^2}$ orbitals. The In $d_{z^2}$ is a core orbital, very low in energy and not participating in bonding, which leaves the Ni $d_{z^2}$ orbitals forming a non-bonding combination in the HOMO-1. We can therefore conclude that there is no bonding interaction along the Ni-In-Ni axis, consistent with the long Ni-In bond lengths of 4.19 Å.

$[(Ni@Ge_9)Ni(Ni@Ge_9)]^{4-}$ shows contrasting behaviour because the metal $d_{z^2}$ atomic orbitals along the Ni-Ni-Ni axis are, of course, degenerate, and are therefore able to interact strongly. They therefore combine to give a bonding combination, which is occupied and forms the HOMO-21, and an antibonding combination, which is the vacant LUMO. This allows us to identify an $[Ni_3]^{2+}$ filament with a 3-centre 4-electron $\sigma$ bond, consistent with the 2.46 Å bond lengths, which are much shorter than their Ni-In counterparts. Tables of Ni-Ni internuclear distances in organometallic complexes suggest that this Ni-Ni bond length is consistent with a single bond[119], rather than the calculated formal bond order of 0.5 for each Ni-Ni pair in $[(Ni@Ge_9)Ni(Ni@Ge_9)]^{4-}$. This comparison shows that the Ni-Ni distances in this cluster are still strongly influenced by the confining effect of the cage.

We now turn to the electronic differences between the $E_9$ sub-units in the two clusters as we must still account for a two-electron difference between them. The $a_{2u}$ HOMO of $[(Ni@Sn_9)In(Ni@Sn_9)]^{5-}$ correlates with the LUMO+3 in $[(Ni@Ge_9)Ni(Ni@Ge_9)]^{4-}$. As described above, this orbital is bonding within the central $Ge_3$ face of each sub-unit but antibonding between the two. Depopulation of this orbital therefore results in an expansion of the triangular face and a closer approach between the two halves of the cluster, as seen in the bond lengths in Figure 3.18. This electronic and geometrical analysis is consistent with the -3 charges which we must assign to the $Ge_9$ units in order to balance the $Ni_3{}^{2+}$ core. This contrasts with previous discussions of this compound, which describe it as two $Ge_9{}^{2-}$ units with a $d^{10}$ Ni(0) atom at the centre, implying no metal-metal bonding.

#### 3.3.3.3 $[(Fe@Sn_9)Fe(Fe@Sn_9)]^{4-}$: an open-shell analogue of $[(Ni@Ge_9)Ni(Ni@Ge_9)]^{4-}$

In 2021, following the completion of our studies on $[(Ni@Sn_9)In(Ni@Sn_9)]^{5-}$, the Sun group characterized a new member of this cluster family, $[(Fe@Sn_9)Fe(Fe@Sn_9)]^{4-}$.

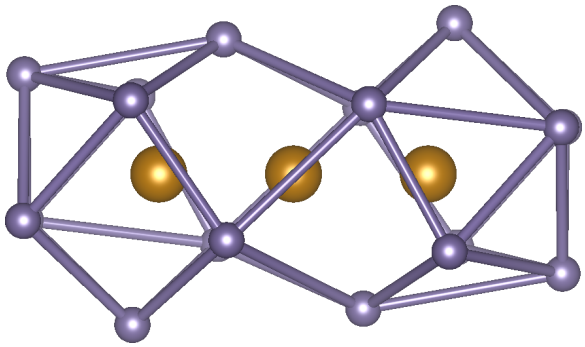


Figure 3.19: Geometry of $[(Fe@Sn_9)Fe(Fe@Sn_9)]^{4-}$ measured by X-ray crystallography by Wei-Xing Chen.

The crystal structure, presently unpublished[1], is shown in Figure 3.19. This species is isostructural to $[(Ni@Ge_9)Ni(Ni@Ge_9)]^{4-}$, with Fe-Fe bonds of 2.43 Å, comparable to double bonds in organometallic complexes[119], but contains six fewer valence electrons. Such a large difference in electron count between the two isostructural clusters implies that the electrons are lost from the transition metals rather than the cage. We will therefore aim to understand the metal-metal interactions in $[(Fe@Sn_9)Fe(Fe@Sn_9)]^{4-}$ using the same orbital analysis procedure as we have applied to the clusters above.

We began our investigation by optimizing the structure in all spin states from singlet to 11-tet (i.e. 0-10 unpaired electrons). Table 3.2 shows the relative energies and computed Fe-Fe bond lengths in all calculated spin states. The bond length in the crystal structure is included for reference. The computed ground state is a

| Spin state | $E_{rel}$ / eV | Fe-Fe / Å |
|---|---|---|
| Singlet | 0.878 | 2.282 |
| Triplet | 0.327 | 2.485 |
| Quintet | 0.383 | 2.495 |
| **Septet** | **0** | **2.478** |
| Nonet | 0.847 | 2.582 |
| 11tet | 1.943 | 2.575 |
| Crystal | | 2.431 |

Table 3.2: Calculated energies and Fe-Fe distances in $[(Fe@Sn_9)Fe(Fe@Sn_9)]^{4-}$ in different spin states.

septet, with six unpaired electrons, so when comparing $[(Fe@Sn_9)Fe(Fe@Sn_9)]^{4-}$ to $[(Ni@Ge_9)Ni(Ni@Ge_9)]^{4-}$ we can say that the six electrons lost from the Ni compound are all parallel-spin. We might then suggest that two spin-down electrons have

[1] Zhong-Ming Sun, *Private communication*

been removed from each metal centre, but the discussion above of strong Ni-Ni-Ni covalency in $[(Ni@Ge_9)Ni(Ni@Ge_9)]^{4-}$ implies that we should see these electrons as being removed from MOs rather than individual atoms. The Fe-Fe bond length in the septet ground state matches the experimental value well, both in an absolute sense and relative to the other spin states. The substantial energy gap to the first excited state and the agreement with the crystal structure inspire confidence in the prediction of the septet ground state, in spite of the challenges for DFT in calculating accurate spin state energies. The remainder of our analysis will therefore focus on the septet. We currently have two main points of comparison between the $Fe_3$ and $Ni_3$ clusters:

1. Can we reconcile the structural similarity with the difference in electron counts?

2. Is the metal-metal bonding qualitatively similar in the two compounds?

Both questions can be answered by examining the MOs with dominant metal $3d$ character, shown in Figure 3.20. We began by identifying the six singly occupied orbitals in $[(Fe@Sn_9)Fe(Fe@Sn_9)]^{4-}$, which are the $25e_{1u}$, $25e_{1g}$ and $26e_{1g}$ orbitals labelled in blue. These all have $\pi$ symmetry along the M-M bonds and are, respectively, non-bonding, bonding, and antibonding combinations of the same metal $d$ orbitals. Removing an equal number of electrons from all three levels therefore has no impact on the formal M-M bond order, which explains the structural similarity between the $Fe_3$ and $Ni_3$ clusters. This is highlighted by the bond lengths at the bottom of Figure 3.20. We note here that the Ge-Ge bond lengths are different from those in Figure 3.18 because these calculations were performed with ADF, due to its superior symmetry analysis utilities, but the qualitative MO description and Ni-Ni bond lengths are the same for the two methods.

The similarity between $\pi$ interactions implies the presence of a 3-centre 4-electron $\sigma$-bonded $[Fe_3]^{2+}$ core just as was found in $[(Ni@Ge_9)Ni(Ni@Ge_9)]^{4-}$. To investigate this suggestion we have plotted the M-M $\sigma$ combinations, labelled in red in Figure 3.20. Once again, we find a low-energy $\sigma$ bonding orbital, $16a_{1g}$, an $a_{2u}$-symmetric non-bonding orbital, and the unoccupied $21a_{1g}$ antibonding counterpart. In both compounds the bonding and non-bonding orbitals are occupied and the antibonding orbitals vacant, so we do indeed have a 3-centre 4-electron bond in the $[Fe_3]^{2+}$ filament, with formal Fe-Fe bond orders of 0.5. For a more quantitative comparison of metal-metal bonding we have calculated the delocalization indices (DI) between bonded metal atoms. The DI, described in detail in the theory chapter, is based on Bader's QTAIM approach to molecular electronic structure, so is entirely separate from MO analysis, and it has been shown to be a bond order measure applicable to

transition metal chemistry. Our values are 0.70 for Fe-Fe and 0.42 for Ni-Ni, both in the region of the formal value of 0.5, and much more similar than might be expected given the valence electron count difference of 6. The greater DI for the Fe-Fe bond may be attributed to greater spatial overlap between more radially extended $3d$ orbitals, due to the lower effective nuclear charge, and perhaps the greater Ge character seen in the relevant MOs in the Ni cluster.

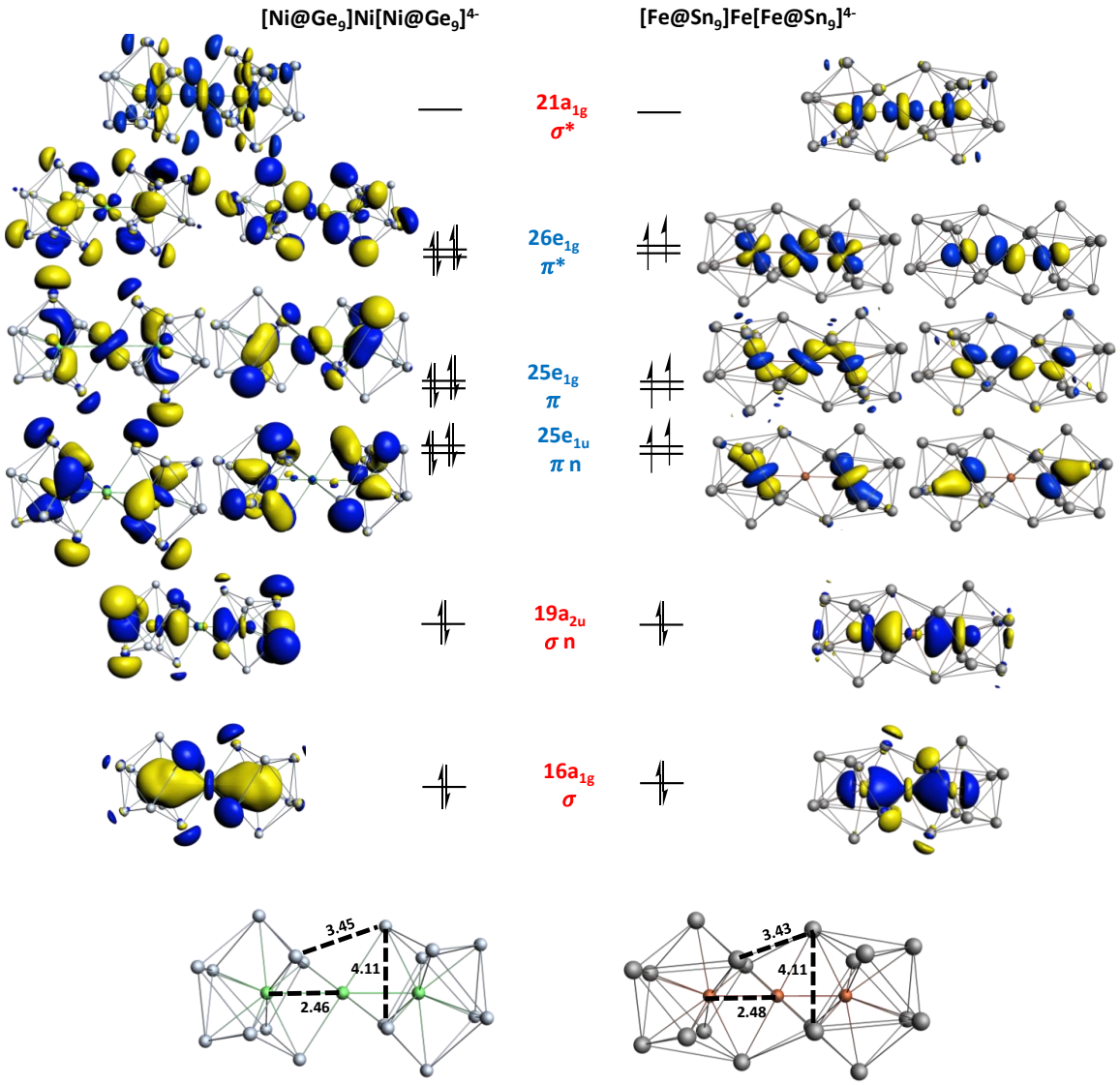



Figure 3.20: Selected MOs in $[(Ni@Ge_9)Ni(Ni@Ge_9)]^{4-}$ and $[(Fe@Sn_9)Fe(Fe@Sn_9)]^{4-}$, highlighting symmetries with respect to M-M-M bonding. Beta-spin orbitals are shown for $[(Fe@Sn_9)Fe(Fe@Sn_9)]^{4-}$. Key bond lengths for both clusters are shown below. Orbitals plotted with isovalue = 0.03.

### 3.3.4 Conclusions

Here we have explored the structure and bonding in $[(Ni@Sn_9)In(Ni@Sn_9)]^{5-}$, a Zintl cluster which can be isolated in two isomeric forms. By exploring the structural landscape we have shown that this isomerism is likely to be the result of intermolecular interactions in the crystalline phase, rather than any differences the synthetic procedure. Examination of the electronic structure shows that this cluster can be described as a pair of $[Ni@Sn_9]^{4-}$ units coordinated to a closed-shell $In^{3+}$ ion by electrostatic attraction, which is consistent with the observed structural diversity.

The relative simplicity of the bonding in this cluster allows it to serve as a reference point when discussing the more complex analogue $[(Ni@Ge_9)Ni(Ni@Ge_9)]^{4-}$, which is structurally similar to the $\eta^3 : \eta^3$ isomer of the cluster discussed above but bears four fewer valence electrons. We have identified the two molecular orbitals which are depopulated by this reduced electron count; one is an Ni-Ni-Ni antibonding orbital, and the other is a Ge-based orbital which is bonding within each $Ge_9$ unit but antibonding between the two. We have therefore assigned formal charges of -3 to each $Ge_9$ unit and +2 to the $Ni_3$ core. The structural differences between these clusters correlate with the shapes of the depopulated orbitals, enabling us to see trends in the shapes of electronically related clusters.

We considered $[(Fe@Sn_9)Fe(Fe@Sn_9)]^{4-}$, isostructural to $[(Ni@Ge_9)Ni(Ni@Ge_9)]^{4-}$ but with six fewer valence electrons. By extending our orbital analysis method we have shown that the six lost electrons are all spin-down and are lost from a set of doubly degenerate $\pi$ bonding, non-bonding and antibonding orbitals, giving a septet ground state and no change in M-M bond order. $[(Fe@Sn_9)Fe(Fe@Sn_9)]^{4-}$ therefore contains a formal 3-centre 4-electron $[Fe_3]^{2+}$ unit with Fe-Fe bond orders of 0.5, a picture supported by directly computed bond orders.

## 3.4 Growth patterns of coinage metal cores in lead shells

### 3.4.1 Introduction

Copper, silver, and gold are known as "coinage metals" as they have been used throughout the ages to produce coins for their low reactivity under everyday conditions, ensuring that money would not dissolve in the rain or ignite in hot weather. The most inert and most precious is gold, but modern gold chemistry has nevertheless expanded to include compounds of various elements and oxidation states befitting its place as a transition metal. All three are subject to intense research for modern technology, beyond established applications in electronics. Heterogeneous and homogeneous catalysts of the coinage metals have been developed, which span the full size range from mononuclear organometallic complexes to nanoparticles to periodic surfaces, for applications in green energy and organic synthesis[120, 121, 122, 123, 124]. Gold clusters have also been developed as fluorescent probes for medical imaging[125]. A particularly striking branch of the chemistry of gold and silver is their ability to form atomically precise clusters - those with a fixed composition and shape, rather than nanoparticles of indeterminate shape and size - with a vast range of sizes and high-symmetry geometries.[126] These are of great interest as they have properties in common with molecules and nanoparticles simultaneously, allowing detailed insights into electronic changes as we move from one size regime to the next, and enabling us to study nanoparticle-like behaviour, such as catalysis, with molecular-precision structural and optical techniques. The first examples of such compounds were gas-phase cationic clusters $Cu_n^+$, $Ag_n^+$ and $Au_n^+$, containing up to 250 atoms, measured by mass spectrometry[127]. Particularly intense peaks were observed for certain cluster sizes - $n = 3, 9, 21, 35, 41, 59, 93$ all of which, bearing a single positive charge, have a valence electron count of $n - 1$. These numbers, often referred to as "magic numbers", can be derived by modelling the valence electrons as moving in a spherical potential formed from the metal valence $s$ orbitals. This model resembles an electron in a hydrogenic atom, differing by the use of an infinite potential at a fixed radius rather than $V = \frac{1}{r}$, so the electronic energy levels can be labelled by analogy to atomic orbitals and clusters described in this way are often called "superatoms". The energy levels are quantized by numbers $n, l, m, s$, which have the same degeneracies as in atoms but, due to the square potential well model, the allowed values and energy

level ordering are slightly different[83, 128]:

$$1S - 1P - 1D - 2S - 1F - 2P \tag{3.17}$$

Filling these levels gives electron counts of 2, 8, 18, 20, 34, 40, corresponding to the early intense peaks in the cluster mass spectra. The structures of small neutral gas-phase clusters have been probed directly by vibrational spectroscopy[129]. $Au_7$ was assigned a planar pseudo-triangular structure, seemingly incompatible with the spherical "superatom" model, and $Au_{20}$ a tetrahedral structure with 4 atoms per edge. While these gas-phase clusters are very numerous, they are hard to study due to their transient existence and the charge-dependence of some analytical techniques. The most important class of atomically precise clusters in current gold chemistry are the "monolayer-protected clusters", which are stabilized by an outer shell of thiolate or phosphine ligands. These can be stabilized in the solution and crystalline states, and can therefore be characterized far more effectively than their "naked" gas-phase counterparts and are better candidates for interesting and useful chemical behaviour. Landmark early examples of these are $Au_{11}X_3(PR_3)_7$[130] and $[Au_{13}(PMe_2Ph)_{10}Cl_2](PF_6)_3$[131], both composed of a gold core surrounded by anions and phosphine ligands. The $Au_{13}$ cluster core is icosahedral, with one gold atom in the centre, and the $Au_{11}$ core may be described as an icosahedron with three vertices condensed to a single point. Larger clusters have since been synthesized using thiolate ligands, such as $Au_{25}(SG)_{18}$[132] (SG is the tripeptide glutathione), $Au_{36}(SR)_{24}$[133], and $Au_{133}(SPh{-}^tBu)_{52}$[134]. These differ from the smaller phosphine clusters in that the Au atoms segregate, some forming the core and others residing in the thiolate shell. This has been termed "divide and protect"[135], and the bonding in these clusters can be described in terms of Au-S covalent bonds and Au-Au non-covalent "aurophilic" interactions. Just as the $Au_{13}$ core is two-layered, formulated as $Au@Au_{12}$, the larger clusters can be described by concentric shells - for example, the $Au_{107}$ core of $Au_{133}(SPh{-}^tBu)_{52}$ can be written as $Au_{13}@Au_{42}@Au_{52}$. $Au_{36}(SR)_{24}$ is particularly interesting in this regard as its core can be formulated as $Au_4@Au_{24}$, but it also has face-centred cubic geometry, highlighting the nature of these clusters as mid-way between molecule and metal (bulk gold also has an FCC structure).

The $5s$ valence electron of silver is more easily removed than the $6s$ electron of gold, as the former is not significantly stabilized by relativistic effects. The lower ionization energy for Ag makes synthesis of analogous clusters challenging, but some examples have nevertheless been synthesized, including $[Ag_{25}(SR)_{18}]^-$[136], directly

analogous to the gold-glutathione cluster $Au_{25}(SG)_{18}$, and the pentagonal bipyramidal $Ag_{374}(SR)_{113}Br_2Cl_2$[137]. There are few clusters with Au and Ag analogues, highlighting the subtle nature of the metal-metal interactions which hold these clusters together. "Alloy clusters" of multiple metals, such as $Au_{25-x}Ag_x(SR)_{18}$ (n=0-11)[138], also exist in various stoichiometries and combinations of late transition metals[126]. In recent years the Sun group have synthesized a range of group 14 Zintl clusters encapsulating cores of copper, silver, and gold. These are shown in Figure 3.21, arranged by the identity of the encapsulated metal. This family shows remarkable structural diversity, and the focus of this chapter is to investigate the structural and electronic relationships between these compounds to gain greater insights into the similarities and differences between these three precious metal elements. Additionally, Cong-Cong Shu (in the Sun group) has synthesized $[Fe_4Pb_{18}]^{4-}$, isostructural to $[Cu_4Pb_{18}]^{4-}$ shown in Figure 3.21 but with twelve fewer valence electrons. Comparison of these two clusters in a computational study will give new insights into open-shell transition metal species in clusters, of which few examples are currently known.

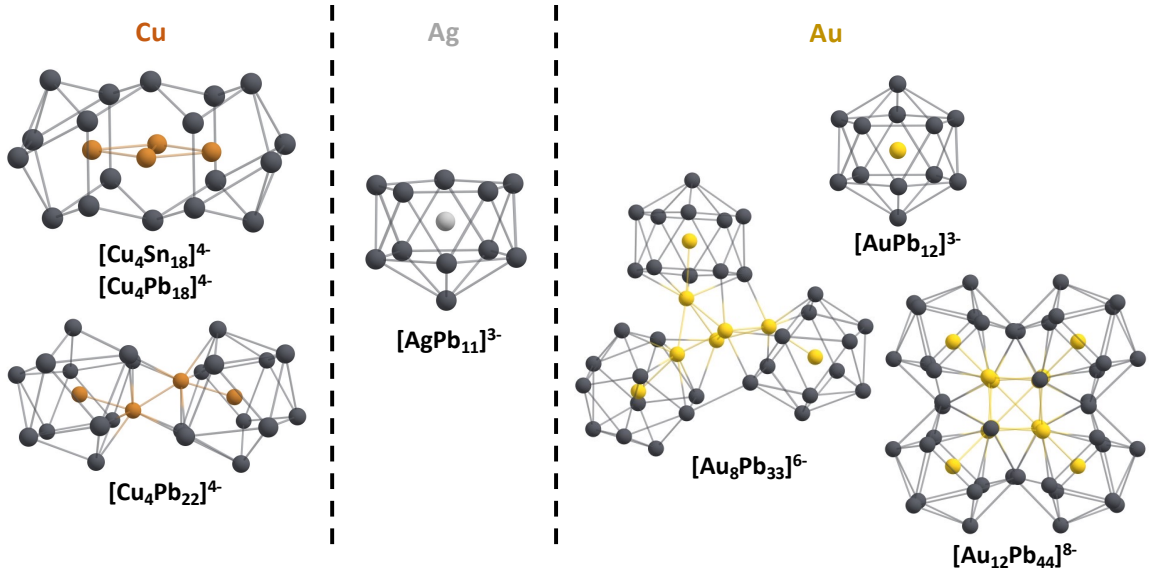



Figure 3.21: Characterized tin and lead clusters containing Cu, Ag and Au cores.

Before describing our detailed investigations into individual species, we can identify some connections between these compounds by examining their structures. The only cluster in Figure 3.21 reported prior to this work is $[AuPb_{12}]^{3-}$, a *closo*- cluster with a distorted icosahedral structure. It has 62 valence electrons, giving 38 skeletal electrons after discounting 12 Pb lone pairs, and was initially formulated as

$[Au^{-}Pb_{12}{}^{2-}]$, implying 12 electrons on Au and 26 on the cluster, as required for a *closo-* icosahedron. However, the distortion away from $I_h$ symmetry and reexamination of the orbitals suggests that a better assignment would be $[Au^{+}Pb_{12}{}^{4-}]$, with a pair of electrons going from Au 6*s* to fill an antibonding orbital on the cage, leading to a structural distortion.

This icosahedron is an important reference point in forming other clusters in this group. $[AgPb_{11}]^{3-}$ can be described as a *nido-* cluster formed by removing one vertex from a $Pb_{12}$ icosahedron. If we replace one Pb vertex by $Cu^{+}/Ag^{+}/Au^{+}$, rather than simply removing it, we get the hypothetical pseudo-icosahedral fragment $[M_2Pb_{12}]^{2-}$, which has not been isolated but is a common structural feature of the larger clusters. $[Cu_4Pb_{22}]^{4-}$ can be constructed by a dimerization of two such fragments, while $[Au_8Pb_{33}]^{6-}$ and $[Au_{12}Pb_{44}]^{8-}$ are trimers and tetramers surrounding cores of Au atoms. In this investigation we will study the structure and bonding in the smaller clusters to better understand their assembly into larger clusters. An essential aspect of this assembly process will be the identification and description of transient fragments which cannot be isolated experimentally but which contribute to the formation of multiple isolated clusters. An algorithm-driven study of Ta-Ge-As clusters identified a tetrahedral $[Ge_2As_2]^{2-}$ fragment as an important species in forming larger clusters[71]. In our case, these fragments are the $[M_2Pb_{12}]^{2-}$ icosahedron described above, and in more detail in Figure 3.24, and the larger unit $[Au_6Pb_{22}]^{4-}$ shown below in Figure 3.37. Our aim is therefore to use this family of clusters, in which we can vary the encapsulated metal to control the size of the products, to simultaneously devise a formation pathway for all observed clusters from a small set of molecular building blocks. These pathways, starting from the synthetic sources of Au and Pb, are shown in the flow diagram in Figure 3.22, which depicts Au clusters but also describes the behaviour of Cu and Ag. By studying each species in the diagram and understanding the bonding interactions by which each is formed from its precursors, we will try to identify the reasons for which each transition metal prefers specific lead cage architectures.

### 3.4.2 Methods

DFT calculations on $[Au_6Pb_{22}]^{4-}$, $[Au_8Pb_{33}]^{6-}$, and $[Au_{12}Pb_{44}]^{8-}$ were performed with ADF[26], version 2017, using the BP86 functional[4]. Calculations on all $[M@Pb_{11}]^{3-}$, $[M_2@Pb_{11}]^{2-}$, $[M_4Pb_{18}]^{4-}$ and $[M_4Pb_{22}]^{4-}$ species were performed with ADF[26], version 2019.304, using the PBE functional[5]. Slater-type TZP basis functions[92] were

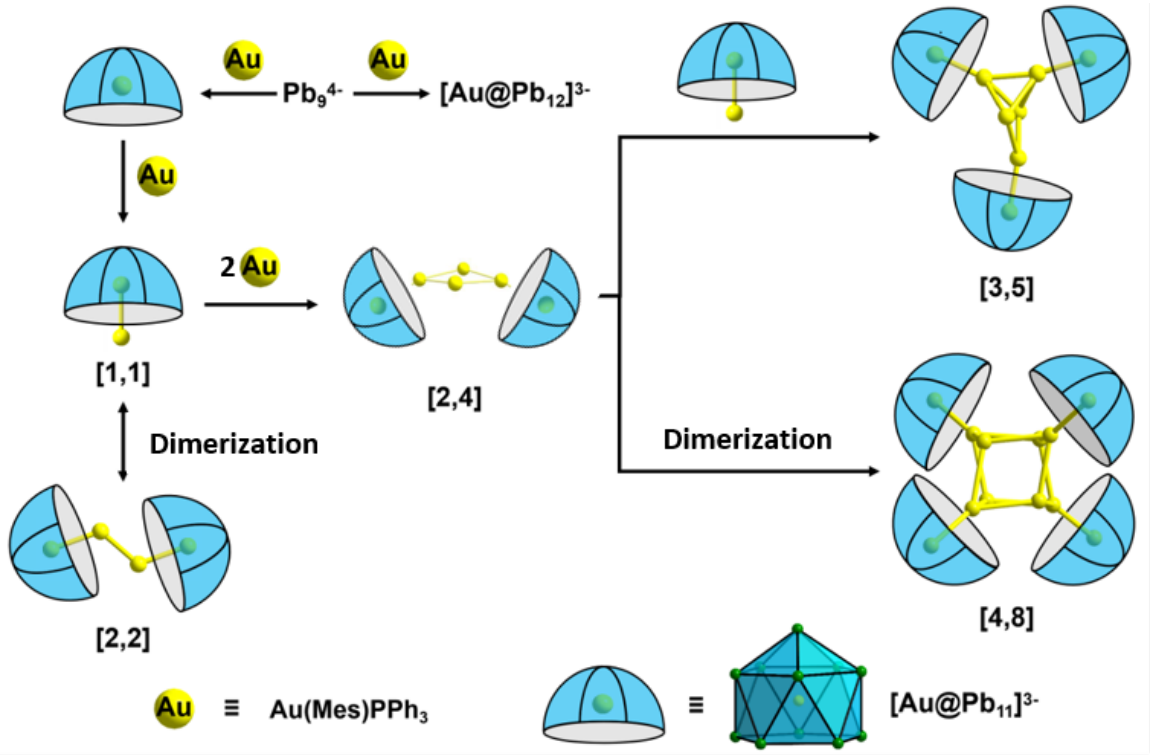



Figure 3.22: Flow diagram showing the assembly pathways of AuPb clusters.

used in all cases. The crystalline environment was modelled using the COSMO continuum solvent model[93] with the dielectric constant of water. Relativistic effects were described by the Zeroth Order Relativistic Approximation (ZORA)[139, 140, 141]. Energy decomposition analysis was performed according to the scheme of Ziegler and Rauk[28].

## 3.4.3 Results

### 3.4.3.1 $[MPb_{11}]^{3-}$ and $[M_2Pb_{11}]^{2-}$

We will begin with the $C_{5v}$ *nido-* cluster $[MPb_{11}]^{3-}$ and the $[M_2Pb_{11}]^{2-}$ fragments described above. The only example of these to have been characterized is $[AgPb_{11}]^{3-}$. Electron-counting gives a skeletal electron count of 36, so assignment of $d^{10}$ $Ag^+$ gives 26 electrons for the Pb cage, which corresponds to the $2n + 4$ required for a *nido-* cluster by the Wade-Mingos rules. Structural optimization of this cluster gives good agreement with the crystal structure, and the $Ag^+$ assignment is supported by dominant Ag $5s$ character in the $a_1$ LUMO+2.

To enable us to compare the three metals, we have optimized $[MPb_{11}]^{3-}$ and $[M_2Pb_{11}]^{2-}$ for Cu, Ag and Au. Geometries are shown in Figure 3.24 with symmetry-inequivalent

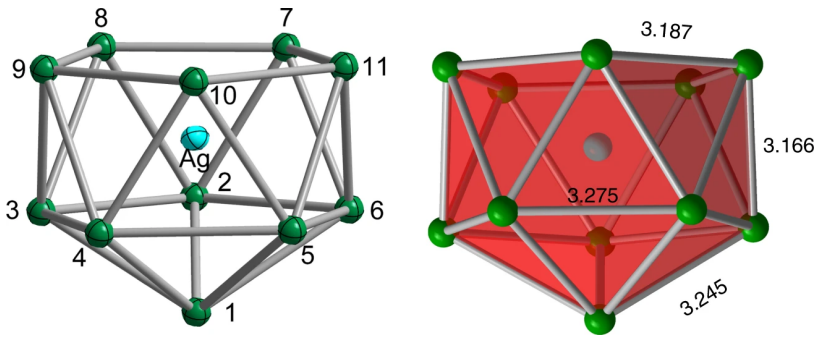



Figure 3.23: Crystal structure of $[AgPb_{11}]^{3-}$ measured by Cong-Cong Shu. Bond lengths are averages over symmetry-equivalent Pb-Pb pairs. Reproduced from ref.[34] under the Creative Commons license http://creativecommons.org/licenses/by/4.0/

bond lengths annotated for all three metals. The proportions of each trio of clusters are much the same, but it is striking that the Ag and Au clusters have very similar geometries but the Cu analogue has markedly shorter bond lengths. This reflects the broad trend in the transition metals of $4d$ and $5d$ metals showing similar behaviour to each other, but different from the $3d$ metals, which is in part due to the effect of the lanthanide contraction on the $5d$ orbitals. The similarity between Pb-Pb bond

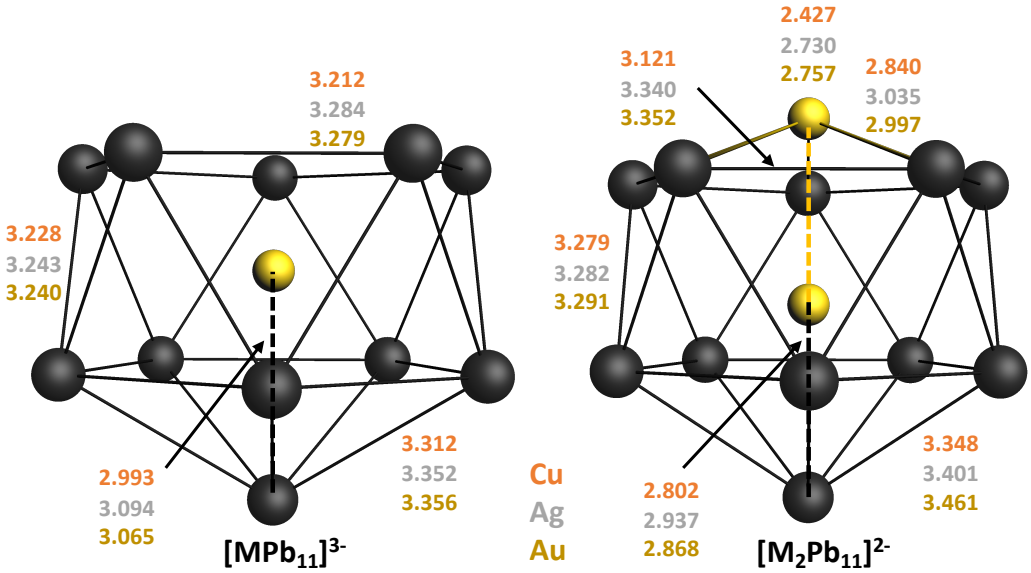



Figure 3.24: Optimized geometries for $[MPb_{11}]^{3-}$ and $[M_2Pb_{11}]^{2-}$ (M=Cu, Ag, Au).

lengths in $[MPb_{11}]^{3-}$ and $[M_2Pb_{11}]^{2-}$ shows that the bonding in the clusters is not significantly affected by addition of $M^+$.

To understand the electronic relationship between the two clusters we have plotted their frontier MOs in Figure 3.25. For this plot, and the discussion of it, we have

used M=Ag, but the behaviour is identical for Cu and Au. As we might expect, the frontier orbitals of $[AgPb_{11}]^{3-}$ are dominated by Pb 6$p$ orbitals at the open $Pb_5$ face. The HOMO is a doubly degenerate $e_1$ orbital, with $\pi$ symmetry along the $C_5$ axis. Slightly lower in energy is an $a_1$ combination of Pb 6$s$ orbitals with $\sigma$ symmetry along the principal axis. The LUMO of $Ag^+$ is the 5$s$, which has $a_1$ symmetry. It therefore

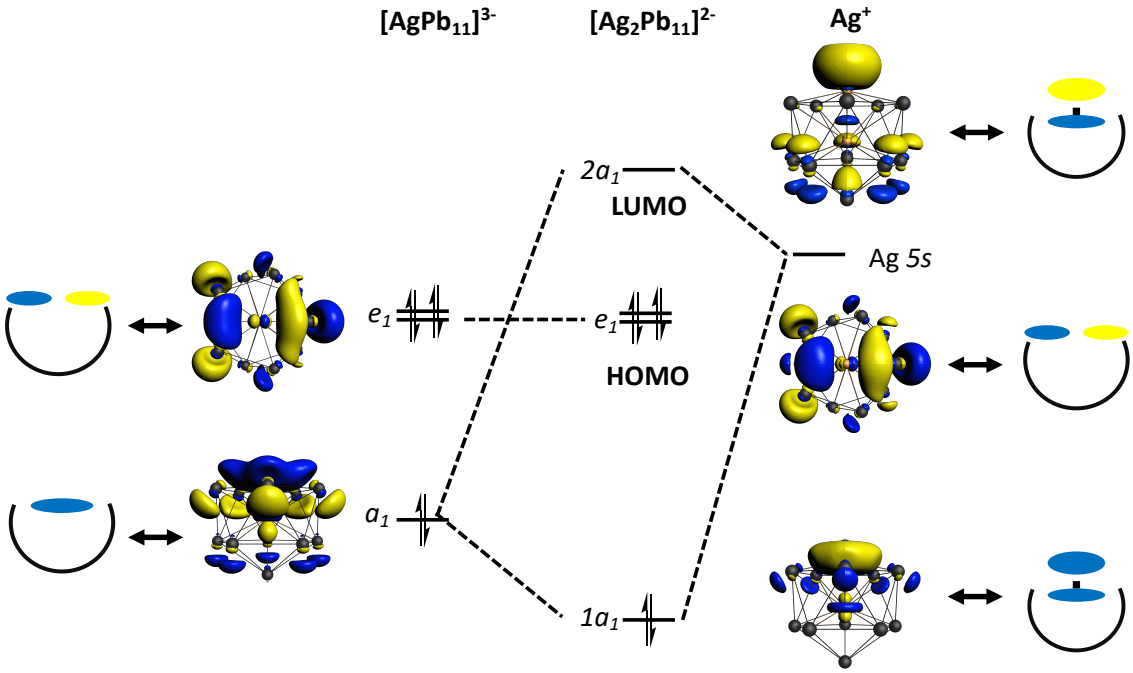



Figure 3.25: MO diagram for $[Ag_2Pb_{11}]^{2-}$ showing the interaction between important orbitals on the $[AgPb_{11}]^{3-}$ and $Ag^+$ fragments. MOs plotted with isovalue = 0.03

interacts with the occupied $a_1$ orbital on the cluster to form bonding and antibonding combinations, as well as binding to the cluster by a strong electrostatic attraction. The bonding orbital has predominantly Pb 6$s$ character, and the antibonding $2a_1$, which is the LUMO of $[Ag_2Pb_{11}]^{2-}$, resembles the Ag 5$s$ orbital directed outwards from the cluster. The $e_1$ HOMO of $[AgPb_{11}]^{3-}$ finds no bonding partner on Ag, since the 5$p$ is too high in energy, and so is non-bonding with respect to Ag and experiences no change in energy when $[Ag_2Pb_{11}]^{2-}$ is formed. It therefore remains the HOMO, giving $[Ag_2Pb_{11}]^{2-}$ $\sigma$-acceptor and $\pi$-donor character, resembling a "Z ligand" like $BR_3$ in organometallic chemistry[142].

The frontier orbitals of $[AgPb_{11}]^{3-}$ suggest that this fragment is isolobal to $C_5H_5^-$, a component of well-known organometallic complexes, and *nido*-$[B_{11}H_{11}]^{4-}$ which can coordinate to transition metals in complexes such as $[Cu(B_{11}H_{11})_2]^{3-}$[143]. This proposed isolobality has been validated by the characterization of $[Cp^*RuPb_{11}]^{3-}$ and

$[Cu@Cp^*RuPb_{11}]^{2-}$ ($Cp^* = C_5Me_5^-$), in which $[Pb_{11}]^{4-}$ and $[CuPb_{11}]^{3-}$ act as ligands in a classic metallocene analogue[144].

Our calculations suggest that all three metals can form $[MPb_{11}]^{3-}$ and $[M_2Pb_{11}]^{2-}$ clusters with qualitatively similar structures and bonding profiles, so we would like to find some explanation for the fact that different clusters have been isolated for each metal, as shown in Figure 3.21. We have calculated the bonding energy of the $[MPb_{11}]^{3-}$ and $M^+$ fragments of $[M_2Pb_{11}]^{2-}$ for all three metals and plotted them in Figure 3.26. For more detailed insight, we have decomposed these bonding energies into orbital, electrostatic, Pauli, and solvation terms by the Morokuma decomposition method[28, 27]. The electrostatic, Pauli and solvation terms largely cancel each other and the residual terms are equal for all three metals, so to investigate the electronic structure of these clusters, we have plotted the orbital components of the bonding energies and their subsequent decomposition into the irreducible representations ("irreps"), or symmetry species, of the $C_{5v}$ point group. The binding energies increase

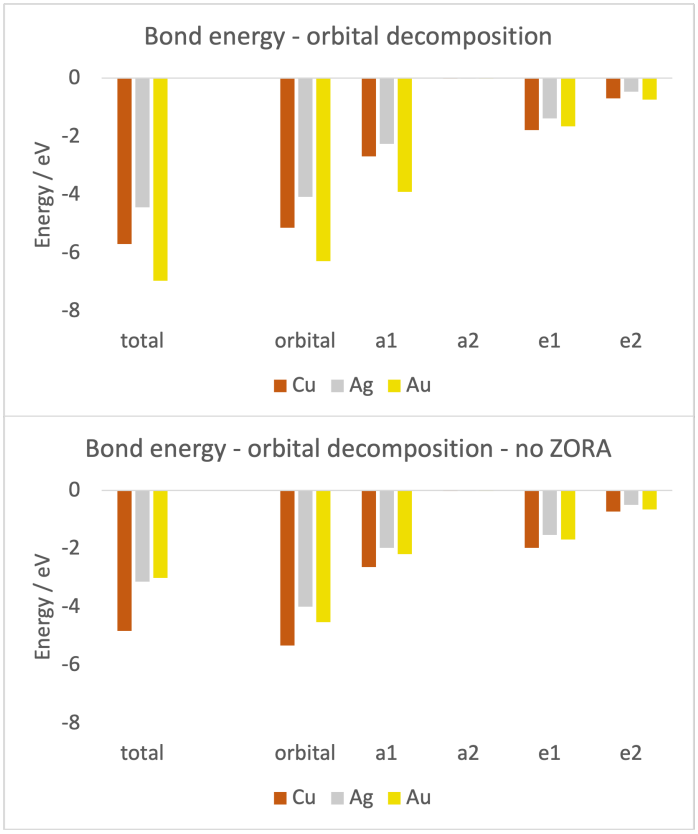



Figure 3.26: Binding energy of $[MPb_{11}]^{3-}$ and $M^+$ fragments of $[M_2Pb_{11}]^{2-}$, with orbital and irreducible representation energy decomposition terms, calculated with and without the ZORA correction.

in the order Ag, Cu, Au, consistent with the fact that $[MPb_{11}]^{3-}$ has been isolated

for Ag only. The orbital components of the bind energies closely follow the observed trend in total binding energies, so it may be valuable in explaining the reason for this trend. Decomposition of these orbital components into irreps shows that the greatest contributor is the totally symmetric $a_1$ irrep, unsurprising since all fully in-phase bonding MOs belong in this group, and that the greater bonding energy for $[Au_2Pb_{11}]^{2-}$ is most pronounced in $a_1$ symmetry. This is a manifestation of the stabilization of the Au 6*s* orbital by relativistically induced mixing with $5d_{z^2}$, a common feature of Au coordination chemistry, which leads to a better energy match between Au 6*s* and Pb. Since the 6*s* orbital lies on the principal rotation axis of the cluster this extra bonding energy affects the $a_1$ orbitals, and is greatest for Au because the strength of the $s - d_{z^2}$ interaction varies with the fourth power of the mass of the nucleus. To test this hypothesis, we repeated the energetic analysis using the same geometry but without the ZORA (zeroth order relativistic approximation) correction. The results, plotted in Figure 3.26, show a modest change in the behaviour of the Cu and Ag clusters but a significant reduction in bonding energy for Au, particularly in the $a_1$-symmetry component. In $e_1$ symmetry, meanwhile, it is Cu which gains the greatest stabilization. This may be related to the position of the *exo*- Cu atom, which is held much closer to the $Pb_5$ face than Ag or Au due to its smaller size. We will proceed to use our insights into the behaviour of these icosahedral cluster fragments to understand the structures of the larger clusters.

#### 3.4.3.2 $[M_4Pb_{22}]^{4-}$ dimers

Dimerization of the icosahedral $[M_2Pb_{11}]^{2-}$ fragment gives $[M_4Pb_{22}]^{4-}$. The crystal structure of $[Cu_4Pb_{22}]^{4-}$ has been fully resolved, showing that the cluster has a $C_{2h}$ geometry, while the Ag and Au analogues have not been resolved crystallographically but mass spectrometry indicates their existence. We have optimized the $C_{2h}$ structure for all three metals, finding good agreement with the crystal structure for Cu, with bond lengths shown in Figure 3.27. The structure may be described as a "slipped dimer" - rather than the two $[M_2Pb_{11}]^{2-}$ halves approaching each other symmetrically, to give a linear $M_4$ core, they are displaced so that the *exo*- M atom approaches two Pb atoms on the opposite $Pb_5$ face. As in the $[M_2Pb_{11}]^{2-}$ we can see that the Ag and Au analogues have very similar structures, while the Cu cluster shows shorter M-M and M-Pb bond lengths.

Dimerization energies for the process

$$2[M_2Pb_{11}]^{2-} \longrightarrow [M_4Pb_{22}]^{4-}$$

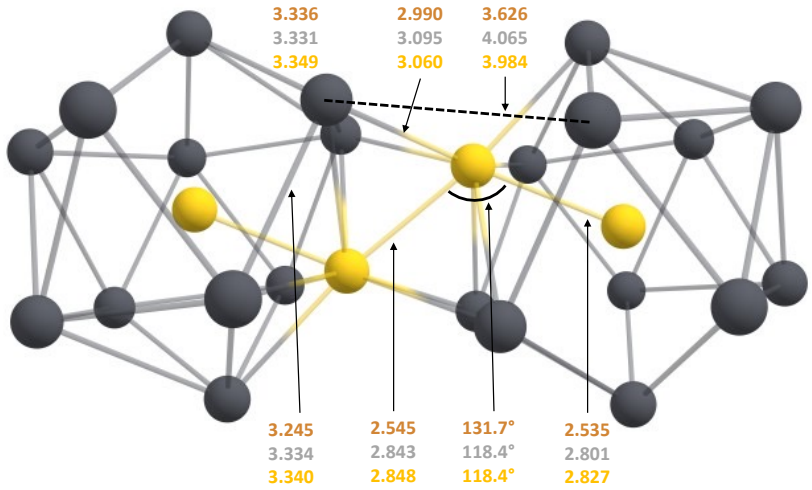



Figure 3.27: Optimized structures of $[M_4Pb_{22}]^{4-}$ clusters (M=Cu, Ag, Au) with selected geometrical parameters for all three metals.

are given in table 3.3. Ag shows the smallest driving force for aggregation, as it did for the formation of $[M_2Pb_{11}]^{2-}$, but the largest dimerization energy is found in Cu rather than Au. Due to the lower symmetry of these clusters ($C_{2h}$) compared to the icosahedral fragments ($C_{5v}$) we cannot easily interpret the decomposition into irreps as we did in Figure 3.26. We can understand this dimerization and the geometry of the

| M | $E_{dimer}$ / eV |
|---|---|
| Cu | -1.341 |
| Ag | -1.018 |
| Au | -1.274 |

Table 3.3: Energies of formation of $[M_4Pb_{22}]^{4-}$ from $[M_2Pb_{11}]^{2-}$ fragments.

$[M_4Pb_{22}]^{4-}$ clusters by examining the frontier orbitals of the icosahedral fragments. Figure 3.25 shows that the fragment HOMO is an $e_1$-symmetry Pb $6p$ combination at the $Pb_5$ face, and the LUMO is the vacant M $s$ orbital directed outwards from the middle of that face. If the two fragments approach each other "nose to nose" then the two HOMOs will interact with each other, as will the two LUMOs, resulting in no net bonding. In their misaligned arrangement, however, one lobe of the HOMO of each $[M_2Pb_{11}]^{2-}$ fragment can donate into the LUMO of the other fragment. This is illustrated by the MO scheme in Figure 3.28. The occupied $b_u$ orbital shown contains Pb-Cu bonding character across the middle of the cluster, while the $a_g$ LUMO contains the lobes of the fragment HOMO which are not stabilized by donation into the opposite fragment LUMO. This is necessarily a much simplified picture since the dramatic changes in symmetry lead to MO mixing, so we cannot identify a single

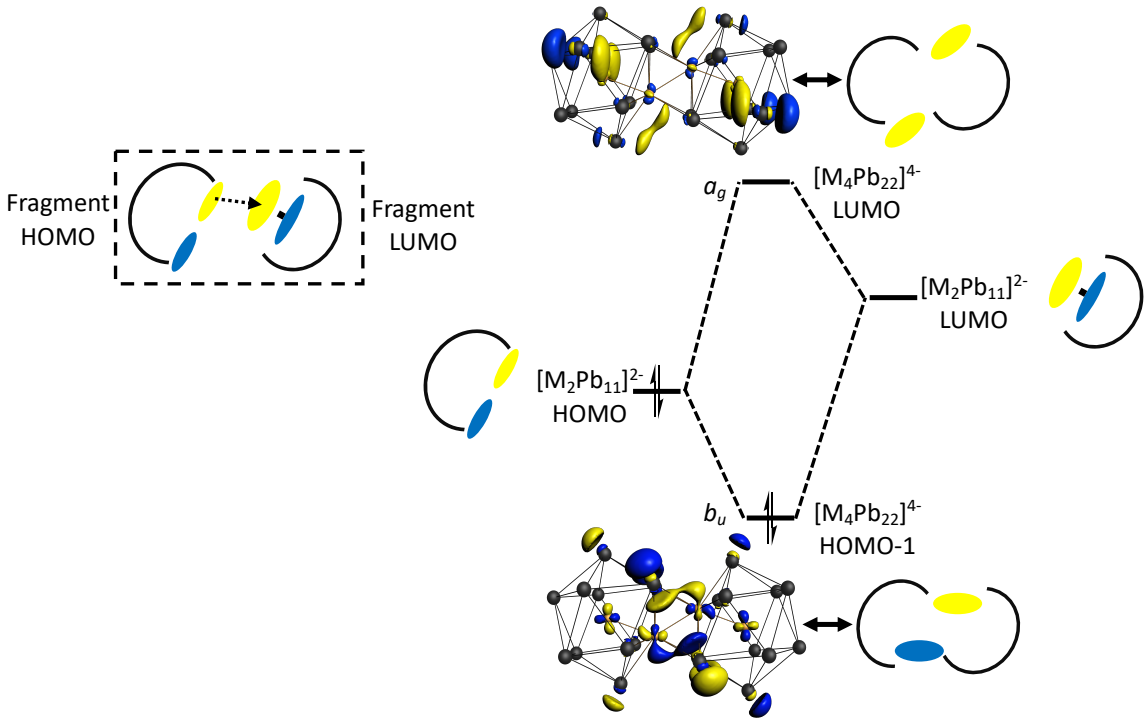



Figure 3.28: Frontier MO interaction in dimerization of $[M_2Pb_{11}]^{2-}$ to form $[M_4Pb_{22}]^{4-}$. The dashed box highlights donation from the HOMO of one fragment to the LUMO of the other fragment, and the MO diagram shows the resultant frontier MOs of $[M_4Pb_{22}]^{4-}$. Orbitals plotted with isovalue = 0.036.

orbital which captures all of the fragment HOMO-LUMO interaction. Nevertheless, the MOs highlighted here illustrate the interaction between the fragments and help us to understand the structure of the $[M_4Pb_{22}]^{4-}$ dimers.

#### 3.4.3.3 $[Cu_4Pb_{22}]^{4-}$ and $[Cu_4Pb_{18}]^{4-}$

For copper, we have a particularly interesting pair of compounds to compare in $[Cu_4Pb_{22}]^{4-}$ and $[Cu_4Pb_{18}]^{4-}$ since they have the same number of encapsulated metal atoms. These are shown side-by-side in Figure 3.21. $[Cu_4Pb_{18}]^{4-}$ is a smaller and more symmetrical cluster, encapsulating the four Cu atoms arranged in a rhombus, rather than the zig-zag linear core of $[Cu_4Pb_{22}]^{4-}$. Another important feature of the smaller cluster is that it cannot obviously be divided into fragments, so we must attempt to understand its structure as a whole. In the preceding sections we described $[MPb_{11}]^{3-}$ and $[M_4Pb_{22}]^{4-}$ clusters as containing $d^{10}$ $M^+$ atoms which, being formally closed-shell, make no net contribution to covalent bonding. Instead, the metal atoms play an electrostatic role, stabilizing the large negative charge on the surrounding Pb cage. We now wish to examine these two clusters to determine whether the Cu atoms

are again dominated by electrostatic character and whether $[M_4Pb_{18}]^{4-}$ clusters may be accessible for Ag and Au.

Our previous analytical tools, such as examination of structural parameters or direct inspection of the MOs, are not so easily applicable here as the clusters do not have the same stoichiometry or easily comparable structures. We have investigated $[Cu_4Pb_{18}]^{4-}$ by calculating properties which can be directly compared to $[Cu_4Pb_{22}]^{4-}$ to allow us to identify significant similarities as well as differences. The first of these properties is the density of states (DOS), shown for both compounds in Figure 3.29. The atom-resolved curves show the contribution of specific atoms to the molecular energy levels as a function of energy. This analytical tool is most widely used in solid-

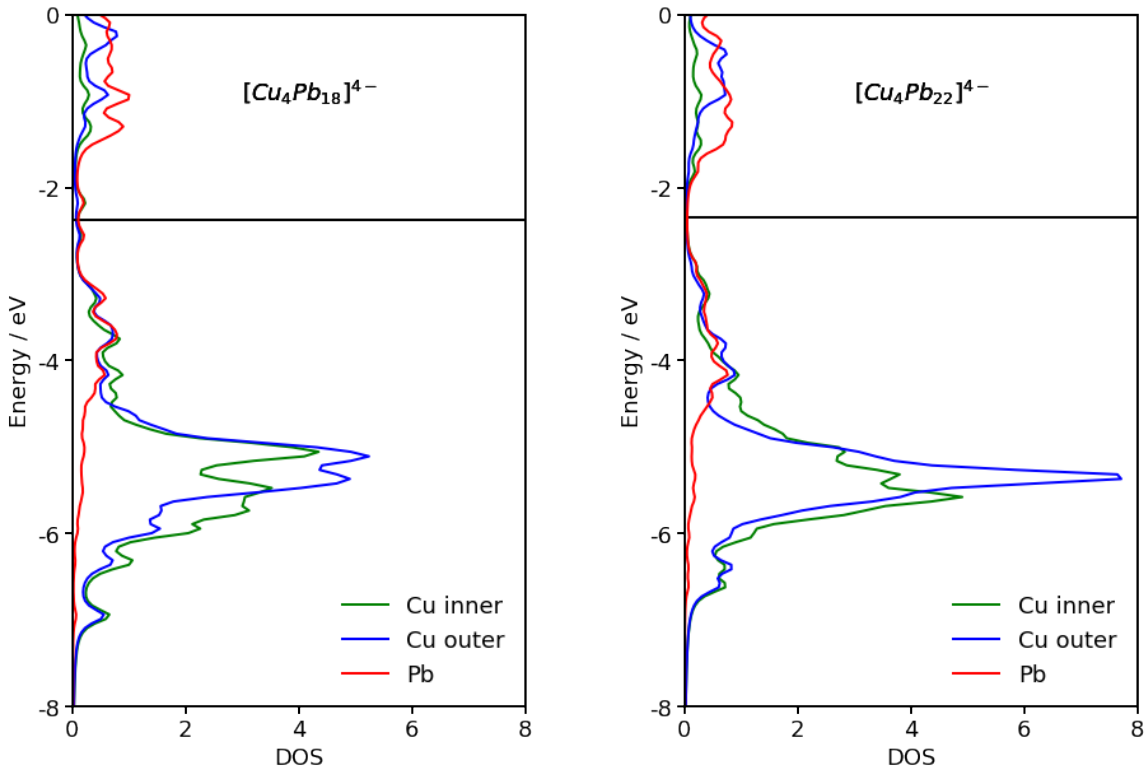



Figure 3.29: Density of states for $[Cu_4Pb_{18}]^{4-}$ and $[Cu_4Pb_{22}]^{4-}$, resolved to show contributions from the symmetry-inequivalent Cu pairs and all Pb atoms, with a Lorenzian broadening of 0.1 eV.

state chemistry, where the DOS describes the number of states in an energy interval dE. In molecular calculations we reproduce this by broadening each MO level with a Lorenzian function with a width of our choosing. The black horizontal lines mark the midpoint of the HOMO-LUMO gap, analogous to the solid-state Fermi level, showing the energy up to which the MOs are occupied.

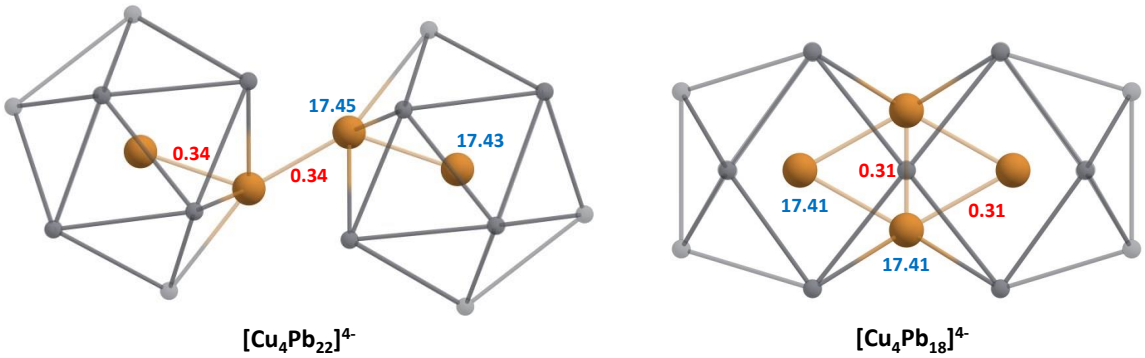



Figure 3.30: Localization indices (blue) and delocalization indices (red) for Cu atoms and Cu-Cu bonds, respectively, in $[Cu_4Pb_{18}]^{4-}$ and $[Cu_4Pb_{22}]^{4-}$.

The most obvious feature of the two plots in Figure 3.29 is that they are extremely similar, in the forms of both inner and outer $Cu_2$ pairs. This strongly suggests that the bonding behaviour of Cu is the same in the two compounds and that the Cu atoms in the two environments of each structure have comparable electronic character. Another informative feature is that the Cu 3*d* orbitals give one major peak well below the Fermi level, meaning that all the *d* orbitals are filled. This supports our assignment of a formal $d^{10}$ configuration to Cu, implying the same closed-shell $Cu^+$ character as we identified by inspection of the MOs in $[MPb_{11}]^{3-}$. Further evidence of this closed-shell character can be found in the fact that the large Cu peak is not coincident with a Pb peak. If these two had significant covalent overlap we would see coincident peaks where both orbitals contribute to the same MOs, but the DOS shows little sign of this.

For a second point of comparison between the two compounds we have explored the topology of the electron density, using Bader's QTAIM. More specifically, we have calculated the localization and delocalization indices (LI and DI) for the Cu atoms and Cu-Cu pairs in both clusters. These values are shown in Figure 3.30, with DIs for the bonds in red and LIs for the atoms in blue. Once again we can see striking similarities between the two clusters. The delocalization indices, which are a topologically founded bond order, are in the range 0.31-0.34 for all neighbouring Cu-Cu pairs across both clusters. The agreement between the values show that the Cu-Cu interactions are alike in the rhombus as in the zig-zag filament, and the small absolute values indicate no substantial Cu-Cu bond. For comparison, recall the DI values of 0.28 for the Co-Co pair in $[Co_2Ge_{16}]^{4-}$, with no formal Co-Co bond, and 0.76 for the Fe-Fe bond in $[Fe_2Ge_{16}]^{4-}$, with a formal bond order of 0.5. The localization indices (LI) indicate the number of electron pairs localized on the atoms, and these too show

that the behaviour of the individual Cu atoms is much the same in both clusters. The LI of an atom can be divided by the QTAIM population to give the "proportional localization index" (PLI), which describes the fraction of the population of the atom which is localized entirely on that atom and measures the closed-shell character of the atom, on a scale from 0 to 1. Here all Cu atoms have populations of 29.2 electrons - another significant similarity - so all have PLIs of 0.60, indicative of dominant closed-shell character. By comparison, the Pb atoms have PLIs around 0.4, demonstrating their more covalent nature.

Having established the electronic nature of copper in both clusters, we wish to investigate the possibility of forming the gold and silver analogues of $[Cu_4Pb_{18}]^{4-}$. Note that $[(Ag/Au)_4Pb_{22}]^{4-}$ have not been crystallised but are thought to exist in solution due to mass spectrometry results. To do this, we have calculated the energy of the reaction

$$[M_4Pb_{18}]^{4-} + 4Pb \longrightarrow [M_4Pb_{22}]^{4-}$$

for all three metals as this will indicate the extent to which each metal favours the larger Pb cage over the smaller one. Our choice of a free Pb atom as our reference state, calculated using exactly the same method as was used for both clusters, is not realistic, but that is unimportant as we are investigating a structural preference rather than a real reaction. This choice does mean that the absolute reaction energies are not directly interpretable, so we have set the reaction energy for Cu to zero and measured those for Ag and Au relative to that. The results, in Table 3.4, show that the larger cage is more strongly favoured by Ag and Au than Cu. One simple interpretation is that the $Pb_{18}$ cage is too small to contain an $M_4$ core of the larger metal atoms.

| M | $\Delta H_r$ / eV |
|---|---|
| Cu | 0 |
| Ag | -0.42 |
| Au | -0.57 |

Table 3.4: Energies of formation of $[M_4Pb_{22}]^{4-}$ from $[M_4Pb_{18}]^{2-} + 4Pb$.

In summary, we have used two distinct methods - MO-based DOS analysis and topology-based QTAIM indices - to study the electronic character of copper in $[Cu_4Pb_{18}]^{4-}$ and $[Cu_4Pb_{22}]^{4-}$. Our results point to all copper atoms having a $d^{10}$ $Cu^+$ configuration, behaving as the encapsulated metal ions in $[MPb_{11}]^{3-}$ clusters do. These copper atoms therefore make little overall contribution to the covalent bonding in the clusters, instead acting as "electrostatic glue" to stabilize the strongly anionic Pb cages

which surround them. By simple reaction energy calculations, we have then shown that Ag and Au favour the $[M_4Pb_{22}]^{4-}$ structure over $[M_4Pb_{18}]^{4-}$ more strongly than Cu does, which may be a result of their size.

#### 3.4.3.4 $[Fe_4Pb_{18}]^{4-}$: an open-shell analogue

$[Fe_4Pb_{18}]^{4-}$, isostructural to $[Cu_4Pb_{18}]^{4-}$, has also been synthesized recently by the Sun group but has not been reported in the literature[2]. As it has twelve fewer valence electrons, $[Fe_4Pb_{18}]^{4-}$ may be seen as an open-shell analogue of $[Cu_4Pb_{18}]^{4-}$ just as $[Fe_3Sn_{18}]^{4-}$ is to $[Ni_3Ge_{18}]^{4-}$ (see previous section of this chapter). We will therefore depart briefly from $d^{10}$ coinage metal cations to consider this new addition to the series of TM-encapsulating lead clusters. A comparison of the geometries, highlighting metal-metal distances, is shown in Figure 3.31(a), with $[Fe_4Pb_{18}]^{4-}$ bond lengths shown in red and $[Cu_4Pb_{18}]^{4-}$ in blue. The red bond lengths shown refer to the $S = 5$ lowest-energy spin state of $[Fe_4Pb_{18}]^{4-}$ - see Figure 3.31(b) and text below for details of spin state energetics. The differences between Fe and Cu are much greater than the

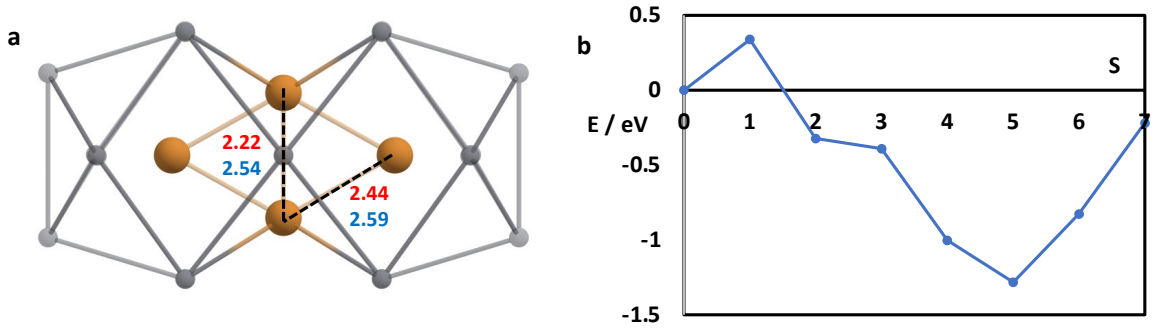



Figure 3.31: (a) M-M distances, in Å, in $[Fe_4Pb_{18}]^{4-}$ (red) and $[Cu_4Pb_{18}]^{4-}$ (blue). Bond lengths are shown for the $S = 5$ state of $[Fe_4Pb_{18}]^{4-}$. (b) Calculated relative energies of spin states of $[Fe_4Pb_{18}]^{4-}$ after geometry optimization.

differences seen in other pairs of compounds, such as $[M_2Ge_{16}]^{4-}$ and $[M_3Ge_{18}]^{4-}$, but nevertheless it is impossible to describe bonding character from internuclear distances alone as the cage strongly influences the preferred positions of the encapsulated atoms. The structural similarity of the $Pb_{18}$ cages in the two clusters suggests that the cages have the same electron counts, which in turn implies that the metals are in the same oxidation state. We therefore formally assign a $d^7$ $Fe^+$ state to all four iron atoms in $[Fe_4Pb_{18}]^{4-}$. An "all high-spin" configuration for the $Fe_4$ rhombus would have twelve unpaired electrons, *i.e.* $S = 6$, which could be viewed as coming from $[Cu_4Pb_{18}]^{4-}$

[2]Zhong-Ming Sun, *Private communication*

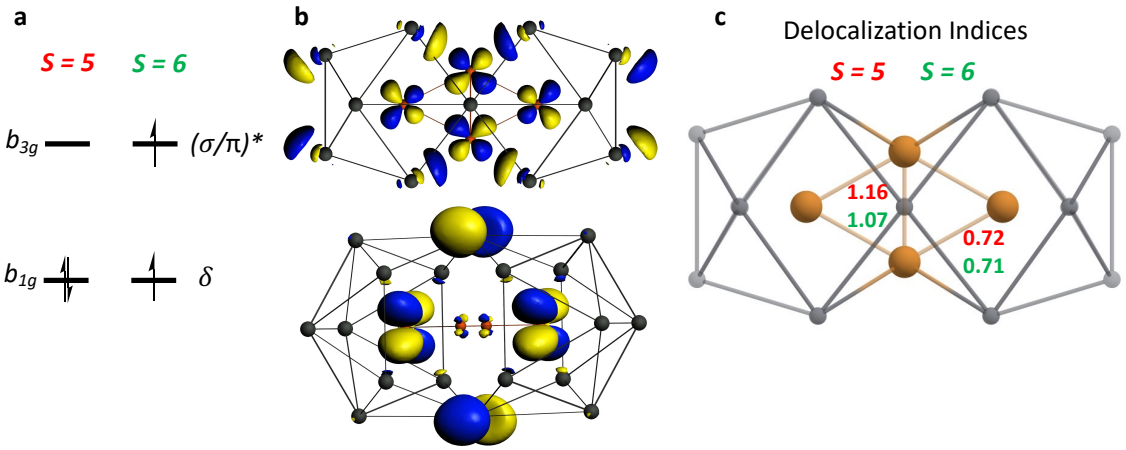



Figure 3.32: Fe-Fe interactions in $[Fe_4Pb_{18}]^{4-}$. (a,b) MOs whose occupancies differ in the $S = 5$ and $S = 6$ states, plotted with isovalue = 0.03. (c) Delocalization indices for nearest-neighbour Fe-Fe pairs, with values for $S = 5$ in red and $S = 6$ in green.

with all twelve electrons removed from the down-spin channel. Figure 3.31(b) shows the energies, relative to the singlet state, of $[Fe_4Pb_{18}]^{4-}$ optimized with all possible values from $S = 0 - 7$. The lowest energy spin state is in fact $S = 5$, with $S = 4, 6$ slightly higher, though we must be mindful here of the well-known errors in DFT when calculating spin state energies. In particular, GGA functionals like PBE tend to favour lower spin configurations than hybrid functionals[82]. We will compare the $S = 5$ and $S = 6$ states as the all-high-spin configuration is a more convenient reference point than the singlet, and is more chemically sensible as it is close to the ground state in energy and electronic character.

The reduction of $S$ by one unit means that two electrons have paired up, possibly in an Fe-Fe bonding orbital, suggesting the possibility of appreciable metal-metal bonding. To investigate this we have identified the MOs whose occupancies differ in the $S = 5$ and $S = 6$ states and plotted them in Figure 3.32. The MOs of particular interest here, shown in Figure 3.32(b), are the $b_{1g}$ $S = 5$ $\beta$-HOMO, which has $\delta$ symmetry but is localized on the "outer" Fe atoms and is therefore non-bonding, and the $b_{3g}$ $S = 5$ $\alpha$-LUMO, which is $\pi^*$ across the centre of the $Fe_4$ rhombus and $\sigma^*$ along the edges. The occupancies in Figure 3.32(a) show that reducing $S$ from 6 to 5 involves transferring an electron from the $b_{3g}$ antibonding orbital to the $b_{1g}$ non-bonding orbital, increasing bonding character in the $Fe_4$ rhombus and particularly across the central bond.

Figure 3.32 shows the Fe-Fe delocalization indices (DIs) for the $S = 5$ and $S = 6$ states of $[Fe_4Pb_{18}]^{4-}$. These *ab initio* bond indices are particularly valuable here

because evaluation of bond orders by inspection of the MOs is very challenging due to the large number of unpaired electrons, and they allow us to compare directly to the values for $[Cu_4Pb_{18}]^{4-}$ shown in Figure 3.30. The differences between DIs for the $S = 5$ and $S = 6$ states qualitatively match the MOs in Figure 3.32(b), with the central Fe-Fe DI increased by depopulation of the $\pi^*$ MO. The absolute increase of 0.09 is smaller than the formal value of 0.5 that we might expect from removing a $\pi^*$ electron in a simple picture of bond order, which can be attributed to the fact that the MOs are very delocalized, as is generally the case in these encapsulated clusters. Indeed, the small change in DI associated with changing MO occupancies suggests that the relatively large Fe-Fe DIs do indeed reflect substantial covalency, as do the differences between inequivalent Fe-Fe pairs. All Cu-Cu pairs in $[Cu_4Pb_{18}]^{4-}$ had a DI of 0.31, while the Fe-Fe DIs are around 1.1 for the central Fe-Fe pair and around 0.7 for the rhombus edges. This highlights two important differences between the metals; the DIs for iron are much larger, and show contrasting character between the central and edge bonds in the rhombus. We described $[Cu_4Pb_{18}]^{4-}$ as containing $d^{10}$ $Cu^+$ ions with no Cu-Cu bonds, so these differences seen for $[Fe_4Pb_{18}]^{4-}$ provide further evidence of Fe-Fe bonding.
As mentioned above, the large number of unpaired electrons renders direct inspection and interpretation of the MOs very difficult. To compare $[Fe_4Pb_{18}]^{4-}$ to $[Cu_4Pb_{18}]^{4-}$ directly we have plotted the atom-resolved DOS in Figure 3.33, using the $S = 5$ state for $[Fe_4Pb_{18}]^{4-}$.

The major difference between the two DOS plots is the strong spin-polarization in $[Fe_4Pb_{18}]^{4-}$, which leads to large $\beta$-spin peaks above the Fermi level, but other differences are also evident. The $\alpha$-spin $[Fe_4Pb_{18}]^{4-}$ curves show broader energy distributions than their $[Cu_4Pb_{18}]^{4-}$ counterparts, indicative of greater covalent bonding character, and the contributions from the inner and outer pairs of atoms in each $M_4$ rhombus are more different from each other for iron. These observations support our conclusion that the M-M interactions have a much more covalent nature in $[Fe_4Pb_{18}]^{4-}$ than in $[Cu_4Pb_{18}]^{4-}$.

#### 3.4.3.5 Larger gold clusters: $[Au_8Pb_{33}]^{6-}$ and $[Au_{12}Pb_{44}]^{8-}$

The most striking members of this cluster family are $[Au_8Pb_{33}]^{6-}$ and $[Au_{12}Pb_{44}]^{8-}$, particularly the latter for its highly symmetrical structure. The crystal structures from X-ray diffraction, measured by Cong-Cong Shu, are shown in Figure 3.34 These clusters are clearly composed of $[Au_2Pb_{11}]^{2-}$ icosahedral units, arranged in a tetrahedron in $[Au_{12}Pb_{44}]^{8-}$ and a rather unsymmetrical triangle in $[Au_8Pb_{33}]^{6-}$, but differ

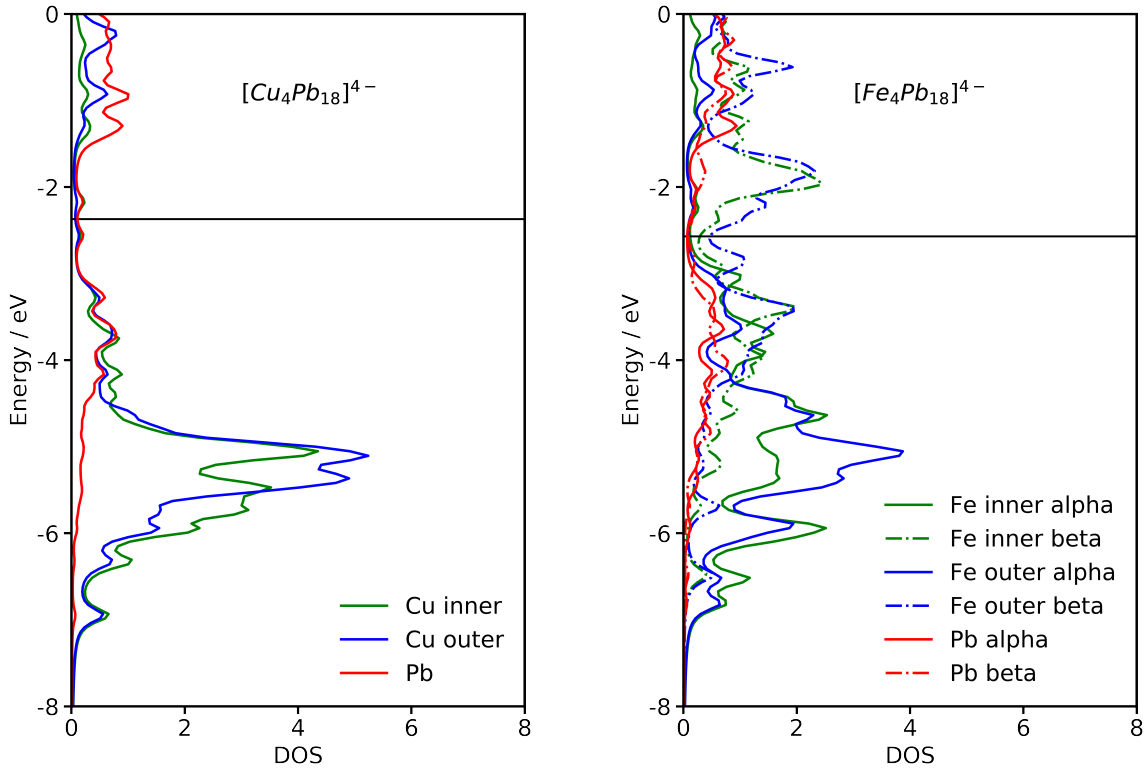



Figure 3.33: Atom-resolved DOS plots for $[Cu_4Pb_{18}]^{4-}$ and $[Fe_4Pb_{18}]^{4-}$ ($S = 5$ state) resolved to show contributions from symmetry-inequivalent Cu/Fe pairs and all Pb atoms, with a Lorenzian broadening of 0.1 eV.

from the smaller members of the series in that the icosahedra now surround small cores of Au atoms. The $Au_2$ core in $[Au_8Pb_{33}]^{6-}$ is a dimer perpendicular to the principal plane of the cluster, and the $Au_4$ core in $[Au_{12}Pb_{44}]^{8-}$ is approximately tetrahedral. While the largest cluster has a tetrahedral core, the Pb atoms in the icosahedra prevent it from possessing the full symmetry of the $T_d$ point group. Instead, our calculations describe it in the $D_{2d}$ point group as this is the highest possible symmetry for all the atoms.

We began our investigation with optimizations of both clusters. For $[Au_8Pb_{33}]^{6-}$ the optimization reproduced the essential features of the crystal structure, but the structure of $[Au_{12}Pb_{44}]^{8-}$ proved to be a more complex issue. The high symmetry raises the possibility of degenerate orbitals, so we optimized the structure in singlet and triplet states, finding the singlet to be lower energy by 0.41 eV. However, both structures differ significantly from the crystal structure in the Au core. The singlet optimization substantially elongated the Au-Au bonds parallel to the principal axis, and both optimizations led to large bond angle distortions which changed the shape

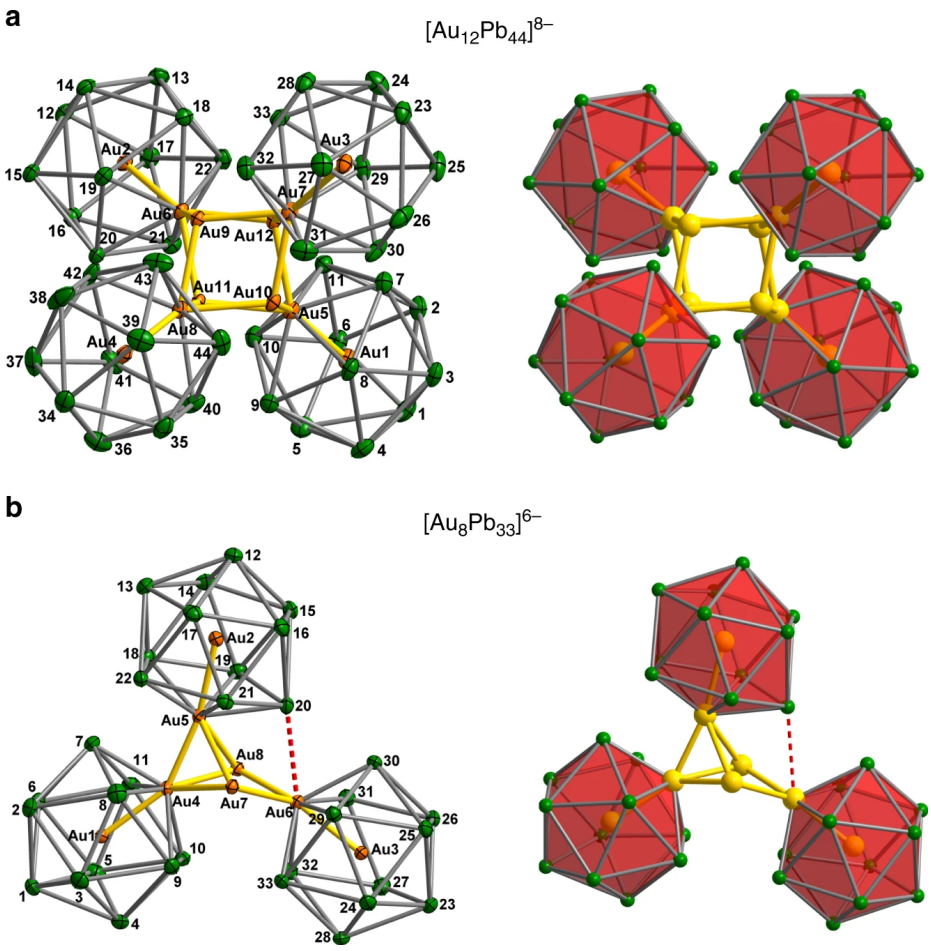



Figure 3.34: Structures of (a) $[Au_{12}Pb_{44}]^{8-}$ and (b) $[Au_8Pb_{33}]^{6-}$ in ball-and-stick and polyehdral representations. Diffraction measurements were performed by Cong-Cong Shu. Figure reproduced from ref.[34] under the Creative Commons license http://creativecommons.org/licenses/by/4.0/

of the cluster core. Concerned that the optimized structures did not reflect the important interactions in the real cluster, we generated a new structure by symmetrizing the crystal structure to $D_{2d}$, i.e. the $D_{2d}$ geometry with the smallest RMSD from the crystal structure. The Au atoms for all of these structures are shown in Figure 3.35. As well as the geometries of the gold cores, we compared these structures by

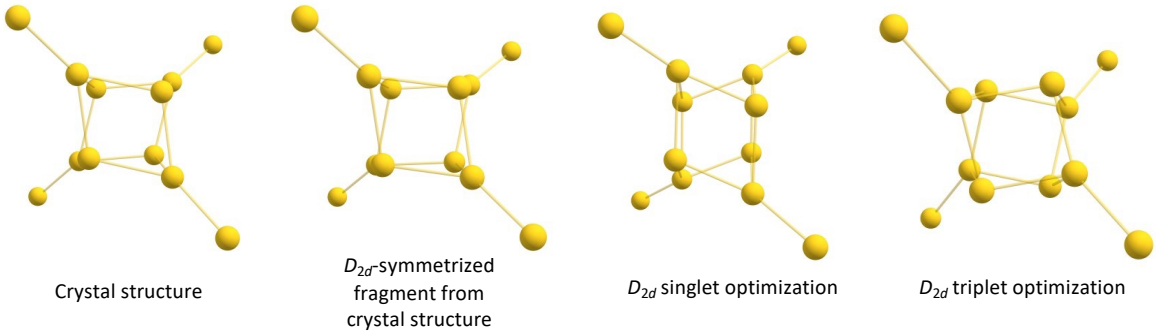



Figure 3.35: Geometries of structures considered for our investigation of $[Au_{12}Pb_{44}]^{8-}$ showing only the Au atoms for clarity.

considering certain Au-Pb bond lengths. Specifically, we tabulated the bond lengths from the Pb atoms in the $Pb_5$ icosahedral faces to the nearest Au atom in the core (i.e. not the Au atom in the $[Au_2Pb_{11}]^{2-}$ icosahedron), as these bond lengths reflect the frontier orbital interactions which we believe to be important in cluster formation as discussed above (e.g. Figure 3.28). We have compared all four structures by tabulating these bond lengths and plotting them in a histogram, shown in Figure 3.36. The data show that the crystal structure and the symmetrized crystal structure have similar and fairly narrow distributions of bond lengths, while the optimized structures have a far greater range of bond lengths and a significant number of bonds far shorter than any found in the crystal structure. On the basis of all this structural information, we proceeded to use the $D_{2d}$-symmetrized structure for the remainder of our investigation into $[Au_{12}Pb_{44}]^{8-}$ as it best reflects the experimental structure while having the interpretive advantages of high symmetry.

We can understand the oligomeric structures of $[Au_8Pb_{33}]^{6-}$ and $[Au_{12}Pb_{44}]^{8-}$ by extending our ideas of fragment assembly by HOMO-LUMO interactions, which we used above to explain the structure of $[Cu_4Pb_{22}]^{4-}$ as a dimer of $[M_2Pb_{11}]^{2-}$. To do this we must introduce a new fragment - $[Au_6Pb_{22}]^{4-}$, the structure of which is shown in Figure 3.37. It is formed by linking two $[M_2Pb_{11}]^{2-}$ icosahedra to a perpendicular $Au_2$ dimer, and may be formulated as $[Au_2(Au_2Pb_{22})_2]^{4-}$ accordingly. Examination

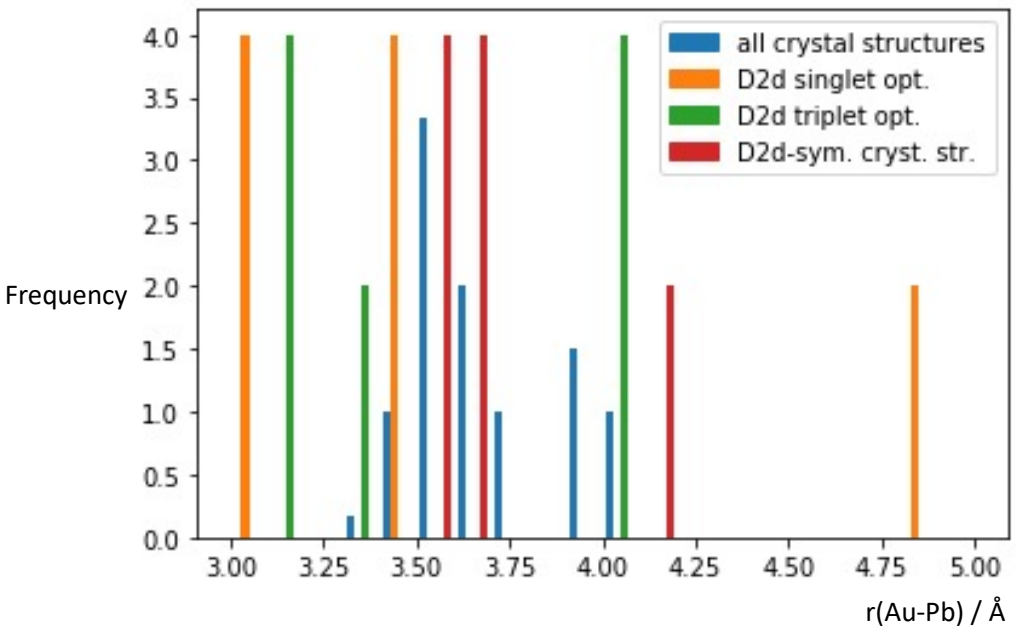



Figure 3.36: Normalized histogram of Au-Pb bond lengths for different geometries of $[Au_{12}Pb_{44}]^{8-}$, showing the sum of three available crystal structures in blue, the $D_{2d}$-symmetrized structure in red, the singlet opimization in orange and the triplet optimization in green.

of the structures of $[Au_8Pb_{33}]^{6-}$ and $[Au_{12}Pb_{44}]^{8-}$ reveals the presence of this fragment, in much the same geometry in both cases. $[Au_8Pb_{33}]^{6-}$ is formed by placing an $[Au_2Pb_{11}]^{2-}$ icosahedron above $[Au_6Pb_{22}]^{4-}$, in a non-linear "slipped" fashion analogous to the geometry of $[Cu_4Pb_{22}]^{4-}$ which leads to the apparently unsymmetrical geometry. Two $[Au_6Pb_{22}]^{4-}$ fragments appear in $[Au_{12}Pb_{44}]^{8-}$ as the upper and lower halves of the cluster, related by an $S_4$ improper rotation (a 90° rotation followed by inversion). Figure 3.37 also shows the frontier orbitals of $[Au_6Pb_{22}]^{4-}$, which we will examine as the frontier orbital shapes in $[M_2Pb_{11}]^{2-}$ have proven instrumental in understanding the cluster assembly pathways so far. The geometry for this MO calculation was generated by isolating the fragment from $[Au_8Pb_{33}]^{6-}$ and then symmetrizing it to $C_{2v}$ so as to minimize the RMSD between the symmetrized and original structures. Optimization of the geometry was not attempted as the structure is not a stable species on its own so optimization may change the structure significantly, reducing comparability to the clusters which we seek to understand.

The HOMO is a linear combination of $[M_2Pb_{11}]^{2-}$ HOMOs, with little character on the central Au atoms. More precisely, it is an out-of-phase combination so the "open face" of the cluster has the same $\pi$ donor character as the icosahedral fragment, but

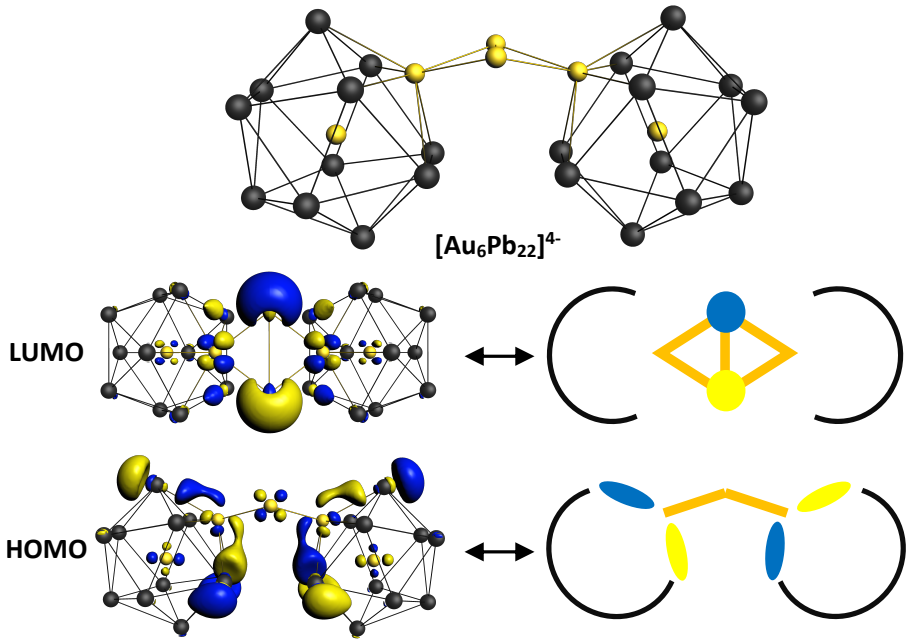



Figure 3.37: Optimized structure of the $[Au_6Pb_{22}]^{4-}$ molecular fragment and its frontier orbitals, shown as isosurfaces (isovalue = 0.03) and cartoon representations.

the lobes are further apart. The LUMO, by contrast, is located on the central Au atoms, clearly resembling the antibonding combination of Au 6*s* orbitals. This therefore gives the cluster $\pi$ acceptor character at its centre.
The dissection of $[Au_8Pb_{33}]^{6-}$ and $[Au_{12}Pb_{44}]^{8-}$ into fragments described above can be justified by examining the relevant frontier orbital interactions, which are shown in cartoon representations in Figure 3.38. In the dimerization to form $[Au_{12}Pb_{44}]^{8-}$, one $[Au_6Pb_{22}]^{4-}$ unit approaches another after a 90° rotation about the axis connecting them. This enables the Pb 6*p* $\pi$ donor HOMO of each to overlap with the Au 6*s* $\pi$ acceptor LUMO of the other, analogous to the dimerization mechanism of $[Cu_4Pb_{22}]^{4-}$. Similar orbital overlaps allow $[Au_6Pb_{22}]^{4-}$ to bond with $[Au_2Pb_{11}]^{2-}$. One lobe of the $\pi$ donor HOMO of $[Au_6Pb_{22}]^{4-}$ can donate into the Au 6*s* LUMO of the icosahedron, and the $\pi$ donor HOMO of the icosahedron can overlap with the $Au_2$ dimer LUMO. This process too has strong parallels with $[Cu_4Pb_{22}]^{4-}$ and results in a non-linearly bound $[Au_2Pb_{11}]^{2-}$. We have now explored the cluster assembly pathways connecting all the structures in Figure 3.21 and identified the electronic interactions between fragments which cause them to react as they do.

In Figure 3.30 we used delocalization indices (DIs) to show that two copper clusters, $[Cu_4Pb_{22}]^{4-}$ and $[Cu_4Pb_{18}]^{4-}$, have effectively identical Cu-Cu interactions despite having very different geometries. Here we will continue this method by calcu-

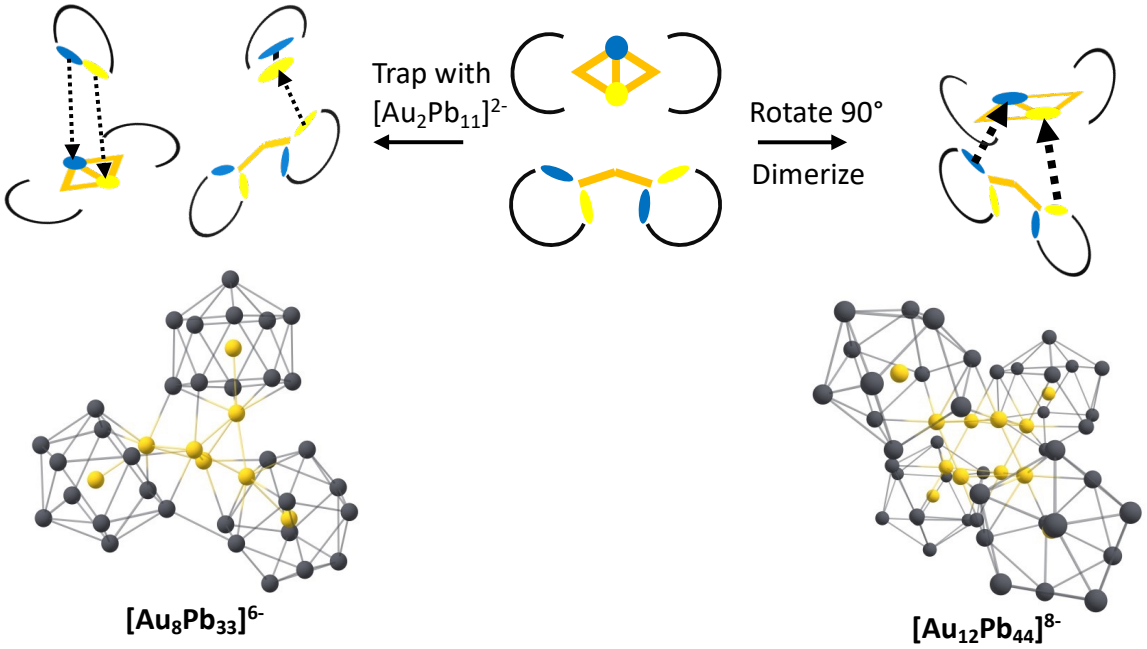



Figure 3.38: Fragment assembly pathways from $[Au_6Pb_{22}]^{4-}$ to $[Au_8Pb_{33}]^{6-}$ and $[Au_{12}Pb_{44}]^{8-}$ showing significant HOMO-LUMO interactions.

lating DIs for the Au-Au interactions in our gold clusters, shown for all symmetry-inequivalent pairs in Figure 3.39. In order to provide a direct comparison to previous results for $[Cu_4Pb_{22}]^{4-}$, in which all Cu-Cu pairs had DIs of 0.34, we begin with $[Au_4Pb_{22}]^{4-}$. As mentioned in the methods section, calculations on $[Au_4Pb_{22}]^{4-}$ in preceding sections were done with the PBE functional, for comparability to $[Cu_4Pb_{22}]^{4-}$, while calculations on the larger clusters described here were done with BP86. To confirm that this change of GGA does not influence our results we have compared the Au-Au DIs for $[Au_4Pb_{22}]^{4-}$ calculated using both methods and found that they deviate from each other by no more than 0.01. Following the recommendation in a report on gold thiolate clusters[22], the QTAIM properties of $[Au_{12}Pb_{44}]^{8-}$ were calculated with a QZ4P basis set, rather than TZP; however, our own subsequent tests showed that the difference in basis set changes the DIs by no more than 0.01. We are therefore confident that we can compare all sets of results and safely draw qualitative conclusions about the nature of bonding.

We can see in Figure 3.39 that, as in the Cu analogue, both Au-Au bonds in $[Au_4Pb_{22}]^{4-}$ have the same DI, suggesting the absence of localized Au-Au bonds, but the values are slightly higher at 0.46. This is not enough to suggest a significant change in our qualitative description of the Au-Au bonding interactions, particularly since the two species are formally isoelectronic, but it may reflect the closed-shell "aurophilic"

interactions often thought to be responsible for aggregation of large numbers of gold atoms into clusters. The larger clusters show a slightly greater range of values. The Au-Au bonds within $[Au_2Pb_{11}]^{2-}$ icosahedra have DIs of 0.43-0.44, very close to $[Au_4Pb_{22}]^{4-}$. In $[Au_8Pb_{33}]^{6-}$ the Au-Au bonds in the core have DIs in the range 0.31-0.59, clustered around the 'reference' value of 0.46. The low symmetry of this cluster makes it difficult to interpret individual values, but it is interesting to note that the DIs in the $Au_4$ rhombus in the $[Au_6Pb_{22}]^{4-}$ fragment span the rather narrower range 0.36-0.42, suggesting that our proposed partitioning of the cluster into $[Au_6Pb_{22}]^{4-}$ and $[Au_2Pb_{11}]^{2-}$ fragments is a fair reflection of its dominant bonding interactions. $[Au_{12}Pb_{44}]^{8-}$ contains four symmetry-inequivalent Au-Au contacts with non-negligible DIs (>0.1). Those within the $[Au_2Pb_{11}]^{2-}$ icosahedra have DIs of 0.43, as described above. The bonds connecting the icosahedra to the $Au_4$ core have DIs of 0.42, and the Au-Au bonds in the tetrahedral core have DIs of 0.13-0.18. As in $[Au_8Pb_{33}]^{6-}$, this indicates that the $[Au_6Pb_{22}]^{4-}$ fragment can still be recognised, and that partitioning $[Au_{12}Pb_{44}]^{8-}$ into two such fragments is justified by the topology of the electron density as well as the structural resemblance. None of these bond orders are substantially larger than those seen in the other Au clusters, and their even distribution between Au-Au pairs suggests strongly delocalized bonding. For a quantitative comparison of delocalized Au-Au bonding, which cannot be described directly by the two-centre DIs, we have divided the sum of the Au-Au DIs by the number of Au atoms in each cluster. These per-atom DIs are 0.35 ($[Au_4Pb_{22}]^{4-}$), 0.52 ($[Au_8Pb_{33}]^{6-}$) and 0.62 ($[Au_{12}Pb_{44}]^{8-}$), demonstrating a clear increase in the number of delocalized bonding electrons in the larger cores. We can conclude that as the $Au_n$ cores grow to larger sizes the nearest-neighbour Au-Au interactions do not change significantly, shown by the similar Au-Au DIs across the series, but the delocalized cluster bonding is significantly stronger in the larger clusters.

### 3.4.4 Summary and conclusions

In this section we have explored patterns connecting structure and bonding in a series of TM-encapsulating lead clusters of different sizes and shapes. We have analysed the energetics of hypothetical reactions describing cluster formation and used qualitative and quantitative analytical tools to understand the similarities and differences between the electronic structures of these clusters. This includes comparisons between the coinage metals - copper, silver, and gold - and a comparison between copper and iron in $[M_4Pb_{18}]^{4-}$ to study open and closed shells in a non-linear tetrameric cluster core.

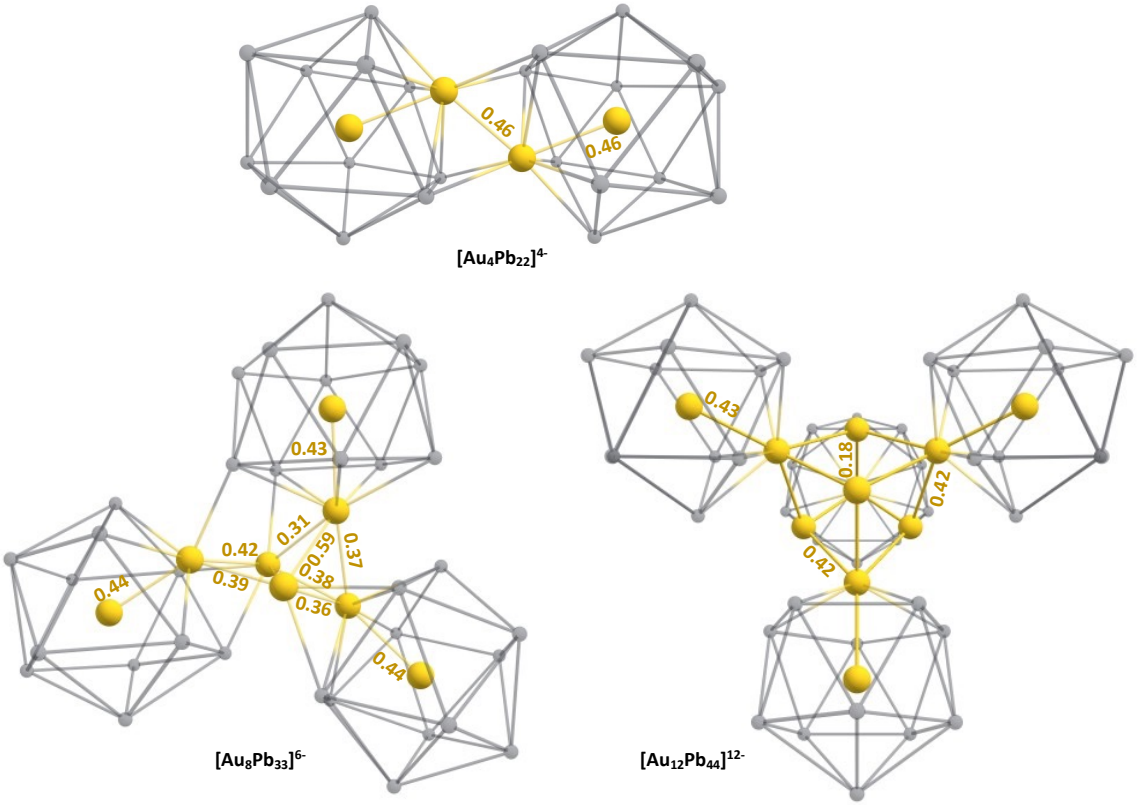



Figure 3.39: Au cores of $[Au_4Pb_{22}]^{4-}$, $[Au_8Pb_{33}]^{6-}$ and $[Au_{12}Pb_{44}]^{8-}$ with delocalization indices for all inequivalent Au-Au bonds.

We began by surveying the characterised clusters in the Cu-Ag-Au-Pb series, shown in Figure 3.21, of which all have been synthesized by the Sun group and most have been reported in the literature. By inspection of common structural features, notably $Pb_{11}$ icosahedra, we proposed a formation pathway linking the clusters together *via* assembly of shared intermediates, namely $[M_2Pb_{11}]^{2-}$ encapsulated icosahedra and $[M_6Pb_{22}]^{6-}$ dimers. Frontier orbital analysis of these fragments shows that they have the correct orbital symmetry properties to form all the observed clusters by straightforward HOMO-LUMO interactions. Energy calculations for some of these fragment association processes are consistent with the observed species formed by each metal, though the fundamental bonding interactions are equally applicable to all three metals so currently unknown analogues, such as $[(Ag/Au)_4Pb_{22}]^{4-}$, may yet be synthetically accessible. We have confirmed that the coinage metal cations behave as $d^{10}$ $M^+$ cations in all small (fewer than four metal atoms) clusters by inspection of molecular orbitals, delocalization indices and density of states. In $[Fe_4Pb_{18}]^{4-}$, an open-shell analogue of $[Cu_4Pb_{18}]^{4-}$, we examined the relationship between spin states, geometry, and metal-metal bonding. While $[Cu_4Pb_{18}]^{4-}$ contains only closed-

shell $Cu^+$ cations with no direct metal-metal bonding, $[Fe_4Pb_{18}]^{4-}$ contains strong Fe-Fe bonds, demonstrating that the structural similarity of the two $M_4$ cores is not an indicator of electronic similarity, due to the confining effect of the cage.
The larger AuPb clusters, $[Au_8Pb_{33}]^{6-}$ and $[Au_{12}Pb_{44}]^{8-}$, have been shown to possess more delocalized bonding than the smaller analogues. We suspect that this covalent effect acts alongside non-covalent "aurophilic" interactions to stabilize polynuclear gold cores, but further study of bonding in conventional thiolate-protected clusters is required to confirm that the two effects are separate. The presence of some Au atoms in the cluster core and others encapsulated by the $Pb_{11}$ icosahedra resembles the "divide and protect" concept in thiolate-protected clusters, particularly since a Zintl ion containing an empty $MPb_{11}$ icosahedron has been characterized[144]. However, these clusters do not follow the "magic number" series associated with the superatom model. They therefore bridge the gap between endohedral Zintl ions and thiolate-protected gold clusters.

## 3.5 Conclusions and outlook

This chapter sought to answer two questions at the forefront of research into encapsulated cluster chemistry:

1. Can we rationalize and predict the structures of endohedral clusters?
2. What are the electronic consequences of encapsulation of paramagnetic metal atoms?

To this end, we have studied a range of cluster families which possess common structural motifs, and which contain pairs of isostructural open-shell and closed-shell analogues. Two main themes have emerged from these investigations, closely related to the questions outlined above; the role of the endohedral metal in controlling cage architecture, and metal-metal bonding between enapsulated paramagnetic centres. Most Zintl clusters containing a transition metal atom are well described as "closed-shell metal, closed-shell cage", where the metal has a $d^{10}$ electron configuration and the cage has the number of electrons needed by Wade's rules for its deltahedral structure. A simple interpretation of the electronic structure of such clusters is that the metal-cage interaction is closed-shell in nature rather than covalent. This model explains the fact that many group 14 Zintl ions can encapsulate TMs without changing their structures, and predicts that any clusters containing multiple metal atoms will have no metal-metal bonds. Some of the clusters described in this chapter fit this description, namely the family of coinage metal clusters in which $Pb_{11}{}^{4-}$ cages encapsulate $d^{10}$ $M^+$ cations, and $[(Ni@Sn_9)In(Ni@Sn_9)]^{5-}$, in which two $[(Ni@Sn_9)]^{4-}$ fragments are bound electrostatically to $In^{3+}$ in multiple isomeric forms. These electrostatically bound clusters, somewhat unusual since many $d^{10}$ metal atoms are neutral or anionic, offer structural flexibility owing to the simple, non-directional nature of the Coulomb. This flexibility manifests as isomerism in $[(Ni@Sn_9)In(Ni@Sn_9)]^{5-}$, and leads to structures in the Cu-Ag-Au-Pb series with different oligomerization states and M:Pb ratios. The structures of these oligomers can be understood by frontier orbital theory, which suggests that a purely electrostatic bonding model for these clusters is insufficient, and we have been able to devise and justify a formation pathway for the full cluster family based on intermediate fragments which have not been isolated but can be seen as part of the structures. The size of the metal atom, while often overlooked, may also control the structure of the cage beyond simple polyhedral distortions. The balance between $[M_4Pb_{18}]^{4-}$ and $[M_4Pb_{22}]^{4-}$ (M = Cu, Ag, Au) appears to be controlled by the size of the cation, with Cu showing a stronger

preference for the smaller cage, and size may also be a factor in determining the preferred oligomerization states of each metal in the $[M_x(M_2Pb_{11})_y]^{q-}$ series, along with relativistic electronic effects. These relationships are shown schematically in Figure 3.40.

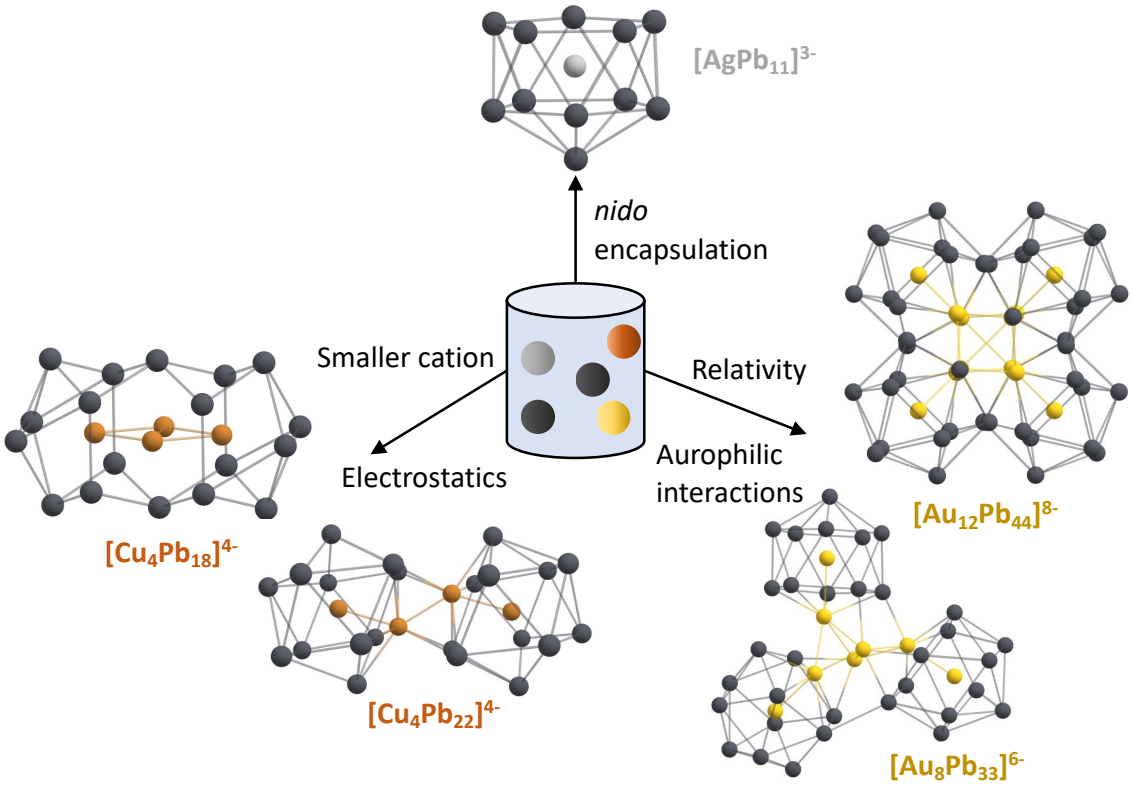



Figure 3.40: Chemical factors influencing the structural preferences of coinage metals.

Cage geometry and connectivity can also be controlled electronically, and we have explored this in two distinct mechanisms. The most intuitive way to influence structure electronically is to change the populations of bonding and antibonding orbitals, resulting in the formation or breakage of bonds in the cage. We saw this in operation when comparing $[(Ni@Sn_9)In(Ni@Sn_9)]^{5-}$ to $[(Ni@Ge_9)Ni(Ni@Ge_9)]^{4-}$ where the reduction in the total valence electron count of the cluster leads to a change in the bonding between the two halves of the cluster across the central metal, as well as a change to metal-metal bonding. A more unusual example of electronic control was investigated in $[M@Ge_{10}]^{3-}$ and $[M_2Ge_{16}]^{4-}$ which have three-connected, rather than deltahedral, structures. We have shown that this is a result of metal-cage covalency, whereby the mid-row metals with high-energy *d* orbitals can transfer electron density to the Ge cages such that the cages become sufficiently electron-rich to move

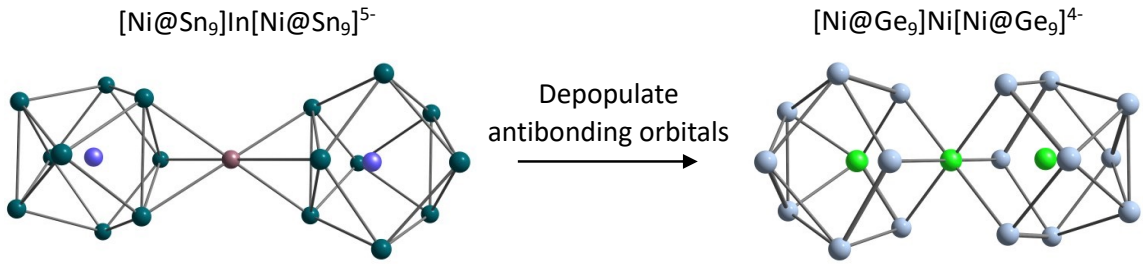



Figure 3.41: Electronic and structural relationship between $[(Ni@Sn_9)In(Ni@Sn_9)]^{5-}$ and $[(Ni@Ge_9)Ni(Ni@Ge_9)]^{4-}$.

from the electron-deficient deltahedral bonding paradigm to that of electron-precise clusters with two-centre two-electron bonds. In the iron analogues, this effect is accentuated by polarization of the density by unpaired electrons localized on iron. We have investigated a number of mechanisms by which encapsulated atoms may control cage geometry, which may act simultaneously, and we hope that this will help to guide design of clusters with particular geometries in the future.

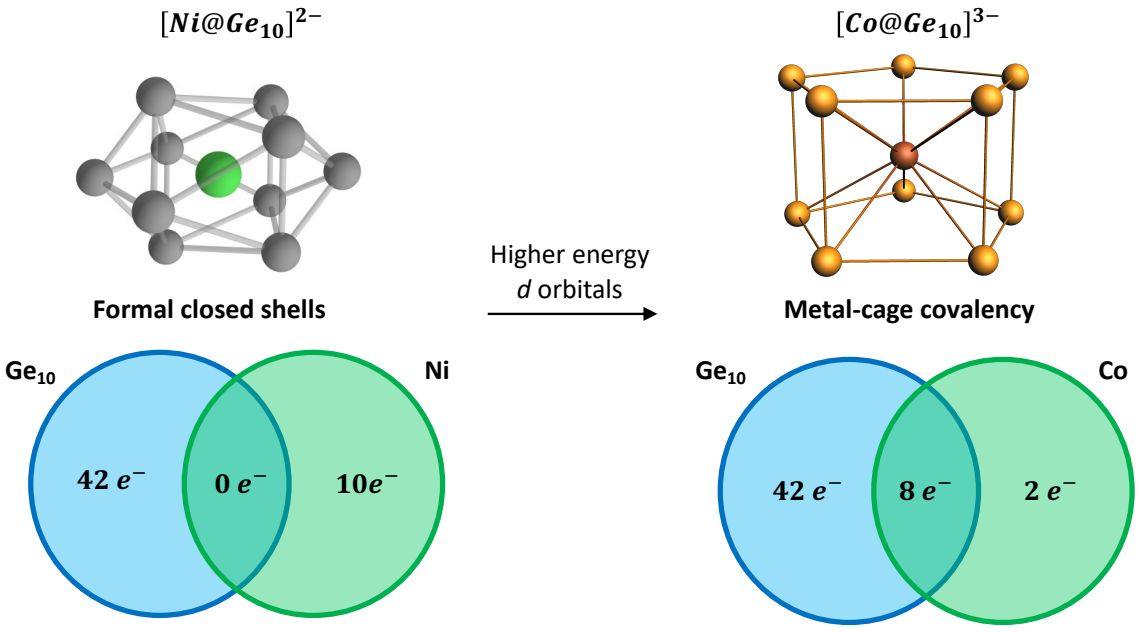



Figure 3.42: Comparison of the structures and jigsaw electron counts of $[Ni@Ge_{10}]^{2-}$ and $[Co@Ge_{10}]^{3-}$.

The second major theme running through this chapter has been the bonding in Zintl ions containing paramagnetic metal centres, as these unquestionably lie outside the "closed-shell metal, closed-shell cage" model. Nevertheless, the open-shell clusters which we have studied have all been isostructural to a closed-shell species, allow-

ing us to make informative comparisons between the two. All the open-shell species considered here have been Fe-encapsulating, but their closed-shell counterparts have contained Co, Ni and Cu, which shows that these clusters can be stable with respect to large changes in valence electron count, and which gives us great hope that more open-shell analogues of known clusters can be synthesized in the near future. The presence of paramagnetic centres can have a number of consequences for the bonding character and properties of the clusters. The most obvious is that they may have a large number of unpaired electrons, as high as ten in $[Fe_4Pb_{18}]^{4-}$, as they have all been predicted to have high-spin ground states due to strong correlation in the Fe 3*d* orbitals. As discussed above, these unpaired electrons can indirectly influence cage bonding by polarizing the remaining electrons, which partly drives the preference for three-connected structures of $[M@Ge_{10}]^{3-}$ and $[M_2Ge_{16}]^{4-}$. In $[Fe_2Ge_{16}]^{4-}$ and $[Fe_4Pb_{18}]^{4-}$ we saw metal-metal bonds form where there were none in the analogous closed-shell clusters, but in $[Fe_3Sn_{18}]^{4-}$ the singly occupied orbitals formed a $\pi$ manifold with no net bonding character so the metal-metal bonding was the same as in $[Ni_3Ge_{18}]^{4-}$. It is presently unclear whether this contrast represents a systematic difference related to electron count, dimensionality, or another aspect of the polynuclear metal cores. This question may be resolved by studying more clusters in this expanding class.

We may also survey the theoretical methods by which we have studied clusters with complex bonding properties. The principal method in our work is DFT, as is commonly the case in current computational chemistry. This is partly due to its low computational cost and applicability to a broad range of chemical systems, but also because it offers a great deal in terms of analysis. In this respect we have used the standard approaches of energetic calculations and MO diagrams, but we have also used more specialized tools including topological information and density of states, which allow us to draw broader comparisons between chemically distinct systems. We have made extensive use of electron counting methods, starting with Wade's rules to rationalize deltahedral structures, and then extending electron counting into three-connected structures with the jigsaw model, providing a new way of rationalizing structures which present a challenge to previous philosophies of electron counting. DFT is, at times, found to be insufficiently accurate in its description of strongly correlated systems such as open-shell transition metal species, so we have demonstrated the value of GASSCF when studying high-symmetry clusters with polyatomic cores which are too large for conventional CASSCF calculations. Perhaps most importantly, we have used these methods in parallel, allowing each to provide a complementary

perspective on a complex chemical problem and ultimately gaining deeper insight than would be possible by any single method.

These two themes may be combined by future research in this area. Our model for fragment-driven lead cluster formation may enable us to design ever-larger clusters encapsulating cores of controllable size and geometry. It may then be possible to predict the properties of analogous structures containing paramagnetic metal atoms. For example, an analogue of $[Au_{12}Pb_{44}]^{8-}$ containing iron atoms would bear a clear resemblence to the $Fe_4S_4$ ferredoxin clusters found in a variety of enzymes, so this cluster design approach could provide a route to transition metal clusters of novel compositions and nuclearities, as indicated in Figure 3.43. Open-shell Zintl clusters are very few in number at present, so in order to understand trends in properties with structure and composition we will need to identify and investigate more examples. This will enable development of a more informed design process for clusters with target properties. Promising directions for Zintl ion research include catalysis and single-molecule magnetism, both of which will require the detailed understanding of their bonding character which we have begun to develop in these investigations.

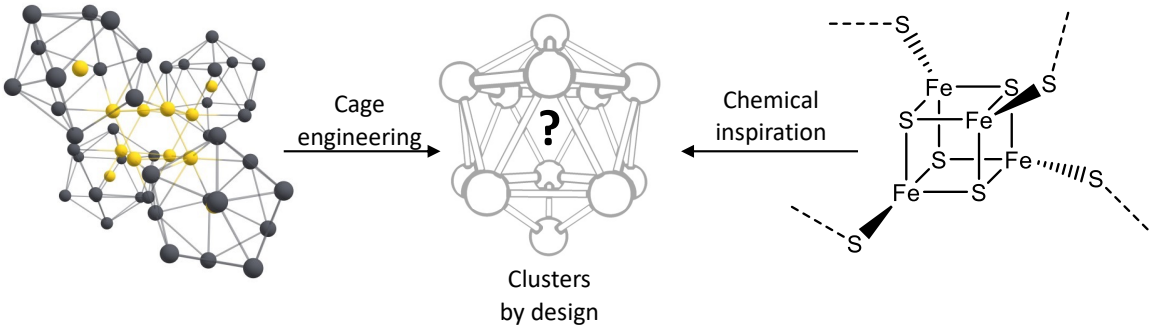



Figure 3.43: A proposed approach to functional cluster design.

# Chapter 4

# Structural processes in Ruddlesden-Popper oxyhydrides

## 4.1 Introduction to oxyhydrides

This chapter describes two investigations into physical properties and transitions in mixed-anion perovskites. The compounds of interest have the Ruddlesden-Popper structure, a perovskite derivative in which the octahedral building blocks are assembled into two-dimensional layers rather than the three-dimensional structure of ordinary perovskites, and are oxyhydrides, formed by replacing some oxide anions by hydrides. In the first part we will examine the structural details of a pressure-induced crystallographic phase transition and its consequences for bonding and conductivity. We will contrast two oxyhydrides which differ by their transition metal ion $d$ electron counts to see how this affects their ambient- and elevated-pressure behaviour. In the second part we will explore hydride conductivity in oxyhydrides containing only closed-shell cations, understanding the roles of different defects and the effect of anion disorder, pressure, and cation substitution, culminating in the prediction of a new material. The first project has been published in *Inorganic Chemistry*[145] and the second in *Chemistry of Materials*[146].

The hydride anion has intrigued chemists for decades, with its unique bonding properties and its role in industrial applications. With a $1s^2$ configuration and spherical symmetry it is the simplest ligand in all chemistry, excluding the elusive electride, but these properties lead to a vast range of accessible structures and bonding modes. Alkali metal hydrides were first synthesized in the early 19th century, but not comprehensively identified for some decades[147]. Two simple examples of this class, NaH and $BaH_2$, are shown in Figure 4.1. These ionic materials are highly reactive and are used as strong bases in organic chemistry and as reducing agents in solid state

synthesis due to the thermodynamic driving forces of formation of hydrogen gas and water.

The earliest molecular hydride complexes were $H_2Fe(CO)_4$[148] and $HCo(CO)_4$[149] (shown in Figure 4.1), discovered by Hieber et al. in the 1930s, but the field only began to burgeon in the 1950s with developments in organometallic hydrides such as Wilkinsons $Cp_2ReH$[150]. The "hydride" character was identified by strongly negative proton NMR shifts, from 0 to -30 ppm, and IR stretches in the region of 1700-2300 $cm^{-1}$, weaker than E-H stretches in organic molecules.

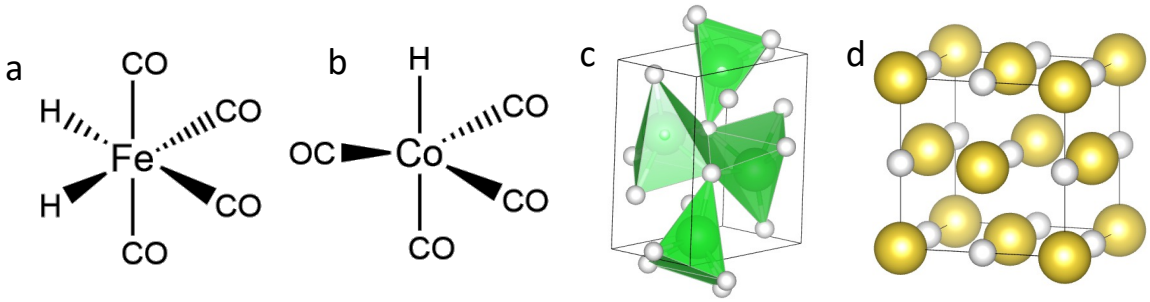



Figure 4.1: Early molecular and crystalline hydride compounds (a) $H_2Fe(CO)_4$ (b) $HCo(CO)_4$ (c) $BaH_2$ (d) NaH. Ba shown in green, Na in yellow and H in white.

Transition metal oxyhydride chemistry was born in 2002 with the synthesis of $LaSrCoO_3H_{0.7}$ by Hayward et al.[151], the first instance of incorporation of the hydride anion into a transition metal oxide lattice. The synthesis was achieved by a "soft chemistry" approach of reducing the Ruddlesden-Popper (RP) oxide $LaSrCoO_4$ with NaH at modest temperatures, demonstrating the remarkable ability of perovskite frameworks to tolerate changes in composition. Antiferromagnetic ordering is maintained at 350 K, indicating very strong coupling between metal centres thanks to good overlap with H 1*s* orbitals. Oxyhydrides have now been synthesized in a number of structure types, mostly in the perovskite family. Examples of cubic perovskites, with $ABO_{3-x}H_x$ compositions, include $MTiO_3$ (M=Ca, Sr, Ba, Eu) and $SrVO_2H$ (Figure 4.2(a, b)), while layered Ruddlesden-Popper derivatives include $La_2LiHO_3$[152], $Sr_2VO_3H$ (both $n = 1$ phases) (Figure 4.2(c, d)) and $Sr_3V_2O_5H_2$ ($n = 2$)[153]. The Ruddlesden-Popper structure is described in Figure 4.3, where $n$ is the number of octahedra in the perovskite layer.

Anion ordering in these compounds is finely balanced, with small changes to the cations able to dramatically alter the anion distribution. Hydride intercalation of $SrVO_3$ gives $SrVO_2H$[153], with hydrides ordered in layers such that every V centre

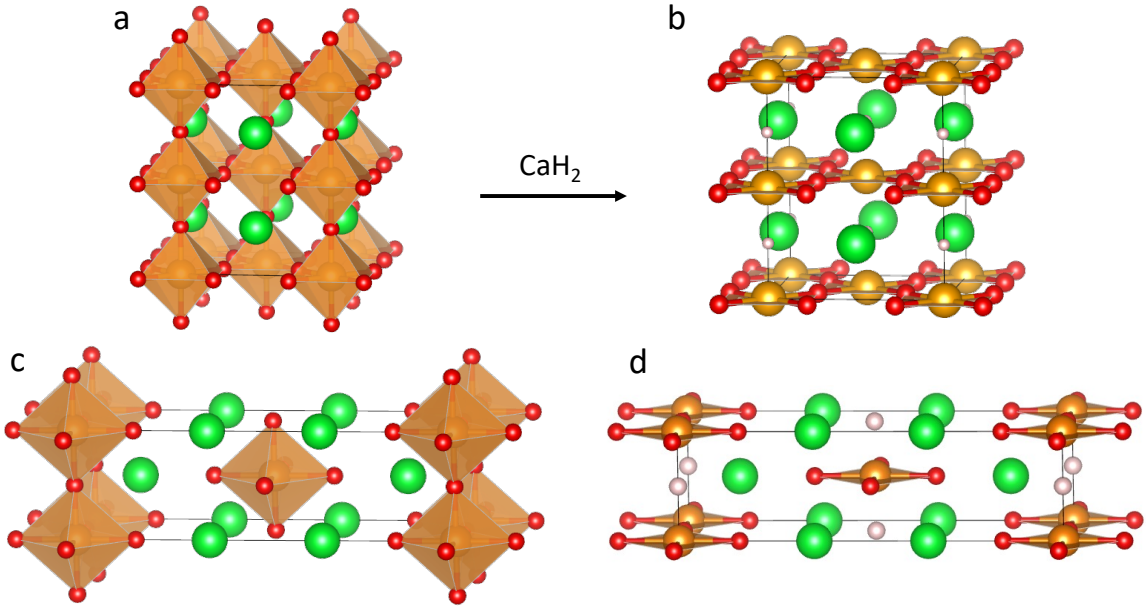



Figure 4.2: Synthesis of vanadium oxyhydrides. (a) Parent cubic perovskite $SrVO_3$. (b) Layered oxyhydride $SrVO_2H$. (c) $n = 1$ Ruddlesden-Popper oxide $Sr_2VO_4$. (d) Ruddlesden-Popper oxyhydride $Sr_2VO_3H$. Green spheres represent strontium, orange vanadium, red oxygen, and white hydrogen.

has two mutually trans hydride ligands, remarkable in itself since the strong $\sigma$ donation by the hydrides generally disfavours a mutually trans arrangement. The analogous starting material doped with 5% Ti, however, reacts to give $SrV_{0.95}Ti_{0.05}O_{1.5}H_{1.5}$, with hydrides and oxides disordered over all anion sites[154]. The different behaviour of these apparently similar phases arises because the stability of layered ordering is a unique feature of a $d^2$ configuration at the TM centre. Ruddlesden-Popper-type oxyhydrides are further complicated by the presence of two distinct anion sites, one contained in the "perovskite" layer and one in the "rock salt" layer, as shown in Figure 4.3. The distribution of anions over these sites is simply dictated by the electrostatic principle that the most charged anion will preferentially coordinate to the most charged cation. If the A cation, in the rock salt layer, bears a higher charge than the B cation, as in $La_2LiHO_3$, then the hydrides will coordinate to the B cation and lie in the perovskite layer, while if the reverse is true, as in $Ba_2ScHO_3$, then the hydrides will occupy the rock salt layer positions[155]. In the latter compound, hydrides and oxides are disordered over the rock salt sites in a 1:1 ratio; substitution of a larger cation on the B site to give $Ba_2YHO_3$ induces ordering whereby one rock salt layer is fully occupied by hydrides and the next by oxides[156]. The consequences of anion ordering for ionic conductivity will be discussed in more depth below. Structure-

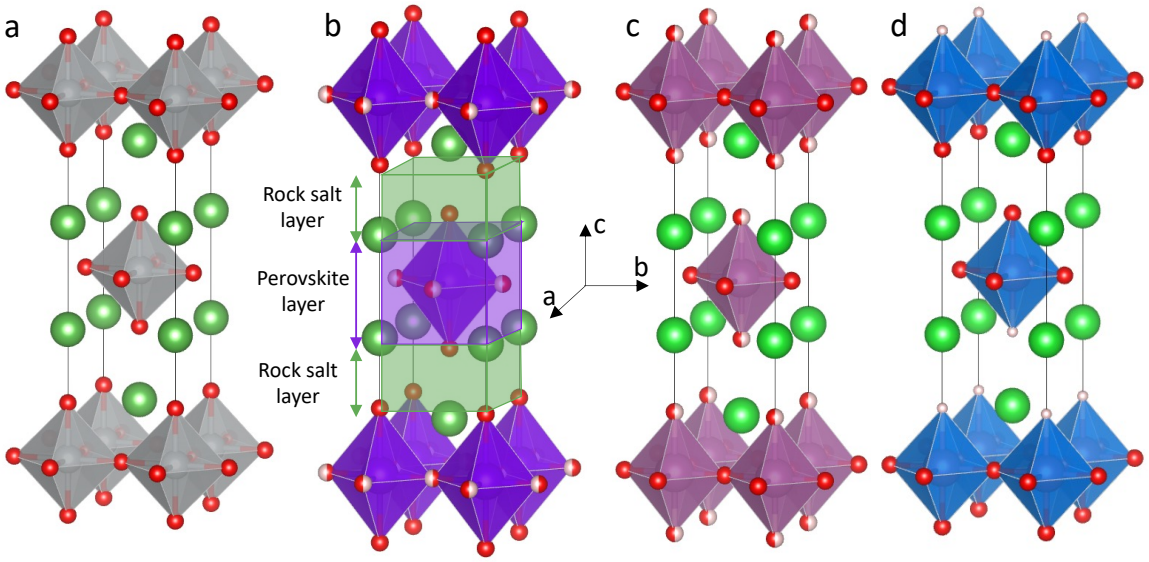



Figure 4.3: Ion-conducting $n = 1$ Ruddlesden-Popper phases displaying different oxide-hydride orderings. (a) $La_2NiO_4$ (b) $La_2LiHO_3$ (c) $Ba_2ScHO_3$ (d) $Ba_2YHO_3$. Light green spheres represent barium, dark green lanthanum, grey nickel, purple lithium, lilac scandium, blue yttrium, red oxygen, and white hydrogen. Mixed red/white spheres indicate oxide/hydride disorder. The set of axes refers to cells (b)-(d).

property relationships in solids can be probed in high-pressure experiments as we can tuneably modify lattice parameters without chemical modification. The changes to structure and bonding in $SrVO_2H$ under pressure demonstrate that hydrides are roughly twice as compressible as oxides[157] consistent with observations on several compounds so compression of the unit cell is strongly anisotropic, with much more significant shortening of the V-H bonds. However, V(III) has only $\pi$-symmetry $d$ orbitals which have no overlap with the $\sigma$-only hydride ligands, which greatly influences the dispersion of the d bands and controls an insulator-metal transition.

Ruddlesden-Popper phases undergo a high-pressure crystallographic phase transition, called the $B1-B2$ transition, in which the perovskite layers shift to change the interlayer spacing from rock salt ordering to CsCl ordering[158]. The associated transition pressure has been measured for a range of compounds and related to the identities of the cations. In the first project in this chapter, we investigated the effect of dimensionality and the $B1-B2$ transition on the possibility of a metal-insulator transition in $Sr_2VO_3H$ and $Sr_3V_2O_5H_2$. These compounds are, respectively, the $n = 1$ and $n = 2$ Ruddlesden-Popper analogues of the cubic perovskite $SrVO_2H$, which could be seen as the n=infinity member of the series. The project was a collaboration with the Hayward group, in Oxford, who synthesized samples of both compounds, and the

Kageyama group, in Kyoto, who performed high-pressure diffraction and resistivity measurements.

Perovskite oxyhydrides have emerged as an important family of hydride ion conductors following the synthesis of the $La_{2-x-y}Sr_{x+y}LiH_{1-x+y}O_{3-y}$ series by Kobayashi[152]. As discussed above and shown in Figure 4.3(b), these phases preferentially place the hydride anions in the perovskite layer, as do phases containing $d^n$ transition metal cations such as $LaSrCoO_3H_{0.7}$ and $Sr_2VO_3H$. Bai et al.[159] have investigated hydride diffusion in the $La_{2-x-y}Sr_{x+y}LiH_{1-x+y}O_{3-y}$ family using ab initio molecular dynamics (AIMD), finding that vacancies played a key role in diffusion of $H^-$ in the perovskite layer. Additionally, Fjellvåg et al.[160] have studied the $La_2LiHO_3$ member of that series and found hydride mobility within the perovskite layer to be more facile than in the rock salt layer, which they link to La-O covalency, and that vacancies promote hydride diffusion[161].

In 2019 Takeiri et al.[155] reported the high-pressure synthesis of $Ba_2ScHO_3$ and observed hydride conduction at 300 °C. This compound also adopts the $n = 1$ RP structure but differs from previous examples in that the hydrides are distributed over the "apical" points of the octahedra and so reside in the rock salt layer (Figure 4.3(c)), for the electrostatic reasons described above. Placing the mobile hydrides on these sites may enable hydride conduction through the rock salt layer, perhaps via interstitial sites inaccessible in other hydride conductors, a phenomenon observed by neutron diffraction in certain oxide conductors[162, 163] but unknown in perovskite oxyhydrides.

In a 2019 preprint[164], Kuwubara et al. used density functional theory (DFT) to calculate the formation energies of various point defects in $Ba_2ScHO_3$ and investigate their mobilities. Their findings indicate that vacancy and interstitial hydride defects form more readily than the corresponding oxide defects and that the ionic conductivity arises from these hydride defects.

Following completion of the work presented here, Nawaz et al. reported the synthesis and characterization of $Ba_2YHO_3$[156], isostructural to $Ba_2ScHO_3$ except that the anions are ordered into alternating all-hydride and all-oxide rock salt layers. This is due to the mismatch in radii between A and B cations, which commonly leads to octahedral tilting but can instead lead to symmetry-lowering anion ordering in polyanionic systems (Figure 4.3(d)). $Ba_2YHO_3$ has approximately five times higher ionic conductivity over $Ba_2ScHO_3$ but a slightly higher activation energy, suggesting that the increased conductivity arises from the number of labile hydrides in the rock salt layer rather than a change in mechanism.

Here we employ DFT to identify the most important mechanisms of hydride conduction in $Ba_2ScHO_3$ by a combined computational approach employing both AIMD simulations and static calculations of transition state energies. AIMD simulations were performed by Harry J. Stroud at the University of Bristol, under the supervision of Prof. Neil L. Allan. Transition state geometries are analysed and trends understood in terms of crystal engineering. We also explore the effects of anion ordering, pressure, and cation substitution on anion transport in order to provide new testable predictions to guide future synthetic searches and device design involving anion conductors.

## 4.2 High-pressure phase transitions in oxyhydrides

### 4.2.1 Methods

Calculations were performed using VASP version 5.4.1[165]. PAW pseudopotentials and the PBE exchange-correlation functional were used[166, 5], with a plane-wave energy cut-off of 600 eV. The Brillouin zone was sampled with k-point grids of $7 \times 7 \times 3$ for $Sr_2VO_3H$, $7 \times 7 \times 2$ for $Sr_3V_2O_5H_2$, and $7 \times 7 \times 1$ for $Ba_2YHO_3$. A Hubbard $U$ correction of 2 eV was applied to the vanadium $3d$ orbitals, consistent with our previous study on the closely related infinite-layer phase $SrVO_2H$[157]. All calculations on vanadium oxyhydrides were done using a $\sqrt{2} \times \sqrt{2} \times 1$ expansion of the crystallographic unit cell, and G-type anti-ferromagnetism was imposed in the starting guess at all pressures. A spin-restricted ansatz was used for calculations on $Ba_2YHO_3$. In all cases the resulting converged density retains the alternating spin polarization characteristic of this G-type arrangement. Calculations on the binary oxides MO, M = Ca, Sr and Ba were performed using the cubic crystallographic unit cells (for both $B1$ and $B2$ forms), a plane-wave cutoff of 600 eV and an $8 \times 8 \times 8$ grid for the sampling of the first Brillouin zone. In analysing the electronic structure of the vanadium phases, we find it useful to define a hypothetical state where there is no polarization of the spin density: this is achieved simply by using a spin-restricted ansatz.
Enthalpies in VASP are calculated by adding the SCF electronic energy and the product of the volume of the cell and the applied external pressure, according to the standard equation:

$$H = E + PV$$

### 4.2.2 $B1 - B2$ transitions in binary oxides

In order to validate our method for investigating high-pressure phase transitions, we explored the $B1 - B2$ transition in the oxides MO (M = Ca, Sr, Ba), which adopt the 6-coordinate rock salt structure under ambient conditions but change to the 8-coordinate CsCl structure above a critical pressure. In recent decades this transition has been studied extensively in many ionic materials, as has the more complex series of phase transitions observed for BaO. A range of theoretical approaches have been employed to investigate thermodynamic and mechanistic aspects[167] including atomistic potentials, Hartree-Fock (HF) theory and, most significantly, Density Functional Theory (DFT). LDA functionals are found to reliably underestimate unit cell volumes while GGA functionals tend to overestimate them, with some GGAs providing better fits to experimental results than others. Including some HF exchange in the functional, i.e. use of a hybrid, can provide good agreement with experiment by careful tuning of the amount of exact exchange for a particular compound, but this approach does not appear to offer a systematic improvement to predictions of phase transition pressures for ionic materials[168]. The PBE functional, a pure GGA widely used in solid state DFT, appears to give good results for oxides in a range of structures[169].
To estimate $B1 - B2$ transition pressures we calculated the enthalpy difference between the rock salt and CsCl structures of each compound:

$$H = E + PV$$

It is necessary to use enthalpy rather than energy here to quantitatively account for the thermodynamic preference for smaller unit cells at high pressure.
The results are plotted in Figure 4.4, where the transition pressure is given by the point on each line where the enthalpy difference is zero. The values are summarized in table 4.1 along with experimental results; we find that our predictions fit closely to the measured values, slightly overestimated in line with the general behaviour of GGA functionals. No experimental measurement is available for Ba because it undergoes a series of intermediate phase transitions before adopting the $B2$ structure.

The trend in critical pressures can be interpreted in terms of the ionic model. As discussed above, this model predicts a preference for higher coordination numbers for systems with large cation:anion radius ratios and systems under pressure. We observe that the oxides of larger metal cations undergo the $B1 - B2$ transition at lower pressures, which supports the idea that larger cations have a preference for 8-coordination

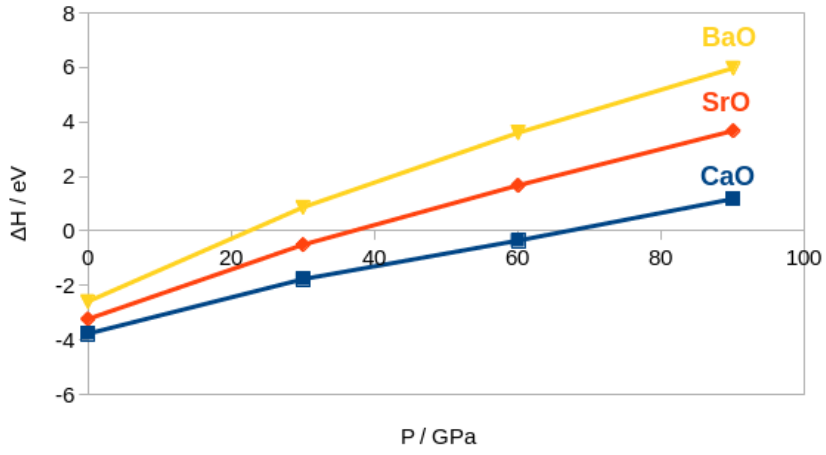



Figure 4.4: Computed enthalpy differences between rock salt and CsCl structures as a function of pressure for alkaline earth oxides. A negative value indicates a preference for the rock salt structure, and the predicted transition pressure for each compound is given by the $x$ intercept.

| Compound | Predicted / GPa | Experiment / GPa |
|---|---|---|
| CaO | 68 | 64[170] |
| SrO | 39 | 36[171] |
| BaO | 22 | - |

Table 4.1: Predicted and experimental $B1-B2$ transition pressures. An experimental value for BaO is unavailable because this compound does not undergo a direct $B1-B2$ transition.

over 6-coordination. The close agreement between calculated and experimental results validates our approach to high-pressure crystallographic phase transitions, so we proceed to study the more complex processes in Ruddlesden-Popper oxyhydrides.

### 4.2.3 Structural changes in vanadium oxyhydrides under pressure

X-ray diffraction shows that $Sr_2VO_3H$ and $Sr_3V_2O_5H_2$ undergo a pressure-induced structural change from an orthorhombic $I$-centered to an orthorhombic $A$-centered lattice in which alternating octahedral chains (ladders) shift halfway along the $b$ axis, from (1/2, 1/2, 1/2) at low pressure to (1/2, 0, 1/2) at high pressure, illustrated in Figure 4.5. Very similar pressure-induced transitions have been observed in the rock-salt inter-growth phases $A_2BO_3$ (A = Sr, Ca, B = Cu, Pd)[158] and $Sr_3Fe_2O_5$[172]. The measured critical transition pressures $P_s$ (the point where the volume fractions

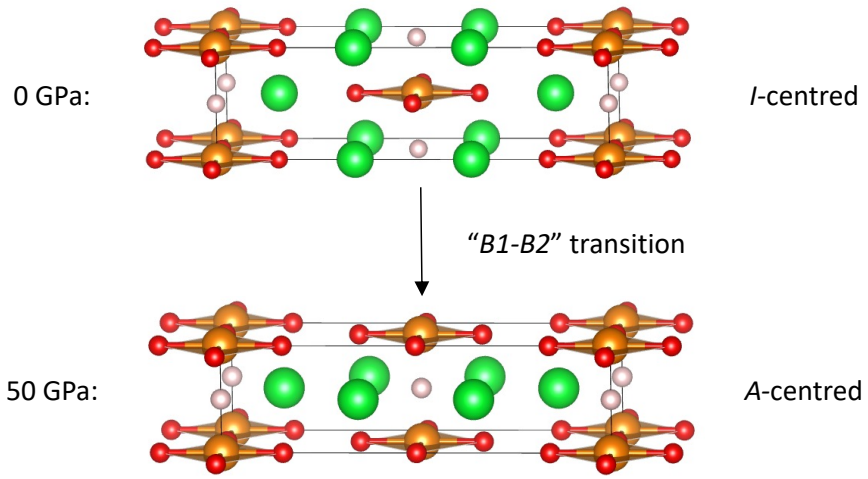



Figure 4.5: $B1 - B2$ transition in $Sr_2VO_3H$ with Sr shown in green, V in orange, O in red and H in white.

of the two phases are equal) are 45 and 43 GPa for $Sr_2VO_3H$ and $Sr_3V_2O_5H_2$, respectively.

The unit cells, shown in Figure 4.6, can be separated into distinct VO blocks and rock-salt or CsCl "blocks" along $c$. In this way the $I$- and $A$- forms can be seen to differ only in the geometry in the interlayer regions, termed the rock-salt and CsCl blocks respectively. The switch from $I$- to $A$-centering is marked by abrupt changes in all three lattice parameters. Most strikingly, $c$ drops from ∼11.9 Å just before the transition to ∼11.4 Å just after it. There is a somewhat smaller compression along $b$ from ∼3.3 Å above ($P_s$) to ∼3.15 Å below it (note the different scales used for $a$, $b$ and $c$). In contrast, there is an expansion along $a$ (∼3.69 Å to ∼3.84 Å) at the critical pressure, which restores the V-O bond lengths almost back to their ambient pressure value of 3.852 Å.

Experimental observations confirm the $B1 - B2$ transition in these oxyhydrides, but suffer from two limitations which must be overcome by computational analysis if we wish to understand the details of this transition. Firstly, high-pressure diffraction measurements do not provide structural information with atomistic resolution and so cannot tell us about changes in bonds oriented along $c$. Secondly, the experiments can of course only probe the structure of the phase present under a given set of conditions; they are blind to the $A$-centered phase at low pressure and to the $I$-centered phase at high pressure. Alongside structural optimizations we can calculate the density of states (DOS) and its projection onto vanadium (PDOS) to explore the behaviour of the bands closest to the Fermi level, namely the vanadium $d$ bands. Once we have characterized the deformations under pressure we will be able to establish a direct

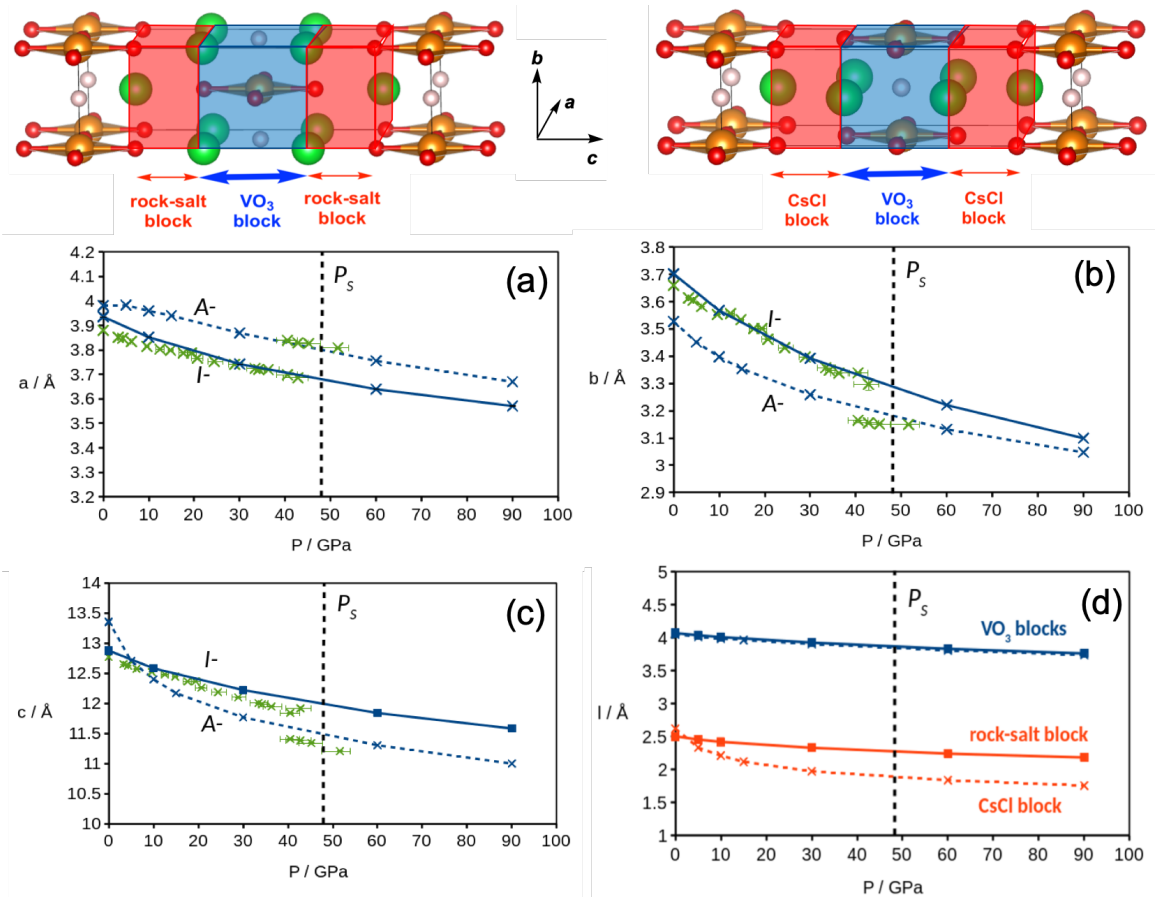



Figure 4.6: (a)-(c) Measured (green) and computed (blue) lattice parameters, $a$, $b$ and $c$ of $Sr_2VO_3H$, respectively. Solid and dashed lines refer to the $I$- and $A$- form, respectively. The black dashed line marked $P_s$ marks the computed transition pressure. (d) Decomposition of the variation in $c$ (computed) into separate contributions from the VO and rock-salt/CsCl blocks. Experimental measurements were performed by Takafumi Yamamoto at Kyoto University.

connection between the structural and electronic changes.

The variations in the computed lattice parameters, $a$, $b$ and $c$ for the $I$- and $A$-centered phases of $Sr_2VO_3H$ are shown as full and dashed blue lines, respectively, in Figure 4.6(a)-(c). There is a striking correspondence between the calculated values and the experimental data (green crosses) for all three parameters, $a$, $b$ and $c$. The critical pressure can be defined as the point where the calculated enthalpy change, $\Delta H_s = \Delta E_s + P\Delta V_s$, equals zero, and the resulting values of 48 GPa and 50 GPa for $Sr_2VO_3H$ and $Sr_3V_2O_5H_2$, respectively, are in excellent agreement with experiment. Perhaps the most striking feature of the curves is the $c$ axis, which, at ambient pressure, is ~0.5 Å *longer* for the $A$-centered unit cell. However, even a very modest increase in pressure has a dramatic impact on the value of $c$ for the $A$-centered

lattice, such that it falls below the $I$-centered structure at ∼5 GPa and by the time this phase becomes accessible to the experiment at the critical pressure of 45 GPa, $c$ is almost 0.5 Å *shorter* in the $A$-centered form. We can obtain more information by breaking up the variations in $c$ into separate contributions from the $VO_2$ layers and the rock-salt/CsCl layers, which are shown in red and blue in Figure 4.6(d) (note that value of $c$ is simply twice the sum of the two components). This decomposition reveals that the different compressibilities of the two structures are caused solely by differences in the rock-salt/CsCl layers: the CsCl block in the $A$-centered lattice is compressed by ∼1.0 Å over the 90 GPa pressure range while the corresponding change in the rock-salt layer is only ∼0.3 Å. The VO blocks in the two cases are, in contrast, almost indistinguishable from each other and, moreover, are not strongly dependent on pressure. Exactly the same patterns emerge in the $Sr_3V_2O_5H_2$ case except that the compressibility of the VO block, with four V-O bonds along the $c$ axis, is now almost exactly double the compressibility of the VO block in $Sr_2VO_3H$ where there are only two such bonds. This reinforces the view that the V-O bonds are essentially invariant to the wider environment. The origin of the very different compressibilities along $c$ in the two structures can be traced to the nature of the nearest-neighbour interactions in the rock-salt/CsCl blocks. In the $I$-centered form, the nearest-neighbour interactions along $c$ are between ions of opposite charge (O/Sr), and the Sr-O separation of 2.50 Å is below the sum of the respective ionic radii ($r$(Sr) + $r$(O) = 2.58 Å) even at 0 GPa. Further compression along $c$ is therefore opposed by the steep repulsive potential imposed by the ionic cores. In the $A$-centered analogue, in contrast, the nearest neighbours have the same charge (O/O in the upper and lower layers, Sr/Sr in the middle layer). Moreover, the nearest neighbours in the $A$-centered form are offset along the $a$ axis, such that the separation between the oxide ions is 3.29 Å, much greater than the sum of the ionic radii (2.52 Å). As a result, compression is opposed only by the relatively shallow increase in potential energy imposed by the long-range electrostatic repulsions, and is consequentially much easier. Just below $P_s$ the pressure gradient in the $I$-centered form is distributed approximately equally over the three orthogonal lattice directions, $a$, $b$ and $c$, but above the transition point the gradient is absorbed mostly by compression along $c$, relieving almost all of the compression that had previously accumulated along the V-O bonds along $a$.

### 4.2.4 Pressure-dependent electronic behaviour of vanadium

The experimentally measured resistivity plots for all three vanadium oxyhydrides are shown in Figure 4.7. The resistances of $Sr_2VO_3H$ and $Sr_3V_2O_5H_2$ show very similar behavior, decreasing significantly with increasing pressure, but neither plot shows any discontinuity coincident with the crystallographic phase transitions described above. It is possible that the absence of such a discontinuity reflects the slow kinetics of the phase transition, but control experiments on $Sr_3V_2O_5H_2$ where an overnight delay was introduced between pressurization (at room temperature) and measurement of resistance gave qualitatively similar results. The decrease in resistance with pressure is broadly similar to the behaviour of $SrVO_2H$ but at each pressure the gradient $\Delta R/\Delta T$ remains negative for both $Sr_2VO_3H$ and $Sr_3V_2O_5H_2$ even up to highest accessible pressures (48 and 57 GPa respectively). In $SrVO_2H$, the gradient is very close to zero at elevated pressures, behaviour that is characteristic of a semi-metal with a zero band gap but zero density of states at the Fermi level.

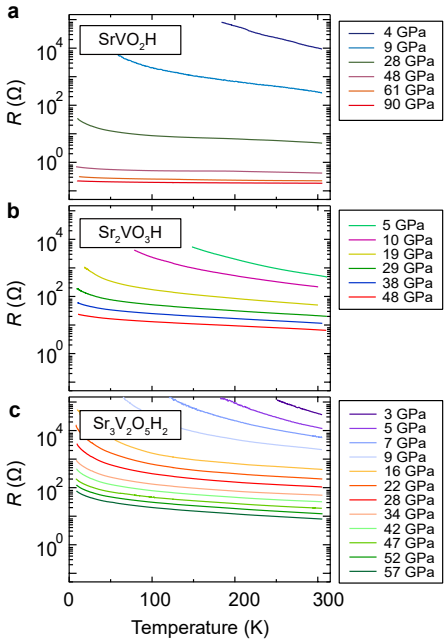



Figure 4.7: Pressure-dependent electrical resistances of vanadium oxyhydrides. Temperature dependence of resistance R at various pressures for (a) $SrVO_2H$, (b) $Sr_2VO_3H$, (c) $Sr_3V_2O_5H_2$. Measurements were performed by Takafumi Yamamoto at Kyoto University.

In order to explore the link between structure and resistance, we have plotted the density of states, projected onto the V 3*d* orbitals, for both the *I*- and *A*-centered

lattices at ambient pressure and at 60 GPa in Figure 4.8. The corresponding data for $SrVO_2H$ are also shown for comparison, and those for $Sr_3V_2O_5H_2$ can be found in Figure 4.9. The projection of the DOS presents a minor problem in that the V-H-V chain is aligned along the crystallographic $c$ axis in $SrVO_2H$ whereas it is aligned along $b$ in $Sr_2VO_3H$ and $Sr_3V_2O_5H_2$. To facilitate the comparison between the three materials, we therefore define a common local axis system where in all cases the V-H-V chain is aligned along the $z$ axis and the infinite V-O-V ladder is aligned along $x$. The ambient pressure plot for $SrVO_2H$ is very typical of a lattice of antiferromagnetically (AFM) coupled V(III) ions ($d^2$). The calculated spin densities at V are $\pm 1.5\,\mu_B$, and the majority-spin components of the V $d_{xz/yz}$ orbitals (green and red) are both occupied and degenerate in tetragonal symmetry while the $d_{xy}$ band (purple) is destabilized by strong in-plane V-O $\pi$ interactions and lies above the Fermi level. Very similar features emerge for both $I$- and $A$- forms of $Sr_2VO_3H$, except that now the degeneracy of the bands below the Fermi level is lifted due to inequivalence of the $a$ and $c$ axes. The dispersion along $a$ (the infinite V-O-V ladder) remains pronounced (red) but the intervening rock-salt/CsCl blocks prevent dispersion along $c$ (green). The $d_{xy}$ band above the Fermi level is also much narrower in $Sr_2VO_3H$ than in $SrVO_2H$, again reflecting the contrast between a 2-dimensional $VO_2$ lattice and a 1-dimensional V-O-V chain. At 60 GPa, the compression of $SrVO_2H$ in the $ab$ plane drives an increase in the dispersion of both the V $d_{xz/yz}$ and V $d_{xy}$ bands, to the extent that they meet at the Fermi level, effectively eliminating the band gap. The DOS at this point is typical of a semi-metallic state, where the resistance is independent of temperature. Turning to the 60 GPa DOS of the $I$- and $A$- forms of $Sr_2VO_3H$, the same general features are apparent: the DOS broadens, most obviously for the red (V $d_{xz}$) and purple (V $d_{xy}$) bands where there is strong dispersion along the infinite V-O-V ladder aligned along $a$. Just as the lower dimensionality of $Sr_2VO_3H$ compared to $SrVO_2H$ led to narrower bands in the former at ambient pressure, it also means that the bands are less sensitive to pressure, and a clear band-gap remains even at 60 GPa. Differences between the $I$- and $A$-centered forms are marginal, but there is slightly greater dispersion in the red $d_{xz}$ band in the $I$-centered form, such that the top of this band defines the Fermi level whereas it is the green $d_{yz}$ band in the $A$-centered analogue. The variations in DOS across the three structures suggest that the presence of a band gap in the high-pressure forms of both $Sr_2VO_3H$ or $Sr_3V_2O_5H_2$, as measured by the negative gradient of the resistance *vs* temperature plot, is primarily due to the presence of an infinite 1-dimensional VO ladder rather than the 2-dimensional $VO_2$ sheet in $SrVO_2H$. The effect of the transition from the $I$- to $A$-centered phases

seems to be of secondary importance because the band gap at 60 GPa is only very marginally larger than in the *A*-centered form. This observation is consistent with the absence of any marked discontinuity at the critical pressure in the resistance vs temperature curves shown in Figure 4.7.

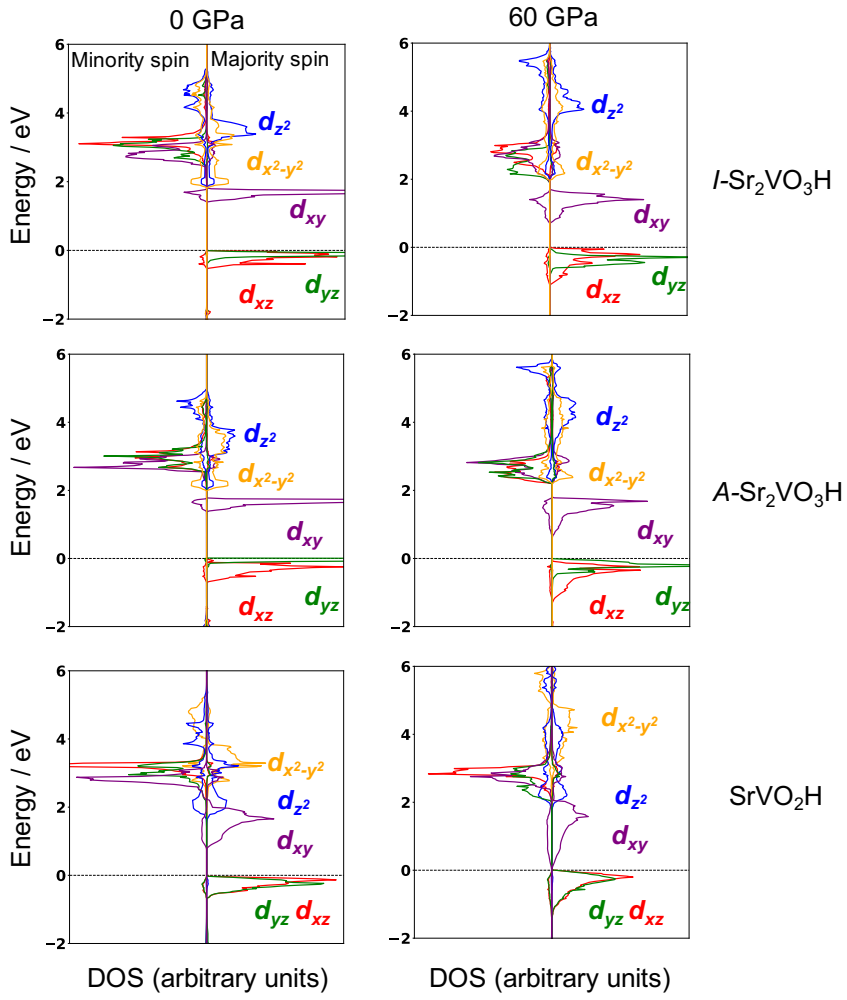



Figure 4.8: Vanadium PDOS plots for *I*-$Sr_2VO_3H$, *A*-$Sr_2VO_3H$ and $SrVO_2H$ at 0 and 60 GPa.

In related studies on the high-pressure behaviour of $Sr_3Fe_2O_5$[172], a transition to a ferromagnetic (FM) metallic state was observed. In the vanadium systems of interest here all FM states were found to lie $0.5 - 1.0$ eV above the AFM ground state across the entire pressure range. We have, however, been able to locate diamagnetic, truly metallic states with entirely delocalized electrons by performing an additional series of calculations using spin-restricted density functional theory, where polarisation of the $\alpha$ and $\beta$ orbitals is prevented by construction. The metallic state proves to be less

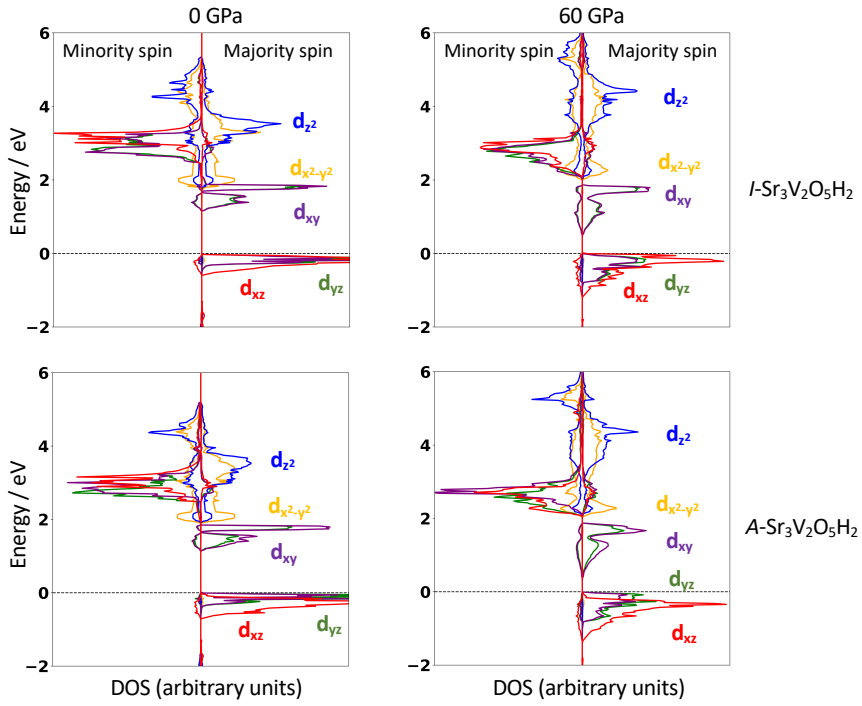



Figure 4.9: Vanadium PDOS plots for *I*- and *A*-$Sr_3V_2O_5H_2$ at 0 and 60 GPa.

stable than the spin-polarized AFM forms described above at all pressures, as shown in Figure 4.10, but in $SrVO_2H$ the separation goes from 3 eV/unit cell at ambient pressure to only 1.1 eV/unit cell at 90 GPa.

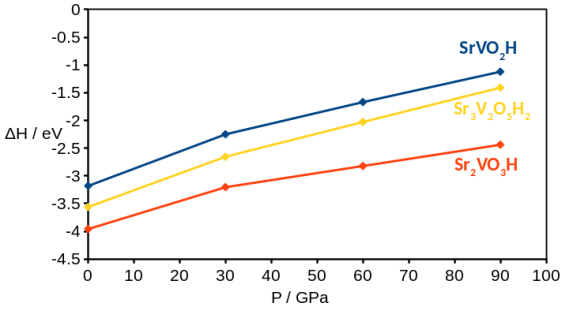



Figure 4.10: Enthalpy differences between antiferromagnetic and diamagnetic states of $Sr_2VO_3H$, $Sr_3V_2O_5H_2$ and $SrVO_2H$ as function of pressure.

The separation between metallic and AFM states is always largest for $Sr_2VO_3H$: the values vary from ∼4 eV/unit cell at 0 GPa to ∼3 eV/unit cell at 90 GPa. The 1-dimensional $Sr_2VO_3H$ ladder is therefore further away from the metallic crossover than 2-dimensional $SrVO_2H$ ladder at all pressures, consistent with the larger band gap and the measured resistance data.

### 4.2.5 Sequential $B1-B2$ transitions in $Ba_2YHO_3$

$Ba_2YHO_3$, recently synthesized by Kobayashi, has a $d^0$ B cation and thus has anion ordering controlled entirely by electrostatics, placing hydrides in the rock salt layer in accordance with the principle that the most charged anion coordinates to the most charged cation. In this compound the anions are segregated into all-oxide and all-hydride layers, in contrast with the closely related $Ba_2ScHO_3$ which has hydrides and oxides disordered over all rock salt sites. This can be explained by the Goldschmidt tolerance factor, which shows that the ionic radii of $Ba_2YHO_3$ deviate from those required for a cubic perovskite, which would ordinarily lead to octahedral tilting distortions but in this case leads to a reduction of symmetry by anion ordering. The remarkable ordering pattern opens up the possibility of high-pressure structural processes previously unobserved in RP chemistry in which half the structure may adopt CsCl ordering while the other retains rock salt ordering within a defined pressure window. In this study we employ DFT calculations to predict the enthalpies of possible unit cells of $Ba_2YHO_3$ under pressure and explore structural deformations in a level of detail inaccessible to experimental methods due to challenges in precisely locating individual atoms, particularly hydrides, in high-pressure powder diffraction experiments. By comparison to previous results on $Sr_2VO_3H$ we aim to understand the effects of dimensionality and electron configuration on these phase transitions.

We have identified four possible structures for $Ba_2YHO_3$ by imposing rock salt or CsCl ordering in the H-Ba and O-Ba layers, as indicated in Figure 4.11. Each is generated from the ambient-pressure "No $B1-B2$" cell by shifting appropriate parts of the cell by $a/2$. Rock salt ordering is favoured by electrostatics as it brings opposite ions into close contact. However, these short distances render the structure incompressible, so CsCl ordering will be enthalpically favoured by $PV$ at high pressure; phase transitions therefore occur when the reduction in volume outweighs the energetic cost of changing the anion ordering. All structures were fully optimized at pressures spanning 0-40 GPa; enthalpies relative to the ambient pressure structure are shown in Figure 4.11($v$). This phase diagram predicts two independent phase transitions confined to separate regions of the cell, a phenomenon which we believe to be unknown in oxyhydride chemistry. The ambient pressure structure is enthalpically favourable up to approximately 15 GPa, when a change to CsCl ordering in the H-Ba layer occurs. Rock salt ordering in the O-Ba layer, however, is retained until around 35 GPa, above which CsCl ordering is adopted in all possible regions to give the conventional $B1-B2$ transition product. The first transition pressure of 15 GPa is unprecedentedly low for RP phases, accessible here because the electrostatic energy

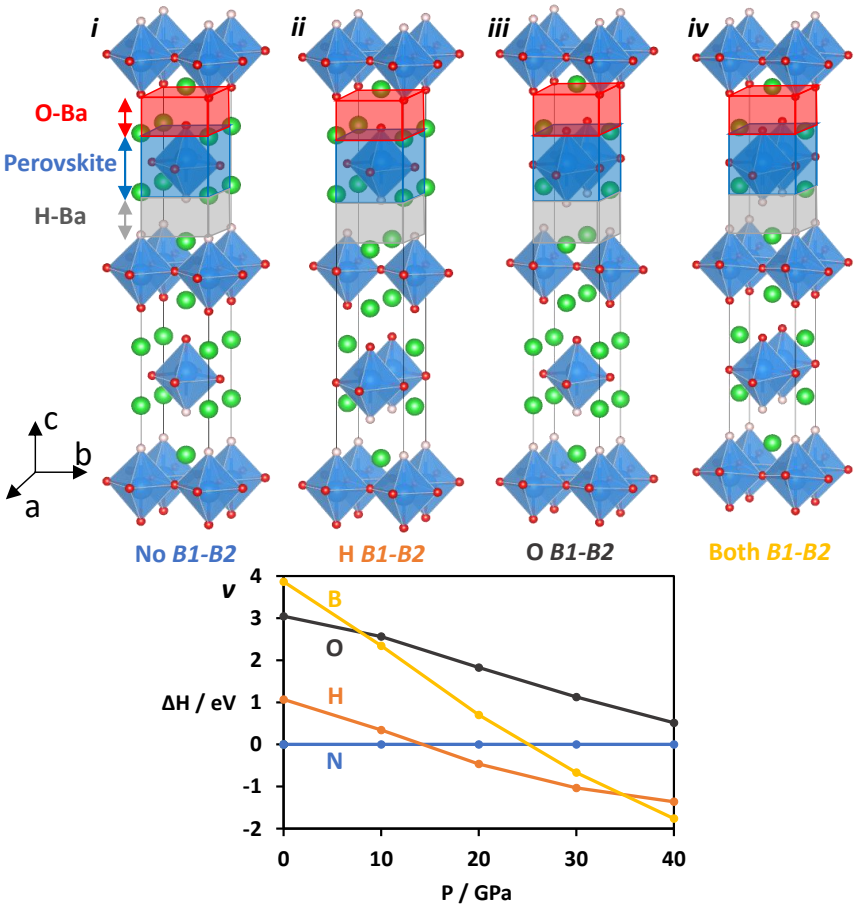



Figure 4.11: High-pressure geometries of $Ba_2YHO_3$ with Ba in green, Y blue, H white and O red. (i)-(iv) Unit cells generated by $B1-B2$ transitions in regions of the cell as indicated. Red and grey boxes mark regions in which the ordering has been changed by a local transition. (v) Enthalpies relative to the "No $B1-B2$" cell as a function of pressure.

associated with the monoanionic hydride is smaller than in more typical divalent oxide systems, reducing the energetic penalty of adopting CsCl ordering. We can also see that the first transition suppresses the second, since the "Both $B1-B2$" cell has a lower enthalpy than "No $B1-B2$" above 25 GPa but is higher than "H-Ba $B1-B2$" until 35 GPa.

To understand this graph more thoroughly we have plotted the lattice parameters as a function of pressure in Figure 4.12. The dashed lines follow the minimum enthalpy structure across the pressure range, showing the values which this model predicts will be measured at any given pressure. This computational experiment allows us to explore the behaviour of all possible cells at all pressures, providing insight unavailable from experimental results alone as any real experiment can probe only the properties

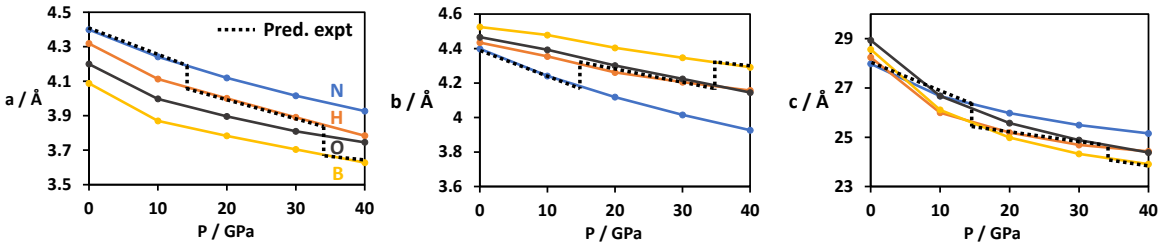



Figure 4.12: Calculated lattice parameters of cells of $Ba_2YHO_3$ as a function of pressure. Dashed black lines mark the predicted experimental measurements at any pressure.

of the ground state under a specified set of conditions.

The trends in $a$ and $b$ should be examined together as these are identical in the "No $B1-B2$" cell, but are rendered inequivalent by any $B1-B2$ transition. The transition shifts the perovskite blocks by $a/2$, changing the ordering in the H-Ba or O-Ba layers such that like ions in these regions now have equal $a$ coordinates, repelling each other more strongly along $b$. This is why the compressibility of $b$ decreases with successive $B1-B2$ transitions while that of $a$ increases. The greater compression along $a$ in the "O-Ba $B1-B2$" cell than in the "H-Ba $B1-B2$" cell may be attributed to the greater $c$ compressibility in the latter, reducing the need for compression along $a$. The trends in $c$ are more interesting; the all-rock salt "No $B1-B2$" cell has the shortest $c$ at 0 GPa but the longest above 10 GPa, the gap between this cell and the others widening as pressure increases further. The greatest change over the measured pressure range is seen in the all-CsCl "Both $B1-B2$" cell, which is the ground state in the high pressure limit.

This trend indicates that the CsCl blocks provide the greatest compressibility, so to explore this further we have plotted the widths of the structural blocks (shown in Figure 4.11) against pressure in Figure 4.13. Figure 4.13(a) shows the width of the perovskite block, while 4.13(b) shows the sum of the O-Ba and H-Ba regions. These two graphs together make up the $c$ lattice parameter, so all factors affecting the compressibility of $c$ are captured here. We can now see the far higher compressibility of the O-Ba and H-Ba blocks over the perovskite blocks - note the different length scales - for all cells except "No $B1-B2$". The O-Ba and H-Ba blocks also give rise to the greatest difference between the cells while there is little absolute variation in the widths of the perovskite blocks between the cells at any pressure, which is unsurprising since the cells only differ in the ion ordering in the O-Ba and H-Ba regions. Above 10 GPa the ordering of perovskite block widths is the reverse of the O/H-Ba widths. The perovskite blocks are all structurally identical, so this trend most likely appears

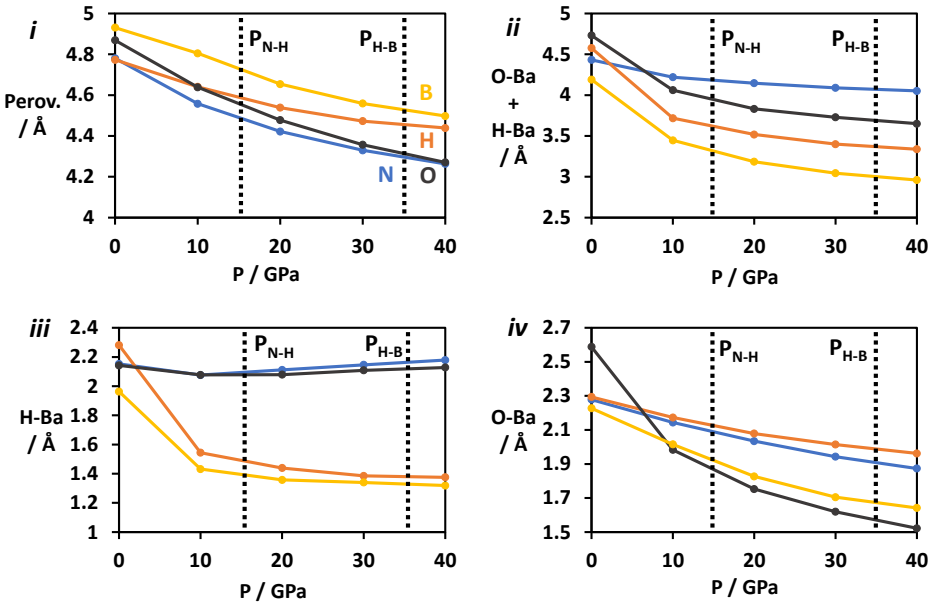



Figure 4.13: Compressibility of $Ba_2YHO_3$ along $c$ in different regions of the unit cell. (i) Perovskite layer. (ii) Sum of O-Ba and H-Ba layers. (iii) H-Ba layer. (iv) O-Ba layer. Vertical dashed lines mark calculated phase transition pressures.

because the cells preferentially compress the O/H-Ba regions, with changes to the perovskite blocks occuring only when the O/H-Ba regions incur more severe repulsive penalties. The "Both $B1-B2$" cell, most stable in the high-pressure limit, in fact has the largest perovskite block, indicating that the $B1-B2$ transitions in the H/O-Ba regions allow for a release of strain in compressed H/O-Sc bonds.

We now turn to Figure 4.13(c) and (d), showing the compressibilites of the H-Ba and O-Ba regions of each cell separately, to explain the remaining differences between the cells. Figure 4.14 shows these regions in more detail in both ordering patterns. Both graphs show two pairs of curves according to whether the relevant region of the cell is in rock salt or CsCl ordering. It is now unambiguous that CsCl ordering affords greater compressibility than rock salt ordering, confirming our interpretation of the trend in $c$ compressibilities in Figure 4.12(c) and agreeing with previous results for $Sr_2VO_3H$. Figure 4.14 explains this geometrically, showing that rock salt ordering maximises electrostatic attractions by bringing opposite ions into contact with one another by aligning them along $c$, so compression along $c$ is resisted by core electron repulsions. CsCl ordering disrupts this alignment, allowing unopposed $c$ compression at the expense of electrostatic energy. Comparison of Figure 4.13(c) and (d) also shows that the H-Ba layer is made far more compressible by the $B1-B2$ transition than the O-Ba layer. This is because CsCl ordering is electrostatically unfavourable,

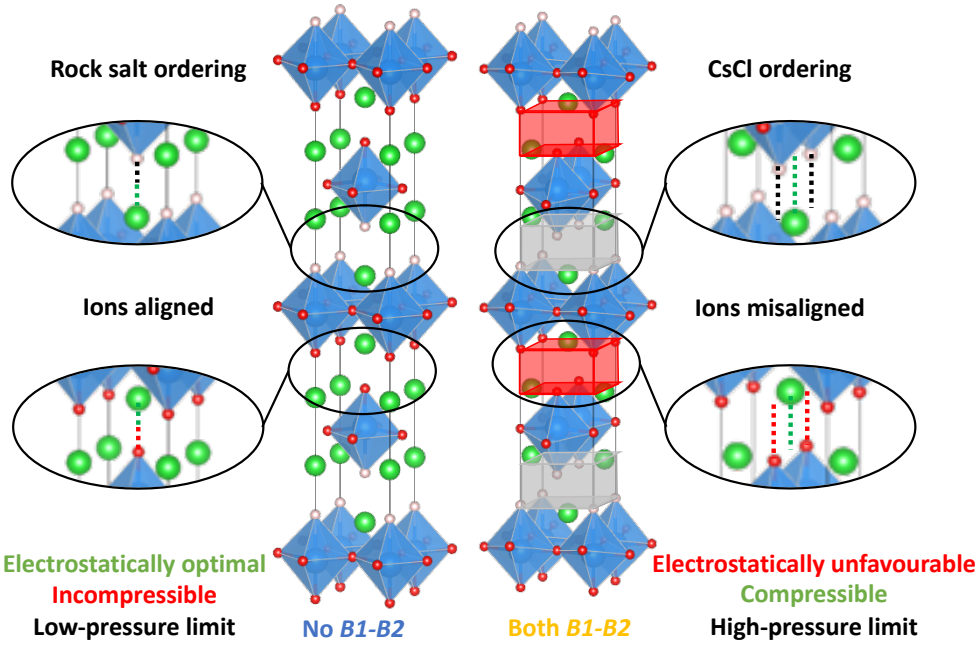



Figure 4.14: Unit cells of $Ba_2YHO_3$ detailing rock salt and CsCl orderings of H-Ba and O-Ba regions with Ba in green, Y blue, H white and O red.

as indicated in Figure 4.14, but this penalty is less severe in the H-Ba layer because the monovalent $H^-$ generates smaller electrostatic energy contributions than the divalent $O^{2-}$. The dramatic compression of the CsCl-ordered H-Ba blocks relative to their rock salt counterparts from 0-10 GPa ultimately leads to the first phase transition, at 15 GPa, while the greater similarity in compressibilities between ordering patterns in the O-Ba layer means that this transition is enthalpically favoured only above 35 GPa. The H-Ba block compressibilites of the "No $B1-B2$" and "O-Ba $B1-B2$" cells at first appear anomalous, compressing slightly at 10 GPa but lengthening at higher pressures. The H-Ba bond lengths fall smoothly across the full pressure range, so this trend is a consequence of Ba-Ba repulsions which are not compensated by favourable interactions with $H^-$ as they are with $O^{2-}$ in the O-Ba layer.

## 4.3 Hydride conduction in scandium oxyhydrides

### 4.3.1 Methods

Calculations were performed using periodic plane-wave DFT implemented in VASP[165] with PAW pseudopotentials[166] and the PBE exchange-correlation functional[5]. For static calculations, a plane-wave cutoff of 600 eV was used. The irreducible part of the Brillouin zone of the crystallographic cell was sampled with a 7×7×2 k-point grid,

and that of the 3×3×1 supercell with a 2×2×2 grid. Reaction barriers were calculated with the climbing image nudged elastic band (CI-NEB) method using the implementation in the VASP Transition State Tools (VTST)[173, 174], with three images used for each calculation. Lattice parameters were fixed during CI-NEB calculations. All AIMD simulations were performed on the 3×3×1 supercell in the canonical (NVT) ensemble with constrained cell shapes and volumes, and a temperature of 700°C. The plane-wave energy cutoff was set to 400 eV and k-point sampling occurred at the gamma point only. Simulations were performed for 100 ps with a 0.5 fs timestep, unless otherwise stated, and data were collected after equilibration periods of up to 6 ps. Temperature was controlled using the Nosé-Hoover thermostat[175, 176]. Static calculations were visualized with VESTA[177], and simulations with VMD[178].
For each of the simulations, the mean squared displacement (MSD) for each ionic species was determined as a function of $\tau = t'' - t'$, where $t'$ and $t''$ are discrete time steps in the AIMD simulation and $t'' > t'$, via the following expression,

$$\langle \Delta r^2(\tau) \rangle = \frac{1}{N}\left(\frac{1}{n_\tau}\right) \sum_{t'=0}^{n_\tau} \sum_{i=1}^{N} \Delta r_i^2(\tau) \tag{4.1}$$

where $N$ is the number of ions of the species, $n_\tau = n_{\text{steps}} - \tau - 1$, $n_{\text{steps}}$ is the total number of steps performed in the AIMD simulation and $\Delta \mathbf{r}_i(\tau) = \mathbf{r}_i(t'') - \mathbf{r}_i(t')$. The gradient of the MSD was used to determine the diffusion coefficient $D$ for each of the ionic species as a function of $\tau$. $D$ is calculated using the Einstein relationship,

$$D = \lim_{t \to \infty} \frac{1}{6} \frac{\partial \langle r^2(t) \rangle}{\partial t} \tag{4.2}$$

As this relationship is valid only in the long time limit, $D$ is calculated from the latter half of the $D(\tau)$ data, to allow the system to equilibrate fully before determining this property.

### 4.3.2 Hydride conduction mechanisms in $Ba_2ScHO_3$

Hydride anion conduction in perovskite oxyhydrides was first shown in 2016 by Kobayashi[152] in the $La_{2-x-y}Sr_{x+y}LiH_{1-x+y}O_{3-y}$ series of $n = 1$ Ruddlesden-Popper phases. These contain hydrides in the perovskite layer of the structure, with hydrides coordinated to lithium rather than lanthanum, and their hydride diffusion pathways have been explored computationally[159, 160, 161]. The synthesis of $Ba_2ScHO_3$ in 2019[155] showed that the alternative anion ordering, placing hydrides in the rock salt layer, was also accessible and that this ordering enabled hydride conduction. However, the mechanism was not established experimentally so here we investigate the

hydride diffusion pathways and use the results to predict the consequences of physical and chemical changes for conductivity. As stated above, all AIMD simulations in this chapter were performed by Harry J. Stroud at the University of Bristol.

We optimized the geometries of different possible unit cells of $Ba_2ScO_3H$ containing two formula units, each with a different anion ordering as shown in Figure 4.15, since the compound contains oxide/hydride disorder over the apical sites. Our results for the relative energies of anion orderings agree with previous calculations[155] and so we focus on the lowest energy arrangement, which contains alternating all-hydride and all-oxide rock salt layers. The cell parameters and atomic positions were optimized, and the resulting lattice parameters *a, b, c* are 4.184 Å, 4.178 Å and 13.046 Å respectively . These are in good agreement with experimental values at 300 °C of 4.18 Å (*a, b*) and 13.7 Å (*c*); our calculations are in the static limit, i.e. 0 K and without lattice vibrations, and orthorhombic distortions at low temperature are common in Ruddlesden-Popper phases.[152]

We have identified four possible movements of hydride ions through the rock salt layer

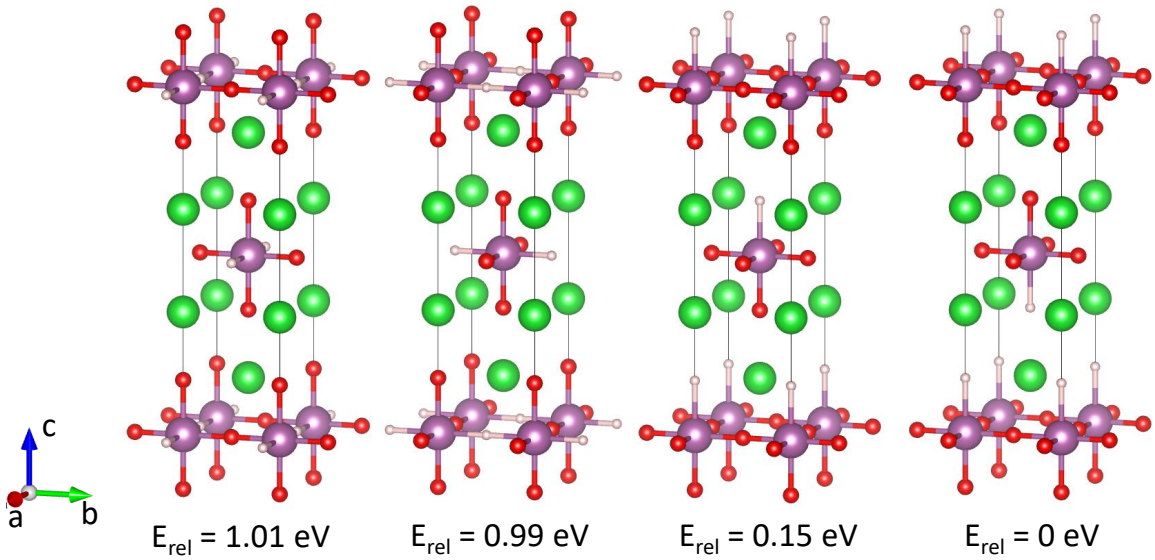



Figure 4.15: Anion orderings for $Ba_2ScHO_3$ and their calculated relative energies, with Ba shown in green, Sc in purple, H in white and O in red.

which account for the roles of interstitial and vacancy defects, the formation energies of which have been calculated[164] as 0.79 eV and 0.72 eV respectively. Defective cells were modelled using a 3×3×1 supercell, and charge neutrality was maintained by means of a compensating background charge. We have confirmed that this background charge has no significant effect on the results  details can be found in Figure

4.17. $Ba_2ScHO_3$ has been shown experimentally to have apical sites occupied by disordered hydride and oxide ions in a 1:1 ratio. As discussed above we chose to model $H^-$ migration in a cell with one rock salt layer entirely occupied by hydride anions and the other entirely occupied by oxide anions, but we find that our results are not strongly dependent on the choice of anion ordering pattern *(vide infra)*.

The migration pathways, CI-NEB barrier heights and transition states are shown in Figure 4.16. The possible hops involving the interstitial defect involve both intersticialcy and interstitial mechanisms. The former involves a knock-on displacement of a hydride on a lattice site by the interstitial ion and the latter describes direct movement of a hydride from one interstitial site to the next. The vacancy hops are termed 'Along' and 'Across' to describe their movement relative to the rock salt layer in that the former mechanism does not change the $c$ coordinate of the mobile hydride. Figure 4.16 shows that the lowest energy pathway is the interstitialcy hop, a correlated motion involving two hydride ions, with a barrier height of 0.35 eV. In the transition state each hydride is in approximately trigonal planar coordination, with three $Ba^{2+}$ cations at 2.56 Å. The highest energy barrier is that for the interstitial hop, at 0.86 eV; in this transition state the mobile hydride has two $Ba^{2+}$ cations at 2.36 Å, describing linear coordination, and four in a second coordination shell at 3.66 Å. There are also two $H^-$ neighbours at 2.39 Å which incur significant electrostatic repulsion, rendering this transition state unfavourable.

The 'Across' and 'Along' vacancy hops are intermediate in energy, at 0.41 eV and 0.62 eV respectively. In both cases, in the transition state the mobile hydride lies within a Ba tetrahedron but is displaced from its centre, towards a tetrahedral edge, shortening the distance travelled between sites. These displacements explain the difference in energies between the two. In the lower-energy 'Across' hop TS the hydride is displaced strongly, with H-Ba bond lengths of 2.55 Å (×2), 3.03 Å and 3.09 Å. The displacement from the centre of the tetrahedron is in the direction of another Ba cation, at 4.47 Å, so it offers some additional stabilization of the TS. Meanwhile, the mobile hydride in the 'Along' hop TS is located much closer to the centre of the Ba tetrahedron, with cations at 2.62 Å and 2.84 Å, because the distortion moves it closer to an oxide anion. This pathway is therefore longer, in order to reduce anion-anion repulsions, and is the higher energy vacancy migration.

The mean square displacement (MSD) plots for both cells show the values for H climbing throughout the simulation, while those for all other elements oscillate around a constant value. This indicates that the hydrides are the only mobile ions in the system, all others vibrating about their lattice positions, as further supported by the

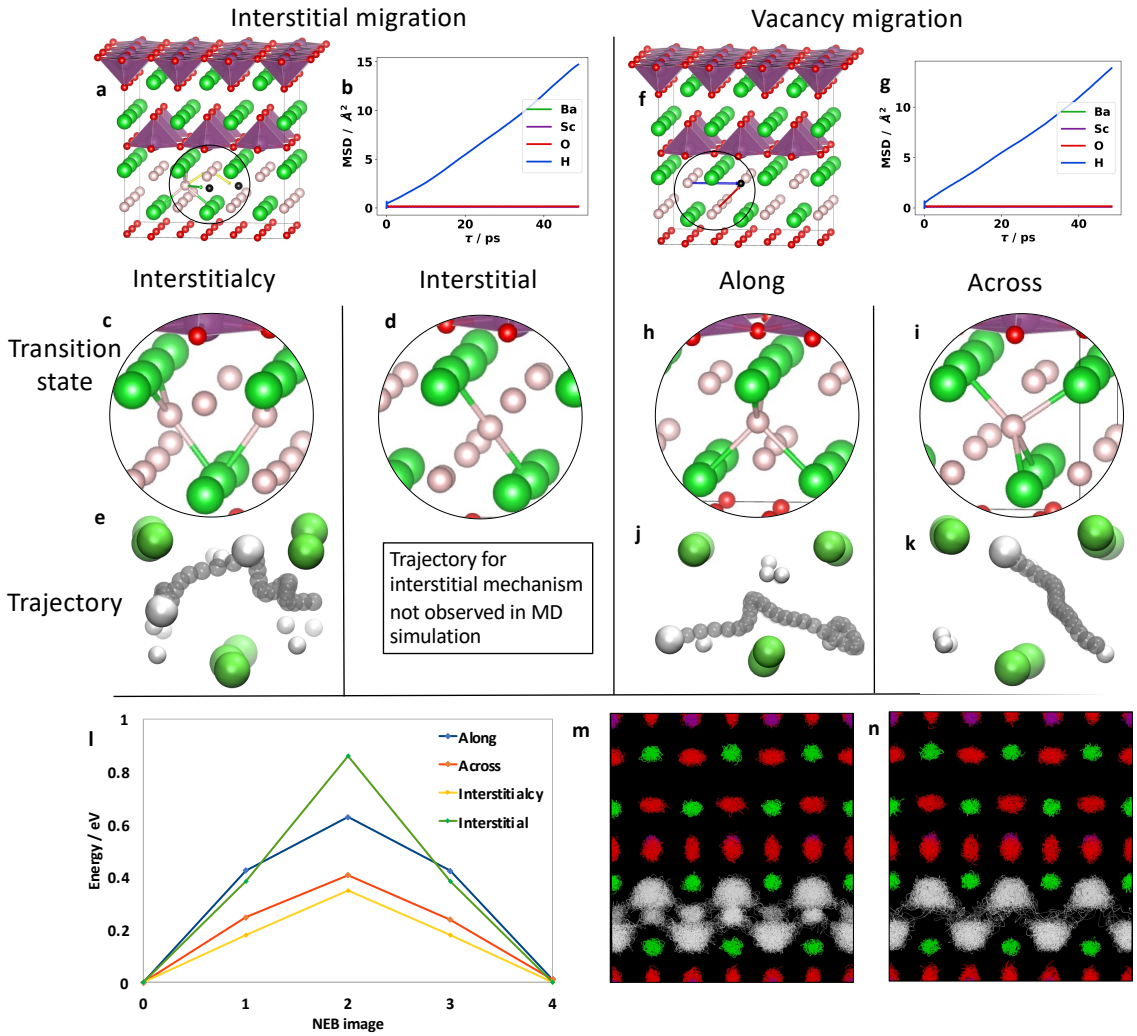



Figure 4.16: Summary of hydride mobility in $Ba_2ScHO_3$ with Ba in green, Sc in lilac, H in white and O in red. (a, f) Pathways considered for an interstitial and a vacancy defect respectively, with colour coded arrows matching the legend on graph (l). Black spheres mark the hop end points and circles highlight the parts of the cell shown in detail in parts (c, d, h, i). (b, g) MSD plots at 700°C for $Ba_2ScHO_3$ containing an interstitial and a vacancy defect respectively. (e) Interstitialcy trajectory, viewed along $a$ with images shown every 4 fs. (j, k) 'Along' and 'Across' trajectories respectively, viewed along $a$ and $b$ respectively. (l) CI-NEB reaction barriers for all pathways. (c, d, h, i) Transition states for Interstitialcy, Interstitial, 'Along' and 'Across' hops respectively. (m, n) 100 ps trajectory of $Ba_2ScHO_3$ containing an interstitial and a vacancy defect respectively, viewed along $a$. AIMD results (b, e, g, j, k, m, n) were collected by Harry Stroud at Bristol University.

trajectories shown in Figure 4.16(m,n). The hopping pathways observed in the simulation are as we expect from the calculated barriers; hydride diffusion in the interstitial cell occurs exclusively by the interstitialcy mechanism, while the vacancies travel by

both mechanisms but the 'Along' mode appears more frequently. From these MSDs we have estimated diffusion constants for the interstitial and vacancy of $1.1 \times 10^{-10}$ $m^2s^{-1}$ and $1.4 \times 10^{-10}$ $m^2s^{-1}$ respectively. These values give us an order-of-magnitude estimate for diffusivity in $Ba_2ScHO_3$ and will be most informative when compared to those for other systems *(vide infra)*.

To investigate the possibility of longer-range correlated motion involving multiple atoms, we considered a pathway of two successive interstitialcy-type displacements. The two displacements occurred on opposite sides of the rock salt layer and therefore proceeded in mutually orthogonal directions. The pathway was found to contain two barriers, both with heights equal to that of the simple two-atom interstitialcy hop, and the energy of the system returned to its minimum value in the middle of the reaction coordinate. This suggests that correlated motion of three atoms does not serve to provide low-energy interstitial motion pathways but does indicate that rapid successive hops of this type may be possible.

The introduction of a charged defect to a unit cell requires some form of charge compensation to maintain overall electroneutrality in the cell. This may be done either by a uniform background charge in the cell or by the introduction of a second defect with opposite charge. To investigate the effect of the choice between these two methods, the interstitialcy hop NEB calculation was done twice, once with a unit positive background charge and once with an oxide replaced by a hydride. This substitution was made in the oxide-containing rock salt layer to minimize the effect of correlation between the defects.

The barriers are shown in Figure 4.17. The energies of the two methods are very close at every image, with a difference between the barrier heights of 0.014 eV. We therefore conclude that our results do not depend on our choice of charge compensation method and employ the background charge method throughout the study.

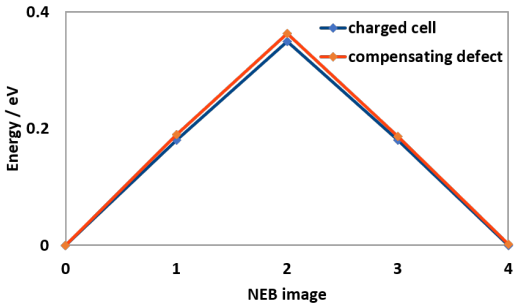



Figure 4.17: Interstitialcy hop barrier calculated with different charge compensation methods.

### 4.3.3 Anion disorder-dependence of diffusivity

$Ba_2ScHO_3$ contains hydride and oxide ions distributed randomly across the rock-salt layer sites in a 1:1 ratio, but for our model we must specify an ordering. As discussed above, our calculations and simulations were performed using the lowest energy ordering, in which the ions are segregated into all-hydride and all-oxide rock salt layers, so it is important to understand the effect of the chosen anion ordering pattern on the calculated hydride hopping barriers. This was investigated by generating a more disordered anion configuration, in which both rock salt layers in the cell contain oxide and hydride ions in equal number and each scandium ion is coordinated to one hydride. Barriers for all four mechanisms were calculated for this anion ordering - Figure 4.18(a,b) show, respectively, the barriers for the disordered configuration and a comparison between this and the lowest energy configuration. MD simulations for this "disordered" cell, containing a vacancy or an interstitial defect, were also run, and a comparison of the hydrogen MSDs between ordered and disordered configurations is shown in Figure 4.18(c).

The barriers in Figure 4.18(a) show that the energetic ordering of the pathways is unchanged by the introduction of anion disorder, with interstitialcy and 'Across' vacancy migration the lowest energy mechanisms. Figure 4.18(b) then shows that there is very little quantitative change to the barriers, so we can conclude that anion disorder does not strongly affect the barriers to hydride migration. However, the H MSDs in Figure 4.18(c) show clearly that the hydride diffusivity is lower in the disordered anion configuration. As the barriers are very similar this difference must arise from the reduced number of hops available to a mobile hydride partially surrounded by oxide anions. The diffusion constants of $1.3 \times 10^{-11}$ $m^2s^{-1}$ and $2.1 \times 10^{-11}$ $m^2s^{-1}$, for the interstitial and vacancy defects respectively, show that diffusivity is reduced by approximately one order of magnitude by the anion disorder. The increased hydride diffusivity in all-hydride rock-salt layers, despite similar migration barriers, is consistent with recent experimental observations on $Ba_2YHO_3$[156], which adopts the anion-ordering pattern which we have used to model $Ba_2ScHO_3$. The conductivity of the former is around five times that of the latter, but the two have very similar estimated activation barriers, in agreement with our calculated trends.

### 4.3.4 High pressure mechanism change

High-pressure studies were central to understanding structural and transport properties in our earlier study, and $Ba_2ScHO_3$ is synthesized under high-pressure conditions,

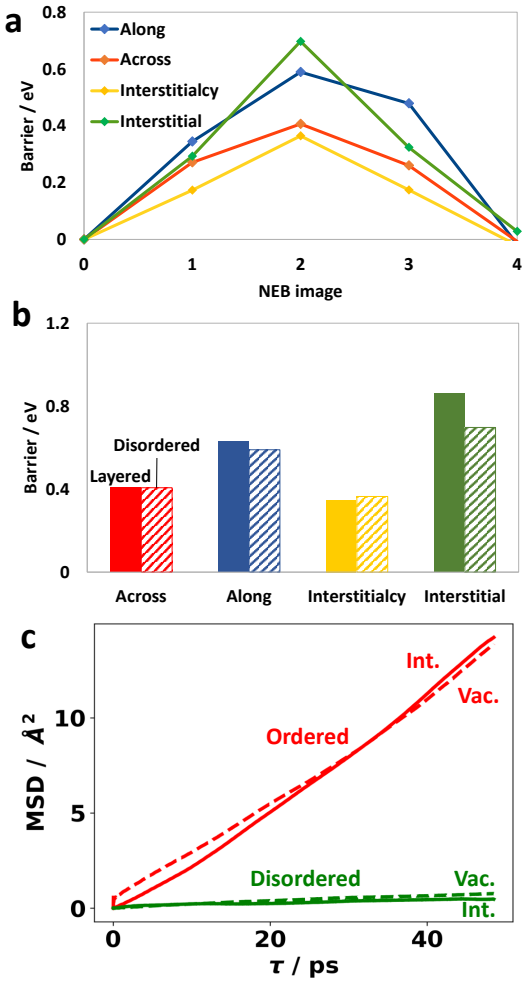



Figure 4.18: Effects of anion ordering in $Ba_2ScHO_3$. (a) Activation barriers for hydride diffusion. (b) Comparison of barriers in the disordered configuration to those for the lowest energy layered configuration. (c) MSD plots at 700°C for hydride ions in interstitial (solid lines) and vacancy (dashed lines) cells in ordered (red) and disordered (green) anion configurations. MSD calculations were performed by Harry Stroud at Bristol University.

so we sought to establish the effects of pressure on hydride mobility. Furthermore, ionic diffusion at high pressure is of considerable interest to deep-earth chemists, though at far more extreme conditions than those used here.

RP phases undergo a pressure-induced phase transition, known as the "$B1-B2$"[158] transition, in which the perovskite layers shift such that the ions in the inter-layer spacing change from rock-salt ordering to CsCl ordering. Our calculated transition pressure in the static limit is approximately 30 GPa, where the enthalpies of the low and high pressure structures are equal. We therefore studied hydride mobility at 20 GPa, high enough to give a clear indication of pressure-dependent behaviour while still well below the transition pressure.

To understand the effect of pressure on the defective cells of $Ba_2ScHO_3$, we carried out an analysis similar to that used for $Sr_2VO_3H$[145] by dividing the cell into octahedral and rock salt blocks, as shown in Figure 4.6(d), and measuring their compressibilities. Vacancy and interstitial cells show the same behaviour; geometrical parameters are reported in Table 4.2. Crucially, the hydride-containing rock salt layer is compressed by around 14 %, the perovskite layer by 10 % and the oxide-containing rock salt layer by 7 %, consistent with results for other RP oxyhydrides which show that hydride ions are twice as compressible as oxides[157].

**Vacancy**

| | $a$ / Å | $b$ / Å | $c$ / Å | V / Å$^3$ | perovskite / Å | O-Ba RS / Å | H-Ba RS / Å |
|---|---|---|---|---|---|---|---|
| 0 GPa | 12.53558 | 12.5359 | 13.99591 | 2199.385 | 4.61247 | 2.66866 | 2.88513 |
| 20 GPa | 11.88494 | 11.88494 | 12.78079 | 1805.309 | 4.17694 | 2.48656 | 2.4822 |
| ratio | 0.948096 | 0.948072 | 0.913180 | 0.820824 | 0.905576 | 0.931764 | 0.860343 |

**Interstitial**

| | $a$ / Å | $b$ / Å | $c$ / Å | V / Å$^3$ | perovskite / Å | O-Ba RS / Å | H-Ba RS / Å |
|---|---|---|---|---|---|---|---|
| 0 GPa | 12.55901 | 12.56015 | 14.0062 | 2209.3813 | 4.62728 | 2.67847 | 2.90334 |
| 20 GPa | 11.92587 | 11.92576 | 12.84467 | 1826.8342 | 4.17872 | 2.48981 | 2.50381 |
| ratio | 0.94958679 | 0.94949185 | 0.9170703 | 0.82685329 | 0.903062 | 0.929564 | 0.86239 |

Table 4.2: Geometrical parameters of vacancy and interstitial cells at 20 GPa. 'RS' denotes 'rock salt'.

Figure 4.19 shows the energies of the transition states for the four pathways at 0 GPa and 20 GPa. Pressure has a pronounced effect on the relative heights of the barriers for different motions as the mobility of vacancies falls far less dramatically than that of interstitials. The vacancy hop barriers rise by less than 50 %, to 0.56 eV ('Across') and 0.78 eV ('Along'), while the interstitial hop barriers more than double to 1.18 eV (interstitialcy) and 1.80 eV (interstitial). For each defect type the zero pressure orderings are preserved, with vacancies more mobile by the 'Across' mechanism and interstitial defects moving preferentially by the interstitialcy mechanism. The MSD plots in Figure 4.19(c,d), for interstitial and vacancy cells respectively, show contrasting hydride behaviour to that observed at zero pressure (Figure 4.16(b,g)). Rather than increasing with time, the hydrogen MSDs indicate that hydride motion is vibrational rather than diffusive and thus migration is greatly hindered by compression to 20 GPa.

The transition states for all hops have similar coordination environments at 20 GPa

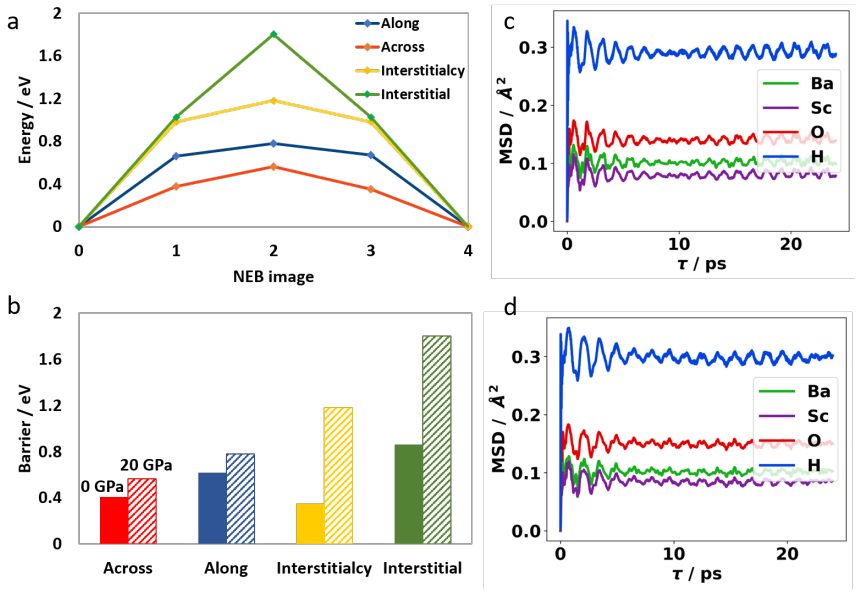



Figure 4.19: Effect of pressure on hydride mobility in $Ba_2ScHO_3$. (a) CI-NEB hydride mobility barriers at 20 GPa. (b) Comparison of barriers at 0 GPa (solid bars) and 20 GPa (hatched bars). (c), (d) MSD plots for the interstitial and vacancy cells, respectively, at 20 GPa. MSD calculations were performed by Harry Stroud at Bristol University.

to those at ambient pressure but, unsurprisingly, compression of the rock salt layer leads to important differences in bond lengths. The interstitialcy transition state still contains trigonally coordinate mobile hydrides, with H-Ba bonds of 2.37 Å, but

the two anions are displaced outwards from the centre of the $Ba_3$ triangles; the trigonal planar site, through which both hydrides must pass, contains far more severe short-range H-Ba repulsions at 20 GPa than at zero pressure, so at 20 GPa each hydride passes through the "local transition state" sequentially. This gives the TS more "di-interstitial" character, with the normal lattice site vacant, and raises the energy relative to the zero pressure case. In the 2-coordinate TS for the interstitial hop, the shortest H-Ba bond lengths are 2.18 Å and the farther four are at 3.33 Å, with the two nearest hydrides at 2.10 Å. The combination of H-H electrostatic repulsions and H-Ba Pauli repulsions once again make this the highest energy pathway.
The mobile hydride in the 'Along' vacancy hop occupies a pseudo-tetrahedral site, as before, with pairs of H-Ba bonds at 2.39 Å and 2.46 Å. In the lower-energy 'Across' case, the hydride is displaced in the same direction as at zero pressure but now lies much closer to the 4-coordinate site, with bond lengths of 2.36 Å (×2), 2.56 Å (×1) and 2.57 Å (×1). This is most likely because the 2-coordinate site on the tetrahedral edge is now too small to contain $H^-$; we were unable to find a TS at this site without significant distortions throughout the unit cell to lengthen the shortest H-Ba bonds.

### 4.3.5 Improved hydride conduction in $Sr_2ScHO_3$

To search for new and improved hydride conductors, we investigated the effect of A-site cation size by replacing barium by strontium to give $Sr_2ScHO_3$. Searches on the Inorganic Crystal Structure Database (ICSD) indicate that this compound is as yet uncharacterized. Full geometry optimization of the unit cell gives lattice parameters in Å of (4.099, 4.084, 13.206) - a reduction of around 2 % in $a$ and $b$ and around 6 % in $c$ relative to the Ba analogue.

Activation barriers were calculated for the same processes described above for $Ba_2ScHO_3$. Results and a comparison between the two compounds are shown in Figure 4.20. The transition states all contain mobile hydride ions in equivalent coordination environments to their $Ba_2ScHO_3$ counterparts. However, the barrier heights between the compounds show significant differences most clearly indicated by the bar chart in Figure 4.20(a). The two-atom interstitialcy mechanism remains the lowest energy pathway, with a barrier of 0.19 eV, and the 'Along' and 'Across' vacancy hops are very close in energy with barriers of 0.24 eV and 0.26 eV respectively. The interstitial mechanism is then far higher, at 1.04 eV. We can compare these results to those for the barium analogue; the three lowest barriers in $Sr_2ScHO_3$, namely the minimum-energy interstitialcy pathway and both vacancy hops, have heights approximately half those seen in $Ba_2ScHO_3$, while the interstitial hop is raised slightly. The

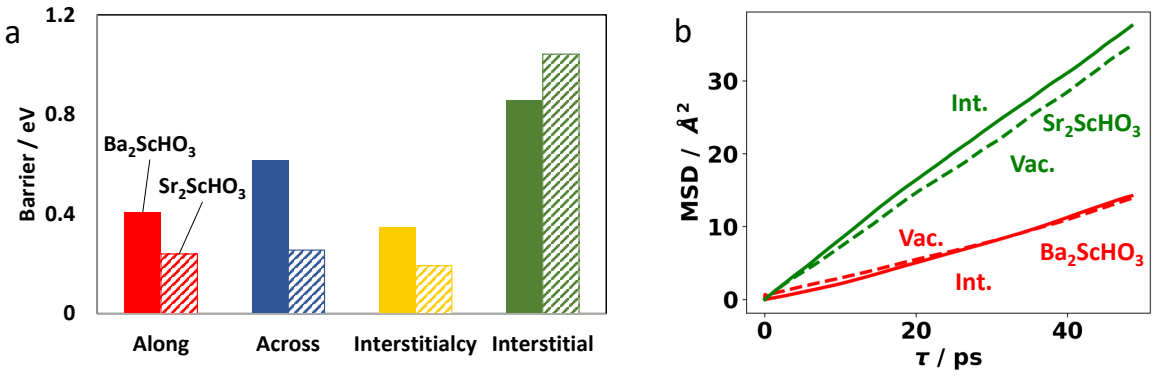



Figure 4.20: Comparison of hydride mobility in $Sr_2ScHO_3$ to $Ba_2ScHO_3$. (a) Comparison of barriers for equivalent processes in $Ba_2ScO_3H$ (solid bars) and $Sr_2ScHO_3$ (hatched bars). (b) MSD plots for hydride ions in interstitial (solid lines) and vacancy (dashed lines) cells of $Sr_2ScHO_3$ (green) and $Ba_2ScHO_3$ (red).

highest energy pathway makes a minimal contribution to hydride mobility, so the most important result is the dramatic reduction in barriers for interstitialcy migration, which remains the lowest energy pathway, and both modes of vacancy migration. The interstitialcy hop transition state contains mobile hydrides in near-trigonal planar coordination with H-Sr bond lengths of 2.44 Å (×2) and 2.41 Å (×1). The high-energy interstitial hop TS has the hydride in linear coordination with H-Sr bond lengths of 2.21 Å and two hydrides at 2.35 Å, with these short-range electrostatic repulsions again explaining why this pathway has the highest barrier. In the 'Along' hop TS, $H^-$ is again displaced along $c$ from the centre of a Sr tetrahedron, giving pairs of H-Sr bond lengths of 2.48 Å and 2.76 Å, and in the 'Across' hop TS $H^-$ is in linear coordination with $Sr^{2+}$ at 2.31 Å.

The MSD plots in Figure 4.20(b) show the displacements for hydrogen climbing constantly, indicating hydride diffusion, with gradients far steeper than those for $Ba_2ScHO_3$, demonstrating much higher mobility. The estimated diffusion constants for these simulations are $1.3 \times 10^{-9}$ $m^2s^{-1}$ for the interstitial cell and $8.9 \times 10^{-10}$ $m^2s^{-1}$ for the vacancy cell. This order-of-magnitude increase matches the substantial reduction in mobility barriers on substitution of Sr for Ba and supports our prediction that $Sr_2ScHO_3$ will show far greater hydride conductivity than $Ba_2ScHO_3$.

The barriers show that an A-site substitution with a smaller cation results in a marked increase in hydride mobility. For the purposes of quantitative structural analysis, we note that the hard-sphere ionic radii of Shannon[179] for $Sr^{2+}$ and $Ba^{2+}$ are 1.31 Å and 1.47 Å respectively, a radius ratio of 89 %. The alternative soft-sphere values of Lang and Smith[180] give the same ratio. We may then use this value as a yardstick

against which to measure the changes in the lattice parameters on on cation substitution - as noted above, these are 2 % for $(a, b)$ and 6 % for $c$. We would expect these values to be 11 % if they were governed in a simple way by the ionic radii, so we must examine the structure more closely to understand our observations. Along $c$ the unit cell contains perovskite layers, spanned by Sc-O and Sc-H bonds, and rock salt layers, spanned by Sr-O and Sr-H bonds, while $a$ and $b$ are fully spanned both by Sc-O and Sr-O bonds. We can thus understand the non-uniformity in the variation of the cell parameters between $Ba_2ScHO_3$ and $Sr_2ScHO_3$. Along $c$ the Sr-O and Sr-H bonds across the rock salt layers can shorten freely to adopt their optimal length, while changes along $a$ and $b$ are largely prevented by the more rigid Sc-O bonds. This makes the Sr-O/H bonds in the $ab$ plane longer than optimal, so the ions have greater freedom to move in this plane and can more readily accommodate mobile hydride ions than in the Ba analogue. This can be seen in the transition state geometries, which feature greater displacements of ions surrounding the mobile hydride.
The consequences of greater in-plane structural flexibility are not confined to the rock salt layers as the TS geometries for $Sr_2ScHO_3$ also show small octahedral tilts which were absent in $Ba_2ScHO_3$. This correlates with the trend in Goldschmidt's tolerance factor $t$ - as the radius of the A cation increases, $t$ falls, suggesting a greater propensity for octahedral tilting. This measure governs cubic perovskites and is therefore only qualitatively applicable to layered oxyhydrides, but it nevertheless captures the relationship between cation size and local distortions which can stabilize transition states.

### 4.3.6 Discussion

$Ba_2ScO_3H$ is of immediate interest in the developing field of hydride conduction because of its unusual anion ordering, which preferentially places hydrides on the lattice sites bordering the rock salt layer in the RP framework. As anticipated, this new ordering enables conduction by pathways as yet unexplored by hydride conductors[155]. The most important lattice site for hydride migration is the tetrahedral site in the rock salt layer in which an anion is surrounded by four A-site cations; this is the geometry both of the interstitial hydride in its resting state and the transition states for vacancy hops. For many hydride conductors these sites are inaccessible as the hydrides are contained entirely in the octahedral layer. In their study of $Ln_2LiHO_3$ (Ln = La, Pr, Nd) Iwasaki et al. [181] calculated a barrier to interstitial migration through the rock salt layer of 1.4 eV. That family of oxyhydrides contains hydride anions in the perovskite layers, so hydrides in the tetrahedral interstitial sites would

have no intersticialcy mechanism available to facilitate hydride transport.

The significance of this tetrahedral site is consistent with RP-phase chemistry in the broader field of oxide conduction. Oxygen-rich phases based on $La_2NiO_4$ have been shown to have high anisotropic oxide mobility[182, 162], arising from conduction through the rock salt layers, and the tetrahedral sites are central to oxide conduction in $Pr_2NiO_{4+\delta}$[163]. Meanwhile, $La_{2-x}Sr_xCuO_{4-y}$ shows in-plane vacancy-driven oxide conduction at low strontium concentration[183]. The tetrahedral sites can also be occupied stoichiometrically, in preference to the "normal" apical site, if cation size constraints require it. This is observed in the series $(La/Nd)_2CuO_4$, where the all-La member has the $K_2NiF_4$ structure, the all-Nd member places all rock-salt-layer oxides in tetrahedral sites, and a 1:1 La:Nd ratio gives alternating behaviour between rock salt layers[184].

At ambient pressure, the lowest barriers for vacancy and interstitial mobility are approximately equal, at 0.41 eV and 0.35 eV respectively. Assuming other, higher-energy pathways make only a minor contribution to the overall ion mobility, we conclude that both types of defect promote hydride conduction equally. It is also interesting that the overall lowest barrier describes a cooperative motion between two hydrides; a defect-rich phase may have access to cooperative motions involving more atoms, providing new low-energy pathways for long-range hydride movement. Takeiri et al.[185] showed B-site doping of $SrTiO_3$ by $Sc^{3+}$ increased the concentration of anion vacancies, so it is plausible that similar strategies could introduce more defects, vacancies or interstitials, into $Ba_2ScHO_3$. We note here that these barriers are somewhat lower than the 0.88 eV measured experimentally; we attribute this difference to possible defect association and the approximations of DFT, but we remain confident in our predicted trends.

Under high pressure, we see significant differences in the behaviour of interstitial and vacancy defects and a change in the principal conduction mechanism. Due to substantial compression of bond lengths in low-coordinate transition states, the barriers to interstitial defect migration rise far more dramatically under pressure than those to vacancy migration. Hydride conduction at 20 GPa may therefore be accessible if mediated by vacancies, but the structural changes immobilize interstitials.

We investigated the effect of changing the A-site cation by studying the hypothetical compound $Sr_2ScHO_3$, which we believe will show significantly improved hydride conductivity over its barium-containing cousin. The improvement is attributed to greater flexibility in the *ab* plane because, despite the smaller A-site cations, $a$ and $b$ do not shorten because of the stiffness of the Sc-O bonds. The behaviour is consistent with

the behaviour of $SrVO_2H$ and $Sr_2VO_3H$ discussed above, where the V-O bonds resist compression most strongly, leading to anisotropic cell deformation[157, 145]. We therefore see another example here of the behaviour of Ruddlesden-Popper derivatives being dominated by their dimensionality; the infinite layers of Sc-O bonds are integral to giving the Sr-H bonds the flexibility needed for improved ion conductivity. The effect of changing the A-site cation has been investigated in other oxyhydride ion conductors. Very similar behaviour was observed in the cubic perovskites $SrTiO_{3-x}H_x$ and $BaTiO_{3-x}H_x$[186, 187], where the barrier to vacancy migration was calculated as 0.17 eV for the former and 0.28 eV for the latter. These cubic perovskites also contain rigid bonding scaffolds, composed of Ti-O bonds, so it is plausible that this represents a three-dimensional example of the effect of Sr-H bond flexibility. This interpretation predicts that conductivity in these perovskite oxyhydrides could be improved further by using a yet smaller cation like $Ca^{2+}$, or an A-site solid solution if such a small cation drives a transition to a new structure type.
In $Ln_2LiHO_3$ the identity of the lanthanide was found to govern hydride conductivity via changes in anion disorder[181] - since the hydrides in those phases are contained in the rock salt layers, and thus coordinated principally to the B cations, it is unsurprising that the effect of changing the size of the A cation is less direct than in our phases. A similar effect was seen in the LnHO series[188], in which the mobile hydrides must pass through a trigonal cation environment reminiscent of the transition state for the interstitialcy mechanism in $Ba_2ScHO_3$, where the size of the "bottleneck" expanded significantly when the size of the cation induced O/H ordering. The authors also found that a "critical bottleneck radius" of 1.18 Å was required for fast ion conduction - we have calculated these radii for the trigonal sites in our interstitialcy mechanisms and found values of 1.15 Å for $Ba_2ScHO_3$ and 1.19 Å for $Sr_2ScHO_3$, consistent with our prediction that $Sr_2ScHO_3$ displays significantly higher conductivity.

## 4.4 Summary and conclusions

In this chapter we have explored structural changes in transition metal oxyhydrides and understood their effects on transport properties. The theme that has emerged from our analysis is that dimensionality plays a defining role in behaviour and trends. In the vanadium oxyhydrides we compared 1D $Sr_2VO_3H$, which undergoes a crystallographic transition at 45 GPa, to 2D $SrVO_2H$, which undergoes an insulator-semimetal transition at 60 GPa. The structural changes under pressure of both compounds show

that the TM-O bonds resist compression most strongly owing to their partial covalent character. In $Sr_2VO_3H$ this leads directly to the $B1 - B2$ transition, whereby the purely ionic inter-layer regions adopt an electrostatically unfavourable arrangement to minimize Pauli repulsions between oppositely charged ions and V-O bond compression. $SrVO_2H$, meanwhile, has no such crystallographic transition available and so cannot avoid appreciable changes to V-O bonding, which results in semimetallic behaviour above 60 GPa, while $Sr_2VO_3H$ is always insulating. These electronic changes were observed computationally by following the V PDOS in both compounds, which showed that the $d$ bands with greatest overlap with O $2p$ broaden the most under pressure.

Our discoveries concerning the high-pressure behaviour of $Sr_2VO_3H$ allowed us to make predictions for the more complex analogue $Ba_2YHO_3$, which contains segregated all-hydride and all-oxide rock salt layers in its unit cell. The prediction of a $B1 - B2$ transition in the hydride layer at the unprecedentedly low pressure of 15 GPa shows that the hydride ion has a dramatic effect on these ionic materials even in $d^0$ transition metal systems.

We then investigated hydride conductivity in $Ba_2ScHO_3$, which differs from $Sr_2VO_3H$ in its anion ordering and $d^0$ metal centre. Transition state calculations, supported by dynamics simulations, revealed that $H^-$ diffusion may be mediated by interstitial and vacancy defects, and we have identified the mechanisms involved. Perhaps the most significant outcome of this study was the prediction of $Sr_2ScHO_3$ as a candidate material for improved $H^-$ conductivity. The enhanced conductivity is thought to arise from increased local structural flexibility on substitution of a smaller A-site cation which lowers $H^-$ migration barriers. As in the vanadium oxyhydrides, the stiffness of TM-O bonds plays a crucial role here. The Sc-O bonds form infinite layers and act as a scaffold, preventing the structure from contracting in the $xy$ plane when a smaller cation is inserted into the rock salt layers.

Our studies of these oxyhydride families shows that structural processes can be understood in terms of the relative rigidity and flexibility of substructures in the crystals. This simple, physical design principle may be of great value to the design of functional polyanionic compounds in the future.

# Perspective

In this thesis we have undertaken two series of theoretical studies of transition metal compounds, one into Zintl clusters and one into solid-state oxyhydride materials. These research themes do not immediately appear to be related to each other. One is molecular, the other periodic; one covalent, the other ionic. However, crossing boundaries between conventionally separate chemical fields is the very essence of transition metal chemistry. We described Zintl clusters with molecular orbital and density of states diagrams alongside each other, allowing us to compare bonding across lengthscales, while the properties of oxyhydrides were understood in terms of the local coordination environments of the transition metal cations and hydride anions. Thus, our decision to study systems from different branches of chemistry allows us to draw broader and more fundamental conclusions about transition metal chemistry. A central theme that has emerged is the contrast between open and closed shell transition metal species. Closed shell cations interact *via* non-directional electrostatic forces, allowing the surrounding anions, ligands and other groups local structural flexibility. In clusters this manifests as isomerism in $[(Ni@Sn_9)In(Ni@Sn_9)]^{5-}$ and metal-dependent oligomerization states in coinage metal clusters. In oxyhydrides we saw hydride conductivity in $Ba_2ScHO_3$, where there are no covalent Sc-H bonds to break, and electrostatically driven anion ordering in $Ba_2YHO_3$. Open shells unlock the door to far greater diversity of electronic properties, from covalent bonding in $Fe_n$ cluster cores to dimension-dependent electron transport transitions in vanadium oxyhydrides. The presence of paramagnetic ions in Zintl clusters is not a guarantee of metal-metal bonding, however, so each compound must be considered in detail, and we anticipate that further studies of this growing family will reveal patterns in structures and bonding. Metal-metal interactions more generally exert a powerful influence on electronic properties, so they must be understood in detail if we are to design new functional materials. At the end of this research project, then, our next task is to harness our new understanding of structural control and $d$ electron chemistry to design new molecules and materials, continuing to work across the classic fields of chemistry to hone our understanding of the transition metals.

"If thou art bored with this wearisome method of calculation, take pity on me, who had to go through with at least seventy repetitions of it, at a very great loss of time." Johannes Kepler, *Astronomia Nova*, **1609**[189]

# Bibliography


[1] E. Clementi and D. L. Raimondi. Atomic screening constants from SCF functions. *Journal of Chemical Physics*, 38(11):2686, 1963.

[2] E. Clementi, D. L. Raimondi, and W. P. Reinhardt. Atomic screening constants from SCF functions. 2. atoms with 37 to 86 electrons. *Journal of Chemical Physics*, 47(4):1300, 1967.

[3] P. Hohenberg and W. Kohn. Inhomogeneous electron gas. *Physical Review B*, 136(3B):B864, 1964.

[4] A. D. Becke. Density functional exchange energy approximation with correct asymptotic behavior. *Physical Review A*, 38(6):3098–3100, 1988.

[5] J. P. Perdew, K. Burke, and M. Ernzerhof. Generalized gradient approximation made simple. *Physical Review Letters*, 77(18):3865–3868, 1996.

[6] C. T. Lee, W. T. Yang, and R. G. Parr. Development of the Colle-Salvetti correlation energy formula into a functional of the electron density. *Physical Review B*, 37(2):785–789, 1988.

[7] P. M. W. Gill. Obituary: Density functional theory (1927-1993). *Australian Journal of Chemistry*, 54(11):661–662, 2001.

[8] J. P. Perdew, M. Ernzerhof, and K. Burke. Rationale for mixing exact exchange with density functional approximations. *Journal of Chemical Physics*, 105(22):9982–9985, 1996.

[9] J. Heyd, G. E. Scuseria, and M. Ernzerhof. Hybrid functionals based on a screened Coulomb potential. *Journal of Chemical Physics*, 118(18):8207–8215, 2003.

[10] I. Solovyev, N. Hamada, and K. Terakura. $t_{2g}$ versus all 3d localization in $LaMO_3$ perovskites (M=Ti-Cu): First-principles study. *Physical Review B*, 53(11):7158–7170, 1996.

[11] F. Weigend and R. Ahlrichs. Balanced basis sets of split valence, triple zeta valence and quadruple zeta valence quality for H to Rn: Design and assessment of accuracy. *Physical Chemistry Chemical Physics*, 7(18):3297–3305, 2005.

[12] G. N. Lewis. The atom and the molecule. *Journal of the American Chemical Society*, 38:762–785, 1916.

[13] I. Cohen. Bond order in LCAO molecular orbital theory. *Journal of Chemical Physics*, 57(12):5076, 1972.

[14] A. J. Bridgeman, G. Cavigliasso, L. R. Ireland, and J. Rothery. The Mayer bond order as a tool in inorganic chemistry. *Journal of the Chemical Society-Dalton Transactions*, (14):2095–2108, 2001.

[15] P. O. Löwdin. Quantum theory of many-particle systems. 2. study of the ordinary Hartree-Fock approximation. *Physical Review*, 97(6):1490–1508, 1955.

[16] K. Ruedenberg. Physical nature of chemical bond. *Reviews of Modern Physics*, 34(2):326, 1962.

[17] J. Poater, M. Sola, M. Duran, and X. Fradera. The calculation of electron localization and delocalization indices at the Hartree-Fock, density functional and post-Hartree-Fock levels of theory. *Theoretical Chemistry Accounts*, 107(6):362–371, 2002.

[18] R. F. W. Bader. A quantum theory of molecular structure and its applications. *Chemical Reviews*, 91(5):893–928, 1991.

[19] V. E. J. Berryman, J. J. Shephard, T. Ochiai, A. N. Price, P. L. Arnold, S. Parsons, and N. Kaltsoyannis. Quantum chemical topology and natural bond orbital analysis of M−O covalency in $M(OC_6H_5)_4$ (M = Ti, Zr, Hf, Ce, Th, Pa, U, Np). *Physical Chemistry Chemical Physics*, 22(29):16804–16812, 2020.

[20] M. Ziolkowski, S. J. Grabowski, and J. Leszczynski. Cooperativity in hydrogen-bonded interactions: Ab initio and "atoms in molecules" analyses. *Journal of Physical Chemistry A*, 110(20):6514–6521, 2006.

[21] D. Cremer and E. Kraka. Chemical bonds without bonding electron density - does the difference electron-density analysis suffice for a description of the chemical bond? *Angewandte Chemie-International Edition in English*, 23(8):627–628, 1984.

[22] J. S. M. Anderson, J. I. Rodriguez, P. W. Ayers, D. E. Trujillo-Gonzalez, A. W. Gotz, J. Autschbach, F. L. Castillo-Alvarado, and K. Yamashita. Molecular QTAIM topology is sensitive to relativistic corrections. *Chemistry - a European Journal*, 25(10):2538–2544, 2019.

[23] J. I. Rodriguez, E. A. Uribe, M. I. Baltazar-Mendez, J. Autschbach, F. L. Castillo-Alvarado, and I. Gutierrez-Gonzalez. Size evolution relativistic DFT-QTAIM study on the gold cluster complexes $Au_4{-}S{-}C_nH_{2n}{-}S{-}Au_4$ (n=2-5). *Chemical Physics Letters*, 660:287–294, 2016.

[24] C. Outeiral, M. A. Vincent, A. M. Pendas, and P. L. A. Popelier. Revitalizing the concept of bond order through delocalization measures in real space. *Chemical Science*, 9(25):5517–5529, 2018.

[25] E. Matito, J. Poater, M. Sola, M. Duran, and P. Salvador. Comparison of the AIM delocalization index and the Mayer and fuzzy atom bond orders. *Journal of Physical Chemistry A*, 109(43):9904–9910, 2005.

[26] G. te Velde, F. M. Bickelhaupt, E. J. Baerends, C. F. Guerra, S. J. A. Van Gisbergen, J. G. Snijders, and T. Ziegler. Chemistry with ADF. *Journal of Computational Chemistry*, 22(9):931–967, 2001.

[27] K. Kitaura and K. Morokuma. A new energy decomposition scheme for molecular interactions within Hartree-Fock approximation. *International Journal of Quantum Chemistry*, 10(2):325–340, 1976.

[28] T. Ziegler and A. Rauk. Theoretical study of the ethylene-metal bond in complexes between $Cu^+$, $Ag^+$, $Au^+$, $Pt^0$ or $Pt^{2+}$ and ethylene, based on the Hartree-Fock-Slater transition-state method. *Inorganic Chemistry*, 18(6):1558–1565, 1979.

[29] V. L. Deringer, A. L. Tchougreeff, and R. Dronskowski. Crystal orbital hamilton population (COHP) analysis as projected from plane-wave basis sets. *Journal of Physical Chemistry A*, 115(21):5461–5466, 2011.

[30] R. Dronskowski and P. E. Blöchl. Crystal orbital hamiltonian populations (COHP) - energy-resolved visualization of chemical bonding in solids based on density-functional calculations. *Journal of Physical Chemistry*, 97(33):8617–8624, 1993.

[31] H. W. T. Morgan, K.-S. Csizi, Y.-S. Huang, Z.-M. Sun, and J. E. McGrady. Open shells in endohedral clusters: Structure and bonding in the $[Fe_2@Ge_{16}]^{4-}$ anion and comparison to isostructural $[Co_2@Ge_{16}]^{4-}$. *The Journal of Physical Chemistry A*, 125(21):4578–4588, 2021.

[32] C. Zhang, H. W. T. Morgan, Z. C. Wang, C. Liu, Z. M. Sun, and J. E. McGrady. Structural isomerism in the $(Ni@Sn_9)In(Ni@Sn_9{}^{5-})$ Zintl ion. *Dalton Transactions*, 48(42):15888–15895, 2019.

[33] L. Qiao, C. Zhang, C. C. Shu, H. W. T. Morgan, J. E. McGrady, and Z. M. Sun. $Cu_4@E_{18}{}^{4-}$ (E = Sn, Pb): Fused derivatives of endohedral stannaspherene and plumbaspherene. *Journal of the American Chemical Society*, 142(31):13288–13293, 2020.

[34] C. C. Shu, H. W. T. Morgan, L. Qiao, J. E. McGrady, and Z. M. Sun. A family of lead clusters with precious metal cores. *Nature Communications*, 11:3477, 2020.

[35] Alfred Stock. *Hydrides of boron and silicon*. George Fisher Baker; 12. Cornell University Press, Ithaca, 1933.

[36] N. N. Greenwood and A. Earnshaw. *Chemistry of the elements*. Elsevier Butterworth-Heinemann, Amsterdam ; Oxford, 2nd edition, 1998.

[37] J. S. Kasper, C. M. Lucht, and D. Harker. The structure of the decaborane molecule. *Journal of the American Chemical Society*, 70(2):881–881, 1948.

[38] H. C. L. Higgins and R. P. Bell. The structure of the boron hydrides. *Journal of the Chemical Society*, pages 250–255, 1943.

[39] K. Wade. Structural significance of number of skeletal bonding electron-pairs in carboranes, higher boranes and borane anions, and various transition-metal carbonyl cluster compounds. *Journal of the Chemical Society D-Chemical Communications*, (15):792, 1971.

[40] D. M. P. Mingos. General theory for cluster and ring compounds of main group and transition elements. *Nature-Physical Science*, 236(68):99, 1972.

[41] E. D. Jemmis, M. M. Balakrishnarajan, and P. D. Pancharatna. A unifying electron-counting rule for macropolyhedral boranes, metallaboranes, and metallocenes. *Journal of the American Chemical Society*, 123(18):4313–4323, 2001.

[42] L. F. Cui, X. Huang, L. M. Wang, J. Li, and L. S. Wang. $Pb_{12}^{2-}$: Plumbaspherene. *Journal of Physical Chemistry A*, 110(34):10169–10172, 2006.

[43] M. McPartlin, C. R. Eady, B. F. G. Johnson, and J. Lewis. X-ray structures of hexanuclear cluster complexes $Os_6(CO)_{18}^{2-}$, $HOs_6(CO)_{18}^{-}$, and $H_2Os_6(CO)_{18}$. *Journal of the Chemical Society-Chemical Communications*, (21):883–885, 1976.

[44] N. N. Greenwood, C. G. Savory, R. N. Grimes, L. G. Sneddon, A. Davison, and S. S. Wreford. Preparation of a stable small ferraborane, $B_4H_8Fe(CO)_3$. *Journal of the Chemical Society-Chemical Communications*, (17):718–718, 1974.

[45] K. Wiesler, K. Brandl, A. Fleischmann, and N. Korber. Tetrahedral $Tt_4^{4-}$ Zintl anions through solution chemistry: Syntheses and crystal structures of the ammoniates $Rb_4Sn_4{\cdot}_2NH_3$, $Cs_4Sn_4{\cdot}2\,NH_3$, and $Rb_4Pb_4{\cdot}2\,NH_3$. *Zeitschrift Fur Anorganische Und Allgemeine Chemie*, 635(3):508–512, 2009.

[46] V. Queneau and S. C. Sevov. $Ge_9^{4-}$: A deltahedral Zintl ion now made in the solid-state. *Angewandte Chemie-International Edition in English*, 36(16):1754–1756, 1997.

[47] J. Witte, H. G. Schnering, and W. Klemm. Das Verhalten der Alkalimetalle zu Halbmetallen. XI. Die Kristallstruktur von NaSi und NaGe. *Zeitschrift Fur Anorganische Und Allgemeine Chemie*, 327(3-4):260–273, 1964.

[48] C. Liu, L. J. Li, Q. J. Pan, and Z. M. Sun. $Ge_5Ni_2(CO)_3^{2-}$: the first functionalized cluster of closo- $Ge_5^{2-}$. *Chemical Communications*, 53(47):6315–6318, 2017.

[49] L. Xu and S. C. Sevov. Oxidative coupling of deltahedral $Ge_9^{4-}$ zintl ions. *Journal of the American Chemical Society*, 121(39):9245–9246, 1999.

[50] A. Ugrinov and S. C. Sevov. $Ge_9{=}Ge_9{=}Ge_9^{6-}$: A linear trimer of 27 germanium atoms. *Journal of the American Chemical Society*, 124(37):10990–10991, 2002.

[51] L. Yong, S. D. Hoffmann, and T. F. Fässler. Oxidative coupling of $Ge_9^{4-}$ Zintl anions - hexagonal rod packing of linear $Ge_9$=$Ge_9$=$Ge_9$=$Ge_9^{8-}$. *Zeitschrift Fur Anorganische Und Allgemeine Chemie*, 630(12):1977–1981, 2004.

[52] C. Downie, Z. J. Tang, and A. M. Guloy. An unprecedented $_{1\infty}[Ge_9]^{2-}$ polymer: A link between molecular zintl clusters and solid-state phases. *Angewandte Chemie-International Edition*, 39(2):338, 2000.

[53] G. S. Armatas and M. G. Kanatzidis. Mesostructured germanium with cubic pore symmetry. *Nature*, 441(7097):1122–1125, 2006.

[54] M. M. Gillett-Kunnath, J. I. Paik, S. M. Jensen, J. D. Taylor, and S. C. Sevov. Metal-centered deltahedral Zintl ions: Synthesis of $Ni@Sn_9^{4-}$ by direct extraction from intermetallic precursors and of the vertex-fused dimer $[(Ni@Sn_8(\mu{-}Ge)_{1/2})_2]^{4-}$. *Inorganic Chemistry*, 50(22):11695–11701, 2011.

[55] A. Spiekermann, S. D. Hoffinann, and T. F. Fässler. The Zintl ion $Pb_{10}^{2-}$: A rare example of a homoatomic closo cluster. *Angewandte Chemie-International Edition*, 45(21):3459–3462, 2006.

[56] M. M. Bentlohner, C. Fischer, and T. F. Fässler. Synthesis and characterization of pristine closo- $Ge_{10}^{2-}$. *Chemical Communications*, 52(63):9841–9843, 2016.

[57] C. Schrenk, F. Winter, R. Pottgen, and A. Schnepf. $[Sn_{10}(Si(SiMe_3)_3)_4]^{2-}$ : A highly reactive metalloid tin cluster with an open ligand shell. *Chemistry-a European Journal*, 21(7):2992–2997, 2015.

[58] C. Liu, X. Jin, L. J. Li, J. Xu, J. E. McGrady, and Z. M. Sun. Synthesis and structure of a family of rhodium polystannide clusters $Rh@Sn_{10}^{3-}$, $Rh@Sn_{12}^{3-}$, $Rh_2@Sn_{17}^{6-}$ and the first triply-fused stannide, $Rh_3@Sn_{24}^{5-}$. *Chemical Science*, 10(16):4394–4401, 2019.

[59] L. F. Cui, X. Huang, L. M. Wang, D. Y. Zubarev, A. I. Boldyrev, J. Li, and L. S. Wang. $Sn_{12}^{2-}$: Stannaspherene. *Journal of the American Chemical Society*, 128(26):8390–8391, 2006.

[60] L. F. Cui and L. S. Wang. Stable icosahedral hollow cage clusters: stannaspherene $Sn_{12}^{2-}$ and plumbaspherene $Pb_{12}^{2-}$. *International Reviews in Physical Chemistry*, 27(1):139–166, 2008.

[61] R. B. King, I. Silaghi-Dumitrescu, and M. M. Uta. Density functional theory study of twelve-atom germanium clusters: conflict between the Wade-Mingos rules and optimum vertex degrees. *Dalton Transactions*, (3):364–372, 2007.

[62] J. Q. Wang, S. Stegmaier, B. Wahl, and T. F. Fässler. Step-by-step synthesis of the endohedral stannaspherene $Ir@Sn_{12}^{3-}$ via the capped cluster anion $Sn_9Ir(cod)^{3-}$. *Chemistry-a European Journal*, 16(6):1793–1798, 2010.

[63] E. N. Esenturk, J. Fettinger, Y. F. Lam, and B. Eichhorn. $Pt@Pb_{12}^{2-}$. *Angewandte Chemie-International Edition*, 43(16):2132–2134, 2004.

[64] R. J. Wilson, N. Lichtenberger, B. Weinert, and S. Dehnen. Intermetalloid and heterometallic clusters combining p-block (semi)metals with d- or f-block metals. *Chemical Reviews*, 119(14):8506–8554, 2019.

[65] B. B. Zhou, T. Kramer, A. L. Thompson, J. E. McGrady, and J. M. Goicoechea. A highly distorted open-shell endohedral Zintl cluster: $Mn@Pb_{12}^{3-}$. *Inorganic Chemistry*, 50(17):8028–8037, 2011.

[66] C. Liu, L. J. Li, I. A. Popov, R. J. Wilson, C. Q. Xu, J. Li, A. I. Boldyrev, and Z. M. Sun. Symmetry reduction upon size mismatch: The non-icosahedral intermetalloid cluster $Co@Ge_{12}^{3-}$. *Chinese Journal of Chemistry*, 36(12):1165–1168, 2018.

[67] G. Espinoza-Quintero, J. C. A. Duckworth, W. K. Myers, J. E. McGrady, and J. M. Goicoechea. Synthesis and characterization of $Ru@Ge_{12}^{3-}$: An endohedral 3-connected cluster. *Journal of the American Chemical Society*, 136(4):1210–1213, 2014.

[68] V. Arcisauskaite, D. Fijan, M. Spivak, C. de Graaf, and J. E. McGrady. Biradical character in the ground state of $[Mn@Si_{12}]^{+}$: a DFT and CASPT2 study. *Physical Chemistry Chemical Physics*, 18(34):24006–24014, 2016.

[69] B. B. Zhou, M. S. Denning, D. L. Kays, and J. M. Goicoechea. Synthesis and isolation of $Fe@Ge_{10}^{3-}$: A pentagonal prismatic Zintl ion cage encapsulating an interstitial iron atom. *Journal of the American Chemical Society*, 131(8):2802, 2009.

[70] J. Q. Wang, S. Stegmaier, and T. F. Fässler. $Co@Ge_{10}^{3-}$: An intermetalloid cluster with Archimedean pentagonal prismatic structure. *Angewandte Chemie-International Edition*, 48(11):1998–2002, 2009.

[71] S. Mitzinger, L. Broeckaert, W. Massa, F. Weigend, and S. Dehnen. Understanding of multimetallic cluster growth. *Nature Communications*, 7:10480, 2016.

[72] B. J. L. Witzel, W. Klein, J. V. Duns, M. Boyko, and T. F. Fässler. Metallocages for metal anions: Highly charged $Co@Ge_9^{5-}$ and $Ru@Sn_9^{6-}$ clusters featuring spherically encapsulated $Co^{1-}$ and $Ru^{2-}$ anions. *Angewandte Chemie-International Edition*, 58(37):12908–12913, 2019.

[73] Y. R. Wang, C. Zhang, X. Y. Wang, J. Q. Guo, Z. M. Sun, and H. B. Zhang. Site-selective $CO_2$ reduction over highly dispersed $RuSnO_x$ sites derived from a $Ru@Sn_9^{6-}$ Zintl cluster. *Acs Catalysis*, 10(14):7808–7819, 2020.

[74] J. M. Goicoechea and S. C. Sevov. (pd-pd)@ge-18 (4-): A palladium dimer inside the largest single-cage deltahedron. *Journal of the American Chemical Society*, 127(21):7676–7677, 2005.

[75] J. M. Goicoechea and S. C. Sevov. $(Ni{-}Ni{-}Ni)@(Ge_9)_2^{4-}$ : A linear triatomic nickel filament enclosed in a dimer of nine-atom germanium clusters. *Angewandte Chemie-International Edition*, 44(26):4026–4028, 2005.

[76] R. J. Eisenhart, P. A. Rudd, N. Planas, D. W. Boyce, R. K. Carlson, W. B. Tolman, E. Bill, L. Gagliardi, and C. C. Lu. Pushing the limits of delta bonding in metal-chromium complexes with redox changes and metal swapping. *Inorganic Chemistry*, 54(15):7579–7592, 2015.

[77] M. M. Bentlohner, L. A. Jantke, T. Henneberger, C. Fischer, K. Mayer, W. Klein, and T. F. Fässler. On the nature of bridging metal atoms in intermetalloid clusters: Synthesis and structure of the metal-atom-bridged zintl clusters $[Sn(Ge_9)_2]^{4-}$ and $[Zn(Ge_9)_2]^{6-}$. *Chemistry-a European Journal*, 22(39):13946–13952, 2016.

[78] B. B. Zhou, M. S. Denning, T. A. D. Chapman, J. E. McGrady, and J. M. Goicoechea. $Pb_9CdCdPb_9^{6-}$: A Zintl cluster anion with an unsupported cadmium-cadmium bond. *Chemical Communications*, (46):7221–7223, 2009.

[79] S. Stegmaier and T. F. Fässler. A bronze matryoshka: The discrete intermetalloid cluster $Sn@Cu_{12}@Sn_{20}^{12-}$ in the ternary phases $A_{12}Cu_{12}Sn_{21}$ (A = Na, K). *Journal of the American Chemical Society*, 133(49):19758–19768, 2011.

[80] T. B. Tai, N. M. Tam, and M. T. Nguyen. Evolution of structures and stabilities of zinc-doped tin clusters $Sn_nZn$, n=1-12. three-dimensional aromaticity of the magic clusters $Sn_{10}Zn$ and $Sn_{12}Zn$. *Chemical Physics*, 388(1-3):1–8, 2011.

[81] T. B. Tai and M. T. Nguyen. Enhanced stability by three-dimensional aromaticity of endohedrally doped clusters $X_{10}M^{0/-}$ with X = Ge, Sn, Pb and M = Cu, Ag, Au. *Journal of Physical Chemistry A*, 115(35):9993–9999, 2011.

[82] V. T. Ngan, K. Pierloot, and M. T. Nguyen. $Mn@Si_{14}^{+}$: a singlet fullerene-like endohedrally doped silicon cluster. *Physical Chemistry Chemical Physics*, 15(15):5493–5498, 2013.

[83] E. Roduner. Superatom chemistry: promising properties of near-spherical noble metal clusters. *Physical Chemistry Chemical Physics*, 20(37):23812–23826, 2018.

[84] A. Hirsch, Z. F. Chen, and H. J. Jiao. Spherical aromaticity in $I_h$ symmetrical fullerenes: The $2(n+1)^2$ rule. *Angewandte Chemie-International Edition*, 39(21):3915, 2000.

[85] J. T. Lau, K. Hirsch, P. Klar, A. Langenberg, F. Lofink, R. Richter, J. Rittmann, M. Vogel, V. Zamudio-Bayer, T. Moller, and B. von Issendorff. X-ray spectroscopy reveals high symmetry and electronic shell structure of transition-metal-doped silicon clusters. *Physical Review A*, 79(5), 2009.

[86] W. Huang, A. P. Sergeeva, H. J. Zhai, B. B. Averkiev, L. S. Wang, and A. I. Boldyrev. A concentric planar doubly $\pi$-aromatic $B_{19}^{-}$ cluster. *Nature Chemistry*, 2(3):202–206, 2010.

[87] T. B. Tai, R. W. A. Havenith, J. L. Teunissen, A. R. Dok, S. D. Hallaert, M. T. Nguyen, and A. Ceulemans. Particle on a boron disk: Ring currents and disk aromaticity in $B_{20}^{2-}$. *Inorganic Chemistry*, 52(18):10595–10600, 2013.

[88] P. V. Schleyer, C. Maerker, A. Dransfeld, H. J. Jiao, and Njrv Hommes. Nucleus-independent chemical shifts: A simple and efficient aromaticity probe. *Journal of the American Chemical Society*, 118(26):6317–6318, 1996.

[89] D. Y. Zubarev and A. I. Boldyrev. Developing paradigms of chemical bonding: adaptive natural density partitioning. *Physical Chemistry Chemical Physics*, 10(34):5207–5217, 2008.

[90] C. Liu, I. A. Popov, L. J. Li, N. Li, A. I. Boldyrev, and Z. M. Sun. $Co_2@Ge_{16}^{4-}$: Localized versus delocalized bonding in two isomeric intermetalloid clusters. *Chemistry-a European Journal*, 24(3):699–705, 2018.

[91] X. Jin, G. Espinoza-Quintero, B. Below, V. Arcisauskaite, J. M. Goicoechea, and J. E. McGrady. Structure and bonding in a bimetallic endohedral cage, $Co_2@Ge_{16}^{z-}$. *Journal of Organometallic Chemistry*, 792:149–153, 2015.

[92] E. Van Lenthe and E. J. Baerends. Optimized Slater-type basis sets for the elements 1-118. *Journal of Computational Chemistry*, 24(9):1142–1156, 2003.

[93] C. C. Pye and T. Ziegler. An implementation of the conductor-like screening model of solvation within the Amsterdam density functional package. *Theoretical Chemistry Accounts*, 101(6):396–408, 1999.

[94] I. F. Galvan, M. Vacher, A. Alavi, C. Angeli, F. Aquilante, J. Autschbach, J. J. Bao, S. I. Bokarev, N. A. Bogdanov, R. K. Carlson, L. F. Chibotaru, J. Creutzberg, N. Dattani, M. G. Delcey, S. J. S. Dong, A. Dreuw, L. Freitag, L. M. Frutos, L. Gagliardi, F. Gendron, A. Giussani, L. Gonzalez, G. Grell, M. Y. Guo, C. E. Hoyer, M. Johansson, S. Keller, S. Knecht, G. Kovacevic, E. Kallman, G. Li Manni, M. Lundberg, Y. J. Ma, S. Mai, J. P. Malhado, P. A. Malmqvist, P. Marquetand, S. A. Mewes, J. Norell, M. Olivucci, M. Oppel, Q. M. Phung, K. Pierloot, F. Plasser, M. Reiher, A. M. Sand, I. Schapiro, P. Sharma, C. J. Stein, L. K. Sorensen, D. G. Truhlar, M. Ugandi, L. Ungur, A. Valentini, S. Vancoillie, V. Veryazov, O. Weser, T. A. Wesolowski, P. O. Widmark, S. Wouters, A. Zech, J. P. Zobel, and R. Lindh. OpenMolcas: From source code to insight. *Journal of Chemical Theory and Computation*, 15(11):5925–5964, 2019.

[95] F. Aquilante, J. Autschbach, A. Baiardi, S. Battaglia, V. A. Borin, L. F. Chibotaru, I. Conti, L. De Vico, M. Delcey, I. F. Galvan, N. Ferre, L. Freitag, M. Garavelli, X. J. Gong, S. Knecht, E. D. Larsson, R. Lindh, M. Lundberg, P. A. Malmqvist, A. Nenov, J. Norell, M. Odelius, M. Olivucci, T. B. Pedersen, L. Pedraza-Gonzalez, Q. M. Phung, K. Pierloot, M. Reiher, I. Schapiro, J. Segarra-Marti, F. Segatta, L. Seijo, S. Sen, D. C. Sergentu, C. J. Stein, L. Ungur, M. Vacher, A. Valentini, and V. Veryazov. Modern quantum chemistry with OpenMolcas. *Journal of Chemical Physics*, 152(21), 2020.

[96] J. Almlof and P. R. Taylor. General contraction of gaussian basis sets. 1. atomic natural orbitals for 1st-row and 2nd-row atoms. *Journal of Chemical Physics*, 86(7):4070–4077, 1987.

[97] K. Pierloot, B. Dumez, P. O. Widmark, and B. O. Roos. Density-matrix averaged atomic natural orbital (ANO) basis sets for correlated molecular wavefunctions. 4. medium-size basis sets for the atoms H-Kr. *Theoretica Chimica Acta*, 90(2-3):87–114, 1995.

[98] B. O. Roos, A. C. Borin, and L. Gagliardi. Reaching the maximum multiplicity of the covalent chemical bond. *Angewandte Chemie-International Edition*, 46(9):1469–1472, 2007.

[99] S. Scharfe and T. F. Fässler. Varying bonding modes of the Zintl ion $Ge_9^{4-}$ in Cu-I complexes: Syntheses and structures of $Cu(\eta^4{-}Ge_9)(PR_3)^{3-}$ (R = iPr, Cy) and $Cu(\eta^4{-}Ge_9)(\eta^1{-}Ge_9)^{7-}$. *European Journal of Inorganic Chemistry*, (8):1207–1213, 2010.

[100] D. F. Hansen, B. B. Zhou, and J. M. Goicoechea. Further studies into the reactivity and coordination chemistry of $Ge_9^{4-}$ Zintl ions. the indium-containing anions $In(Ge_9)_2^{5-}$), $(Ge_9)_2In(C_6H_5)^{4-}$ and $Ge_9[In(C_6H_5)_3]_2^{4-}$. *Journal of Organometallic Chemistry*, 721:53–61, 2012.

[101] F. S. Geitner, W. Klein, and T. F. Fässler. Formation of the intermetalloid cluster $AgSn_{18}^{7-}$ - the reactivity of coinage metal NHC compounds towards $Sn_9^{4-}$. *Dalton Transactions*, 46(18):5796–5800, 2017.

[102] L. Yong, M. B. Boeddinghaus, and T. F. Fässler. $Sn_9HgSn_9^{6-}$: An intermetalloid Zintl ion with two $Sn_9$ connected by heteroatom. *Zeitschrift Fur Anorganische Und Allgemeine Chemie*, 636(7):1293–1296, 2010.

[103] K. Mayer, L. A. Jantke, S. Schulz, and T. F. Fässler. Retention of the Zn-Zn bond in $Ge_9Zn{-}ZnGe_9^{6-}$ and formation of $(Ge_9Zn){-}(Ge_9){-}(ZnGe_9)^{8-}$ and polymeric $_{1\infty}{-}(Ge_9Zn)^{2-}$. *Angewandte Chemie-International Edition*, 56(9):2350–2355, 2017.

[104] A. Spiekermann, S. D. Hoffmann, F. Kraus, and T. F. Fässler. $Au_3Ge_{18}^{5-}$ - a gold-germanium cluster with remarkable Au-Au interactions. *Angewandte Chemie-International Edition*, 46(10):1638–1640, 2007.

[105] M. S. Denning and J. M. Goicoechea. $Hg_3(Ge_9)_4^{10-}$: a nanometric molecular rod precursor to polymeric mercury-linked cluster chains. *Dalton Transactions*, (43):5882–5885, 2008.

[106] A. Nienhaus, R. Hauptmann, and T. F. Fässler. $_{1\infty}HgGe_9^{2-}$ - a polymer with Zintl ions as buliding blocks covalently linked by heteroatoms. *Angewandte Chemie-International Edition*, 41(17):3213, 2002.

[107] M. B. Boeddinghaus, S. D. Hoffmann, and T. F. Fässler. Synthesis and crystal structure of $K[2.2-crypt]_2[HgGe_9](dmf)$. *Zeitschrift Fur Anorganische Und Allgemeine Chemie*, 633(13-14):2338–2341, 2007.

[108] A. Spiekermann, S. D. Hoffmann, T. F. Fässler, I. Krossing, and U. Preiss. $Au_3Ge_{45}^{9-}$ - a binary anion containing a $Ge_{45}$ cluster. *Angewandte Chemie-International Edition*, 46(28):5310–5313, 2007.

[109] E. N. Esenturk, J. C. Fettinger, and B. W. Eichhorn. Synthesis, structure, and dynamic properties of $Ni_2Sn_{17}^{4-}$. *Journal of the American Chemical Society*, 128(1):12–13, 2006.

[110] H. Y. He, W. Klein, L. A. Jantke, and T. F. Fässler. Metal-centered Zintl ions isolated by direct extraction from endohedral intermetallic precursor: $Co_{1-x}@Sn_9^{4-}$ ($x \sim 0.32$) and $Co_2@Sn_{17}^{5-}$. *Zeitschrift Fur Anorganische Und Allgemeine Chemie*, 640(14):2864–2870, 2014.

[111] B. Kesanli, J. E. Halsig, P. Zavalij, J. C. Fettinger, Y. F. Lam, and B. W. Eichhorn. Cluster growth and fragmentation in the highly fluxional platinum derivatives of $Sn_9^{4-}$: Synthesis, characterization, and solution dynamics of $Pt_2@Sn_{17}^{4-}$ and $Pt@Sn_9H_3$. *Journal of the American Chemical Society*, 129(15):4567–4574, 2007.

[112] F. Neese. The ORCA program system. *Wiley Interdisciplinary Reviews-Computational Molecular Science*, 2(1):73–78, 2012.

[113] K. Eichkorn, O. Treutler, H. Ohm, M. Haser, and R. Ahlrichs. Auxiliary basis sets to approximate Coulomb potentials. *Chemical Physics Letters*, 240(4):283–289, 1995.

[114] V. Barone and M. Cossi. Quantum calculation of molecular energies and energy gradients in solution by a conductor solvent model. *Journal of Physical Chemistry A*, 102(11):1995–2001, 1998.

[115] C. Liu, L. J. Li, X. Jin, J. E. McGrady, and Z. M. Sun. Reactivity studies of $Co@Sn_9^{4-}$ with transition metal reagents: Bottom-up synthesis of ternary functionalized Zintl clusters. *Inorganic Chemistry*, 57(6):3025–3034, 2018.

[116] C. Hoch, M. Wendorff, and C. Rohr. Tetrapotassium nonastannide, $K_4Sn_9$. *Acta Crystallographica Section C-Crystal Structure Communications*, 58:I45–I46, 2002.

[117] J. M. Goicoechea and S. C. Sevov. Deltahedral germanium clusters: Insertion of transition-metal atoms and addition of organometallic fragments. *Journal of the American Chemical Society*, 128(12):4155–4161, 2006.

[118] S. C. Sevov and J. M. Goicoechea. Chemistry of deltahedral Zintl ions. *Organometallics*, 25(24):5678–5692, 2006.

[119] R. H. D. Lyngdoh, H. F. Schaefer, and R. B. King. Metal-metal (MM) bond distances and bond orders in binuclear metal complexes of the first row transition metals titanium through zinc. *Chemical Reviews*, 118(24):11626–11706, 2018.

[120] H. Lee, X. J. Wu, and L. C. Sun. Copper-based homogeneous and heterogeneous catalysts for electrochemical water oxidation. *Nanoscale*, 12(7):4187–4218, 2020.

[121] V. K. Y. Lo, A. O. Y. Chan, and C. M. Che. Gold and silver catalysis: from organic transformation to bioconjugation. *Organic and Biomolecular Chemistry*, 13(24):6667–6680, 2015.

[122] X. Y. Dong, Z. W. Gao, K. F. Yang, W. Q. Zhang, and L. W. Xu. Nanosilver as a new generation of silver catalysts in organic transformations for efficient synthesis of fine chemicals. *Catalysis Science and Technology*, 5(5):2554–2574, 2015.

[123] G. Li and R. C. Jin. Atomically precise gold nanoclusters as new model catalysts. *Accounts of Chemical Research*, 46(8):1749–1758, 2013.

[124] L. G. AbdulHalim, M. S. Bootharaju, Q. Tang, S. Del Gobbo, R. G. AbdulHalim, M. Eddaoudi, D. E. Jiang, and O. M. Bakr. $Ag_{29}BDT_{12}TPP_4$: A tetravalent nanocluster. *Journal of the American Chemical Society*, 137(37):11970–11975, 2015.

[125] N. Kaur, R. N. Aditya, A. Singh, and T. R. Kuo. Biomedical applications for gold nanoclusters: Recent developments and future perspectives. *Nanoscale Research Letters*, 13:12, 2018.

[126] I. Chakraborty and T. Pradeep. Atomically precise clusters of noble metals: Emerging link between atoms and nanoparticles. *Chemical Reviews*, 117(12):8208–8271, 2017.

[127] I. Katakuse, T. Ichihara, Y. Fujita, T. Matsuo, T. Sakurai, and H. Matsuda. Mass distributions of copper, silver and gold clusters and electronic shell structure. *International Journal of Mass Spectrometry and Ion Processes*, 67(2):229–236, 1985.

[128] W. A. de Heer. The physics of simple metal clusters: experimental aspects and simple models. *Reviews of Modern Physics*, 65(3):611–676, 1993.

[129] P. Gruene, D. M. Rayner, B. Redlich, A. F. G. van der Meer, J. T. Lyon, G. Meijer, and A. Fielicke. Structures of neutral $Au_7$, $Au_{19}$, and $Au_{20}$ clusters in the gas phase. *Science*, 321(5889):674–676, 2008.

[130] V. G. Albano, P. L. Bellon, M. Manassero, and M. Sansoni. Intermetallic pattern in metal-atom clusters - structural studies on $Au_{11}X_3(PR_3)_7$ species. *Journal of the Chemical Society D - Chemical Communications*, (18):1210, 1970.

[131] C. E. Briant, B. R. C. Theobald, J. W. White, L. K. Bell, D. M. P. Mingos, and A. J. Welch. Synthesis and x-ray structural characterization of the centered icosahedral gold cluster compound $Au_{13}(PMe_2PH)_{10}Cl_2(PF_6)_3$ - the realization of a theoretical prediction. *Journal of the Chemical Society-Chemical Communications*, (5):201–202, 1981.

[132] T. G. Schaaff, G. Knight, M. N. Shafigullin, R. F. Borkman, and R. L. Whetten. Isolation and selected properties of a 10.4 kDa gold : Glutathione cluster compound. *Journal of Physical Chemistry B*, 102(52):10643–10646, 1998.

[133] C. J. Zeng, H. F. Qian, T. Li, G. Li, N. L. Rosi, B. Yoon, R. N. Barnett, R. L. Whetten, U. Landman, and R. C. Jin. Total structure and electronic properties of the gold nanocrystal $Au_{36}(SR)_{24}$. *Angewandte Chemie-International Edition*, 51(52):13114–13118, 2012.

[134] A. Dass, S. Theivendran, P. R. Nimmala, C. Kumara, V. R. Jupally, A. Fortunelli, L. Sementa, G. Barcaro, X. B. Zuo, and B. C. Noll. $Au_{133}(SPh{-}tBu)_{52}$ nanomolecules: X-ray crystallography, optical, electrochemical, and theoretical analysis. *Journal of the American Chemical Society*, 137(14):4610–4613, 2015.

[135] H. Häkkinen, M. Walter, and H. Gronbeck. Divide and protect: Capping gold nanoclusters with molecular gold-thiolate rings. *Journal of Physical Chemistry B*, 110(20):9927–9931, 2006.

[136] C. P. Joshi, M. S. Bootharaju, M. J. Alhilaly, and O. M. Bakr. $Ag_{25}(SR)_{18}{}^{-}$: The "golden" silver nanoparticle. *Journal of the American Chemical Society*, 137(36):11578–11581, 2015.

[137] H. Y. Yang, Y. Wang, X. Chen, X. J. Zhao, L. Gu, H. Q. Huang, J. Z. Yan, C. F. Xu, G. Li, J. C. Wu, A. J. Edwards, B. Dittrich, Z. C. Tang, D. D. Wang, L. Lehtovaara, H. Häkkinen, and N. F. Zheng. Plasmonic twinned silver nanoparticles with molecular precision. *Nature Communications*, 7:12809, 2016.

[138] Y. Negishi, T. Iwai, and M. Ide. Continuous modulation of electronic structure of stable thiolate-protected $Au_{25}$ cluster by Ag doping. *Chemical Communications*, 46(26):4713–4715, 2010.

[139] E. Vanlenthe, E. J. Baerends, and J. G. Snijders. Relativistic regular 2-component Hamiltonians. *Journal of Chemical Physics*, 99(6):4597–4610, 1993.

[140] E. Vanlenthe, E. J. Baerends, and J. G. Snijders. Relativistic total energy using regular approximations. *Journal of Chemical Physics*, 101(11):9783–9792, 1994.

[141] E. van Lenthe, A. Ehlers, and E. J. Baerends. Geometry optimizations in the zero order regular approximation for relativistic effects. *Journal of Chemical Physics*, 110(18):8943–8953, 1999.

[142] M. L. H. Green. A new approach to the formal classification of covalent compounds of the elements. *Journal of Organometallic Chemistry*, 500(1-2):127–148, 1995.

[143] J. G. Kester, D. Keller, J. C. Huffman, M. A. Benefiel, W. E. Geiger, C. Atwood, A. R. Siedle, G. A. Korba, and L. J. Todd. Synthesis and properties of copper and nickel complexes of the general formula $(B_{11}H_{11})_2M^{N-}$ - crystal structure of $(n{-}Bu)_4N_3Cu(B_{11}H_{11})_2$. *Inorganic Chemistry*, 33(24):5438–5442, 1994.

[144] A. M. Li, Y. Wang, P. Y. Zavalij, F. Chen, A. Muñoz Castro, and B. W. Eichhorn. $Cp^*RuPb_{11}^{3-}$ and $Cu@Cp^*RuPb_{11}^{2-}$: centered and non-centered transition-metal substituted Zintl icosahedra. *Chemical Communications*, 56(74):10859–10862, 2020.

[145] T. Yamamoto, H. W. T. Morgan, D. H. Zeng, T. Kawakami, M. A. Patino, M. A. Hayward, H. Kageyama, and J. E. McGrady. Pressure-induced transitions in the 1-dimensional vanadium oxyhydrides $Sr_2VO_3H$ and $Sr_3V_2O_5H_2$, and comparison to 2-dimensional $SrVO_2H$. *Inorganic Chemistry*, 58(22):15393–15400, 2019.

[146] H. W. T. Morgan, H. J. Stroud, and N. L. Allan. Improving hydride conductivity in layered perovskites via crystal engineering. *Chemistry of Materials*, 33(1):177–185, 2021.

[147] Eduard Farber. The development of metal hydride chemistry. *Chymia*, 8:165–180, 1962.

[148] W. Hieber and F. Leutert. Information on the coordinative bonded carbon oxide - the formation of iron carbonyl hydrogen. *Naturwissenschaften*, 19:360–361, 1931.

[149] W. Hieber, F. Muhlbauer, and E. A. Ehmann. Derivatives of cobalt and nickel carbonyl (XVI. announcement on the metal carbonyls). *Berichte Der Deutschen Chemischen Gesellschaft*, 65(7):1090–1101, 1932.

[150] G. Wilkinson and J. M. Birmingham. Biscyclopentadienylrhenium hydride - a new type of hydride. *Journal of the American Chemical Society*, 77(12):3421–3422, 1955.

[151] M. A. Hayward, E. J. Cussen, J. B. Claridge, M. Bieringer, M. J. Rosseinsky, C. J. Kiely, S. J. Blundell, I. M. Marshall, and F. L. Pratt. The hydride anion in an extended transition metal oxide array: $LaSrCoO_3H_{0.7}$. *Science*, 295(5561):1882–1884, 2002.

[152] G. Kobayashi, Y. Hinuma, S. Matsuoka, A. Watanabe, M. Iqbal, M. Hirayama, M. Yonemura, T. Kamiyama, I. Tanaka, and R. Kanno. Pure $H^-$ conduction in oxyhydrides. *Science*, 351(6279):1314–1317, 2016.

[153] F. D. Romero, A. Leach, J. S. Moller, F. Foronda, S. J. Blundell, and M. A. Hayward. Strontium vanadium oxide-hydrides: "square-planar" two-electron phases. *Angewandte Chemie-International Edition*, 53(29):7556–7559, 2014.

[154] M. A. Patino, D. H. Zeng, S. J. Blundell, J. E. McGrady, and M. A. Hayward. Extreme sensitivity of a topochemical reaction to cation substitution: $SrVO_2H$ versus $SrV_{1-x}Ti_xO_{1.5}H_{1.5}$. *Inorganic Chemistry*, 57(5):2890–2898, 2018.

[155] F. Takeiri, A. Watanabe, A. Kuwabara, H. Nawaz, N. I. P. Ayu, M. Yonemura, R. Kanno, and G. Kobayashi. $Ba_2ScHO_3$: $H^-$ conductive layered oxyhydride with $H^-$ site selectivity. *Inorganic Chemistry*, 58(7):4431–4436, 2019.

[156] Haq Nawaz, Fumitaka Takeiri, Akihide Kuwabara, Masao Yonemura, and Genki Kobayashi. Synthesis and $H^-$ conductivity of a new oxyhydride $Ba_2YHO_3$ with anion-ordered rock-salt layers. *Chemical Communications*, 56(71):10373–10376, 2020.

[157] T. Yamamoto, D. H. Zeng, T. Kawakami, V. Arcisauskaite, K. Yata, M. A. Patino, N. Izumo, J. E. McGrady, H. Kageyama, and M. A. Hayward. The role of $\pi$-blocking hydride ligands in a pressure-induced insulator-to-metal phase transition in $SrVO_2H$. *Nature Communications*, 8:1217, 2017.

[158] T. Yamamoto, Y. Kobayashi, T. Okada, T. Yagi, T. Kawakami, C. Tassel, S. Kawasaki, N. Abe, K. Niwa, T. Kikegawa, N. Hirao, M. Takano, and H. Kageyama. B1-to-B2 structural transitions in rock salt intergrowth structures. *Inorganic Chemistry*, 50(22):11787–11794, 2011.

[159] Q. Bai, X. F. He, Y. Z. Zhu, and Y. F. Mo. First-principles study of oxyhydride $H^-$ ion conductors: Toward facile anion conduction in oxide-based materials. *Acs Applied Energy Materials*, 1(4):1626–1634, 2018.

[160] O. S. Fjellvåg, J. Armstrong, P. Vajeeston, and A. O. Sjåstad. New insights into hydride bonding, dynamics, and migration in $La_2LiHO_3$ oxyhydride. *Journal of Physical Chemistry Letters*, 9(2):353–358, 2018.

[161] O. S. Fjellvåg, M. Krzystyniak, P. Vajeeston, A. O. Sjåstad, and J. Armstrong. A combined deep inelastic neutron scattering and ab initio lattice dynamics study of the hydride anion dynamics and bonding in $La_2LiHO_3$ oxyhydride. *Journal of Physics Communications*, 3(10):7, 2019.

[162] J. M. Bassat, P. Odier, A. Villesuzanne, C. Marin, and M. Pouchard. Anisotropic ionic transport properties in $La_2NiO_{4+\delta}$ single crystals. *Solid State Ionics*, 167(3-4):341–347, 2004.

[163] M. Yashima, M. Enoki, T. Wakita, R. Ali, Y. Matsushita, F. Izumi, and T. Ishihara. Structural disorder and diffusional pathway of oxide ions in a doped $Pr_2NiO_4$-based mixed conductor. *Journal of the American Chemical Society*, 130(9):2762, 2008.

[164] Akihide Kuwabara, Fumitake Takeiri, Haq Nawaz, and Genki Kobayashi. First-principles calculations of point defect formation and anion diffusion mechanism in oxyhydride $Ba_2ScHO_3$. *ChemRxiv*, 10.26434/chemrxiv.12121254.v1, 2020.

[165] G. Kresse and J. Furthmuller. Efficient iterative schemes for ab initio total-energy calculations using a plane-wave basis set. *Physical Review B*, 54(16):11169–11186, 1996.

[166] P. E. Blöchl. Projector augmented wave method. *Physical Review B*, 50(24):17953–17979, 1994.

[167] C. E. Sims, G. D. Barrera, N. L. Allan, and W. C. Mackrodt. Thermodynamics and mechanism of the B1-B2 phase transition in group-I halides and group-II oxides. *Physical Review B*, 57(18):11164–11172, 1998.

[168] M. Alfredsson, J. P. Brodholt, P. B. Wilson, G. D. Price, F. Cora, A. Calleja, R. Bruin, L. J. Blanshard, and R. P. Tyer. Structural and magnetic phase transitions in simple oxides using hybrid functionals. *Molecular Simulation*, 31(5):367–377, 2005.

[169] A. J. Cinthia, G. S. Priyanga, R. Rajeswarapalanichamy, and K. Iyakutti. Structural, electronic and mechanical properties of alkaline earth metal oxides MO (M=Be, Mg, Ca, Sr, Ba). *Journal of Physics and Chemistry of Solids*, 79:23–42, 2015.

[170] J. F. Mammone, H. K. Mao, and P. M. Bell. Equations of state of CaO under static pressure conditions. *Geophysical Research Letters*, 8(2):140–142, 1981.

[171] Y. Sato and R. Jeanloz. Phase transition in SrO. *Journal of Geophysical Research*, 86(NB12):1773–1778, 1981.

[172] T. Yamamoto, C. Tassel, Y. Kobayashi, T. Kawakami, T. Okada, T. Yagi, H. Yoshida, T. Kamatani, Y. Watanabe, T. Kikegawa, M. Takano, K. Yoshimura, and H. Kageyama. Pressure-induced structural, magnetic, and transport transitions in the two-legged ladder $Sr_3Fe_2O_5$. *Journal of the American Chemical Society*, 133(15):6036–6043, 2011.

[173] D. Sheppard, P. H. Xiao, W. Chemelewski, D. D. Johnson, and G. Henkelman. A generalized solid-state nudged elastic band method. *Journal of Chemical Physics*, 136(7):8, 2012.

[174] G. Henkelman, B. P. Uberuaga, and H. Jonsson. A climbing image nudged elastic band method for finding saddle points and minimum energy paths. *Journal of Chemical Physics*, 113(22):9901–9904, 2000.

[175] W. Humphrey, A. Dalke, and K. Schulten. VMD: Visual molecular dynamics. *Journal of Molecular Graphics and Modelling*, 14(1):33–38, 1996.

[176] S. Nose. A unified formulation of the constant temperature molecular dynamics methods. *Journal of Chemical Physics*, 81(1):511–519, 1984.

[177] K. Momma and F. Izumi. VESTA: a three-dimensional visualization system for electronic and structural analysis. *Journal of Applied Crystallography*, 41:653–658, 2008.

[178] W. G. Hoover. Canonical dynamics - equilibrium phase-space distributions. *Physical Review A*, 31(3):1695–1697, 1985.

[179] R. D. Shannon. Revised effective ionic radii and systematic studies of interatomic distances in halides and chalcogenides. *Acta Crystallographica Section A*, 32(SEP1):751–767, 1976.

[180] P. F. Lang and B. C. Smith. Ionic radii for group 1 and group 2 halide, hydride, fluoride, oxide, sulfide, selenide and telluride crystals. *Dalton Transactions*, 39(33):7786–7791, 2010.

[181] Y. Iwasaki, N. Matsui, K. Suzuki, Y. Hinuma, M. Yonemura, G. Kobayashi, M. Hirayama, I. Tanaka, and R. Kanno. Synthesis, crystal structure, and ionic conductivity of hydride ion- conducting $Ln_2LiHO_3$ (Ln = La, Pr, Nd) oxyhydrides. *Journal of Materials Chemistry A*, 6(46):23457–23463, 2018.

[182] S. J. Skinner and J. A. Kilner. Oxygen diffusion and surface exchange in $La_{2-x}Sr_xNiO_{4+\delta}$. *Solid State Ionics*, 135(1-4):709–712, 2000.

[183] E. J. Opila, H. L. Tuller, B. J. Wuensch, and J. Maier. Oxygen tracer diffusion in $La_{2-x}Sr_xCuO_{4-y}$ single crystals. *Journal of the American Ceramic Society*, 76(9):2363–2369, 1993.

[184] N. L. Allan, P. S. Baram, W. C. Mackrodt, and M. J. Turner. Differences between high-Tc oxides containing 6-fold, 5-fold, 4-fold and 2-fold coordinated copper. *Molecular Simulation*, 9(2):115–128, 1992.

[185] F. Takeiri, K. Aidzu, T. Yajima, T. Matsui, T. Yamamoto, Y. Kobayashi, J. Hester, and H. Kageyama. Promoted hydride/oxide exchange in $SrTiO_3$ by introduction of anion vacancy via aliovalent cation substitution. *Inorganic Chemistry*, 56(21):13035–13040, 2017.

[186] X. Liu, T. S. Bjorheim, L. Vines, O. S. Fjellvåg, C. Granerod, O. Prytz, T. Yamamoto, H. Kageyama, T. Norby, and R. Haugsrud. Highly correlated hydride ion tracer diffusion in $SrTiO_{3-x}H_x$ oxyhydrides. *Journal of the American Chemical Society*, 141(11):4653–4659, 2019.

[187] X. Liu, T. S. Bjorheim, and R. Haugsrud. Formation and migration of hydride ions in $BaTiO_{3-x}H_x$ oxyhydride. *Journal of Materials Chemistry A*, 5(3):1050–1056, 2017.

[188] H. Ubukata, T. Broux, F. Takeiri, K. Shitara, H. Yamashita, A. Kuwabara, G. Kobayashi, and H. Kageyama. Hydride conductivity in an anion-ordered fluorite structure LnHO with an enlarged bottleneck. *Chemistry of Materials*, 31(18):7360–7366, 2019.

[189] Arthur Koestler. *The sleepwalkers; a history of man's changing vision of the universe*. London : Hutchinson, 1959.